

AD-762 297

INVESTIGATION OF ROTATING STALL IN  
AXIAL FLOW COMPRESSORS AND THE DEVELOP-  
MENT OF A PROTOTYPE ROTATING STALL  
CONTROL SYSTEM

Gary R. Ludwig, et al

Calspan Corporation

Prepared for:

Air Force Aero Propulsion Laboratory

May 1973

DISTRIBUTED BY:

**NTIS**

National Technical Information Service  
U. S. DEPARTMENT OF COMMERCE  
5285 Port Royal Road, Springfield Va. 22151

AFAPL-TR-73-45

AD 762297

INVESTIGATION OF ROTATING STALL IN AXIAL FLOW  
COMPRESSORS AND THE DEVELOPMENT OF A  
PROTOTYPE ROTATING STALL CONTROL SYSTEM

G.R. Ludwig, J.P. Nenni and R.H. Arendt

Calspan Corporation

TECHNICAL REPORT AFAPL-TR-73-45

MAY 1973

Approved for public release;  
Distribution unlimited.

DDC  
RECEIVED  
JUN 28 1973  
RECEIVED  
B

Reproduced by  
NATIONAL TECHNICAL  
INFORMATION SERVICE  
U S Department of Commerce  
Springfield VA 22151

U.S. AIR FORCE AERO PROPULSION LABORATORY  
AIR FORCE SYSTEMS COMMAND  
WRIGHT-PATTERSON AIR FORCE BASE, OHIO

Reproduced From  
Best Available Copy

280

UNCLASSIFIED

Security Classification

## DOCUMENT CONTROL DATA - R &amp; D

(Security classification of title, body of abstract and indexing annotation must be entered when the overall report is classified)

1. ORIGINATING ACTIVITY (Corporate author) Calspan Corporation Buffalo, New York 14221		2a. REPORT SECURITY CLASSIFICATION UNCLASSIFIED	
		2b. GROUP	
3. REPORT TITLE INVESTIGATION OF ROTATING STALL IN AXIAL COMPRESSORS AND THE DEVELOPMENT OF A PROTO-TYPE ROTATING STALL CONTROL SYSTEM			
4. DESCRIPTIVE NOTES (Type of report and inclusive dates) Final Report			
5. AUTHOR(S) (First name, middle initial, last name) Gary R. Ludwig Joseph P. Nenni Rudy H. Arendt			
6. REPORT DATE May 1973	7a. TOTAL NO. OF PAGES 287	7b. NO. OF REFS 14	
8a. CONTRACT OR GRANT NO. F33615-70-C-1122	9a. ORIGINATOR'S REPORT NUMBER(S) Calspan Report No. Mk-2932-A-13		
b. PROJECT NO. 3066	9b. OTHER REPORT NO(S) (Any other numbers that may be assigned this report) AFAPL-TR-73-45		
c. 306603			
d. 3066034			
10. DISTRIBUTION STATEMENT Approved for public release; Distribution unlimited.			
11. SUPPLEMENTARY NOTES		12. SPONSORING MILITARY ACTIVITY U.S. Air Force Aero Propulsion Laboratory Wright-Patterson Air Force Base, Ohio	
13. ABSTRACT This report summarizes the results of a three year program on rotating stall in axial flow compressors conducted at Calspan Corporation (formerly Cornell Aeronautical Laboratory). The work encompassed both experimental and theoretical investigations of rotating stall and the development of a prototype rotating stall control system. The experimental portion of the program included investigation of the effects of blade chord and solidity upon rotating stall properties and inception as well as an investigation of the effect of blade row rotation on blade row performance. In addition, an experiment to determine the stability of the flow through a blade row was conducted. A two-dimensional small-disturbance stability theory was developed to predict the inception of rotating stall. A single blade row and two blade row version of the theory were developed. The theory identifies the mechanism of rotating stall and indicates that blade row spacing controls the number of stall cells that develop at inception. Good correlation between the theory and present data were generally obtained. A prototype rotating stall control system was developed and tested on a low speed compressor stage. This was done in conjunction with an experimental investigation to determine the best sensor configuration to determine incipient rotating stall in a compressor. Tests on the complete control system indicate that there are several sensor configurations that result in a satisfactory system. For these configurations it was possible to keep the compressor stage out of stall in the presence of a primary engine control that was calling for the stage to operate beyond the rotating stall boundary.			

DD FORM 1473  
1 NOV 64Reproduced From  
Best Available Copy

UNCLASSIFIED

Security Classification

UNCLASSIFIED

Security Classification

14 KEY WORDS	LINK A		LINK B		LINK C	
	ROLE	WT	ROLE	WT	ROLE	WT
Rotating Stall Compressor Cascade Control Systems Fluid Mechanics Jet Engines						

UNCLASSIFIED  
Security Classification

NOTICE

When Government drawings, specifications, or other data are used for any purpose other than in connection with a definitely related Government procurement operation, the United States Government thereby incurs no responsibility nor any obligation whatsoever; and the fact that the Government may have formulated, furnished, or in any way supplied the said drawings, specifications, or other data, is not to be regarded by implication or otherwise as in any manner licensing the holder or any other person or corporation, or conveying any rights or permission to manufacture, use, or sell any patented invention that may in any way be related thereto.

COPY CHECK LIST	
White Section	<input checked="" type="checkbox"/>
Blue Section	<input type="checkbox"/>
...	<input type="checkbox"/>
RESTRICTION/AVAILABILITY CODES	
CLASS.	GROUP. REF. OR SPECIAL
A	

Copies of this report should not be returned unless return is required by security considerations, contractual obligations, or notice on a specific document.

INVESTIGATION OF ROTATING STALL IN AXIAL FLOW  
COMPRESSORS AND THE DEVELOPMENT OF A  
PROTOTYPE ROTATING STALL CONTROL SYSTEM

G.R. Ludwig, J.P. Nenni and R.H. Arendt

TECHNICAL REPORT AFAPL-TR-73-45

MAY 1973

Approved for public release;  
Distribution unlimited.

10

## FOREWORD

This report describes the work performed by Calspan Corporation (formerly Cornell Aeronautical Laboratory) Buffalo, New York for the United States Air Force Systems Command, Air Force Aero Propulsion Laboratory, Wright Patterson Air Force Base, Ohio. The work was performed over a three year period starting in March 1970 under U. S. Air Force Contract No. F33615-70-C-1122, Project No. 3066. Mr. Marvin A. Stibich/AFAPL/TBC, Turbine Engine Division, Components Branch administered the Project for the Air Force.

The report contains the results of analytical and experimental studies of flow processes basic to the problem of rotating stall and is a continuation of a research program initiated prior to 1959 under U. S. Air Force Contract AF 33(616)-3558 and continued since 1962 under U. S. Army Contract DA 49-186-AMC - 13(X) and U. S. Air Force Contracts AF 33(615)-1240, AF 33(615)-3537 and F33615-67-C-1552. Calspan has assigned number MK-2932-A-13 to this publication. The authors submitted this document for U. S. Air Force review in May 1973.

Dr. G. R. Ludwig was principal investigator for Calspan. Dr. Ludwig was primarily responsible for overall supervision of the program and the experimental aspects of this program. Mr. J. P. Nenni was responsible for the theoretical phases of the program while Mr. R. H. Arendt assisted Dr. Ludwig in design of the prototype rotating stall control system and was responsible for its fabrication. The contributions of Mr. S. Samet who assisted in developing computer programs under the theoretical phases of the program, and Mr. J. Nemeth who assisted in the experimental program are gratefully acknowledged.

Publication of this report does not constitute Air Force approval of the report's findings or conclusions. It is published only for the exchange and stimulation of ideas.

  
E. C. SIMPSON

Chief, Turbine Engine Division

## ABSTRACT

This report summarizes the results of a three year program on rotating stall in axial flow compressors conducted at Calspan Corporation (formerly Cornell Aeronautical Laboratory). The work encompassed both experimental and theoretical investigations of rotating stall and the development of a prototype rotating stall control system. The experimental portion of the program included investigation of the effects of blade chord and solidity upon rotating stall properties and inception as well as an investigation of the effect of blade row rotation on blade row performance. In addition an experiment to determine the stability of the flow through a blade row was conducted.

A two-dimensional small-disturbance stability theory was developed to predict the inception of rotating stall. A single blade row and two blade row version of the theory were developed. The theory identifies the mechanism of rotating stall and indicates that blade row spacing controls the number of stall cells that develop at inception. Good correlation between the theory and present data were generally obtained.

A prototype rotating stall control system was developed and tested on a low speed compressor stage. This was done in conjunction with an experimental investigation to determine the best sensor configuration to determine incipient rotating stall in a compressor. Tests on the complete control system indicate that there are several sensor configurations that result in a satisfactory system. For these configurations it was possible to keep the compressor stage out of stall in the presence of a primary engine control that was calling for the stage to operate beyond the rotating stall boundary.



TABLE OF CONTENTS

SECTION	PAGE
I INTRODUCTION . . . . .	1
II EXPERIMENTAL ROTATING STALL RESEARCH . . . . .	3
A. DESCRIPTION OF ANNULAR CASCADE FACILITY WITH STATIONARY HUB . . . . .	5
1. General Description . . . . .	5
2. Calibration of Stationary Inlet Guide Vanes . . . . .	9
B. INVESTIGATION OF EFFECT OF BLADE CHORD ON ROTATING STALL . . . . .	11
C. DESCRIPTION OF ANNULAR CASCADE FACILITY WITH ROTATING HUB. . . . .	21
1. General Description . . . . .	21
2. Calibration of Rotating Guide Vanes . . . . .	24
D. INVESTIGATION OF EFFECT OF BLADE ROTATION ON ROTATING STALL. . . . .	27
1. Experiments on Stator Set No. 6 (Stationary Rotor) . . . . .	28
2. Experiments on Rotor Set No. 1 . . . . .	31
3. Comparison of Stationary and Rotating Blade Row Results . . . . .	36
E. CONCLUDING REMARKS . . . . .	41
III THEORETICAL ROTATING STALL RESEARCH . . . . .	43
A. SINGLE BLADE-ROW THEORY. . . . .	46
B. TWO BLADE-ROW THEORY . . . . .	57
C. CONSTANT PRESSURE BOUNDARY CONDITIONS . . . . .	62
D. INVESTIGATION OF TIME DELAY . . . . .	66
E. CONCLUDING REMARKS ON THEORETICAL WORK . . . . .	70

TABLE OF CONTENTS (Cont'd)

SECTION	PAGE
IV DEVELOPMENT OF A PROTOTYPE ROTATING STALL CONTROL SYSTEM . . . . .	72
A. SENSOR INVESTIGATION . . . . .	74
B. DESCRIPTION OF ROTATING STALL CONTROL . . .	79
C. TESTS OF ROTATING STALL CONTROL SYSTEM . .	84
D. CONCLUDING REMARKS . . . . .	92
V SUMMARY AND CONCLUSIONS . . . . .	94
APPENDIX A EXPERIMENTAL INVESTIGATION OF THE STABILITY OF FLOW THROUGH A BLADE-ROW	97
APPENDIX B DETAILED DEVELOPMENT OF THE TWO BLADE-ROW ROTATING STALL STABILITY THEORY . .	105
REFERENCES . . . . .	258

## ILLUSTRATIONS

FIGURE		PAGE
1	Notation for Annular Cascade with Stationary Hub	115
2	Plan View of Research Annular Cascade Facility Attached to Calspan/Air Force One-Foot High-Speed Wind Tunnel	116
3	Overall View of Annular Cascade Test Section	117
4	View of Annular Cascade Test Section	118
5	Details of Annular Cascade Facility with Stationary Hub	119
6	Average Inlet Swirl Angle, $\bar{\beta}_{1M}$ , at Mid-Annulus and Overall Inlet Swirl Angle, $\bar{\beta}_1$ , as a Function of Inlet Guide Vane Stagger Angle	120
7	Overall Total Pressure Loss Through Inlet Guide Vanes	121
8	Rotating Stall Inception Boundaries on Stator Sets No. 1, 4, and 5	122
9	Radial Distributions of Average Swirl Angle Downstream of Stator Set No. 4	123
	(a) Stator Stagger Angle, $\delta_{SM} = 28.2$ deg.	123
	(b) Stator Stagger Angle, $\delta_{SM} = 37.2$ deg.	124
	(c) Stator Stagger Angle, $\delta_{SM} = 47.2$ deg.	125
10	Radial Distribution of Total Pressure Upstream and Downstream of Stator Set No. 4	126

ILLUSTRATIONS (Cont'd)

FIGURE		PAGE
	(a) Stator Stagger Angle, $\delta_{SM} = 28.2$ deg. (4 Sheets)	126
	(b) Stator Stagger Angle, $\delta_{SM} = 37.2$ deg. (4 Sheets)	130
	(c) Stator Stagger Angle, $\delta_{SM} = 47.2$ deg. (5 Sheets)	134
11	Overall and Mid-Annulus Flow Turning Performance of Stator Set No. 1	139
12	Overall and Mid-Annulus Flow Turning Performance of Stator Set No. 4	140
13	Overall and Mid-Annulus Flow Turning Performance of Stator Set No. 5	141
14	Overall Total Pressure Loss Through Stator Set No. 1	142
15	Overall Total Pressure Loss Through Stator Set No. 4	143
16	Overall Total Pressure Loss Through Stator Set No. 5	144
17	Rotating Stall Propagation Velocity and Number of Cells on Stator Sets No. 1, 4, and 5 (2 Sheets)	145
18	Notation for Annular Cascade with Rotating Hub	147
19	Partial Rear View of Rotor Assembly	148
20	Partial Front View of Rotor Assembly	149
21	Details of Rotating Hub Configuration of Annular Cascade Facility	151

ILLUSTRATIONS (Cont'd)

FIGURE		PAGE
22	Average Swirl Angle Distribution Along a Radius Downstream of Rotating Guide Vanes, Guide Vane Stagger Angle at Hub, $\delta_{GV} = 36.1$ Degrees (2 Sheets)	153
23	Radial Distribution of Total Pressure Downstream of Rotating Guide Vanes, Guide Vane Stagger Angle at Hub, $\delta_{GV} = 36.1$ Degrees	155
24	Overall Inlet Swirl Angle Downstream of Rotating Guide Vanes, Guide Vane Stagger Angle at Hub $\delta_{GV} = 36.1$ Degrees	156
25	Overall Total Pressure Downstream of Rotating Guide Vanes, Guide Vane Stagger Angle at Hub, $\delta_{GV} = 36.1$ Degrees	157
26	Average Swirl Angle Distributions Along a Radius Downstream of Stator Set No. 6	158
	(a) Stator Stagger Angle, $\delta_{SM} = 30$ Degrees	158
	(b) Stator Stagger Angle, $\delta_{SM} = 40$ Degrees	159
	(c) Stator Stagger Angle, $\delta_{SM} = 50$ Degrees	160
27	Radial Distributions of Average Total Pressure Loss Through Stator Set No. 6	161
	(a) Stator Stagger Angle, $\delta_{SM} = 30$ Degrees	161
	(b) Stator Stagger Angle, $\delta_{SM} = 40$ Degrees	162
	(c) Stator Stagger Angle, $\delta_{SM} = 50$ Degrees	163
28	Overall Flow Turning Performance of Stator Set No. 6	164
29	Overall Total Pressure Loss Through Stator Set No. 6	165

ILLUSTRATIONS (Cont'd)

FIGURE		PAGE
30	Rotating Stall Propagation Velocity and Number of Cells on Stator Set No. 6	166
31	Average Swirl Angle Distribution Along a Radius Downstream of Rotor Set No. 1, Absolute Coordinate System	167
	(a) Rotor Stagger Angle, $\delta_{RM} = 30$ Degrees	167
	(b) Rotor Stagger Angle, $\delta_{RM} = 40$ Degrees	168
	(c) Rotor Stagger Angle, $\delta_{RM} = 50$ Degrees	169
32	Radial Distributions of Total Pressure Downstream of Rotor Set No. 1, Absolute Coordinate System	170
	(a) Rotor Stagger Angle, $\delta_{RM} = 30$ Degrees	170
	(b) Rotor Stagger Angle, $\delta_{RM} = 40$ Degrees	171
	(c) Rotor Stagger Angle, $\delta_{RM} = 50$ Degrees	172
33	Average Swirl Angle Distributions Along a Radius Downstream of Rotor Set No. 1, Coordinate System Moving with Rotor	173
	(a) Rotor Stagger Angle, $\delta_{RM} = 30$ Degrees	173
	(b) Rotor Stagger Angle, $\delta_{RM} = 40$ Degrees	174
	(c) Rotor Stagger Angle, $\delta_{RM} = 50$ Degrees	175
34	Radial Distributions of Average Total Pressure Loss Through Rotor Set No. 1, Coordinate System Moving with Rotor	176
	(a) Rotor Stagger Angle, $\delta_{RM} = 30$ Degrees	176
	(b) Rotor Stagger Angle, $\delta_{RM} = 40$ Degrees	177
	(c) Rotor Stagger Angle, $\delta_{RM} = 50$ Degrees	178
35	Overall Inlet Swirl Angle, $\bar{\beta}_{1R}$ , Relative to Rotor Set No. 1 as a Function of Rotor RPM	179

ILLUSTRATIONS (Cont'd)

FIGURE		PAGE
36	Flow Turning Performance of Rotor Set No. 1, Coordinate System Relative to Rotor	180
37	Overall Total Pressure Loss Through Rotor Set No. 1, Coordinate System Relative to Rotor	181
38	Rotating Stall Propagation Velocity and Number of Cells on Rotor Set No. 1	182
39	Finite Thickness Actuator Model for Single Blade Row Theory	183
40	Rotating Stall Inception Boundary on Stator Set No. 1 and Comparison with Theory	184
41	Rotating Stall Inception Boundary on Stator Set No. 4 and Comparison with Theory	185
42	Rotating Stall Inception Boundary on Stator Set No. 5 and Comparison with Theory	186
43	Rotating Stall Inception Boundary on Stator Set No. 6 and Comparison with Theory	187
44	Rotating Stall Inception Boundary on Rotor Set No. 1 and Comparison with Theory	188
45	Theoretical Stability Characteristics of Stator Set No. 1	189
	(a) Stator Stagger Angle, $\delta_{SM} = 28.2$ Deg.	189
	(b) Stator Stagger Angle, $\delta_{SM} = 57.2$ Deg.	190

## ILLUSTRATIONS (Cont'd)

FIGURE		PAGE
46	Theoretical Stability Characteristics of Stator Set No. 4	191
	(a) Stator Stagger Angle, $\delta_{SM} = 28.2$ Deg.	191
	(b) Stator Stagger Angle, $\delta_{SM} = 37.2$ Deg.	192
	(c) Stator Stagger Angle, $\delta_{SM} = 47.2$ Deg.	193
47	Theoretical Stability Characteristics of Stator Set No. 5	194
	(a) Stator Stagger Angle, $\delta_{SM} = 28.2$ Deg.	194
	(b) Stator Stagger Angle, $\delta_{SM} = 29.2$ Deg.	195
	(c) Stator Stagger Angle, $\delta_{SM} = 38.2$ Deg.	196
	(d) Stator Stagger Angle, $\delta_{SM} = 47.2$ Deg.	197
	(e) Stator Stagger Angle, $\delta_{SM} = 57.2$ Deg.	198
48	Theoretical Stability Characteristics of Stator Set No. 6	199
	(a) Stator Stagger Angle, $\delta_{SM} = 30$ Deg.	199
	(b) Stator Stagger Angle, $\delta_{SM} = 40$ Deg.	200
	(c) Stator Stagger Angle, $\delta_{SM} = 50$ Deg.	201
49	Theoretical Stability Characteristics of Rotor Set No. 1	202
	(a) Rotor Stagger Angle, $\delta_{RM} = 30$ Deg.	202
	(b) Rotor Stagger Angle, $\delta_{RM} = 40$ Deg.	203
	(c) Rotor Stagger Angle, $\delta_{RM} = 50$ Deg.	204
50	Finite Thickness Actuator Model for Two Blade Row Theory	205
51	Theoretical Effect of Halving the Blade Row Spacing on Stator Set No. 4	206
	(a) $\delta_{SM} = 28.2$ Deg., $n = 3$	206
	(b) $\delta_{SM} = 28.2$ Deg., $n = 8$	207



ILLUSTRATIONS (Cont'd)

FIGURE		PAGE
52	Theoretical Stability Characteristics of Rotor Set No. 1 Assuming Constant Pressure Just Downstream of Rotor	208
	(a) Rotor Stagger Angle, $\delta_{RM} = 30$ Deg.	208
	(b) Rotor Stagger Angle, $\delta_{RM} = 40$ Deg.	209
	(c) Rotor Stagger Angle, $\delta_{RM} = 50$ Deg.	210
53	Annular Cascade Configuration Used to Test Prototype Rotating Stall Control and Sensors	211
54	Razor Blade Yaw Probe	212
55	Cylindrical Yaw Probe	213
56	Unsteady Pressure Records from Various Rotating Stall Sensor Configurations, Inlet Guide Vane Stagger Angle, $\delta_{GV} = 24.5$ Degrees	214
	(a) Sensors ⑦ and ③, Stator Row 5 Unloaded	214
	(b) Sensors ① and ⑤, Stator Row 5 Unloaded	215
	(c) Sensors ② and ⑥, Stator Row 5 Unloaded	216
	(d) Sensors ⑦ and ④, Stator Row 5 Unloaded	217
	(e) Sensors ⑧ and ⑨, Stator Row 5 Unloaded	218
	(f) Sensors ④ and ③, Stator Row 5 Loaded	219
	(g) Sensors ② and ⑥, Stator Row 5 Loaded	220
57	Unsteady Pressure Records from Various Rotating Stall Sensor Configurations, Inlet Guide Vane Stagger Angle, $\delta_{GV} = 40.5$ Degrees	221
	(a) Sensors ⑦ and ③, Stator Row 5 Unloaded	221
	(b) Sensors ① and ⑤, Stator Row 5 Unloaded	222
	(c) Sensors ② and ⑥, Stator Row 5 Unloaded	223
	(d) Sensors ⑦ and ④, Stator Row 5 Unloaded	224

ILLUSTRATIONS (Cont'd)

FIGURE		PAGE
	(e) Sensors ⑧ and ⑨ , Stator Row 5 Unloaded	225
	(f) Sensors ④ and ③ , Stator Row 5 Loaded	226
	(g) Sensors ② and ⑥ , Stator Row 5 Loaded	227
58	Signal Processing Subsystem	228
59	Signal Processing Subsystem with Two Time Constants	229
60	Electronics Control Panel for Prototype Rotating Stall Control System	230
61	Actuator Valve and Feedback Potentiometer Assembly	231
62	Installation of Rotating Stall Control System on Rotating Annular Cascade	232
63	Installation of Electro-Hydraulic Actuator on Rotating Annular Cascade	233
64	Effect of Detector Reference Level and Integrator Gain on Performance of Rotating Stall Control Annular Cascade Configuration: Stator Row 5 Unloaded, Guide Vane Stagger Angle, $\delta_{GV} = 32.5$ Deg. Detector Signal: Sum of [Sensor ⑤ (Outer Wall 1/4 Chord Static, Stator Row 4)] + 0.23 [ Sensor 7 (Rotor Outer Wall)]	235
	(a) Detector Reference Level = 1000	235
	(b) Detector Reference Level = 70 and 80	236
	(c) Detector Reference Level = 90 and 100	237
65	Effect of Integrator Gain on Performance of Rotating Stall Control	238

## ILLUSTRATIONS (Cont'd)

FIGURE

PAGE

Annular Cascade Configuration: Stator Row 5 Unloaded,  
Guide Vane Stagger Angle,  $\delta_{GV} = 32.5$  Deg.

Detector Signal: Sum of [Sensor (5) (Outer Wall  
1/4 Chord Static, Stator Row 4)] + 0.23 [Sensor (7)  
(Rotor Outer Wall)]

- |     |                               |     |
|-----|-------------------------------|-----|
| (a) | Integrator Gain = 200 and 400 | 238 |
| (b) | Integrator Gain = 600 and 800 | 239 |
| (c) | Integrator Gain = 1000        | 240 |

66 Performance of Rotating Stall Control at Various  
Detector Reference Levels with Integrator Gain = 800.  
Detector Signal: Sensor (2) , Mid-Annulus Total  
Pressure, Stator Row 5

- |     |   |     |
|-----|---|-----|
| (a) | Annular Cascade Configuration: Stator Row 5<br>Loaded, Guide Vane Stagger Angle,<br>$\delta_{GV} = 24.5$ Deg. | 241 |
| (b) | Annular Cascade Configuration: Stator Row 5<br>Loaded, Guide Vane Stagger Angle,<br>$\delta_{GV} = 32.5$ Deg. | 242 |
| (c) | Annular Cascade Configuration: Stator Row 5<br>Loaded, Guide Vane Stagger Angle,<br>$\delta_{GV} = 40.5$ Deg. | 243 |
| (d) | Annular Cascade Configuration: Stator Row 5<br>Loaded, Guide Vane Stagger Angle,<br>$\delta_{GV} = 48.5$ Deg. | 244 |

67 Performance of Rotating Stall Control at Various  
Detector Reference Levels with Integrator Gain = 800.  
Detector Signal: Sensor (7) , Rotor Outer Wall  
Annular Cascade Configuration: Stator Row 5 Loaded,  
Guide Vane Stagger Angle,  $\delta_{GV} = 24.5$  Deg.

ILLUSTRATIONS (Cont'd)

FIGURE		PAGE
68	<p>Performance of Rotating Stall Control at Various                      Detector Reference Levels with Integrator Gain =                      800.</p> <p>Detector Signal: Sensor (6) , Outer Wall 1/4 Chord                      Static, Stator Row 5</p> <p>Annular Cascade Configuration: Stator Row 5 Loaded,                      Guide Vane Stagger Angle, <math>\delta_{GV} = 24.5</math> Deg.</p>	246
69	<p>Performance of Rotating Stall Control During Rotor                      Acceleration from 1000 rpm (Normally Unstalled) to                      1250 rpm (Normally Stalled)</p> <p>Annular Cascade Configuration: Stator Row 5 Loaded,                      Guide Vane Stagger Angle, <math>\delta_{GV} = 24.5</math> Deg.</p> <p>(a) Detector Signal: Sensor (5) , Mid-Annulus                      Total Pressure, Stator Row 5</p> <p>(b) Detector Signal: Sensor (7) , Rotor Outer Wall</p> <p>(c) Detector Signal: Sensor (6) , Outer Wall                      1/4 Chord Static, Stator Row 5</p>	247 248 249
70	<p>Sketch of Disturbance Generators Used in Experi-                      mental Damping Investigation</p>	251
71	<p>Disturbance Generator Drive Mounted on Annular                      Cascade</p>	252
72	<p>Schematics of Relationship Between Disturbance                      Generators and Quarter-Chord Static Pressure Taps                      Used in Experimental Damping Investigation</p>	253

ILLUSTRATIONS (Cont'd)

FIGURE		PAGE
73	Damping Measurements on Stator Set No. 1	254
	(a) Stator Stagger Angle, $\delta_{SM} = 28.2$ deg.	254
	(b) Stator Stagger Angle, $\delta_{SM} = 37.2$ deg.	255
	(c) Stator Stagger Angle, $\delta_{SM} = 47.2$ deg.	256
	(d) Stator Stagger Angle, $\delta_{SM} = 57.2$ deg.	257

## SYMBOLS

- $a$  flow deflection parameter in single blade row theory  $\left(\frac{\partial \delta_2}{\partial \delta_1}\right)$
- $a_{ij}$  matrix element, see page 107
- $A_i, B_i, C_i$  constants of integration in fundamental disturbance velocity solutions
- $b_{ij}$  function used in two blade-row theory, see page 110
- $C$  complex exponent of disturbance velocity solutions
- $C_I, C_R$  imaginary and real part of  $C$  respectively
- $\bar{C}_{P_{r_i}}$  total pressure coefficient in flow region  $i$  averaged in circumferential direction, see Equation 3
- $\bar{\bar{C}}_{P_{r_i}}$  radially averaged value of  $\bar{C}_{P_{r_i}}$ , see Equation 4
- $d$  blade chord in single blade-row theory
- $d_i$  blade chord of  $i^{\text{th}}$  blade row in two blade-row theory
- $\vec{f}$  friction force in fluid dynamic equations
- $g_i$  flow deflection parameter of  $i^{\text{th}}$  blade row in two blade-row theory  $\left(\frac{\partial \delta_i}{\partial \delta_{i-1}}\right)$
- $H_i$  total pressure in flow region  $i$
- $j$   $\sqrt{-1}$

SYMBOLS (Cont'd)

- $k$  normalized value of  $c, (\frac{cr}{nU_0})$
- $M_1, M_2$  functions used in single blade-row theory, see page 52
- $M_3, M_4$  functions used in single blade-row theory, see page 64
- $\tilde{M}_1, \tilde{M}_2$  functions used in single blade-row theory, see page 68
- $M_{3i}$  functions used in two blade-row theory, see page 110
- $n$  number of stall cells
- $\eta_{3i}$  functions used in two blade-row theory, see page 110
- $p$  static pressure
- $p_i$  perturbation pressure in flow region  $i$
- $\tilde{p}_i$  perturbation pressure function, see page 63
- $q \quad \frac{dn}{r} \sec \delta$
- $q_i \quad \frac{d_i n}{r} \sec \delta_i$
- $Q_1, Q_2, Q_3$  functions used in two blade-row theory, see page 109
- $\bar{Q}_1, \bar{Q}_2, \bar{Q}_3$  functions used in single blade-row theory, see pages 52 and 64
- $r$  mean blade-row radius
- $\vec{r}$  radius vector to points in cartesian space

## SYMBOLS (Cont'd)

- $S_i$  absolute swirl in flow region  $i$ , ( $\tan \bar{\beta}_i$ )
- $\delta_i$  relative swirl in flow region  $i$  relative to first blade row
- $\delta_i^+$  relative swirl in flow region  $i$  relative to second blade row
- $t$  time in laboratory fixed coordinate system
- $t_0$  time in blade fixed coordinate system
- $T$  spacing between leading edges of blade rows
- $u_i$   $x$  component of perturbation velocity in flow region  $i$
- $u_{0i}$   $x$  component of perturbation velocity in flow region  $i$  relative to blade row
- $U_i$   $x$  component of mean velocity in flow region  $i$
- $U_{0i}$   $x$  component of mean velocity in flow region  $i$  relative to blade row
- $\hat{U}_i$   $x$  component of total velocity in flow region  $i$
- $V_p$  propagation velocity of disturbance or of rotating stall
- $w_i$   $y$  component of disturbance velocity in flow region  $i$
- $w_{0i}$   $y$  component of disturbance velocity in flow region  $i$  relative to blade row
- $W_i$   $y$  component of mean velocity in flow region  $i$



SYMBOLS (Cont'd)

- $W_{0i}$   $y$  component of mean velocity in flow region  $i$  relative to blade row
- $\hat{W}_i$   $y$  component of total velocity in flow region  $i$
- $W_b$  blade-row velocity in single blade-row analysis
- $W_{bi}$  blade-row velocity of  $i^{\text{th}}$  blade row in two blade-row analysis
- $x, y, z$  cartesian coordinates in laboratory-fixed coordinate system
- $x_0, y_0, z_0$  cartesian coordinates in blade fixed-coordinate system
- $X$  total pressure loss coefficient in single blade-row theory
- $X_i$  total pressure loss coefficient of  $i^{\text{th}}$  blade row in two blade-row theory
- $X'_i = \frac{\partial X}{\partial \delta_i}$  in single blade-row theory
- $X'_i = \frac{\partial X_i}{\partial \delta_{i-1}}$  in two blade-row theory
- $\bar{\beta}_i$  mean steady absolute flow angle in flow region  $i$  (for Section III) (averaged in circumferential direction for Section II)
- $\bar{\beta}_{im}$  mean steady absolute flow angle in flow region  $i$  at mid annulus (averaged in circumferential direction)
- $\bar{\bar{\beta}}_i$  radially averaged value of  $\bar{\beta}_i$ , see Equation 2
- $\hat{\beta}_i$  total absolute swirl angle in flow region  $i$
- $\bar{\beta}_{0i}$  mean steady flow angle relative to blade row in flow region  $i$

## SYMBOLS (Cont'd)

- $\beta'_{0i}$  unsteady flow angle relative to blade row in flow region  $i$
- $\Gamma$  circulation
- $\delta$  stagger angle in single blade-row theory
- $\delta_i$  stagger angle of  $i^{\text{th}}$  blade row in two blade-row theory
- $\delta_{RM}$  rotor stagger angle at mid-annulus
- $\delta_S$  stator stagger angle
- $\delta_{SM}$  stator stagger angle at mid-annulus
- $\delta_{G.V.}$  guide vane stagger angle
- $\Delta$  time delay factor in control system
- $\overline{\Delta C_{P_T}}$  change in  $\overline{C_{P_T}}$  across blade row, see Equation 5
- $\overline{\Delta C_{P_T}}$  change in  $\overline{C_{P_T}}$  across blade row, see Equation 6
- $\Delta r$  distance from hub of cascade or rotor
- $\eta$   $z$  component of vorticity
- $\theta$   $\theta$  azimuthal coordinate in annular cascade
- $\lambda$  velocity solution  $C + \overline{\Omega}$
- $\rho$  density
- $\tau$  time delay factor

## SYMBOLS (Cont'd)

- $\bar{\tau}$  normalized time delay factor
- $\phi_i$  velocity function in flow region  $i$ , see page 47
- $\psi_i$  stream function in flow region  $i$
- $\bar{\Omega}$  normalized blade velocity in single blade-row theory
- $\bar{\Omega}_i$  normalized velocity of  $i^{\text{th}}$  blade row in two blade-row theory
- $\omega$  vorticity vector

## SECTION I

### INTRODUCTION

The flow phenomenon known as rotating stall was first encountered in axial flow compressors during the mid-1940's. It was observed that there were large zones where the flow was separated from the compressor blades. These separated zones propagated relative to the blade row. The propagating or rotating feature gave the phenomenon its name. The fundamental flow processes involved in a compressor stage undergoing rotating stall has traditionally been explained in terms of a flow blockage analog which produces a relieving effect on one side of a stalled blade or blade group and an aggravating effect on the other side. This simple explanation, while quite plausible, has not led to satisfactory theoretical progress in predicting the flow conditions which accompany the inception of rotating stall. The current technique for preventing turbo-jet engines from operating in a rotating stall regime is to preschedule engine control programs. This approach generally results in the requirement for a substantial stall margin under all operating conditions with attendant loss of performance and efficiency.

For the past several years Calspan Corporation (formerly Cornell Aeronautical Laboratory) has carried out a sequence of research programs under AFAPL sponsorship devoted to the phenomena of rotating stall. The work at Calspan has been both theoretical and experimental in nature and has been aimed at obtaining a sufficient understanding of the rotating stall phenomena such that its onset can be predicted and controlled. Substantial progress has been made towards this goal in that suitable precursor signals have been found, the fundamental blade row aerodynamic characteristics that influence rotating stall inception have been identified, and a prototype control system has been developed and demonstrated at low speeds on a representative compressor stage in the Calspan/Air Force Annular Cascade Facility.

This report summarizes the latest three year research program at Calspan. The report has been divided into three main sections which are

Experimental Rotating Stall Research, Theoretical Rotating Stall Research and Development of a Prototype Rotating Stall Control System. The description of an experiment to investigate the stability of flow through a blade row is given in Appendix A and details of the two blade row theoretical development are presented in Appendix B.

## SECTION II

### EXPERIMENTAL ROTATING STALL RESEARCH

As a part of the work under a previous program Contract AF 33(615)-3357 , an annular cascade facility was designed and fabricated. Its purpose is to provide detailed fundamental experimental data during and prior to the occurrence of rotating stall in order to improve our understanding of the phenomena and for use as a guide in improving the theoretical analysis.

During the program immediately preceding the current investigation, the annular cascade facility was used to study the flow field associated with rotating stall inception on three sets of stator blades, each with different profile shapes. Thorough investigations of the flow velocity and angularity distributions upstream and downstream of the stators were made. The results of these investigations were presented in Reference 1. In the course of performing these experiments, three questions arose which were not answered during that program. These were:

- 1) Does the blade-chord dimension have an effect on rotating stall which is independent of the effect of solidity ratio (ratio of the blade-chord length to the blade spacing)?
- 2) Are the results of rotating stall studies performed on stator rows directly applicable to blade rows which are rotating?
- 3) Is the inception of rotating stall the result of instability of the flow to small disturbances?

The current investigation was designed to obtain experimental information which could help answer these questions. In addition, the experimental data was to be in sufficient detail to allow correlation with the prediction of the theory which is presented in Section III. The latter requirement made it necessary to measure blade row loss distributions as well as the flow velocity and angularity distributions.

The results from those portions of the experimental program designed to answer questions 1 and 2 are presented in this section. The investigation of question 3 is presented separately in Appendix A. Since substantial amounts of experimental data were obtained during the program, an outline of the order of presentation used in the remainder of this section is given below.

Both rotating and non-rotating blade row tests were performed in the present program and most experimental configurations consisted of a guide vane row to provide controlled inlet conditions and a stator row on which rotating stall was studied. Initial tests were made with stationary blade rows. Later tests were performed while rotating either the guide vane row or the stator row. The cases where both blade rows are stationary is discussed first.

A description of the annular cascade facility with a stationary hub is presented in Section II-A. This version of the facility was used to investigate the effect of blade-chord dimension on rotating stall. The experimental equipment used for all of the tests is also described here, and the calibration of the flow downstream of the guide vanes is included since this is the inlet flow to the stator rows tested.

Section II-B presents the results of the experimental investigation to determine the effect of blade chord on the properties of rotating stall. A total of three stator rows were tested in this portion of the program. Extensive surveys were made to determine the circumferentially averaged radial distributions of swirl angle and total pressure downstream of all three stator sets near the inception boundary for rotating stall. In addition, the inception boundary and the propagation velocity and number of cells which occur after inception were measured for each of the stator sets.

After completion of the above tests, the facility was modified so that either of the two blade rows could be rotated. A description of the annular cascade facility after it was modified to provide a rotating capability is presented

in Section II-C. The calibration of a set of rotating guide vanes is also described there.

Section II-D presents the results of the investigation of the effect of blade-row rotation on rotating stall. In this investigation, tests were performed on a single blade row under two different conditions. First it was held stationary and the inlet flow was tailored to provide a wheel-type of inlet swirl by using rotating guide vanes upstream. Next, the guide vanes were removed and the tests were repeated with the blade row rotating as an isolated rotor. In this way the inlet swirl angle distributions relative to the blades were kept the same for both tests. As in the blade chord experiments, extensive measurements of flow angle and total pressure were made near rotating stall inception; after inception, rotating stall propagation velocity and number of cells were measured.

Finally, in Section II-F, a summary of the experimental program is presented along with those conclusions which can be drawn from inspection of the results. That portion of the program described in Appendix A is complete in itself and is not included in Section II-F.

## A. DESCRIPTION OF ANNULAR CASCADE FACILITY WITH STATIONARY HUB

### 1. General Description

The annular cascade facility consists of a test section built around the outer front casing of a J-79 jet-engine compressor, and inlet and outlet ducting to provide a smooth flow of air into and away from the test section. The notation used with this configuration is illustrated in Figure 1. A schematic planview of the annular cascade and the wind tunnel to which it is attached is shown in Figure 2. The wind tunnel, which is used in an open-circuit configuration, provides variable suction at the downstream end of the annular cascade. The microsonic leg of the wind tunnel is isolated from the



circuit when cascade tests are conducted. Photographs of the complete annular cascade facility and of the test-section portion of the facility are shown in Figures 3 and 4, respectively. Details of the stationary hub configuration of the annular cascade are shown in Figure 5.

The test section of the annular cascade forms a circular annulus with an outer diameter of 29.35 inches and an inner diameter of 23.35 inches which provides a hub-to-tip ratio of 0.80. The blading consists of an inlet guide-vane row and a stator row, both with variable stagger angle (angle between the blade chord and the axial direction). The variable stagger angle feature allows the investigation of rotating stall for a variety of combinations of inlet swirl to the stator row and outlet swirl from the stator row.

The guide vanes provide a variable mean inlet swirl angle to the stator row ranging between approximately 36 to 68 degrees. An NACA 63-(24A<sub>4</sub>K<sub>6</sub>)10 guide-vane profile was used for these blades. This profile shape is a ten-percent-thick version of the six-percent profile series reported in Reference 2. The use of the thicker profile was dictated by structural considerations. The blades are made from epoxy resin fortified with aluminum powder, molded around 1/8-inch steel shafts. They are untwisted, with a linear taper from a 3.00-inch chord at the outer annulus diameter to a 2.30-inch chord at the inner annulus diameter. The guide vane-row was mounted at the third-stage stator location in the J-79 compressor housing. At this location, there are 36 blades in all, giving a constant solidity ratio of 1.17 across the test-section annulus.

The stator row was located at the position of the fifth-stage stators of the J-79 compressor casing. Three different sets of stator blades were tested during the portion of the program which used stationary blade rows. The first set tested was the fifth-stage stator blading from a J-79 jet-engine compressor, unmodified except for the blade length which was shortened from 4.87 to approximately 2.98 inches in order to fit the blades into the three-inch annulus. This set of stator blades has been designated as Stator Set No. 1. Geometric properties of this stator row are listed in Table I.

TABLE I

## Geometric Characteristics of Stator Set No. 1

Blade Length		2.98 inches
Blade Chord at Outer Diameter		1.316 inches
Blade Chord at Inner Diameter		1.290 inches
Blade Thickness at Outer Diameter		0.1524 inch
Blade Thickness at Inner Diameter		0.1132 inch
Blade Camber Angle (angle between tangents to mean camber line of leading and trailing edges)		35.6 degrees
Blade Twist; positive twist reduces stagger	Outer Diameter	0 degree
	Mid-Annulus	0.28 degree
	Inner Diameter	1.42 degree
Number of Blades		54
Solidity at Mid-Annulus		0.85

The two other stator rows which were tested consisted of blades identical to those in Stator Set No. 1 except for the chord length. The chord length was double that of the blades in Stator Set No. 1. These stator rows have been designated Stator Sets No. 4 and 5. Stator Set No. 4 contained the same number of blades as Stator Set No. 1 while Stator Set No. 5 had every other blade removed. Thus Stator Set No. 4 had twice the solidity ratio as Stator Set No. 1 while Stator Set No. 5 had the same solidity ratio as Stator Set No. 1. The blades in Stator Sets No. 4 and 5 were manufactured from epoxy resin in a fashion similar to the inlet guide vanes. In these cases, however, the blades were molded around nearly rectangular cores made from cut-down J-79 compressor blades.

The stationary annular cascade had provision for boundary-layer suction. This was provided at three stations. The location of these stations

is illustrated in Figure 5 along with some other details. Each suction station consisted of a double row of small holes extending around the circumference of the inner or outer annulus wall. Each ring of holes was backed by an annular plenum chamber with a baffle. The suction applied to each station was independently adjustable. Tests with boundary-layer suction were reported in Reference 1. It was shown that the use of suction in the annular cascade did not produce any measurable change in the properties of rotating stall. Thus, the suction was not used in the current work.

In addition to the location of the boundary-layer suction holes, Figure 5 also shows the location of traversing stations for hot-wire and total pressure probes. Two types of mountings for the probes are included in the facility. The simplest mount allows radial traverse only. Three of these mounts were built into the test section -- one upstream of the guide-vane row (not shown), one approximately midway between the guide vane and stator rows, and one downstream of the stator row. The second type of traverse mounting for the probes allows both radial and circumferential movement of the probe. There are two of these traverse mounts -- one between the guide vane and stator rows, and one downstream of the stator row.

A linearized two-channel, constant-temperature, hot-wire anemometer system was used in conjunction with a crossed-wire probe for the velocity and swirl angle measurements. Readout for the hot-wire system was made by means of a two-channel integrator-digital voltmeter system. Each linearized hot-wire signal was integrated for either 25 or 30 seconds and the time average was calculated from the readings on the digital voltmeters.

Total pressure surveys were made through circumferential traverses with a multiple-tube total pressure rake. The total pressure rake was aligned with the flow in two different ways. Initially, alignment was based on the swirl angle measurements made with the hot-wire system. In later tests, alignment was made by using a Conrad arrowhead style yawmeter incorporated

on the rake. In all tests, the pressures detected by the rake were photographically recorded from a multitube inclined manometer.

## 2. Calibration of Stationary Inlet Guide Vanes

The swirl angle distributions generated by the stationary inlet guide vanes had been measured prior to initiation of the current program. Detailed results are reported in Reference 1 and will not be repeated here. For the purposes of the present investigation it is sufficient to note that extensive circumferential and radial surveys were performed to obtain circumferentially averaged radial distributions of the swirl angle. The swirl angles measured downstream of the guide vanes are summarized in Figure 6. These angles have been called inlet swirl angles because they provide the inlet conditions to the stator row under test.

Two types of average swirl angles downstream of the guide vanes are presented in Figure 6 as a function of guide vane stagger angle,  $\delta_{GV}$ . These are the circumferentially averaged inlet swirl angle,  $\bar{\beta}_{iM}$ , measured at mid-annulus and the overall inlet swirl angle,  $\bar{\beta}_i$ , obtained by integrating the circumferentially averaged swirl angle distributions along a radius. General definitions of these two swirl angles are as follows: The circumferential or azimuthal average swirl angle,  $\bar{\beta}_i$ , in flow region  $\lambda$  is given by

$$\bar{\beta}_i(r) \equiv \frac{1}{(\theta_b - \theta_a)} \int_{\theta_a}^{\theta_b} \frac{\beta_i(r)}{\frac{\rho}{2} U_o^2} d\theta \quad (1)$$

The overall swirl angle is given by

$$\bar{\beta}_i \equiv \frac{2}{(r_t^2 - r_h^2)} \int_{r_h}^{r_t} r \bar{\beta}_i(r) dr \quad (2)$$

where  $r$  is the radius

$U_o$  is the axial velocity upstream of the guide vanes

$\beta_i(r)$  is the swirl angle

$\theta$  is the azimuth angle

$\rho$  is the air density

and subscripts

$i = 0$  refer to conditions upstream of the guide vanes

$i = 1$  refer to conditions between the guide vanes and the stators

$i = 2$  refer to conditions downstream of the stators

$h$  refer to inner wall (hub)

$t$  refer to outer wall (tip)

The azimuth angle limits,  $\theta_a$  and  $\theta_b$ , were governed by the physical limits of the traverse mechanism. In the experimental surveys, the increment in azimuth angle ( $\theta_b - \theta_a$ ) was large enough in all cases to cover at least one complete space between adjacent blades.

The radial surveys of inlet swirl angle reported in Reference 1 showed that the distribution of these angles with radius was relatively uniform. This result is reflected in Figure 6 where the overall inlet swirl angle,  $\bar{\beta}_1$ , is close to the average value measured at mid annulus,  $\bar{\beta}_{1M}$ . The largest difference between these two angles is less than two degrees.

In addition to the inlet swirl angle surveys, radial distributions of total pressure were measured downstream of the guide vanes. These data were obtained during the current program. They were reduced to coefficient form referenced to the dynamic pressure at the inlet to the annular cascade. As with the swirl angles, the total pressures were averaged in two ways. The corresponding coefficients are defined as a circumferential average total pressure coefficient,  $\bar{C}_{P_{T_i}}$ , in flow region  $i$  which is given by

$$\bar{C}_{P_{T_i}} \equiv \frac{1}{(\theta_b - \theta_a)} \int_{\theta_a}^{\theta_b} \frac{H_i - H_o}{\frac{\rho}{2} U_o^2} d\theta \quad (3)$$

The corresponding overall total pressure coefficient is

$$\bar{\bar{C}}_{P_{T_i}} \equiv \frac{2}{(r_t^2 - r_h^2)} \int_{r_h}^{r_t} r \bar{C}_{P_{T_i}}(r) dr \quad (4)$$

where  $H_{\lambda}$  is the total pressure in flow region  $\lambda$ , and the remainder of the notation is the same as that used for Equations (1) and (2).

The overall total pressure coefficient,  $\bar{C}_{p_{T_1}}$ , downstream of the guide vanes is shown in Figure 7 as a function of guide vane stagger angle,  $\delta_{GV}$ . Presentation of radial distributions of the circumferentially averaged total pressure coefficient,  $\bar{C}_{p_{T_1}}$ , is delayed until Section II-B so that they may be compared directly to similar data,  $\bar{C}_{p_{T_2}}$ , measured downstream of one of the stator rows.

## B. INVESTIGATION OF EFFECT OF BLADE CHORD ON ROTATING STALL

This portion of the experimental program was designed to determine whether the blade-chord (or more properly stated, the blade chord normalized by a typical compressor dimension such as its circumference) has an effect on rotating stall which is independent of the effect of solidity ratio.

In the experiments reported in Reference 1, rotating stall properties were measured on three blade rows, each with different profile shape. Two of these rows, each with a different profile shape. Two of these rows had identical blade chords and solidity ratios while for the third, both of these parameters were approximately halved. It was found that rotating stall on the blade row with the smaller chord and solidity ratios propagated at nearly twice the velocity observed on the other two blade rows. Since blade profile shape appeared to have little influence on the rotating stall propagation velocity, this indicated that the propagation velocity difference could be due either to differences in solidity ratio or blade-chord. The data were not sufficient to distinguish between the effects of blade chord and solidity ratio. However, other data available in the literature, Reference 3, showed little change in propagation velocity with a two-to-one change in solidity ratio. Thus, it was suggested in Reference 1, that blade-chord may be a major factor in determining rotating stall propagation velocity and that such a possibility warranted

further consideration. The experimental program described in the following paragraphs is designed to investigate this possibility.

The stationary annular cascade was used for this investigation. It is described in Section II. A and the notation used is shown in Figure 1. In these experiments the mean axial flow velocity,  $U_o$ , was held constant at 60 feet per second. The experiments consisted of measuring the flow properties prior to inception and during the occurrence of rotating stall on three different stator rows. These stators have been designated as Stator Sets No. 1, 4, and 5. Their geometric properties are listed in Section II. A. Briefly, the blades in all three stator sets had the same profile shape and twist distribution. However, the blade-chord lengths and solidity ratios were different. The combinations of blade chord and solidity ratio are listed in Table II.

TABLE II  
Comparison of Stator Sets No. 1, 4, and 5

	Stator Set No. 1	Stator Set No. 4	Stator Set No. 5
Blade Length, inches	2.98	2.98	2.98
Blade Chord at Mid-Annulus, inches	1.30	2.60	2.60
Number of Blades	54	54	27
Solidity at Mid-Annulus	0.85	1.70	0.85
Aspect Ratio (Blade Length/Blade Chord)	2.28	1.14	1.14

The combinations of blade chord and solidity ratio given by the above grouping are sufficient to study any direct effect of blade chord independent of solidity ratio on the properties of rotating stall.

The rotating stall inception boundary for all three stator sets are shown in Figure 8 in terms of inlet guide vane and stator stagger angles. The behavior of the inception curves for Stator Sets No. 1 and 5 are of the most interest because these two blade rows are identical in all geometric quantities (including solidity) except for the blade chord and aspect ratio. The overall

behaviors of both curves are similar. In particular, both Stator Sets No. 1 and 5 exhibit an onset of turbulence and possible small amplitude rotating stall prior to large amplitude rotating stall for stator stagger angles less than approximately 32 degrees. There is, however, a difference of 4 to 5 degrees in inlet guide vane stagger angle at which rotating stall occurs for the two curves. Since only the chord and aspect ratio of these two stator rows are different, it may be that the differences in the inception boundaries are due primarily to end effects which change the blade row turning and loss performance. As will be shown, these performance parameters are different for all three stator sets.

The turning performance of each stator set was measured through radial surveys with a crossed hot-wire probe. These surveys were made at three different circumferential locations,  $\theta_r$ , and the results were averaged to obtain,  $\bar{\beta}_2$ . As a check on the accuracy of the three point average, a more extensive circumferential average,  $\bar{\beta}_{2M}$ , was made at mid-annulus for each case. The mid-annulus average was calculated from a minimum of eight points. A complete set of swirl angle distributions for Stator Set No. 4 is shown in Figure 9. The results shown are typical of all three stator sets. (The corresponding data for Stator Set No. 1 have been presented in Reference 1 and those for Stator Set No. 5 are in the Eighth Quarterly Progress Report for the current program, CAL Report No. MK-2932-A-8.)

Figures 9 (a), (b) and (c) show the radial distributions of swirl angle,  $\bar{\beta}_2$ , for stator stagger angles of 28.2, 37.2, and 47.2 degrees, respectively. On each set of radial distributions, the corresponding mid-annulus circumferential averages,  $\bar{\beta}_{2M}$ , are shown also for comparison. The three point average data,  $\bar{\beta}_2$ , obtained at mid-annulus are generally in agreement with the more extensive mid-annulus averages,  $\bar{\beta}_{2M}$ . An exception to this good agreement occurs near rotating stall inception for a stator stagger angle of 28.2 degrees (Figure 9 (a)). The circumferential variations in the local values of  $\beta_2$  for this case were relatively large ( $\pm 3$  degrees at inception) and it may be that the three point average used for  $\bar{\beta}_2$  does not contain enough points to give an accurate value. However, there is evidence that



the differences between  $\bar{\beta}_{2M}$  and  $\bar{\beta}_2$  are caused at least partially by the fact that the flow downstream of the stators is not completely repeatable on a day-to-day basis. That is, although repeated check points in any one continuous series of tests showed excellent agreement, repeated experiments over a period of weeks showed deviations as large as the differences between  $\bar{\beta}_{2M}$  and  $\bar{\beta}_2$ . The same phenomenon was observed on Stator Set No. 5 in the current work and on Stator Set No. 2 in Reference 1. However, the observed deviations on Stator Sets No. 4 and 5 were not as large as those observed on Stator Set No. 2, and they did not occur over as large a range of stator stagger angles and inlet conditions.

In spite of the apparent day-to-day changes in blade turning performance, the inlet swirl angle for inception of rotating stall on Stator Sets No. 2, 4, and 5 did not vary for any given stator stagger angle. Thus, the observed changes do not appear to be important in determining the rotating stall inception point. It is worth mentioning that the values of  $\bar{\beta}_{2M}$  and  $\bar{\beta}_2$  obtained with Stator Set No. 1 generally showed less deviation than those obtained with Stator Sets No. 4 and 5.

The radial distributions of swirl angle shown in Figure 9 illustrate a feature which is common to all of the stator sets which have been tested to date. The swirl angle distributions downstream of the stators are highly nonuniform along the radius. This leads to a problem in using the data as inputs to the theory since the theory is essentially two-dimensional. A number of alternative methods for using the data in the theory were considered, including using a blade-element approach which would apply the theory locally along streamtubes. It was decided to evaluate the theory first by using the simplest form of the input data as possible. Thus, initial correlations were performed using mid-annulus average data,  $\bar{\beta}_{2M}$  (Equation 1). Later correlations were performed using overall averages,  $\bar{\beta}_2$  (Equation 2). As will be shown in Section III, the use of  $\bar{\beta}_2$  (and  $\bar{\beta}_1$ ) along with similarly averaged loss data in the theory provides good correlation between experimental and theoretical rotating stall inception points and reasonable correlation for propagation velocities and numbers of cells just after inception.

Radial distributions of total pressure coefficient,  $\bar{C}_{P_{T_i}}$  (Equation 3), measured upstream and downstream of Stator Set No. 4 are shown in Figure 10 for the same stator stagger angles that were used for the flow angularity surveys. (Similar data for Stator Sets No. 1 and 5 were presented respectively in the Fifth and Seventh Quarterly Progress Reports for the current program, CAL Reports MK-2932-A-5 and -7.) Each data point in Figure 10 represents a circumferential average of nine equally spaced total pressure readings. In a few cases, values of  $\bar{C}_{P_{T_1}}$  were not available from the guide vane calibration at exactly the same guide vane stagger angle used for the determination of  $\bar{C}_{P_{T_2}}$ . In these cases, the  $\bar{C}_{P_{T_1}}$  data which are shown were obtained by interpolation of the existing data.

For given guide vane and stator stagger angles, the difference between the upstream and downstream total pressure coefficient curves represents the loss through the stator row,  $\Delta \bar{C}_{P_T}$ . That is

$$\Delta \bar{C}_{P_T}(r) \equiv \bar{C}_{P_{T_1}}(r) - \bar{C}_{P_{T_2}}(r) \quad (5)$$

An overall loss coefficient for the stator row,  $\Delta \bar{\bar{C}}_{P_T}$ , is defined as

$$\Delta \bar{\bar{C}}_{P_T} \equiv \bar{\bar{C}}_{P_{T_1}} - \bar{\bar{C}}_{P_{T_2}} \quad (6)$$

where  $\bar{\bar{C}}_{P_{T_i}}$  is given by Equation (4).

The value of  $\Delta \bar{\bar{C}}_{P_T}$  is always positive since the stator row removes energy from the flow. The same is generally true of  $\Delta \bar{C}_{P_T}(r)$ , although redistribution of the local total pressure through the blade row can cause some instances where  $\Delta \bar{C}_{P_T}(r)$  is slightly negative at a given radius. Some locally negative values of  $\Delta \bar{C}_{P_T}(r)$  are apparent in Figure 10 near the hub. (Note that in Figure 10, the horizontal axis is plotted with negative  $\bar{C}_{P_T}$  values.)

It is apparent from Figure 10 that the radial distributions of stator row loss coefficient are highly nonuniform. The same is true for the losses measured through Stator Sets No. 1 and 5. As with the flow angularity data, the overall loss coefficient (Equation 6) was used in application of the theory. The overall flow angularity data for all three stator sets are shown in Figures 11 through 13 and the corresponding loss data are shown in Figures 14 through 16.

The flow angularity in Figures 11 through 13 are presented both in terms of mid-annulus averages  $\bar{\beta}_{\lambda_M}$  and in terms of overall averages  $\bar{\beta}_{\lambda}$ . Where possible, the data were gathered at identical stator stagger angles for each stator set. However, there is some lack of overlap in stagger angles. This arose because Stator Set No. 1 was tested first at three widely spaced values of stagger angle. When performing later tests on Stator Set No. 4, it was discovered that rotating stall could not be obtained at the largest stator stagger angle ( $\delta_{SM} = 57.2$  degrees) that had been tested on Stator Set No. 1. The inlet swirl angles available from the guide vanes did not reach high enough values. Later, a somewhat similar situation was discovered on Stator Set No. 5 at  $\delta_{SM} = 28.2$  degrees. However, in this case, it was possible to generate a large amplitude rotating stall by increasing  $\delta_{SM}$  only one degree, that is  $\delta_{SM} = 29.2$  degrees.

In each of Figures 11 through 13, rotating stall inception is indicated by an arrow (dashed for the mid-annulus averages and solid for the overall averages). Rotating stall was detected through the use of quarter-chord pressure taps at mid-annulus on the suction surface of the stator blades. As in Reference 1, these detectors indicated two types of rotating stall inception. At the higher stator stagger angles on Stator Sets No. 1 and 5 and at all stagger angles on Stator Set No. 4, the detectors indicated a relatively clean flow over the blades prior to rotating stall inception. Rotating stall began intermittently with relatively small amplitude. As inlet swirl angle was increased beyond inception, the intermittency rapidly disappeared and the amplitude increased with increasing inlet swirl angle. This type of behavior has been called small amplitude inception and is indicated in the figures by an arrow pointing downward.

At the lower stator stagger angles on Stator Sets No. 1 and 5, the pressure detectors indicated turbulence in the flow prior to the detection of rotating stall. In these turbulent cases, it is easy to recognize the sudden onset of a large amplitude rotating stall pattern. This second type of rotating stall inception has been called large amplitude rotating stall inception and is indicated by an arrow pointing upward in Figures 11 through 13. It was also

found possible to discern a small amplitude rotating stall in some cases, notably on Stator Set No. 1, prior to the sudden onset of large amplitude rotating stall. The small amplitude rotating stall is very difficult to discern because of the turbulence and it could easily be missed. Hence, it is possible that the large amplitude rotating stall shown in Figure 13 for a stator stagger angle  $\delta_{SM} = 29.2$  degrees was preceded by an undetected small amplitude rotating stall and that a similar undetected rotating stall existed for  $\delta_{SM} = 28.2$  degrees where no rotating stall is indicated. The onset of turbulence for these two cases is indicated in Figure 13 to show the range over which an undetected small amplitude rotating stall could exist.

There are some features to the turning performance curves of Figures 11 through 13 that are worth comment. First, the mid-annulus average data,  $\bar{\beta}_{2M}$ , do not appear to give a good indication of the overall flow turning performance,  $\bar{\beta}_2$ , of the stator sets. This is particularly true at the higher stator stagger angles in all cases and is caused by the large nonuniformities in the radial distributions in swirl angle near the hub at high stagger angles (e. g. Figure 9 (c)). Note that at these high stator stagger angles, the differences discussed previously between values of  $\bar{\beta}_{2M}$  and  $\bar{\beta}_2$  at mid-annulus were very small on all three stator sets. Second, the overall average swirl angles,  $\bar{\beta}_2$ , show a smoother variation with inlet swirl angle than the mid-annulus averages,  $\bar{\beta}_{2M}$ . Here the most notable differences occur at the low stator stagger angles on Stator Set No. 5 (Figure 13). This is one of the cases where the flow at any given radius appeared to be unstable on a day-to-day basis. Both the day-to-day variations in  $\beta_2$  at a given location, and the irregularities in the circumferential averages at mid-annulus,  $\bar{\beta}_{2M}$ , could be caused by changes in the radial distributions of swirl angle which have little effect on the overall turning performance as given by  $\bar{\beta}_2$ . Both of the above observations lead to the conclusion that the flow turning performance of the stators was not well represented by data measured at mid-annulus alone. Thus, the overall turning performance given by  $\bar{\beta}_2$  versus  $\bar{\beta}_1$  was used in the application of the theory which is presented in Section III.

It is of interest to compare the overall turning performance of the three stator sets shown in Figures 11 through 13 while recalling that the solidity of Stator Set No. 4 is double that of Stator Sets No. 1 and 5 (Table II). As expected, Stator Set No. 4 provides the most flow turning for any given stagger angle and inlet swirl angle because of its higher solidity ratio. The extra turning is greatest at low stator stagger angles. More significantly, Stator Sets No. 1 and 5, which have the same solidity, did not provide identical turning performance or rotating stall inception points. For stator stagger angles of 28.2 and 37.2 degrees, at a fixed value of  $\bar{\beta}_1$ , Stator Set No. 5 (large chord) turns the flow more than Stator Set No. 1 (small chord) with the greatest difference occurring for  $\delta_{SM} = 28.2$  degrees. At the highest stagger angle tested,  $\delta_{SM} = 57.2$  degrees, the behavior is reversed, Stator Set No. 1 turns the flow slightly more than Stator Set No. 5 for a given value of  $\bar{\beta}_1$ . Moreover, rotating stall generally occurs at larger inlet swirl angles on Stator Set No. 5 than on Stator Set No. 1. Apparently differences in end effects on the blades in Stator Sets No. 1 and 5 are sufficient to cause the above behavior. Although the solidity and other geometry were the same for these two stator sets, the aspect ratio as well as the chord length were different.

The overall total pressure loss through Stator Sets No. 1, 4 and 5 are shown in Figures 14, 15, and 16, respectively. As in the previous swirl angle presentation, rotating stall inception is indicated by an arrow. The loss curves for all three stator sets are different from each other when considering a given stator stagger angle. However, the loss curves of the equal solidity Stator Sets No. 1 and 5 are only moderately different in regions where the inlet swirl angles overlap. The largest discrepancies occur at  $\delta_{SM} = 57.2$  degrees. This is in contrast with the flow turning performance where the greatest difference between these two stator sets was observed at the smallest stagger angle  $\delta_{SM} = 28.2$  degrees. The loss data do not show a consistent pattern among the three stator sets. For a given inlet swirl angle, the high solidity Stator Set No. 4 generally has the lowest loss at  $\delta_{SM} = 28.2$  degrees and the highest loss at  $\delta_{SM} = 47.2$  degrees. At  $\delta_{SM} = 37.2$  degrees, the loss curves cross each other depending on the value of inlet swirl angle. Here, as with the flow angle data, the differences which were

obtained are probably attributable to end losses for those cases where the solidity was held constant.

The final data presented for Stator Sets No. 1, 4, and 5 are the propagation velocity and number of cells which occur during rotating stall. These were obtained from simultaneous measurements at two different circumferential locations. For Stator Sets No. 4 and 5, the detectors used in these measurements were quarter-chord pressure taps on the suction surfaces of the stator blades. The same quantities had been measured previously on Stator Set No. 1 using hot wires mounted upstream of the stator row (Reference 1). The measurements on Stator Set No. 1 were not repeated using the pressure taps since past experience had indicated that both types of detectors, hot-wire or pressure, give similar results.

The experimental rotating stall propagation velocities for all three stator sets are compared in Figure 17. The propagation velocities have been nondimensionalized by the mid-annulus average of the swirl velocity,  $\bar{W}_{1M}$ , measured upstream of the stator row and are plotted as a function of the mid-annulus average inlet swirl angle,  $\bar{\beta}_{1M}$ . As can be seen from the inlet guide vane calibration curve (Figure 6), the mid-annulus averages upstream of the stator row are not very different from the overall averages. Presentation of the data in this form allows direct comparison, if desired, with data presented for Stator Sets No. 2 and 3 in Reference 1.

At the beginning of this subsection, it was noted that the evidence available at the time this work was undertaken suggested that blade chord might be a major factor in determining rotating stall propagation velocity. If this were true, the argument provided that Stator Sets No. 4 and 5 should have the same propagation velocity and that this should be very close to half the velocity found on Stator Set No. 1. Inspection of Figure 17 indicates that this result was not obtained. Propagation velocities measured on Stator Set No. 4 are almost exactly half those measured on Stator Set No. 1 but those measured on Stator Set No. 5 are closest to, but in all cases less than, those for Stator Set No. 1. If one were to ignore the propagation velocity results

obtained for a stagger angle of 32.2 degrees, the reasonably close agreement between the results for Stator Sets No. 1 and 5 could lead to the conclusion that the solidity is more important than blade chord in determining propagation velocities. However, the data obtained at  $\delta_{SM} = 32.2$  degrees and the results presented in Reference 3 are clearly at odds with this conclusion. Therefore, neither blade-chord nor solidity ratio appear to have a consistent effect on rotating stall propagation velocities.

The number of cells which occurred during rotating stall on the three stator sets are shown in Figure 17 as numbers near the data points. Not all the data points have numbers, since some of the records were not adequate for determining the number of cells, even though propagation velocities could be determined. All three stator sets demonstrate similar behavior in the number of stall cells which occur. One or two cells usually occur very close to inception where the stall is intermittent and then rapidly increase to four or five cells for most cases as  $\bar{\beta}_{1,M}$  is increased and the stall becomes steady. Exceptions to this general rule occurred for Stator Sets No. 1 and 5 at stagger angles of 28.2 and 29.2, respectively. (Stator Set No. 5 is shown for  $\delta_{SM} = 29.2$  degrees because rotating stall was not detected for  $\delta_{SM} = 28.2$  degrees.) Here the numbers of cells observed near inception were between four and six. In these cases, small amplitude rotating stall and turbulence preceded the onset of large amplitude rotating stall (see Figures 11 and 13). In general, the upper number of cells observed was about the same for all three stator sets. This suggests that blade chord and solidity ratio are not important in determining the number of cells.

In summary of the experimental investigation described above, it can be stated that the results provided no evidence that either the blade chord or the solidity have a consistent effect on rotating stall propagation velocity, number of cells, or for that matter, the rotating stall inception boundary. Differences in these quantities were observed but they did not form a consistent pattern with either blade chord or solidity. Rather, the observed differences are probably due to the measured differences in flow turning and loss performance in the stator sets. These performance parameters are affected not only by

solidity ratio but also by the end losses on the blades. For a given solidity ratio, the end losses depend on such features as aspect ratio (and hence in this program on blade chord) and blade tip clearance. The generally good correlations between the theory of Section III (which uses the measured performance) and the experiments of this section tend to bear out the above statement.

### C. DESCRIPTION OF ANNULAR CASCADE FACILITY WITH ROTATING HUB

After completion of the experimental investigation described in Section II. B, the annular cascade was modified so that either a guide vane row or the blade row under test could be rotated. The modified facility and the calibration of the rotating guide vanes are described in the following paragraphs.

#### 1. General Description

The principal modification to the annular cascade facility was the provision of a new hub design which allowed rotation of either a set of guide vanes or of a downstream blade row. A simplified sketch of the new blade row configuration is shown in Figure 18 along with the notation which is used. Figures 19 and 20 show slightly different views of the main portions of the rotating hub assembly. These photographs were taken before final installation, while the rotors were being balance tested. The horizontal steel tubes fastened to the outer ring frame in the photos were temporary spacer bars used in place of the J-79 outer casing. (The casing was being used in the stationary annular cascade at the time.) The rubber tube at the drive end of the rig was also temporary. It was used to couple the rotor to an external electric motor for dynamic balance tests. In these photographs, the smaller chord blades are the set which was tested both as a stator row and as a rotor row. The larger chord blades are the upstream guide vane row used to provide wheel type swirl when the tested blade row was held stationary.



Details of the rotating hub installation in the annular cascade are shown in Figure 21. The main features of the design are as follows. There are two rotor assemblies, one centered at the axial location of the third stage rotor in the original J-79 compressor and one centered at the original J-79 fifth stage rotor. Both of these rotors are driven by a common drive shaft. However, either rotor can be decoupled from the drive shaft and held stationary while the other rotor is driven. Alternatively, both rotors can be driven, but only at identical velocities in the same direction. Only the rotor assemblies rotate, the outer skin on the hub upstream and downstream of the rotors and between the rotors is held stationary. The drive shaft to the rotors is powered by a 24 horsepower hydraulic motor. Rotational speed is infinitely variable in either direction between zero and approximately 1500 rpm. An external hydraulic pump system powered by a 30 horsepower electric motor is used to provide power for the hydraulic motor.

The inlet and outlet ducting to the rotating annular cascade are the same as those used in the stationary cascade (Figure 2). Wind-tunnel suction is still used to provide the desired mass flow through the facility. This is the reason the rotor drive does not require as much power as one might expect. At the same time, the combination of powered rotor plus independent mass flow control provides exceptional versatility to the complete test rig.

The upstream (third stage) rotor assembly was fitted with large chord guide vanes to provide variable wheel-type inlet swirl to the fifth stage rotor blades during one series of tests in which the fifth stage rotor was held stationary. These guide vane blades are made from epoxy resin molded around steel cores in a fashion similar to Stator Sets No. 4 and 5. The new blades differ from the older stator blades in that they are mounted on the upstream rotating hub rather than on the outer casing. The method of fastening the blades to the hub allows individual adjustment of the stagger angle. Details of the blade fastenings are shown in an insert in Figure 21. The guide vane blades have a NACA 63 24 ( $A_4K_6$ )10 profile shape with a constant chord of 3 inches and a linear twist of 8.7 degrees increasing towards the tip. The rotating guide vane row has a total of 36 blades. The magnitude of the wheel swirl generated by the guide vanes is adjustable through control of the rotational speed of the third stage rotor.

The downstream (fifth stage) rotor assembly was fitted with steel blades. These blades were made from the fifth stage rotor blades of a J-79 compressor, unmodified except for the blade lengths which were shortened in order to fit the three inch annulus of the test rig. The tip portion of the J-79 rotor blades were used. There are 46 blades in all, the same as the original J-79 fifth stage rotor. These were mounted on CALSPAN manufactured bases similar to the rotating guide vane bases (Figure 21). The blades had a nominal twist of 14.5 degrees and an approximately constant chord length of 1.45 inches over the three inch span. However, measurements showed that in practice, the twist over the center 2-1/2 inches in these production J-79 blades varied between 10.8 and 14.4 degrees with an average value of 12.9 degrees. The blades were installed in a sequence which distributed the nonuniformities in twist over the complete circumference. Particular attention was paid to the circumferential region where surveys downstream of the stationary blades were to be made. In this region, the blades were selected to have twist values as close to the average as possible. This blade row has been designated as Stator Set No. 6 when tested as a stator row, and as Rotor Set No. 1 when tested as an isolated rotor.

A blade tip clearance problem was encountered on installation of the rotor assembly in the annular cascade. The J-79 compressor outer casing used in the annular cascade is about one-tenth inch out of round with the split line diameter being the largest. In final assembly, the rotor was mounted in the casing with shims along the split line which provided the following tip clearances: 0.025 inch on the top and bottom and 0.058 inch on the sides for the guide vanes, and 0.030 inch on the top and bottom and 0.046 to 0.048 inch on the sides for the downstream rotor. Since the stagger angles of both the guide vanes and the rotor blades are adjustable, the quoted tip clearances apply only to the mid-chord pivot points. Clearance at the blade leading and trailing edges vary slightly with changes in stagger angle from the angle for which the tip contour was determined. For each blade row, the stagger angle used to determine the tip contour was the maximum which was expected to be used. The choice of lower reference stagger angles would have resulted in interference between the blades and outer casing at stagger angles much larger than the reference. This is particularly true of the guide vanes which have large chords.

The flow measuring equipment used in the tests performed in the rotating annular cascade is the same as that used with the stationary annular cascade. This equipment has been described in Section II. A.

## 2. Calibration of Rotating Inlet Guide Vanes

The rotating guide vanes were designed to provide a wheel-type swirl angle distribution for the flow approaching the downstream blade row. The design calculations indicated that the blade row should be capable of providing the proper swirl distributions when the stagger angle is selected to provide the largest mean swirl angle with the blade row held stationary, and that smaller mean swirl angles would be attainable by allowing the row to rotate as a turbine with the speed controlled through the hydraulic drive system. The choice of turbine rather than compressor mode of operation for the guide vanes was made because of the high swirl angles required for some of the tests. It was believed that the pressure drop across the turbine would allow greater mean swirl angles to be achieved prior to stall of the guide vanes. The turbine mode of operation is made possible because the air flow through the annular cascade facility is independently controlled by the wind tunnel compressor to which it is attached. The mean axial velocity,  $U_o$ , was held constant at 60 feet per second during these tests and the following tests on the effects of blade row rotation.

In the initial calibrations of the guide vanes, it was found that using the guide vanes as a turbine only did not provide the best wheel-type swirl angle distributions. A better procedure appeared to consist of setting the guide vane stagger angle to give a mean swirl angle roughly mid-way between the extremes of the desired range and to operate the row as a turbine to obtain lower swirl angles and as a compressor to obtain higher swirl angles. The initial tests considered four different stagger angle settings of the guide vanes,

$\delta_{GV} = 48.1, 36.1, 28.1$  and  $18.1$  degrees. The listed guide vane stagger angles were measured at the hub. On the basis of these tests, the two lowest stagger angles were eliminated. Complete total pressure and swirl angle surveys were then made for the guide vane stagger angles of  $\delta_{GV} = 48.1$  and  $36.1$  degrees.

In the total pressure and swirl angle surveys, only one circumferential location was used. Since the guide vanes were rotating in all of the tests, the circumferential averages indicated by Equations 1 and 3 can be replaced by time averages at a fixed circumferential location. Thus the quantities,  $\bar{\beta}_1$ , and  $\bar{C}_{pT_1}$ , presented in the following paragraphs are actually time averages, but the definitions given previously are applicable.

Prior to the complete calibration of the rotating guide vanes, rotating stall inception on Stator Set No. 6 was determined for three stator stagger angles (30, 40, and 50 degrees measured at mid-annulus) and for guide vane stagger angles of 36.1 and 43.1 degrees. This stator set is the one which was later tested in combination with the rotating guide vanes. The inception boundaries were determined at this point in order to provide limits for the ranges over which the swirl angle calibrations of the guide vanes were required. Following the determination of the inception boundaries, Stator Set No. 6 was removed and the guide vanes were calibrated for swirl angle and total pressure over a range sufficient to include rotating stall inception in all cases.

Although the calibrations were performed for guide vane stagger angles of 36.1 and 43.1 degrees, only the data measured with  $\delta_{GV} = 36.1$  degrees will be presented. This value gave the best swirl angle distributions and was the one used for the main body of the tests on Stator Set No. 6. The results obtained at both guide vane stagger angles are presented in the Tenth Quarterly Progress Report for this program (CAL Report MK-2932-A-10).

The radial distributions of swirl angle,  $\bar{\beta}_1$ , measured downstream of the rotating guide vanes are shown in Figure 22 for a guide vane stagger angle of 36.1 degrees. The crossed hot-wire system was used to measure the swirl angles. Each radial distribution shown in Figure 22 is for a different guide vane rpm. Positive rpm's correspond to rotation as a turbine and negative rpm's correspond to rotation as a compressor (see Figure 18). Since the rotating guide vanes were designed to provide an inlet swirl angle distribution similar to that seen by an isolated rotor in a blade fixed coordinate system, it is of interest to compare the calibration results with this type of distribution. This has been done on Figure 22. The distributions seen by an

isolated rotor are shown on each graph as solid lines labeled "Desired Swirl Angle Distribution". In each case, the solid curves have been selected so that they integrate radially to the same value of  $\bar{\beta}_1$  as the experimental distributions.

Inspection of Figure 22 shows that the measured swirl angle distributions approach the desired swirl angle distributions most closely at the negative values of rpm with the best agreement obtained between -150 and -250 rpm. Rotating stall inception was found to occur on Stator Set No. 6 in this same range of guide vane rpm. Thus the guide vanes generate swirl angle distributions closest to the desired values in the range which is most useful. In general, the deviations in swirl angle from the desired values for all rpm's in Figure 22 are considerably less than the measured variations in stator blade twist noted previously for Stator Set No. 6, except very close to the tip at low guide vane rpm's and close to the hub at the largest negative rpm.

Radial distributions of total pressure coefficient,  $\bar{C}_{p_r}$ , measured downstream of the rotating guide vanes are shown in Figure 23. The distributions are most uniform at positive rpm's and become increasingly distorted as rpm is increased negatively. Unfortunately, the large negative values of rpm are required to generate the swirl angles necessary to cause rotating stall. The total pressure distributions associated with the high negative rpm's would normally present unacceptable distortion patterns to a rotor row because of the associated relative angle variations. However, these flows are being used as the inlet conditions to a stator row where the nonuniformities in total pressure do not represent relative angle of attack variations as they would on a rotor. The swirl angle surveys presented in Figure 22 have shown that the flow angle distributions are reasonably close to the desired distributions.

Radially integrated values of swirl angle,  $\bar{\beta}_1$ , and of total pressure coefficient,  $\bar{C}_{p_r}$ , downstream of the rotating guide vanes are shown in Figure 24 and 25, respectively, as a function of guide vane rpm. The definitions of  $\bar{\beta}_1$  and  $\bar{C}_{p_r}$  are given in Equations (2) and (4). These quantities are used in the theory to provide the description of the inlet flow to Stator Set No. 6.

#### D. INVESTIGATION OF EFFECT OF BLADE ROTATION ON ROTATING STALL

Prior to this portion of the experimental program, all of the rotating stall studies which have been performed in the annular cascade facility used stationary stator rows. It has not been demonstrated that the results of such studies are directly applicable to blade rows which are rotating. Indeed, there is reason to suspect that blade rotation could effect rotating stall in a manner which cannot be accounted for simply by referring all parameters to a blade-fixed coordinate system. For example, the radial distribution of pressure rise across the blade row is dependent on blade rotation even if the turning of the flow relative to a blade-fixed coordinate system is held constant. The significance of this effect to the phenomenon of rotating stall has not been established. Hence, this portion of the experimental investigation was performed to determine the effect of blade row rotation on the inception and properties of rotating stall.

In this investigation, tests were performed on a single blade row under two different conditions. First the blades were held stationary and the inlet flow was tailored by the rotating guide vanes to provide a wheel-type of inlet swirl. In this configuration, the tested blade row has been designated as Stator Set No. 6. Next, the guide vanes were removed and the tests were repeated with the blade row rotating as an isolated rotor. When used as a rotor, the blade row is designated as Rotor Set No. 1. Both series of tests then provided nearly the same inlet swirl angle distributions in a coordinate system fixed to the blades.

The tests performed on Stator Set No. 6 and Rotor Set No. 1 consisted of measuring the radial distributions of swirl angle and total pressure downstream of the blade row near the inception of rotating stall. In addition, the propagation velocities and number of cells occurring during rotating stall were measured. The results obtained with each configuration will be presented in an absolute coordinate system, and with the rotor configuration, the results will also be presented in a coordinate system moving with the blades. In the

following paragraphs, the results obtained on Stator Set No. 6 are presented first. This is followed by a presentation of the results for Rotor Set No. 1. Finally the two sets of data are compared and conclusions are presented.

### 1. Experiments on Stator Set No. 6 (Stationary Rotor)

The methods used to determine blade row performance and the properties of rotating stall were the same in this case as those used previously on Stator Sets No. 1, 4 and 5. All measurements were performed for three stator stagger angles,  $\delta_{RM} = 30, 40$  and  $50$  degrees. Since the blades in this set have considerable twist over the three inch span and since inspection of the blades showed that this twist varies from blade to blade (see Section II-C), the stagger angles were measured at mid-annulus on each individual blade. This procedure provides approximately the same overall mean stagger angle for all of the blades and reduces the variations in stagger angle at the hub and at the tip from blade to blade.

The average swirl angle distributions,  $\bar{\beta}_2$ , along a radius downstream of Stator Set No. 6 are shown in Figure 26 (a), (b), and (c) for respective stator stagger angles of 30, 40 and 50 degrees. The more extensive circumferential averages at mid-annulus,  $\bar{\beta}_{2M}$ , were not determined for this stator row. Instead, the number of circumferential measuring locations used to obtain an average was increased from the three locations used in previous work to four locations for these data.

Each curve on Figure 26 is for a different guide vane rpm and hence for a different overall inlet swirl angle,  $\bar{\beta}_1$ . The guide vane rpm at which rotating stall was first detected is indicated as a note on each of Figures 26(a), (b), and (c). For more negative values of guide vane rpm, rotating stall was always present. As in the previous stator tests, two types of rotating stall inception were observed: a small amplitude rotating stall in which the stall detectors indicated a relatively clean flow prior to inception, and a large amplitude rotating stall preceded by turbulence which could mask a small amplitude rotating stall. Here again, the large amplitude rotating stall

preceded by turbulence was observed only at the lowest stagger angle tested,  $\delta_{SM} = 30$  degrees (Figure 26 (a)).

The swirl angle distributions downstream of Stator Set No. 6 display similarities with the previous stator sets. Comparing Figures 9 and 26, the radial distributions of swirl angle for both cases are nonuniform with radius and the nonuniformity increases as the stator stagger angle is increased. The large twist in Stator Set No. 6 is in such a direction as to make the outlet swirl angles more negative at the tip than at the hub. In contrast, Stator Set No. 4 has practically no twist, so that ideally the outlet swirl angles should be nearly constant with radius. Allowing for these differences in twist, it can be seen that most of the nonuniformities occur at the hub on both stator sets and that the nonuniformities increase as rotating stall is approached. These nonuniformities are caused by a tendency for stator blades to stall first near the hub when the swirl angles in the flow are high. As explained in Reference 1, the hub stall arises because the largest pressure rise occurs at the hub under high swirl conditions.

Radial distributions of the average total pressure loss through Stator Set No. 6 are shown in Figure 27 for all three stator stagger angles which were tested. In this figure, the difference,  $\Delta \bar{C}_{p_T}$ , between the upstream and downstream total pressure coefficients as defined by Equation (5) is shown. As described previously, the upstream total pressure measurements were obtained from a time average at one circumferential location. However, because Stator Set No. 6 was stationary in these tests, averages from nine equally-spaced circumferential locations were used to define the downstream total pressure.

The tendency for the stators to stall near the hubs is quite apparent in Figure 27; the losses become very high in regions slightly removed from the hub. As with Stator Set No. 4, slightly negative values of  $\Delta \bar{C}_{p_T}$  are attained on Stator Set No. 6 near the hub and tip in some instances. However, as will be shown, the overall loss coefficient  $\Delta \bar{C}_{p_T}$  is always positive.



The overall flow turning performance and the overall total pressure losses through Stator Set No. 6 are shown in Figures 28 and 29. Rotating stall inception is indicated by arrows as in the previous presentations. The point at which the quarter-chord pressure tap indicated turbulence is also shown in Figure 28 for  $\delta_{SM} = 30$  degrees. Another feature is indicated in Figure 28 for  $\delta_{SM} = 30$  degrees. Over a small range of inlet swirl angles,  $\bar{\beta}_1$ , well removed from indications of either turbulence or rotating stall, the quarter chord pressure detectors showed a small but clear indication of the passage of the rotating guide vane wakes. At both lower and higher values of inlet swirl angle, the wake passage was not apparent. The reason for this limited sensitivity of the stator suction surface pressure to the guide vane wakes is not known at present.

The final results for Stator Set No. 6 are presented in Figure 30. These are the propagation velocity and number of cells observed during the occurrence of rotating stall. Propagation velocities have been nondimensionalized by dividing by  $U_o \tan \bar{\beta}_1$ . This quantity is almost identical to the overall average of the inlet swirl velocity  $\bar{W}_1$ . A comparison has shown the two parameters to agree within 3 percent which is within the limits of experimental error for the hot-wire equipment.

The data shown for stator stagger angles,  $\delta_{SM}$  of 40 and 50 degrees were obtained from quarter-chord pressure taps on the blades of Stator Set No. 6. The data shown for  $\delta_{SM} = 30$  degrees were obtained with a different probe arrangement. As noted previously, in this case, detectable rotating stall was preceded by a region in which the quarter-chord pressure trace became highly irregular as it had on Stator Sets No. 1 and 5 at low stator stagger angles. However, on Stator Set No. 6, the quarter-chord pressure signals became so irregular that it was impossible to measure propagation velocities and numbers of cells from photographic records. A number of other probe arrangements were tried, both upstream and downstream of the stator row. The arrangement which provided the clearest records was a small total pressure probe upstream of the stator row with the probe tip oriented approximately 90 degrees from its usual position, that is with the probe

tip in a cross flow. The data shown in Figure 30 for  $\delta_{SM} = 30$  degrees were analyzed from records obtained with this detector configuration.

In general, both the propagation velocities and the numbers of cells in Figure 30 behave in a fashion similar to that found for the other stator sets (Figure 17). With the non-dimensionalization used, the propagation velocities are approximately constant and take values similar to those observed on Stator Set No. 1. The upper limit on the numbers of cells observed was between 4 and 6 with occasionally fewer cells being observed in the intermittent region very close to inception. This again agrees with the previous stator data.

## 2. Experiments on Rotor Set No. 1.

The flow measuring techniques used on Rotor Set No. 1 were the same as those used in the calibration of the rotating guide vanes. All circumferential averages were replaced by time averages measured at a single circumferential location. Rotor stagger angles,  $\delta_{RM}$ , were set to the same three values as those used in the investigation of Stator Set No. 6. Since the flow surveys required only one circumferential measuring location, a much greater range of inlet conditions to the rotor were covered in an amount of time equal to that required for the stator investigations.

Radial distributions of swirl angle and total pressure coefficient measured downstream of Rotor Set No. 1 are shown in Figures 31 and 32 respectively for a wide range of rotor rpm's. The results shown in these figures are referenced to a laboratory fixed frame of reference (absolute coordinate system). The data obtained in the absence of rotating stall are shown as open symbols connected by solid lines. The data measured while rotating stall was occurring are shown as solid symbols connected by dashed lines. With the rotor, rotating stall displayed a considerable amount of hysteresis for a rotor stagger angle,  $\delta_{RM} = 50$  degrees and a small amount of hysteresis for  $\delta_{RM} = 40$  degrees. That is, as rotor rpm was increased rotating stall occurred at a higher value of rpm than the value at which it disappeared on decreasing the rotor rpm. No hysteresis was detected for  $\delta_{RM} = 30$  degrees

or in any of the stator tests. In those cases where hysteresis did occur, the swirl angle and total pressure data were measured both with and without the presence of rotating stall. The results for both cases are shown in Figures 31 and 32. In addition, occasional surveys were repeated to check on the consistency of the data. These repeat data are shown as symbols with tails and are listed in the legend on the figures as repeat points. The repeatability of both the swirl angle and the total pressure data were excellent.

The data presented in Figures 31 and 32 are referenced to an absolute coordinate system and the rotor blades are moving with respect to this coordinate system. In order to compare the results with those obtained on Stator Set No. 6 and also to use it in the theory, it is necessary to convert the data to a coordinate system fixed to the rotor blades. This has been accomplished through the following system of equations which relate the quantities relative to the rotor blades (designated by a subscript "R") to the quantities measured in the absolute coordinate system.

The notation for the absolute coordinate system and the sign convention used for both relative and absolute coordinate systems are shown in Figure 18. For the isolated rotor tests, the guide vanes in Figure 18 are absent and thus

$$U_1 = U_0 ; \quad W_1 = \beta_1 = 0 \quad (7)$$

With the simplification provided by Equation (7), the following expressions can be derived.

$$\bar{\beta}_{1R}(r) = -\tan^{-1} \left( \frac{W_b(r)}{U_0} \right) \quad (8)$$

$$\bar{\beta}_{2R}(r) = -\tan^{-1} \left( \frac{W_b(r) - \bar{W}_2(r)}{\bar{U}_2(r)} \right) \quad (9)$$

$$\bar{\beta}_{1R} = \frac{-2}{(r_t^2 - r_h^2)} \int_{r_h}^{r_t} r \tan^{-1} \left( \frac{W_b(r)}{U_0} \right) dr \quad (10)$$

$$\bar{\beta}_{2R} = \frac{-2}{(r_t^2 - r_h^2)} \int_{r_h}^{r_t} r \tan^{-1} \left( \frac{W_b(r) - \bar{W}_2(r)}{\bar{U}_2(r)} \right) dr \quad (11)$$

$$\Delta \bar{C}_{P_{TR}}(r) = \Delta \bar{C}_{P_T}(r) + \frac{2 W_b(r) \bar{W}_2(r)}{U_o^2} \quad (12)$$

$$\Delta \bar{\bar{C}}_{P_{TR}} = \Delta \bar{\bar{C}}_{P_T} + \frac{2}{(r_t^2 - r_h^2)} \int_{r_h}^{r_t} r \frac{2 W_b(r) \bar{W}_2(r)}{U_o^2} dr \quad (13)$$

$$\frac{V_{PR}}{W_{1R}} = 1 - \frac{V_P}{W_b} \quad (14)$$

The parameters without the subscript R are measured in the absolute coordinate system. All parameters have been defined previously in Equations (1) through (6) except for the following:

$\bar{U}_2(r)$  = circumferential average of the axial velocity downstream of the rotor

$V_p$  = rotating stall propagation velocity, positive in the same sense as  $W$

$\bar{W}_2(r)$  = circumferential average of the swirl velocity component downstream of the rotor

$W_b$  = rotor blade velocity, positive in the same sense as  $W$

The above equations were applied to convert the data measured in the absolute coordinate system to a blade-fixed coordinate system. The values of  $\bar{U}_2$  and  $\bar{W}_2$  were obtained from the results of the hot-wire surveys. It was found that simplifying assumptions which implied  $\tan \bar{\beta}_2 \approx \frac{\bar{W}_2}{U_o}$  could lead to large errors in the calculation of  $\Delta \bar{\bar{C}}_{P_{TR}}$  for large values of  $W_b$ . Thus, it was necessary to evaluate the integral expressions in these equations numerically.

Radial distributions of relative outlet swirl angle,  $\bar{\beta}_{2R}$ , are shown in Figure 33, and of relative total pressure loss coefficient,  $\Delta \bar{C}_{pR}$ , are shown in Figure 34. The method of presentation is similar to that used for the absolute coordinate system. Data obtained in the absence of rotating stall are shown as open symbols connected by solid lines. Data measured in the presence of rotating stall are shown as solid symbols connected by dashed lines. Repeated surveys are shown as symbols with tails. These data can be compared directly with the corresponding swirl angle and loss data for Stator Set No. 6 (Figures 26 and 27). This will be discussed in the next subsection.

A calibration curve of relative overall inlet swirl angle,  $\bar{\beta}_{1R}$ , versus rotor rpm is shown in Figure 35. It was obtained by analytical solution of Equation (8). With the aid of this figure, the relative overall turning and loss performance can be presented in a fashion similar to that used for Stator Set No. 6 (Figure 28 and 29). The results are presented in Figures 36 and 37 for Rotor Set No. 1.

A few comments regarding Figures 36 and 37 are warranted at this point. The rotating stall detectors used with the rotor for stagger angles of 40 and 50 degrees were pressure taps on the outer wall situated at an axial location corresponding to the quarter-chord on the rotor blades. These detectors picked up regular rotor blade passage signals which increased in amplitude as the rotor rpm was increased, that is as  $\bar{\beta}_1$  was increased in magnitude. However, for both of these stagger angles, when rotating stall occurred the rotating stall pressure signals were much larger than the regular blade passage signals. Thus the inception of rotating stall was quite clear in the photographic records. These inception points are indicated in Figure 36 along with the extent of the hysteresis in inception which has been described previously.

With the rotor at a stagger angle of 30 degrees, the outer wall detector signals became very unsteady prior to detection of a definite rotating stall pattern. The amplitude of these unsteady signals grew large enough as

$\bar{\beta}_1$  was increased to mask the possible presence of a rotating stall. Thus, as with Stator Set No. 6, small total pressure probes upstream of the rotor with their tips in a cross-flow were used to detect rotating stall for  $\delta_{RM} = 30$  degrees. The records showed that the rotating stall which occurs at  $\delta_{RM} = 30$  degrees is much more erratic than the relatively regular rotating stall that occurs at  $\delta_{RM} = 40$  and 50 degrees. Figure 36 shows both the region where erratic rotating stall is occurring and the region where the unsteady signals from the outer wall detectors are increasing in amplitude.

Figure 36 also shows a region for  $\delta_{RM} = 30$  degrees in which a third phenomenon was detected. For rotor speeds between approximately 750 and 850 rpm ( $-55^\circ \gtrsim \bar{\beta}_1 \gtrsim -59^\circ$ ), a nearly periodic disturbance with very small amplitude was indicated by the cross-flow total pressure tubes upstream of the rotor. On either side of the above rpm range, the disturbance died out. The small disturbance had the largest amplitude and was the most nearly periodic at about 800 rpm on the rotor. The disturbance frequency at this point was approximately 85 Hertz, much less than the 613 Hertz blade passage frequency but greater than the rotational frequency of the rotor ( $\approx 13$  Hertz). It was not possible from the records to determine if a propagation velocity similar to that for rotating stall was associated with the small disturbance. The cause of this phenomenon is not known at present, but it can be speculated that there is some relation between it and the previously observed sensitivity of Stator Set No. 6 to the rotating guide vane wakes over a small range of inlet swirl angles.

The rotating stall propagation velocity and number of cells observed on Rotor Set No. 1 are shown in Figure 38 for all three rotor stagger angles. The regions of hysteresis in the inception point are also indicated. Note that the propagation velocities are presented in a coordinate system fixed to the rotor blades. Thus these data can be compared directly to the results obtained on Stator Set No. 6 (Figure 30).

### 3. Comparison of Stationary and Rotating Blade Row Results

Before proceeding to a comparison of the overall performance of the rotor and stator versions of the same blade row, the radial distributions of the swirl angle,  $\bar{\beta}_2$ , downstream of the blade rows and the loss coefficient,  $\Delta \bar{C}_{p_T}$  through the blade rows will be discussed. Recall that the inlet swirl angle distribution to the stator row was tailored by the rotating guide vanes to provide a flow angle distribution over the span of the stator blades which is nearly the same as those the rotor blades see in a coordinate system moving with the rotor. Thus one would expect the flow turning and loss distributions to be similar unless the differences in centrifugally induced effects become significant.

The loss distributions through the stator and rotor will be considered first. These are shown in Figure 27 for Stator Set No. 6 and in Figure 34 for Rotor Set No. 1. The loss distributions for the stator show that, at all three stagger angles, these blades stall first near the hub and that the stalled region grows in extent and severity as rotating stall inception conditions are approached. In contrast to this, the rotor at a stagger angle of 30 degrees (Figure 34(a)) shows a tendency to stall most severely near the tip as rotating stall inception is approached. At stagger angles of 40 and 50 degrees, the rotor blade stall is spread more uniformly over the complete span of the blades. It is for these latter two cases that a hysteresis in rotating stall inception was observed. Note that the difference between the loss distributions with and without rotating stall are largest for that case ( $\delta_{RM} = 50$  degrees, Figure 34(c)) where the extent of the hysteresis is largest.

Static pressure measurements on the outer casing and on the hub were made for both the rotor and the stator. These showed that, on the rotor, the largest static pressure rise occurs at the blade tip, while on the stator the largest rise occurs at the hub. The greatest difference between the static pressure rise at the hub and at the tip occurs on the stator, which stalled near the hub at all stagger angles. The rotor, which displays a definite tip stall

only for a stagger angle of 30 degrees and a more uniform stall at the other two stagger angles, had less spanwise difference in static pressure rise across the blade row. Thus the stalling characteristics observed on the rotor and on the stator are consistent with the static pressure rise across these blade rows.

The swirl angle distributions downstream of the stator row (Figure 26) and of the rotor row (Figure 33) behave in a fashion which one would expect after inspection of the loss distributions. As rotating stall inception is approached on the stator row, the flow near the hub progressively turns less and less (larger negative values of  $\bar{\beta}_2$ ) compared with the flow near the tip. (Note that because of the twist in the blades, both the rotor and the stator should show about 10 to 14 degrees more negative values of  $\bar{\beta}_2$  at the tip than at the hub in the unstalled condition.) For the rotor at  $\delta_{RM} = 30$  degrees, which stalled near the tip, the reverse occurs. The flow near the tip is turned less. With  $\delta_{RM} = 40$  and 50 degrees on the rotor, where the spanwise loss distribution was more uniform, the spanwise distribution of  $\bar{\beta}_{2R}$  also becomes more uniform as rotating stall is approached. An interesting feature of the rotor is that it apparently turns the flow more just after rotating stall inception than it does just prior to inception. This is most noticeable near the hub for  $\delta_{RM} = 50$  degrees (Figure 37(c)).

It is apparent from the above discussion that the detailed behavior of the rotor is different from that of the stator. This is particularly true near rotating stall inception where the blade row losses are high. How much these detailed differences affect the overall performance of the blade row can be determined by comparison of the overall flow turning and loss performance curves. The overall turning performance of Stator Set No. 6 is shown in Figure 28 and of Rotor Set No. 1 in Figure 36. The differences in the overall turning performance of the rotor and the stator are not as great as one might expect. In the range of  $\bar{\beta}_1$ , near inception on Stator Set No. 6, the rotor and stator overall turning performance curves are nearly parallel for stagger angles of 40 and 50 degrees. However the stator turns the flow approximately 3 degrees less in both cases. For a stagger angle of 30 degrees, the two



turning performance curves are very close at the lowest overlapping values of overall inlet swirl angle, ( $\bar{\beta}_1 \approx -50$  degrees), but the slope of the curve for the stator is less than that for the rotor. The maximum difference at 30 degrees stagger angle occurs at  $\bar{\beta}_1 = 60$  degrees. At this point, the stator turns the flow approximately 1.5 degrees more than the rotor. Both the stator and the rotor show a maximum in the turning performance curves near rotating stall inception for a stagger angle of 30 degrees. However this peak is closer to detectable inception on the stator than it is on the rotor.

The data in Figures 28 and 36 display other parallel features near rotating stall inception for a stagger angle of 30 degrees. Both the stator and the rotor display indications (irregular unsteady pressure disturbances) of a non-rotating steady state stall on the blades prior to detectable rotating stall inception. In addition, both the rotor and the stator display possibly related phenomena well before detectable inception of either rotating stall or steady-state stall. The stators showed an unusual sensitivity to the rotating guide vane wakes, while the flow upstream of the rotor displayed a small, nearly periodic, disturbance in the approaching flow. Both of these phenomena occurred over only a small range of overall inlet swirl angles and died away outside of these small ranges. However the inlet swirl angle range was not the same in each case.

One feature of the overall turning performance which is different for the rotor and the stator is the behavior at high stagger angles after rotating stall inception. The rotor displayed a relatively large hysteresis in the inception point for rotating stall at a stagger angle of 50 degrees. The stator did not. In this range of hysteresis on the rotor, the turning performance curve shows a definite discontinuity. The flow is turned more while rotating stall is occurring than when it is not. No discontinuity is apparent in the corresponding data for the stator.

The overall loss performance curves for the stator and the rotor are shown in Figures 29 and 37 respectively. At each stagger angle and at

comparable overall inlet swirl angles, the loss curves for the stator are steeper than they are for the rotor. At the lowest overlapping inlet swirl angles, the overall loss through the stator is less than that through the rotor, while at higher inlet swirl angles, the stator displays the highest overall loss coefficient. For a stagger angle of 50 degrees, the rotor displays a large discontinuous jump in loss coefficient when rotating stall is present. This does not occur on the stator.

The propagation velocity and number of cells observed on the stator and on the rotor are given in Figures 30 and 38 respectively. Table III on the next page gives a summary of the results from these figures along with a comparison of the conditions at rotating stall inception.

Inspection of Table III shows that there are more differences than similarities in the rotating stall properties on the stator and the rotor. In all cases, rotating stall is delayed to higher overall inlet swirl angles on the rotor than on the stator. Both the rotor and the stator display clean flow prior to inception at stagger angles of 40 and 50 degrees and irregular disturbances prior to inception for a stagger angle of 30 degrees. However, the rotating stall amplitude at inception is different for the two cases. Moreover, as noted previously, the rotor displayed hysteresis in the inception point at high stagger angles but the stator did not. Propagation velocities on the stator are approximately constant for all stagger angles. On the rotor, propagation velocities increase as stagger angle is increased, being lower than those for the stator at 30 degrees stagger angle and about the same at 50 degrees. Finally, in all cases, the stator generates a higher number of rotating stall cells than the rotor. (The difference in the number of cells is probably attributable to the presence of the guide vane row ahead of the stator. This effect will be discussed in Section III.)

As discussed previously, for a given inlet swirl angle distribution relative to the blade row, the rotor generates a higher static pressure rise at the tip than at the hub. With the same inlet swirl angles, the stator has the highest static pressure rise at the hub. This loads the rotor so that it

TABLE III

Comparison of Rotating Stall Inception Points and Properties  
for Stator Set No. 6 and Rotor Set No. 1

<u>Property</u>	<u>Stagger Angle</u>	<u>Stator Set No. 6</u>	<u>Rotor Set No. 1</u>
Overall Inlet Swirl Angle, $\bar{\beta}_1$ (degrees), at Rotating Stall Inception	30	-62.4, Intermittent -63.1, Continuous	-65.3, Intermittent -65.8, Continuous but Erratic
	40	-58.9, Intermittent -59.2, Continuous	-61.7, rpm decreasing -62.7, rpm increasing (Hysteretic Inception)
	50	-60.0, Intermittent -60.5, Continuous	-65.4, rpm decreasing -68.4, rpm increasing (Hysteretic Inception)
Type of Rotating Stall Inception	30	Sudden Large Amplitude Preceded by Flow Turbulence	Small Amplitude Preceded by Irregular Disturbances at Rotor Tip
	40	Small Amplitude Preceded by Clean Flow	Large Amplitude Preceded by Clean Flow
	50	Small Amplitude Preceded by Clean Flow	Large Amplitude Preceded by Clean Flow
Range of Dimensionless Propagation Velocity	30	0.41 - 0.51	0.23 - 0.30 (one point at 0.37)
	40	0.47 - 0.55	0.33 - 0.48
	50	0.41 - 0.49	0.41 - 0.51
Number of Stall Cells	30	5-6 (Single cell observed once in intermittent region)	1 (Two cells observed once)
	40	4-5	1, near inception 2, at high $\bar{\beta}_1$
	50	2-5, in intermittent region 4-6, after intermittent region	1

stalls first at the tip or else approximately uniformly over the span, while the stator always stalls first at the hub (at least for the twist distribution on the tested blades). As a result, the overall turning and loss performance, as well as the radial distributions in blade turning and loss, differ between the rotor and the stator. However, as will be shown in the next section, if the overall turning and loss performance are known, then the properties of rotating stall on either blade row are satisfactorily predicted by the two-dimensional theory presented therein. Thus it would appear that there is no direct effect of blade rotation on the properties of rotating stall. The effect is indirect, through changes in the steady-state blade row performance characteristics. Moreover, for the high hub-to-tip ratio used in this program, it appears adequate to represent the steady state performance characteristics by overall results, integrated over the span of the blades.

#### E. CONCLUDING REMARKS

The results of two separate experimental investigations of rotating stall have been presented in Section II. In the first investigation, Section II-B, the experiments were designed to determine if the blade-chord length has a direct effect on the properties of rotating stall. It had been noted in Reference 1, that the experimental evidence available at the time suggested that this might be the case. In particular, there was the possibility that rotating stall propagation velocities decreased in inverse proportion to the blade-chord length and that this effect was independent of the blade row solidity ratio. In the experiments of Section II-B, both the blade chord and the solidity ratio were varied independently. It was found that blade chord does not have any large direct effect on rotating stall propagation velocities. Some differences with blade chord were noted, but these were small. In contrast, solidity ratio showed a relatively large effect in these experiments. However this result is in contradiction with the findings of Reference 3. On the basis of these results, and with anticipation of the correlations between theory and experiment presented in Section III, it is concluded that differences

in rotating stall properties which are observed, arise primarily from the effect of blade chord and solidity ratio on the steady state turning and loss performance of a blade row. If these performance characteristics are known, then the properties of rotating stall can be predicted.

In the second experimental investigation, Section II-D, the effects of blade-row rotation on the properties of rotating stall were studied. In this program, the same blade row was tested under two different conditions. First it was held stationary and the inlet flow was tailored to provide a wheel-type of inlet swirl by using rotating guide vanes upstream. Next, the guide vanes were removed and the tests were repeated with the blade row rotating as an isolated rotor. In this way the inlet swirl angle distributions relative to the blades were kept nearly the same for both tests. The results of these tests lead to a conclusion similar to that for the blade-chord experiment. The conditions for inception and the properties of rotating stall were different for the stator and the rotor. However, so were the steady state turning and loss performance of the stator and rotor. If these steady state performance differences are known, then the inception conditions and properties of rotating stall for each case are predictable by the theory of Section III. Thus, as with blade chord and solidity ratio, the effect of blade row rotation is indirect in that differences in rotating stall arise from rotation induced differences in steady state turning and loss performance of the blade row.

In addition to the results discussed above, both experimental investigations provided a large amount of data obtained on a variety of blade rows, with each blade row at several blade stagger angles. These results were invaluable for guidance in the theoretical development and for assessing the success of the theory through correlations between theoretical predictions and experimental results.

### SECTION III

#### THEORETICAL ROTATING STALL RESEARCH

Rotating stall has, traditionally, been explained in terms of a flow blockage analog whereby the induced flow angularity from the blockage alleviates the stalling of blades on one side of the stall zone and promotes the stalling of blades on the opposite side of the stall zone. Whereas this idea appears to be fundamentally correct, the present work shows that the induced velocities from the unsteady vortex wakes of the stalled blade groups are also essential for the occurrence of the phenomenon.

The first theories of rotating stall were given by Sears<sup>4\*</sup>, Marble<sup>5</sup>, Stenning et al<sup>6</sup>, and Emmons et al<sup>7</sup>. The emphasis in these early works was on the prediction of propagation speed and number of stall cells whereas the emphasis in the present work is on prediction of inception conditions. Various blade row properties were assumed in these early studies and the salient features of these works are discussed and summarized at length in References 8 and 9. The details of these works, therefore, will not be recounted here except to mention that the concept of a boundary layer lag time was considered important<sup>4, 6, 8</sup>. Generally, good correlation with experiment was only obtained in those analyses in which the boundary layer lag time (or equivalently phase angle) was left free for adjustment. Moreover, when several sets of data were analyzed in the same fashion, no general conclusion could be drawn about the required phase lags.<sup>8</sup> (In the present analysis, satisfactory correlation is obtained without considering this phenomenon).

Takata and Nagano<sup>10</sup>, have recently presented a theory which correlates well with their limited amount of data. Their theory is nonlinear and requires extensive calculation to analyze any given configuration. While this type of analysis can be quite good for any given case, it is difficult to identify the fundamental phenomena involved and to generalize from numerical solutions.

---

\* Superscripts denote reference numbers listed at the end of the report.

Takata also concludes that the nonlinearities in the equations of motion are not significant but that the nonlinearities of the cascade properties dominate. (The same conclusion may be drawn from the present work). Therefore, the present work was limited to a linearized analysis to allow ready identification of the important blade row characteristics. It may also be argued that a linear theory should be adequate for prediction of inception conditions whereas this is probably not true for analysis of the flow after rotating stall has been established.

The present analysis is a natural extension of the methods of formulation developed by Brady<sup>11</sup>. Although the previous theoretical investigation at Calspan were unsuccessful, the primary deficiency was identified in Reference 1 as the absence of blade row losses in the flow model. They have been included in the present flow model and the resulting correlation of theory and experiment validates the conclusion of Reference 1.

Although the details of the formulation of the present work are quite different from the previous theories<sup>4-7, 10</sup> the resulting flow model bears some similarity to that of Sears' channel flow theory<sup>4</sup> and corresponds somewhat to a linearized version of the theory of Takata and Nagano. Some of the differences will be pointed out at the appropriate places in the following text. There is only slight connection between the present theory and those of References 5 and 6.

The present theory is a small disturbance stability theory in that time dependent small disturbances are superimposed on the steady mean flow through a blade row, and the growth of the disturbances with time are determined for various flow configurations. The flow is considered stable if the disturbances die out or are damped with time, unstable if the disturbances grow or are amplified in time, and neutrally stable if the disturbance amplitude is not changing with time. The stall inception is assumed to correspond to the neutral stability boundary. The theory has been formulated for an isolated blade row and a two blade row configuration. The isolated or single

blade row analysis will be described in the greatest depth since this model is much easier to understand and produces numerical results which are close to the two blade row case. Most of the details of the two blade row development are presented in Appendix B, and only the results will be presented and discussed in the main text.

The present theory, as have been all the previous rotating stall theories<sup>4-7, 10</sup> is an incomplete theory in that blade row performance data must be used as input to the theory. At present, it appears that the only satisfactory source of these data is experiment.

It was found not necessary to include the phenomena of hysteretic behavior in the blade lift curves or a lag time for boundary layer separation to achieve satisfactory correlation of theory and experiment. However, it was found necessary to use accurate blade row loss data to achieve satisfactory correlation. The single blade row theory was formulated with a lag time, but numerical results were never obtained because data were not available to specify the lag time and moreover, satisfactory correlation was obtained without considering this phenomena. The formulation of the theory with lag time is, however, presented because of the interesting character of the resulting model.

In addition, the effects of two different downstream constant pressure boundary conditions on the theoretical model and resulting predictions were determined.

The flow model presently used is an incompressible two-dimensional finite-thickness actuator sheet model and is described in detail in the following sections. It is assumed that for high hub-to-tip ratios and low subsonic relative blade velocities that the flow through a compressor blade row may be approximated by the flow through a two-dimensional cascade.



## A. SINGLE BLADE ROW THEORY

The flow through an isolated blade row in incompressible flow is considered. A finite-thickness two-dimensional actuator-sheet was used to model the blade row and is shown in Fig. 39 (The subscript o's indicate quantities in a blade fixed coordinate system.) The transformation between blade fixed coordinates and the laboratory fixed system is given by

$$\begin{aligned}x_o &= x \\y_o &= y - W_b t \\t_o &= t\end{aligned}$$

where  $W_b$  is the blade velocity in the laboratory fixed system. The conditions upstream of the blade row are denoted by a subscript 1 while conditions downstream of the blade row are denoted with a subscript 2. The mean flows upstream and downstream of the blade row are uniform but of different swirl angles. The finite thickness of the actuator retains the effects of the inertia of the fluid within the blade row and leads to propagation velocities which are weakly dependent upon blade chord. The mean absolute swirl angle in each region is denoted as  $\bar{\beta}_x$  and the tangent of  $\bar{\beta}_x$  is defined as  $S_x$ , the absolute swirl. The blade row is moving with an absolute velocity of  $W_b$  and the non-dimensional blade velocity is given by  $\bar{\Omega} = \frac{W_b}{U_o}$ . The relative swirl with respect to the blade row is given by  $\mathcal{J}_x = S_x - \bar{\Omega}$ .

It may be seen then that the fundamental differences between the flow model used in this investigation and the channel flow model used in Reference 1 is: (1) the finite thickness of the actuator, and (2) allowance for turning of the mean flow through the blade row in the present analysis. We must proceed further to point out the differences between the present work and Reference 10.

Following References 1 and 11, all of the total flow quantities, which are denoted by a hat, are decomposed into steady and unsteady parts as

$$\begin{aligned}\hat{W}_x &= W_x + w_x(t) \\ \hat{U}_x &= U_x + u_x(t) \\ \hat{\beta}_x &= \bar{\beta}_x + \beta'_x(t)\end{aligned}$$

where the  $\lambda$  designates the flow region. The unsteady parts are considered to be much smaller than the steady parts such that the equations of motion may be linearized. The linearization process is exactly the same as that used in Reference 11 and a solution for the disturbance stream function of the form  $\psi_\lambda = \phi_\lambda(x) e^{j(ct + n y/r)}$  is sought such that  $u_\lambda = \frac{\partial \psi_\lambda}{\partial y}$  and  $w_\lambda = -\frac{\partial \psi_\lambda}{\partial x}$ . Here  $C$  is complex i. e., ( $C = C_R + j C_I$ ) and  $n$  is the number of stall cells. The resulting disturbance is spatially periodic in the  $y$  direction with period  $\frac{2\pi r}{n}$  where  $r$  is the mean radius of the blade row. Neutral stability occurs when  $C_I = 0$ , instability when  $C_I < 0$  and stability when  $C_I > 0$ . The appropriate  $\phi_\lambda$  are readily determined from the linearized Euler equations as

$$\phi_\lambda(x) = A_\lambda e^{-\frac{nx}{r}} + B_\lambda e^{\frac{nx}{r}} + D_\lambda e^{-j \frac{nx}{r} \left( \frac{cr}{nU_0} + S_\lambda \right)} \quad (15)$$

where the  $A_\lambda$ ,  $B_\lambda$  and  $D_\lambda$  are constants to be determined by the boundary conditions.

To keep the flow quantities bounded at infinity upstream and downstream, we must have

$$A_1 = B_2 = 0$$

Further, requiring that the flow be irrotational at upstream infinity implies that  $D_1 = 0$  since the  $A_\lambda$  and  $B_\lambda$  terms are irrotational.

These considerations reduce the number of undetermined constants to three and the disturbance velocities may then be expressed as

$$u_1 = B_1 j \frac{n}{r} \exp \left[ j \left( ct + \frac{ny}{r} \right) + \frac{nx}{r} \right] \quad (16a)$$

$$w_1 = -B_1 \frac{n}{r} \exp \left[ j \left( ct + \frac{ny}{r} \right) + \frac{nx}{r} \right] \quad (16b)$$

$$u_2 = j \frac{n}{r} \left\{ A_2 \exp \left[ j \left( ct + \frac{ny}{r} \right) - \frac{nx}{r} \right] + D_2 \exp \left[ j \left( ct + \frac{ny}{r} \right) - j \frac{nx}{r} \left( \frac{cr}{nU_0} + S_2 \right) \right] \right\} \quad (16c)$$

$$\omega_2 = \frac{n}{r} A_2 \exp \left[ j \left( ct + \frac{ny}{r} \right) - \frac{nx}{r} \right] \quad (16d)$$

$$+ j \frac{n}{r} \left( \frac{cr}{nU_0} + S_2 \right) D_2 \exp \left[ j \left( ct + \frac{ny}{r} \right) - j \frac{nx}{r} \left( \frac{cr}{nU_0} + S_2 \right) \right]$$

The downstream disturbances are then composed of an irrotational component (the terms proportional to  $A_2$ ) and vortex waves which are convected along the mean flow streamlines (the terms proportional to  $D_2$ ).

The remaining constants ( $B_1$ ,  $A_2$  and  $D_2$ ) are determined by the matching conditions across the actuator which relate upstream and downstream flow conditions.

The matching conditions used are

- 1) Conservation of mass flow
- 2) Vorticity compatibility (conservation of vorticity)
- 3) Flow deflection relation

The conservation of mass flow through the actuator requires that

$$u_{o_1} (x_{o_1}, y_{o_1}, t_o) = u_{o_2} (x_{o_2}, y_{o_2}, t_o) \quad (17)$$

where

$$x_{o_1} = 0 \quad ; \quad x_{o_2} = d \cos \delta$$

and

$$y_{o_2} = y_{o_1} + d \sin \delta$$

The vorticity compatibility relation is essentially an extension of Helmholtz's law to consider flows with losses. It may be derived from first principles as follows:

In vector form, the fluid dynamic equations are

$$\frac{D\vec{V}}{Dt} = -\frac{1}{\rho} \nabla p + \vec{f} \quad (18)$$

where

$$\frac{D}{Dt} \equiv \frac{\partial}{\partial t} + V_x \frac{\partial}{\partial x} + V_y \frac{\partial}{\partial y} + V_z \frac{\partial}{\partial z}$$

$$\nabla \equiv i \frac{\partial}{\partial x} + j \frac{\partial}{\partial y} + k \frac{\partial}{\partial z}$$

$$\vec{V} = i V_x + j V_y + k V_z$$

$\rho$  = the density (assumed constant)

$p$  = the static pressure

$\vec{f}$  = the friction force

For a closed circuit  $C$  the circulation is defined as  $\Gamma = \oint_C d\vec{r} \cdot \vec{V}$  where  $\vec{r}$  is the radius vector to points on  $C$ . Then

$$\frac{D\Gamma}{Dt} = \oint_C d\vec{r} \cdot \frac{D\vec{V}}{Dt} = \oint_C d\vec{r} \cdot \left(-\frac{1}{\rho} \nabla p + \vec{f}\right) = \oint_C d\vec{r} \cdot \vec{f} \quad (19)$$

since

$$\oint_C d\vec{r} \cdot \nabla p = 0$$

(Our previous analysis<sup>1, 11</sup> used  $\frac{D\Gamma}{Dt} = 0$  which corresponds to assuming no losses in the flow through the cascade).

Using the vector identity

$$\vec{V} \cdot \nabla \vec{V} = \frac{\partial \vec{V}}{\partial t} + \frac{1}{2} \nabla (\vec{V} \cdot \vec{V}) - \vec{V} \times \vec{\omega}$$

where  $\vec{\omega}$  is the vorticity vector, we have

$$\frac{D\Gamma}{Dt} \equiv \frac{\partial \Gamma}{\partial t} - \oint_C d\vec{r} \cdot (\vec{V} \times \vec{\omega})$$

whereupon Equation (19) becomes

$$\frac{\partial \Gamma}{\partial t} - \oint_C d\vec{r} \cdot (\vec{V} \times \vec{\omega}) = \oint_C d\vec{r} \cdot \vec{f} \quad (20)$$

This equation is strictly applicable to a flow model in which the blade rows are present. For the present type of flow model where the blades are modeled by an actuator,  $\vec{f}$  must be modified to include a body force which represents all the forces exerted on the fluid by the blade row.

However, only the loss producing or nonconservative forces need to be considered in Equation (20). The line integral of a conservative force, such as produced by blade lift, around a close circuit vanishes.

Equation (20) is the fundamental vorticity compatibility relation. A closed contour,  $C$ , is chosen which encloses a portion of the actuator sheet as in Figure 39. Sides ① and ③ are the boundary of the actuator and sides ② and ④ are parallel to the blade chords. It is assumed that the unsteady velocity through the actuator is parallel to the blade chords and equal to  $u_o \sec \delta$ . It is also assumed that the frictional forces act essentially parallel to the local flow direction such that their contribution to the right hand side of Equation (20) may be neglected along sides ① and ③. Use is then made of the following relationship which is derived from integration of the unsteady form of the momentum equation through the actuator.

$$\int_{x_{o_1}}^{x_{o_2}} d\vec{r} \cdot \vec{f} = \frac{1}{2} X (\hat{U}_{o_1}^2 + \hat{W}_{o_1}^2) - d \sec \delta \frac{\partial u_{o_1}}{\partial t_o}$$

Where  $X$  is the total pressure loss coefficient defined such that it is positive for loss through the blade row. That is

$$X = \frac{H_1 - H_2}{\frac{1}{2} \rho (\hat{U}_{o_1}^2 + \hat{W}_{o_1}^2)}$$

and  $H_x$  is the total pressure relative to the blade row in region  $x$ . Then the limit of Equation (20) as side ② approaches side ④ is

$$\begin{aligned} \frac{\partial}{\partial t_o} (\omega_{o_2} - \omega_{o_1}) - d \sec \delta \frac{\partial^2 u_{o_1}}{\partial t_o \partial y_o} + U_o (\eta_{o_2} - \eta_{o_1}) \\ = \frac{\partial}{\partial y_o} \left\{ \frac{1}{2} X \left[ (U_o + u_{o_1})^2 + (W_{o_1} + \omega_{o_1})^2 \right] \right\} \end{aligned} \quad (21)$$

Here  $\eta_o$  is the  $Z_o$  component of the vorticity vector and all quantities with a subscript 1 are evaluated at  $x_{o_1}$  and  $y_{o_1}$ , while all quantities with a subscript 2 are evaluated at  $x_{o_2}$  and  $y_{o_2}$ .

Equation (21) essentially states that the vorticity shed into the wake is the sum of the time rate of change of the bound vorticity in the actuator plus the vorticity shed due to the loss variation along the actuator axis.

Equation (21) is also the essential working form of the pressure loss relation developed in Reference 10. However, it has been developed here from the viewpoint of conservation of vorticity.

The steady state turning performance of the cascade is assumed to be expressible in the form

$$\tan \bar{\beta}_{o_2} = G_{SS} (\tan \bar{\beta}_{o_1}) \quad (22)$$

where the subscript SS means steady state. For small unsteady variations in inlet angle about  $\bar{\beta}_{o_1}$ , the first two terms in the Taylor Series expansion of Equation (22) are used to obtain the quasi-steady relation

$$G_{QS} (\tan \hat{\beta}_{o_1}) \approx G_{SS} (\tan \bar{\beta}_{o_1}) + \sec^2 \bar{\beta}_{o_1} a \tan \beta'_{o_1} \quad (23)$$

where

$$a = \frac{\partial G_{SS}}{\partial \tan \beta_{o_1}}$$

Then the flow turning relationship between upstream and downstream swirls is given by

$$\omega_{o_2} - \mathcal{J}_2 u_{o_2} = a [\omega_{o_1} - \mathcal{J}_1 u_{o_1}] \quad (24)$$

where use of the following approximation has been made

$$\tan \hat{\beta}_{o_1} \approx \frac{w_{o_1}}{U_{o_1}} + \frac{\omega_{o_1} - \mathcal{J}_1 u_{o_1}}{U_o} \quad (25)$$

and Equation (21) is evaluated similarly to Equation 21. The approximation involved in Equation (23) is not valid for fully established rotating stall but it should be valid prior to inception. Equations (17), (21), and (24) then are the matching conditions between flow conditions upstream and downstream of the blade row. They embody the aerodynamic characteristics attributed to the blade row.

Substitution of the velocity components, Equations (16a), (16b), (16c), and (16d) into the matching conditions Equations (17), (21), and (24) yields the following homogeneous system of equations for the unknown constants  $B_1$ ,  $A_2$  and  $D_2$ .

$$\begin{bmatrix} 1 & -e^{\bar{q}_1} & -e^{\bar{q}_3} \\ -j\lambda(1+q) - M_1 & -j\lambda e^{\bar{q}_1} & -[(\lambda + \mathcal{S}_2)\mathcal{S}_2 + 1]e^{\bar{q}_3} \\ aM_2 & (1 - j\mathcal{S}_2)e^{\bar{q}_1} & j\lambda e^{\bar{q}_3} \end{bmatrix} \begin{bmatrix} B_1 \\ A_1 \\ D_2 \end{bmatrix} = 0 \quad (26)$$

where

$$M_1 = (1 + j\mathcal{S}_1) \left[ \frac{j}{2} (1 + \mathcal{S}_1^2) X' + X \right]$$

$$M_2 = 1 + j\mathcal{S}_1$$

$$\lambda = \frac{cr}{nU_0} + \bar{\Omega}$$

$$q = \frac{dn}{r} \sec \delta$$

$$\bar{q}_1 = -\frac{nX_{02}}{r} + \frac{dn}{r} \sin \delta$$

$$\bar{q}_3 = j \left[ \frac{dn}{r} \sin \delta - \frac{nX_{02}}{r} (\lambda + \mathcal{S}_2) \right]$$

$$X' = \frac{\partial X}{\partial \tan \beta_{01}}$$

The requirement for a nontrivial solution to Equation (26) is

$$\begin{vmatrix} 1 & -1 & -1 \\ -j\lambda(1+q) - M_1 & -j\lambda & -[(\lambda + \mathcal{S}_2)\mathcal{S}_2 + 1] \\ aM_2 & (1 - j\mathcal{S}_2) & j\lambda \end{vmatrix} = 0 \quad (27)$$

This is the characteristic equation which determines the allowable values of  $\lambda$  for a nontrivial solution. This equation is a quadratic equation in  $\lambda$  and the first root is found to be the zero amplitude solution previously encountered<sup>1, 11</sup>

$$\lambda_1 = -(\mathcal{S}_2 + j) \quad (28)$$

which has no physical significance. The second root is

$$\lambda = -\frac{1}{2+q} \left\{ \frac{1}{2} (1 + \mathcal{S}_1^2) X' + \mathcal{S}_1 X + a(\mathcal{S}_1 + \mathcal{S}_2) \right\} + \frac{j}{2+q} \left\{ X + 1 + \mathcal{S}_2^2 + a(1 - \mathcal{S}_1 \mathcal{S}_2) - \frac{\mathcal{S}_1}{2} (1 + \mathcal{S}_1^2) X' \right\} \quad (29)$$

or in terms of  $C$

$$\frac{rC_R}{nU_0} = -\bar{\Omega} - \frac{1}{2+q} \left\{ \frac{1}{2} (1 + \mathcal{J}_1^2) X' + \mathcal{J}_1 X + a(\mathcal{J}_1 + \mathcal{J}_2) \right\} \quad (30a)$$

$$\frac{rC_I}{nU_0} = \frac{1}{2+q} \left\{ X + 1 + \mathcal{J}_2^2 + a(1 - \mathcal{J}_1 \mathcal{J}_2) - \frac{\mathcal{J}_1}{2} (1 + \mathcal{J}_1^2) X' \right\} \quad (30b)$$

Now  $C_I = 0$  implies neutrally stable conditions,  $C_I < 0$  implies unstable conditions and  $C_I > 0$  implies stable conditions. The propagation velocity of an admissible disturbance is given by

$$V_p = - \frac{r}{n} C_R \quad (31)$$

The fundamental mechanisms of rotating stall may be identified by analyzing Equation (30b). First we note that  $q$ ,  $X$  and the product  $\mathcal{J}_1 X'$  are positive in regions of interest. Then we see that the only possible destabilizing contributions to  $C_I$  come from the last two terms inside the large brackets. The term proportional to  $a$  originates in the flow deflection relationship, Equation (24), and may be either stabilizing or destabilizing. The term proportional to  $X'$  originates in the vorticity compatibility relation, Equation (21), and is always destabilizing. This term may be linked to the vorticity shed into the blade wake by the variation in the time rate of change of losses along the cascade. Without losses and the flow deflection condition, no instabilities are possible as was found in Reference 1.

From Equation (30b) the following must be true at the neutral stability points

$$X + 1 + \mathcal{J}_2^2 + a(1 - \mathcal{J}_1 \mathcal{J}_2) - \frac{\mathcal{J}_1}{2} (1 + \mathcal{J}_1^2) X' = 0 \quad (32)$$

Although the propagation velocity and the damping factor,  $\frac{rC_I}{nU_0}$ , are in general dependent upon the number of stall cells, Equation (32) demonstrates that the neutral stability boundary is not.



Equations (30a) and (30b) have been correlated with all the rotating stall inception data obtained under the experimental phase of this program. This has been accomplished under the following assumptions for Stator Sets Nos. 1, 4, 5, and 6

$$\begin{aligned} \mathcal{J}_1 &= \tan \bar{\beta}_1 \\ \mathcal{J}_2 &= \tan \bar{\beta}_2 \\ X &= \frac{1}{1 + \mathcal{J}_1^2} \overline{\Delta C_{P_T}} \end{aligned}$$

That is, we have chosen to compare the two dimensional theory to the three dimensional experimental data by using the radially averaged flow quantities from the experiments.  $\mathcal{J}_2$  and  $X$  were spline fit as functions of  $\mathcal{J}_1$ , the resulting spline fits were differentiated to obtain  $a$  and  $X'$ . That is,  $\mathcal{J}_1$  was considered as the independent variable. The blade row loss data used is shown in Figures 14, 15, 16, and 29. The blade row turning performance used is shown in Figures 11, 12, 13 and 28. The resulting damping factors were calculated for various  $\mathcal{J}_1$ , and the zero crossings were extracted. The resulting values of  $\mathcal{J}_1$  satisfy Equation (32) and have been translated back into terms of inlet guide vane stagger angle,  $\delta_{GV}$ , using the inlet guide vane calibration curves, Figure 6. The resulting calculations for Stator Sets Nos. 1, 4, 5 and 6 are shown as the circular points in Figures 40, 41, 42 and 43. Note that the comparison is only possible at those stator stagger angles where both loss and turning performance measurements were made. The predictions of the two blade row theory which will be discussed in Section III-B are also shown on these figures for ease of presentation. The number of stall cells noted next to the theoretical points apply only to the two blade row theoretical results since as mentioned previously the single blade row neutral stability points are independent of the number of stall cells. Overall, the theoretical inception boundary agrees well with the experimental boundary with the exception of Stator Set No. 1 at  $\delta_{SM} = 37.2^\circ$  where no theoretical instability is found. This may be attributed to the loss curve for this condition (see Figure 14) where insufficient experimental points were obtained to define the loss curve adequately near inception conditions.

For correlation with the data for Rotor Set No. 1, the following assumptions were made

$$\begin{aligned} \mathcal{S}_1 &= \frac{-W_b}{U_o} \\ \mathcal{S}_2 &= \tan \beta_{2R} \\ X &= \frac{1}{1 + \mathcal{S}_1^2} \overline{\Delta C_{PT_R}} \end{aligned}$$

The data required for the last two relations may be obtained from Figures 26 and 37. The predicted inception points for Rotor Set No. 1 are shown in Figure 44. The experimental and theoretical points shown correspond to increasing rpm.

It should be remembered that all of the blade sets except Rotor Set No. 1 have a set of guide vanes upstream to provide the desired inlet flow angles. The guide vanes were sufficiently far upstream that they did not produce any effect upon the mean blade row characteristics; however, their effect upon rotating stall is uncertain. The previous experiments performed at Calspan<sup>1</sup> indicated that for one configuration investigated the inlet swirl at inception was not affected. However, there are insufficient data to generalize this conclusion. The good correlation between the single blade row theory and data would tend to confirm the conclusion, however. The effects of the guide vanes will be discussed further in the section on the two blade row theory.

The damping factors,  $\frac{rC_I}{nU_o}$ , and the propagation velocities for admissible disturbances (i. e., admissible values of  $\lambda$ ) have been calculated for each blade set using the relationships expressed in Equations (30a) and (30b). This has been done for a range of inlet conditions for each blade set and the results are shown as the dashed curves in Figures 45 through 49. The number of stall cells,  $n$ , was chosen to agree with the number experimentally observed at inception of steady rotating stall. The zero damping points of these curves correspond to the inception points shown in Figures 40 through 44. The arrows in Figures 45 through 49 correspond to the boundary for intermittent rotating stall. It should be noted that the propagation velocities for Rotor Set No. 1 shown in Figure 50(a) through 50(b) are the propagation velocity in the laboratory fixed coordinate system as opposed to the relative velocities shown in Figure 36. The absolute velocity is equal to one minus the relative velocity.

Since the calculations shown in Figures 45 through 49 involved curve fitting and differentiation of the resulting curve, they are somewhat dependent upon the type of curve fairings used. The early fairings were done by hand calculations using power series representations of the data. The results that are presented here were obtained by using a spline fit routine in the IBM 370/175 computing machine. It was felt that this would give the most consistent handling of the data. Comparison of the various curve fitting procedures indicated that inlet angles for neutral stability were independent of the procedure used to within a quarter of a degree. More pronounced variations were evident in the damping factors beyond inception. Therefore the calculations in these regions shown in Figures 45 through 49 must be considered more qualitative than quantitative. However, the character of the stability of the flow may be inferred from these curves.

Moreover, it may be seen that generally the transition from stable to unstable conditions occurs over a very small change in inlet conditions. The cases where these curves do not show this sharp change, i. e., Figures 45(a), 47(a) 47(b) and 48(a), correspond to conditions where the experimental observations show that some sort of turbulence preceded the onset of rotating stall. It might be concluded that whenever the damping factor for a given flow condition was less than, say, 0.2, some sort of unsteadiness was observed in the flow.

Inspection of Figures 45 through 49 shows that in those cases where the experimental inception of rotating stall is clean the theory predicts inception generally within two percent on relative inlet swirl. The swirl is the critical item from the standpoint of design pressure ratio for a compressor stage.

The good correlation between theory and experiment obtained here not only tends to verify the fundamental mechanisms identified by the theory, but also tends to indicate that three dimensional effects, per se, are not

significant for the high hub-to-tip ratio configuration investigated. Although the inlet and outlet swirl angles to a blade row and the total pressure loss through the blade row show considerable radial variations, as may be seen from Figures 9, 10, 26, 27, 33, and 34, the simple operation of radially averaging these flow quantities proves adequate to handle the three dimensional effects in the present investigation.

The correlation of theory and experiment was limited to data obtained in the present program, primarily, because this was the only set of data that was sufficiently complete to allow calculations.

Experience with the numerical evaluation of Equation (30b) and the cascade data has shown that the  $X'$  term dominates the  $a$  term in controlling the stability of a given flow configuration. From Equation (30b) it is seen that when

$$X' > \frac{2}{\mathcal{J}_1(1+\mathcal{J}_1^2)} \left\{ X + 1 + \mathcal{J}_2^2 + a(1 - \mathcal{J}_1 \mathcal{J}_2) \right\}$$

an instability results. This relation may be compared to Equation 53 of Reference 4. This comparison would indicate that the use of a more accurate blade row loss representation and the allowance for turning of the flow through the blade row are probably the major reasons that better correlation has been obtained in the present work.

## B. TWO BLADE ROW THEORY

The previous analysis considered only a single blade row. In most practical compressors there are many blade rows closely stacked, hence, it is desirable to develop an applicable theory to handle an arbitrary number of blade rows. The first step of this task, namely a two blade row theory, was developed under the present program.

The question of the mechanism that controls the number of stall cells also remains open. The number of cells is certainly determined by one

of the physical lengths of the problem, but the identification of the specific one is incomplete. The single blade row analysis shows that the blade chord does not determine the number of cells. The remaining lengths to be included in the flow model are blade row spacing and pitch distance between blades on the same row. At present, the actual blades cannot be modeled so that no conclusions can be drawn about the pitch spacing. However, the spacing between blade rows can be modeled within the context of the present analysis.

The type of analysis employed for the single blade row case was extended to a configuration of two arbitrary blade rows. The development of this theory will be outlined and summarized here and additional detail will be given in Appendix B. The geometry of the problem to be considered is shown in Figure 50.

There are three flow regions to be considered. Region 0 (i. e.,  $x = 0$ ) is upstream of the first actuator. Region 1 is downstream of the first actuator and upstream of the second actuator. Region 2 is downstream of the second actuator. The mean absolute swirl angle in each region is denoted as  $\bar{\beta}_x$  and the tangent of  $\bar{\beta}_x$  is defined as  $S_x$ . The blade rows are moving at absolute velocities of  $W_{b_j}$ , and the non-dimensional blade velocities are defined as  $\bar{\Omega}_j = \frac{W_{b_j}}{U_0}$ . The tangents of the relative angles with respect to the first actuator (blade row) are then given by  $\beta_1^+ = S_1 - \bar{\Omega}_1$  and with respect to the second actuator by  $\beta_2^+ = S_2 - \bar{\Omega}_2$ . The blade row stagger angles are noted as  $\delta_1$  and the blade chords by  $\alpha_1$ .

Then as in the single blade row case the disturbance velocity in each region is determined from a disturbance stream function  $\psi_1$  of the form

$$\psi_1 = \phi_1(x) e^{j(ct + ny/r)}$$

such that  $u_1 = \frac{\partial \psi_1}{\partial y}$  and  $w_1 = -\frac{\partial \psi_1}{\partial x}$

and  $c$  is complex  $c = c_R + j c_I$

Neutral stability then corresponds to  $C_I = 0$  and instability to  $C_I < 0$ . The fundamental solutions for the  $\phi_i$  are again known from Reference 1 as

$$\phi_i(x) = A_i e^{-nx/r} + B_i e^{nx/r} + D_i e^{-j \frac{nx}{r} \left( \frac{cr}{nU_0} + S_i \right)}$$

There are then nine constants (the  $A_i$ ,  $B_i$  and  $D_i$ ) to be determined from the boundary conditions. The boundary conditions used are:

- 1) Boundedness of the solution far upstream and far downstream
- 2) Continuity matching condition at each actuator
- 3) Vorticity compatibility at each actuator
- 4) Flow deflection relation at each actuator
- 5) No vorticity upstream of the first actuator

No time lags were assumed in any of these conditions. The single actuator correlations indicated time lags were not necessary.

Condition 1 implies that  $A_0 = B_2 = 0$  and condition 5 implies  $D_0 = 0$ . The remaining conditions then lead to a sixth order characteristic determinant. One solution may be determined by inspection as  $k = -(S_2 + j)$  where  $k = \frac{cr}{nU_0}$ . This is essentially the same zero amplitude disturbance that has always been found. The remaining characteristic equation then becomes,

$$M_{31} \eta_{31} e^{\frac{n(T-x_1)}{r}} + M_{32} \eta_{32} e^{\frac{n(T-x_1)}{r}} + M_{33} \eta_{33} e^{-j \frac{n}{r} (T-x_1)(k+S_1)} = 0 \quad (33)$$

where the  $M_{jk} \eta_{jk}$  are polynomials in  $k$  which are given in Appendix B and  $T$  is the spacing between leading edges of the actuators.

Equation (33) is transcendental because of the last exponential term and must in general be solved numerically. However, certain analytic behavior may be deduced from the equation. First, in the limit as the spacing between blade rows becomes large (i.e.,  $T \rightarrow \infty$ ), Equation (34) becomes

$$M_{31} \eta_{31} = 0 \quad (34)$$

Now it may be verified that  $\mathcal{M}_{32} = 0$  corresponds to the characteristic equation for the second blade row in isolation and  $\mathcal{N}_{32} = 0$  corresponds to the characteristic equation for the first blade row in isolation. Then, as is physically plausible, the isolated blade row results are obtained for large spacing between the blade rows. Equation (34) also obtains when the number of stall cells becomes large. These two observations prove useful for obtaining numerical solutions to Equation (33).

Secondly, we may also see from Equation (33) that the neutral stability boundary, as well as the propagation velocity, is now a function of the number of stall cells.

The same experimental input data are required to solve Equation (33) as was required for the single blade row case with the additional requirement of the guide vane row loss and turning performance. The guide vane data were also spline fit to obtain the required values and slopes for Equation (33). Equation (33) was then solved numerically using a modified Newton-Raphson scheme. This is an iterative scheme and usually the isolated blade row solution for the second blade row was used as a first guess to start the iteration. This usually was a good starting point and the solution generally converged in four or five iterations. The solution scheme was programmed on the IBM 370/175 and generally required less than 0.02 seconds running time per point. The number of stall cells,  $n$ , was a fixed parameter during each sequence of calculations.

The overall results of these calculations are shown as the triangles in Figures 40 through 42. The calculated damping factors and propagation velocities are shown as the solid curves in Figures 45 through 48. The results are shown in this fashion so that simultaneous comparisons may be made between the single and two blade row theories and the data.

The previously observed analytic behavior of Equation (33) was verified by the numerical results. In general, there was a minimum number of stall cells,  $n$ , below which no unstable solutions were found. This minimum

number of stall cells corresponded to the number experimentally observed for steady rotating stall near inception except for Stator Set No. 6 at stator stagger angles of 30 degrees and 50 degrees. For the 30-degree case, the theoretical minimum  $n$  was 3 whereas  $n=6$  was observed at inception. For the 50-degree case, the theoretical minimum  $n$  was 5 whereas  $n=2$  was observed at inception. The neutral stability point at the minimum  $n$  always occurred at a higher absolute value of the inlet swirl than the single blade row prediction. However, as the number of stall cells was increased, the predicted two blade row neutral stability point approached the single blade row neutral stability point rapidly. This behavior is seen in Figures 40, 41, and 42 where the higher inception points and corresponding minimum number of stall cells are shown as well as the number of stall cells at which the two blade row theory and single blade row theory essentially are the same. Only the single blade row theoretical results are in Figure 43 since both predictions were close for all  $n$ .

The situation may be summarized, then, by stating that the swirl for inception is predicted better by the single blade row theory and the number of stall cells at inception corresponds to the minimum  $n$  at which the two blade row theory allows an unstable solution.

Calculations were made using the loss and turning performance of Stator Set No. 4 to determine the effects of blade row spacing upon the theoretical inception of rotating stall. This was done by halving the blade row spacing between the guide vanes and stator row in the calculation procedure. Calculations were made at  $\delta_{SM} = 28.2, 37.2, \text{ and } 47.2$  degrees. The results were similar at all three values of  $\delta_{SM}$ . Consequently, typical results for 28.2 degrees are presented in Figures 51(a) and 51(b). The results are presented for  $n=3$  which was the minimum  $n$  for an instability with regular spacing and for  $n=8$  which was the minimum  $n$  for an instability with half spacing. As  $n$  is increased, the neutral stability points again approach each other and the single blade row results. In general, the theoretical results correspond to a similar experimental investigation that was performed on Stator Set No. 3 and presented in Reference 6. That is, decreasing the



spacing between blade rows increased the number of stall cells, slightly decreased the propagation velocity and did not appreciably affect the inception inlet swirl.

Since the present flow model has the same time dependence in each flow region, one should, strictly, speak of the stability of the system as a whole and not the stability of a single blade row. For the two blade row configurations studied in the present investigations, it is clear that the stator rows dominated the stability of the system so that for all practical purposes it may be stated that the stall initiated on the stator rows or a particular blade row. This, however, may not be representative of a typical compressor stage since there was usually a static pressure drop across the guide vanes in the present investigation and rotating stall has never been observed on such a blade row in isolation. Under these conditions, the guide vanes would not be expected to significantly influence the inception conditions. However, the theory indicates that the presence of the guide vanes and the axial spacing controls the number of stall cells that develop.

### C. CONSTANT PRESSURE BOUNDARY CONDITIONS

In the preceding single blade row and two blade row theories, the requirement that the velocity disturbances be bounded at downstream infinity was imposed as a boundary condition. This is equivalent to imposing a requirement for constant pressure at downstream infinity. In the past, there has been some uncertainty as to the proper downstream boundary condition to impose. The condition of constant pressure just downstream of the blade row was used by Stenning<sup>6</sup> and both conditions were investigated numerically by Takata<sup>10</sup>. Such questions are not well suited for numerical investigations. Therefore, to explore the question further, the condition of constant pressure just downstream of the blade row was used to replace the bounded velocity requirements at downstream infinity (constant pressure at downstream infinity) in the single blade row analysis. The predictions of the resulting theories are then compared.

The flow configuration shown in Figure 39 and the general form for the disturbance velocities (found from Equation (15)) apply again. Then it may be shown that the linearized equations of motion admit a solution for the perturbation pressure of the following form

$$P_i = \tilde{P}_i(x) e^{j(ct + ny/r)} \quad (35)$$

in each flow region  $i$ . The tangential momentum equation may be used to relate  $\tilde{P}_i$  to  $\phi_i$ . The result is

$$\tilde{P}_i = -j\rho U_0 \left\{ \frac{r}{n} \phi_i'' + j \left( \frac{cr}{nU_0} + S_i \right) \phi_i' \right\} \quad (36)$$

where the primes denote differentiation with respect to  $x$ . Now requiring the upstream flow conditions to be bounded and free of vorticity results in

$$A_1 = D_1 = 0 \quad \text{as before,}$$

and the disturbance velocities become

$$u_1 = B_1 j \frac{n}{r} \exp \left\{ j \left( ct + \frac{ny}{r} \right) + \frac{nx}{r} \right\} \quad (37a)$$

$$w_1 = -B_1 \frac{n}{r} \exp \left\{ j \left( ct + \frac{ny}{r} \right) + \frac{nx}{r} \right\} \quad (37b)$$

$$\begin{aligned} u_2 = & A_2 j \frac{n}{r} \exp \left\{ j \left( ct + \frac{ny}{r} \right) - \frac{nx}{r} \right\} + B_2 j \frac{n}{r} \exp \left\{ j \left( ct + \frac{ny}{r} \right) - \frac{nx}{r} \right\} \\ & + D_2 j \frac{n}{r} \exp \left\{ j \left( ct + \frac{ny}{r} \right) - j \frac{nx}{r} \left( \frac{cr}{nU_0} + S_2 \right) \right\} \end{aligned} \quad (37c)$$

$$\begin{aligned} w_2 = & A_2 \frac{n}{r} \exp \left\{ j \left( ct + \frac{ny}{r} \right) - \frac{nx}{r} \right\} - B_2 \frac{n}{r} \exp \left\{ j \left( ct + \frac{ny}{r} \right) - \frac{nx}{r} \right\} \\ & + D_2 j \frac{n}{r} \left( \frac{cr}{nU_0} + S_2 \right) \exp \left\{ j \left( ct + \frac{ny}{r} \right) - j \frac{nx}{r} \left( \frac{cr}{nU_0} + S_2 \right) \right\} \end{aligned} \quad (37d)$$

The upstream velocities are as before; however, now there are four constants to be determined, i.e.,  $B_1$ ,  $A_2$ ,  $B_2$ , and  $D_2$ . They are determined by the following matching conditions between upstream and downstream flows

- 1) Conservation of mass flow
- 2) Vorticity compatibility
- 3) Flow deflection relation
- 4) Constant pressure just downstream of the blade row  
(no variation with  $y$ )

The first three conditions are as before and result in Equation (17), (21), and (24) respectively. The fourth condition follows from Equation (36) as

$$\phi_2''(\chi_{o_2}) + \frac{n_j}{r} \left( \frac{cr}{nU_0} + S_2 \right) \phi_2'(\chi_{o_2}) = 0 \quad (38)$$

where  $\chi_{o_2} = d \cos \delta$ . Combining Equations (37) with Equations (17) (21), (24), and (38), the following homogeneous system of equations results.

$$\begin{bmatrix} 1 & -e^{\bar{Q}_1} & -e^{\bar{Q}_2} & -e^{\bar{Q}_3} \\ -j\lambda(1+q) - M_2 & j\lambda e^{\bar{Q}_1} & -j\lambda e^{\bar{Q}_2} & [1 + S_2(\lambda \cdot S_2)] e^{\bar{Q}_3} \\ a M_2 & (1 - j S_2) e^{\bar{Q}_1} & (1 + j S_2) e^{\bar{Q}_2} & j\lambda e^{\bar{Q}_3} \\ 0 & M_3 e^{\bar{Q}_1} & M_4 e^{\bar{Q}_2} & 0 \end{bmatrix} \begin{bmatrix} B_1 \\ A_2 \\ B_2 \\ D_2 \end{bmatrix} = 0 \quad (39)$$

where

$$M_3 = 1 - j S_2 - j \lambda$$

$$M_4 = 1 + j S_2 + j \lambda$$

$$Q_2 = \frac{dr}{r} \sin \delta + n \frac{\chi_{o_2}}{r}$$

and the other symbols are as defined previously. This system has a nontrivial solution when the characteristic determinant is zero, i. e.,

$$\begin{vmatrix} 1 & -1 & -1 & -1 \\ -j\lambda(1+q) - M_1 & j\lambda & -j\lambda & 1 + \mathcal{S}_2(\lambda - \mathcal{S}_2) \\ aM_2 & 1 - j\mathcal{S}_2 & -(1 + j\mathcal{S}_2) & j\lambda \\ 0 & M_3 & M_4 & 0 \end{vmatrix} = 0 \quad (40)$$

This is a cubic equation in  $\lambda$  which has two trivial roots

$$\lambda_1 = -(j + \mathcal{S}_2) \quad (41a)$$

$$\lambda_2 = j - \mathcal{S}_2 \quad (41b)$$

which have no physical significance. The remaining root is

$$\lambda = -\frac{1}{1+q} \left[ \frac{1}{2} (1 + \mathcal{S}_1^2) X' + \mathcal{S}_1 X + a \mathcal{S}_2 \right] \quad (42)$$

$$+ \frac{1}{1+q} \left[ X + 1 + \mathcal{S}_2^2 - \frac{\mathcal{S}_1}{2} (1 + \mathcal{S}_1^2) X' - a \mathcal{S}_1 \mathcal{S}_2 \right]$$

or in terms of  $C$ ,

$$\frac{rC_R}{nU_0} = -\bar{\Omega} - \frac{1}{1+q} \left\{ \frac{1}{2} (1 + \mathcal{S}_1^2) X' + \mathcal{S}_1 X + a \mathcal{S}_2 \right\} \quad (43a)$$

$$\frac{rC_1}{nU_0} = \frac{1}{1+q} \left\{ X + 1 + \mathcal{S}_2^2 - \frac{\mathcal{S}_1}{2} (1 + \mathcal{S}_1^2) X' - a \mathcal{S}_1 \mathcal{S}_2 \right\} \quad (43b)$$

The neutral stability boundary may be deduced from Equation (43b) as

$$X + 1 + \mathcal{S}_2^2 - \frac{\mathcal{S}_1}{2} (1 + \mathcal{S}_1^2) X' - a \mathcal{S}_1 \mathcal{S}_2 = 0 \quad (44)$$

which is extremely similar to Equation (32). There are obviously no new mechanisms introduced by use of this boundary condition. Equation (44) will generally be satisfied at a slightly smaller inlet swirl than Equation (32) and the damping factor predicted by Equation (43b) will generally be larger than those predicted by Equation (39b). The propagation velocity is more strongly influenced than the inception boundary by the choice of constant pressure

boundary conditions. Equations (43a) and (43b) have been correlated with the data in the same fashion that Equations (36a) and (36b) were. The correlation, however, was only made for Rotor Set No. 1 since these were the only isolated blade row tests performed in this program. The results are shown in Figures 52(a) through 52(c) and should be compared with Figure 49(a) through 49(c). There is little to choose between the two boundary conditions in terms of inception conditions since both predict inception quite well in this case. However, the condition of constant pressure at downstream infinity results in a much better prediction of the propagation velocity.

Further, if we examine the expression for the downstream pressure perturbation, an anomaly arises. In terms of  $A_2$ ,  $B_2$ , and  $D_2$  Equation (36) becomes

$$\tilde{P}_2 = -j\rho \frac{rU_0}{n} \left\{ A_2 [1 - j(\lambda - \mathcal{L}_2)] e^{-nx/r} + B_2 [1 + j(\lambda - \mathcal{L}_2)] e^{nx/r} \right\} \quad (45)$$

First note that the rotational velocity terms (i. e., terms multiplied by  $D_2$ ) do not contribute to the pressure fluctuations and secondly that even if  $A_2$  and  $B_2$  are selected such that  $\tilde{P}_2$  is zero at  $x = \infty$  (excluding the trivial solutions) the pressure is not zero elsewhere in region 2; in fact, it becomes unbounded at downstream infinity. Hence, the boundary condition of bounded disturbances at downstream infinity has been selected in the present work.

#### D. INVESTIGATION OF TIME DELAY

As mentioned previously, the concept of a time delay for boundary layer separation was thought to be important in the early works on rotating stall. Reference 4 assumed a phase lag in the actuator characteristics and time delay factors were used in References 6 and 10. The type of time delay used in References 6 and 10 has been investigated in the context of the present theory. This type of time delay was incorporated into the flow deflection relation and the blade row loss characteristic for the single blade row case. The resulting characteristic equation has been obtained and analyzed.

The type of lag time used in References 6 and 10 is incorporated into the blade row turning performance in the following fashion. It is assumed that the unsteady turning performance of the blade row is expressed in functional notation as

$$\tan \hat{\beta}_{o_2} = G(\tan \hat{\beta}_{o_1}) \quad (46)$$

where  $G$  satisfies the relationship

$$\frac{\partial G}{\partial t_o} + \frac{1}{\tau} G = G_{q.s.} \quad (47)$$

and where  $\tau$  is the time delay and  $G_{q.s.}$  is the quasi-steady turning performance of the blade row given by Equation (23). Then with the use of Equation (25), Equation (47) may be integrated to give the blade row response to small sinusoidal inputs in inlet swirl, namely

$$\begin{aligned} G(\tan \hat{\beta}_{o_1}) = G_{ss}(\tan \bar{\beta}_{o_1}) \\ - \frac{a B_1 \frac{n}{r U_o} (1 + j \delta_1)}{1 + j \tau \frac{n U_o}{r} \lambda} \left\{ \exp j \left[ \lambda \frac{n U_o}{r} t_o + \frac{n y_o}{r} \right] - \exp \left( -\frac{t_o}{\tau} \right) \right\} \end{aligned} \quad (48)$$

where  $G_{ss}$  is the steady state turning performance of the blade row. Now, although the transient term in Equation (48) (the second exponential term) will modify the wave shape and change it from a pure sine, it should not affect the long term stability of the system. Hence, it will be discarded in the following analysis.

The loss performance of the blade row is treated similarly. (That is, the same time delay  $\tau$ , has been assumed to apply to both the loss and turning relation). Functionally, it is assumed that

$$X = X(\tan \hat{\beta}_{o_1})$$

and that  $X$  satisfies a relation similar to Equation (47). Then the following loss behavior may be deduced

$$\begin{aligned} X = X_{ss}(\tan \bar{\beta}_{o_1}) \\ - \frac{b_1 X_{ss} \frac{n}{r U_o} (1 + j \delta_1)}{1 + j \tau \frac{n U_o}{r} \lambda} \left\{ \exp j \left[ \lambda \frac{n U_o}{r} t_o + \frac{n y_o}{r} \right] - \exp \left( -\frac{t_o}{\tau} \right) \right\} \end{aligned} \quad (49)$$

where  $X_{ss}$  is the steady state loss performance of the blade row and again the transient term will be ignored for stability purposes.

Incorporation of Equation (48) into the flow deflection matching condition results in

$$\begin{aligned} \omega_{o_2}(x_{o_2}, y_{o_2}, t_o) - \mathcal{L}_2 u_2(x_{o_2}, y_{o_2}, t_o) \\ = \frac{a}{1 + j\bar{\tau}\lambda} \left\{ \omega_{o_2}(x_{o_1}, y_{o_1}, t_o) - \mathcal{L}_1 u_{o_1}(x_{o_1}, y_{o_1}, t_o) \right\} \end{aligned} \quad (50)$$

where  $\bar{\tau} = \frac{\tau n U_o}{r}$ . This replaces Equation (24) of the previous single blade row analysis. Equation (49) may be incorporated directly into Equation (21) to produce the appropriate vorticity compatibility relation for this case. The continuity matching condition remains unchanged for this case and the requirement of bounded flow at upstream and downstream infinity plus the requirement for no vorticity in the incoming flow are used again. Then Equations (16), (17), (21), and (50) may be combined to give the following homogeneous system for the unknown constants.

$$\begin{bmatrix} 1 & -e^{\bar{a}_1} & -e^{\bar{a}_3} \\ -j\lambda(1+q) - \tilde{M}_1 & -j\lambda e^{\bar{a}_1} & -[(\lambda + \mathcal{L}_2)\mathcal{L}_2 + 1]e^{\bar{a}_3} \\ \alpha \tilde{M}_2 & (1 - j\mathcal{L}_2)e^{\bar{a}_1} & j\lambda e^{\bar{a}_3} \end{bmatrix} \begin{bmatrix} B_1 \\ A_2 \\ D_2 \end{bmatrix} = 0 \quad (51)$$

where

$$\begin{aligned} \tilde{M}_1 &= (1 + j\mathcal{L}_1) \left\{ \frac{j}{2} \frac{(1 + \mathcal{L}_1') X'_{ss}}{1 + j\bar{\tau}\lambda} + X_{ss} \right\} \\ \tilde{M}_2 &= \frac{1 + j\mathcal{L}_1}{1 + j\bar{\tau}\lambda} \end{aligned}$$

and the other terms have been defined previously. This system has a non-trivial solution when the characteristic determinant is zero, i.e.,

$$\begin{vmatrix} 1 & -1 & -1 \\ -j\lambda(1+q) - \tilde{M}_1 & -j\lambda & -[(\lambda + \mathcal{S}_2)\mathcal{S}_2 + 1] \\ a\tilde{M}_2 & (1 - j\mathcal{S}_2) & j\lambda \end{vmatrix} = 0 \quad (52)$$

This is a cubic equation in  $\lambda$  as opposed to quadratic in the previous case. Again, the first solution is the trivial one

$$\lambda_1 = -(j + \mathcal{S}_2) \quad (53)$$

After this has been factored out, Equation (52) becomes:

$$\bar{A}\lambda^2 + \bar{B}\lambda + \bar{C} = 0 \quad (54)$$

where

$$\bar{A} = -(2+q)\bar{\tau}$$

$$\bar{B} = j(2+q) + j\bar{\tau} \left[ (1+j\mathcal{S}_1)X_{ss} + (1+\mathcal{S}_2^2) \right]$$

$$\bar{C} = (1+j\mathcal{S}_1) \left[ X_{ss} + \frac{1}{2}(1+\mathcal{S}_1^2)X'_{ss} + a(1+j\mathcal{S}_2) \right] + (1+\mathcal{S}_2^2)$$

which has roots

$$\lambda = \frac{-\bar{B} \pm \sqrt{\bar{B}^2 - 4\bar{A}\bar{C}}}{2\bar{A}} \quad (55)$$

The mechanisms involved are not readily evident from Equation (55). However, some interesting properties of this solution may be obtained by examining the limit as  $\bar{\tau} \rightarrow 0$ .

First, the solution to the previous case without time delay is denoted as  $\lambda_0$  (i.e., the values of  $\lambda$  given by Equation 29). Then  $\bar{C} = j(2+q)\lambda_0$  and it is seen from Equation (54) that  $\lambda_0$  is a solution when  $\bar{\tau} \rightarrow 0$ . Furthermore, if either Equation (54) or (55) is expanded for small  $\bar{\tau}$ , the following approximate result is obtained, namely

$$\lambda = \lambda_0 + j \frac{\bar{\tau}\lambda_0}{2+q} \left\{ (2+q)\lambda_0 + j \left[ (1+j\mathcal{S}_1)X_{ss} + (1+\mathcal{S}_2^2) \right] \right\} \quad (56)$$

or in terms of the  $\bar{C}$ ,



$$\frac{rC_R}{nU_c} \approx -\bar{\Omega} - \left( \frac{1}{2+q} - \frac{a\bar{\tau}}{(2+q)^2} \right) \left\{ \mathcal{J}_1 X_{SS} + a(\mathcal{J}_1 + \mathcal{J}_2) + \frac{1}{2} (1 + \mathcal{J}_1^2) X'_{SS} \right\} \quad (57a)$$

$$- \frac{\bar{\tau}}{(2+q)^2} \left[ \frac{1}{2} (1 + \mathcal{J}_2^2) X'_{SS} - a \mathcal{J}_2 \right] \left[ 1 + \mathcal{J}_2^2 + X_{SS} + a(1 - \mathcal{J}_1 \mathcal{J}_2) - \frac{1}{2} \mathcal{J}_1 (1 - \mathcal{J}_1^2) X'_{SS} \right]$$

$$\frac{rC_I}{nU_c} \approx \left( \frac{1}{2+q} - \frac{a\bar{\tau}}{(2+q)^2} \right) \left\{ X + 1 + \mathcal{J}_2^2 + a(1 - \mathcal{J}_1 \mathcal{J}_2) - \frac{\mathcal{J}_1}{2} (1 + \mathcal{J}_1^2) X'_{SS} \right\} \quad (57b)$$

$$- \frac{\bar{\tau}}{(2+q)^2} \left\{ \left[ \frac{1}{2} (1 + \mathcal{J}_1^2) X_{SS} - a \mathcal{J}_2 \right]^2 + \left[ \frac{1}{2} (1 + \mathcal{J}_1^2) X_{SS} - a \mathcal{J}_2 \right] \left[ \mathcal{J}_1 X_{SS} + a(\mathcal{J}_1 + 2\mathcal{J}_2) \right] \right\}$$

which are in a form to compare with Equations (16a) and (16b). Equations (56) and (57) are well behaved in the limit  $\bar{\tau} \rightarrow 0$ , reducing to the  $\bar{\tau} = 0$  case. This is an interesting result since the limiting behavior is not deducible from the fundamental form (e. g., Equation (47)) in which the time delay was introduced into the analysis.

Recall that  $C_I < 0$  corresponds to instability and that  $\bar{\tau}$  is always positive. Then, since  $X_{SS}$  is positive and generally dominates the  $a$  terms in the vicinity of the stall boundary, Equation (57b) would indicate that addition of small time lag to the flow model is usually destabilizing. In fact for lossless flows (i. e.,  $X_{SS} = 0$ ) it becomes the primary destabilizing phenomenon. Hence, it was thought to be an important phenomenon in the early investigations<sup>4, 6, 8</sup>. However, the lack of correlation when considering several sets of data<sup>6</sup> plus the good correlation obtained in the present work would indicate that the blade row loss behavior is the important blade row characteristic to model in the theory.

#### E. CONCLUDING REMARKS ON THEORETICAL WORK

A two dimensional small disturbance theory for the prediction of the inception of rotating stall has been developed. The neutral stability boundary

predicted by the theory correlates well with the experimentally determined boundary for inception of rotating stall. In addition, the propagation velocities are reasonably well predicted. A single blade row and a two blade row version of the theory have been developed. The inception conditions are better predicted by the single blade row version; however, the number of stall cells experimentally observed at inception correlates well with the minimum number of cells for which the two blade row theory indicates that an instability is possible.

The theory indicates that the unsteady vorticity shed into the blade wakes by the variation in loss along the cascade axis is the mechanism controlling the stability of a given flow configuration. In this context, the stability is controlled by the slope of the curve of blade row losses as a function of inlet swirl. Moreover, the two blade row version of the theory indicates that blade row interference controls the number of stall cells that develop at inception.

## SECTION IV

### DEVELOPMENT OF A PROTOTYPE ROTATING STALL CONTROL SYSTEM

The optimum performance of a turbo-propulsion system is usually achieved when the compressor is operating near its maximum pressure ratio. However, this optimum is generally not attainable because it occurs close to compressor stall and its resultant unstable flow conditions. In actual operation a stall margin must be provided to prevent the compressor from penetrating the stall boundary and developing destructive unsteady flow phenomena such as rotating stall and surge. This is usually done by prescheduling the engine controls. When an aircraft has a varied flight envelope, the prescheduling approach can lead to the requirement for a large stall margin to keep the engine out of stall under all possible transient and steady flight conditions. This stall margin represents a significant performance penalty. It is clear then, that an engine control system that can sense incipient destructive unsteady flow in the compressor and take corrective action would minimize the need for prescheduling and thus lead to a large engine performance gains. Quantitative studies of the benefits which could be obtained are discussed in Reference 12

In many instances of engine failure, rotating stall has been identified as a precursor to destructive unsteady flows in an engine. Moreover, blade fatigue considerations will not allow a compressor to operate for prolonged periods in a large-amplitude rotating stall mode. It is then desirable for several reasons to develop an engine control system that would sense the onset of rotating stall and keep the engine from operating in the rotating stall mode.

The functional requirements for a rotating stall control system have been discussed in Reference 1. Briefly they can be summarized as follows:

1. An unambiguous signal of the presence of rotating stall must be generated.
2. The control must be capable of processing this signal so that action on some compressor variable can be taken which will eliminate rotating stall.

3. When rotating stall is detected, control action must occur within a time period on the order of milliseconds, and its effect on the compressor should be almost immediate.
4. When rotating stall is absent, the control should have no effect on the compressor operation. Return to normal compressor operation after rotating stall dies away need not be as rapid as initial control action when rotating stall first occurs.

In the work reported herein, the requirement for a fast acting control system is attacked through sensing pressure fluctuations within the compressor itself and using these signals to provide direct mechanical action on compressor geometry (such as stator stagger angle or bleed port openings). It is believed that more indirect control action, such as fuel flow control, would not provide a fast enough response.

The primary task to be treated before rotating stall control systems are feasible is the establishment of an incipient stall signature that can be sensed by such a system. In previous work (Reference 1), a limited search for stall sensors was conducted in the annular cascade facility with stationary stator rows. It was found that a pressure tap located on the suction surface of a stator blade near the quarter-chord showed promise of providing a satisfactory signal. In the current work, the search for suitable sensor signals was expanded to more sensor configurations and was performed on a configuration of the annular cascade facility which included both stationary and rotating blade rows. Several other promising sensor configurations arose from this study. A number of these have been tested with a closed-loop rotating stall control system which was designed and fabricated during the current investigation.

In this section, the results of the experimental search for sensors which might provide a useful signature are presented first. This is followed by a description of a rotating stall control which used these signatures. Finally, the results of testing the rotating stall control are presented.

## A. SENSOR INVESTIGATION

In the sensor studies reported in Reference 1, the experiments were performed on a relatively simple configuration of the annular cascade with stationary blade rows. Although a sensor configuration was found which appeared to provide a suitable rotating stall signature, it was not certain that this sensor would continue to perform satisfactorily in the presence of blade-passage signals from rotating blade rows. In the current investigation, experimental tests of this sensor configuration and various alternative configurations were performed in the annular cascade after it was modified to provide rotating blade rows as well as stator rows.

A sketch of the configuration used in this investigation and a list of the various sensors are presented in Figure 53. The annular cascade contained three stationary blade rows and one rotor row. In sequence from the inlet, these were: an inlet guide vane row, a stator row (stator row 4), a rotor row (rotor row 5), and finally another stator row (stator row 5). The numbering system for the rotor and stator rows is based on their locations in the original J-79 compressor. The guide vane row is the stationary guide vane row described in Section II-A. Rotor row 5 and stator row 5 are the same as Rotor Set No. 1 and Stator Set No. 1 of Section II. Stator row 4 consists of shortened stator blades from the original stator row 4 in the J-79. The stagger angles of the guide vanes and of the stator rows were varied during the tests while the rotor stagger was held fixed at 40 degrees. The guide vanes were used to vary the inlet swirl angle to stator row 4. Stator rows 4 and 5 were used as receptacles for some of the sensors and their variable stagger angle feature provided a means of controlling rotating stall on themselves and on the rotor.

The stagger angles of stator rows 4 and 5 were locked together through a mechanical linkage so that they varied in unison. The relationship between the stagger angles of stator rows 4 and 5 could be changed if desired. The combination of variable inlet guide vanes and variable stators allowed testing under conditions in which rotating stall first occurred either on stator row 4, on the rotor, or on stator row 5. Sensor performance was studied under all of these conditions.

All of the sensors studied detected unsteady pressure fluctuations in the annular cascade. Sensors sensitive to other properties, such as unsteady fluid velocity or temperature, were not considered. It is believed that pressure signals have the greatest potential of providing a signature which can be detected by relatively simple and rugged equipment. The description of the sensors in Figure 53 is self-explanatory except for the razor blade and cylindrical yaw probes.

Photographs of the razor blade and the cylindrical yaw probes are shown in Figure 54 and 55 respectively. Although both of these sensors use pressure measuring equipment, they are sensitive to angle fluctuations as well as pressure. The razor blade yaw probe consists of two total pressure tubes separated by a portion of a razor blade. The differential pressure between the two tubes is a function of the flow angle incident on the razor blade. Although this probe was not calibrated in steady flow, the pressure differential should change sharply when the incident flow switches from one side of the razor blade to the other. The cylindrical yaw probe has two static pressure holes separated by an included angle of approximately 90 degrees. It is basically a two-dimensional yaw probe and should provide a pressure differential signal which is a smooth function of incident flow angle measured from the bisector between the two static pressure holes. Of course, both of the yaw probes will respond to total pressure fluctuations in the incident flow as well as to flow angle fluctuations.

Tests were conducted on the two yaw probes located as shown in Figure 53 for the various combinations of rotating stall. It was found that both probes, and in particular the razor blade yaw probe could provide large unsteady pressure signals at rotating stall inception. However, the performance of these probes was extremely sensitive to their orientation in the flow. If the probes were not correctly positioned relative to the incoming flow just prior to inception of rotating stall, the unsteady signals deteriorated to such an extent that they would not provide a clear indication of rotating stall inception. Thus, it became necessary to have independent knowledge of when rotating

stall was about to occur in order to position the probes. In view of this limitation, these two sensors were eliminated from further testing. The pressure records which were obtained from these sensors are not presented in this report because of their limited interest.

The remaining sensors (configuration and location shown in Figure 53) were tested at four different stagger angle settings of the inlet guide vanes,  $\delta_{GV} = 24.5, 32.5, 40.5,$  and  $48.5$  degrees. At the two lowest settings,  $\delta_{GV} = 24.5$  and  $32.5$  degrees, a large amplitude rotating stall was encountered on the rotor, while at the highest settings,  $\delta_{GV} = 40.5$  and  $48.5$  degrees, a smaller amplitude rotating stall was encountered on the stators. In the latter cases, it was possible to obtain rotating stall either on stator row 4, upstream of the rotor, or on stator row 5, downstream of the rotor, by adjusting the mechanical linkage between these stator rows. Sensor outputs were recorded for two stagger angle relationships between stator rows 4 and 5. In the first case, stator row 5 was adjusted to follow stator row 4 with a stagger angle approximately 13 degrees larger than stator row 4. This case has been designated as "stator row 5 unloaded." In the second case, the stagger angle of stator row 5 was set approximately 6 degrees larger than that of stator row 4. This case has been designated as "stator row 5 loaded."

Records of the signals generated by the various sensors are presented in Figures 56 and 57 for inlet guide vane stagger angles of 24.5 degrees and 40.5 degrees respectively. Records obtained for a guide vane stagger angle of 32.5 degrees are similar to those in Figure 56 while those obtained for a guide vane stagger angle of 48.5 degree are similar to those in Figure 57. Thus the records presented are representative of all of the cases tested. Throughout the sensor tests, the rotor speed was held constant at 1250 rpm and the mean axial velocity of the flow in the annulus was held at approximately 54 feet per second. Preliminary tests showed that rotating stall could be excited on either the rotor or on the stators through variation of the guide vane stagger angle alone if the rotor rpm and the axial flow velocity were held at the above values. This feature was convenient for testing purposes.

In the records presented for a guide vane stagger angle of 24.5 degrees (Figure 56), large amplitude rotating stall occurred on the rotor. Figures 56(a) through (e) show signals generated by the various sensors when stator row 5 is unloaded. Figures 56(f) and (g) repeat some of the sensor signals with stator row 5 loaded. On each page of Figure 56, signals from two sensors are presented for three different stagger angle settings of stator row 4 ( $\delta_{SM_4} = 45.8, 33.8, \text{ and } 29.8$  degrees). For this guide vane setting and with stator row 5 unloaded, rotating stall first occurred as  $\delta_{SM_4}$  was reduced to a value just slightly smaller than 33.8 degrees. Thus for Figures 56(a through e), the upper photo shows the sensor signals for a case far from rotating stall inception, the middle photo shows the signals just prior to inception, and the lower photo shows the signals while rotating stall is occurring. With stator row 5 loaded, Figures 56(g and f), rotating stall occurred on the rotor when  $\delta_{SM_4}$  was approximately equal to 33.8 degrees so that the sensor records show only one case without rotating stall and two with rotating stall.

When comparing photos in Figure 56 and 57, note that the oscilloscope vertical sensitivity, listed to the left of each photo, is sometimes varied. The larger this sensitivity value (expressed in millivolts per centimeter) the larger the sensor pressure signal must be to obtain a given vertical deflection on the photographic records. In general, larger sensitivity values were selected for the cases with stator row 5 loaded, Figures 56(f) and (g) and 57(f) and (g), than those with stator row 5 unloaded, Figures 56(a) through (e) and 57(a) through (e). Thus some of the sensor signals obtained with stator row 5 loaded appear smaller (when they really are not smaller) than their counterparts with stator row 5 unloaded.

It is apparent from inspection of the sensor records in Figure 56 that all of the sensors provide an indication of large amplitude rotating stall on the rotor. However, some of the rotating stall "signatures" are better defined than others. The poorest signature is from Sensor 8, (outer wall static pressure midway between the blades of stator row 4, Figure 56(e)). A few of the fluctuating signals increase in amplitude even before rotating stall occurs. The latter feature is particularly noticeable for Sensor 2 (mid-annulus total pressure on



row 5, Figure 56(c)) and Sensor 7 (outer wall static pressure at rotor quarter chord, Figures 56(a) and (d)). With Sensor 7, the signal fluctuations appear to be caused primarily by rotor blade passage while Sensor 2 is probably responding both to blade passage and turbulence in the flow. The increase in amplitude of the fluctuating signals prior to inception is useful in cases where large amplitude rotating stall inception is hysteretic, that is when large amplitude rotating stall first occurs at a smaller stator stagger angle than that which is required to eliminate it after it has started. As will be seen in the presentation of the control system tests, hysteretic behavior of rotating stall can lead to hunting of the control system if it is set to detect only the presence of rotating stall. On the other hand, setting the control to detect the increase in signal amplitude prior to inception of large amplitude rotating stall considerably reduces the hunting behavior.

The signatures obtained from the large amplitude rotating stall on the rotor with stator row 5 loaded (Figures 56(f) and (g)) are not very different from those obtained with stator row 5 unloaded (Figures 56(a) through (e)). Although not shown, the behavior immediately prior to rotating stall inception on the rotor is also similar for these two cases. Evidently under the conditions of these particular tests, it is the rotor which controls the main features of the rotating stall and loading the downstream stator row has very little effect. The largest apparent change occurred in the stator stagger angle at rotating stall inception. With stator row 5 unloaded, inception occurred at  $\delta_{SM_4} \approx 33$  degrees, and with stator row 5 loaded it occurred at  $\delta_{SM_4} \approx 34$  degrees.

Figure 57 shows records from the same sensors that were used in Figure 56. In this case, the inlet guide vane stagger angle was larger,  $\delta_{GV} = 40.5$  degrees, and rotating stall occurred on the stator rows. The rotating stall signatures are of higher frequency and smaller amplitude. Inception of rotating stall is gradual, starting with small amplitude and growing to larger amplitude as stator stagger angle is decreased. First indication of rotating stall occurred at  $\delta_{SM_4} \approx 35$  degrees with stator row 5 unloaded, and at  $\delta_{SM_4} \approx 42$  degrees with stator row 5 loaded. Not all of the sensors provide

useful signatures for this type of rotating stall. Sensors 8 and 9 provide very poor, if not useless signatures. Both of these sensors are outer wall static pressure taps remote from the stator blades. Previous tests reported in Reference 1 had suggested that this type of sensor would make a poor detector for rotating stall which occurs on the stator blades. The remaining sensors did provide signatures for this type of rotating stall, but with varying degrees of success. Of particular note, is the performance of similar sensors mounted on stator row 4 and on stator row 5. When rotating stall occurs on the upstream stator row (stator row 4), sensors mounted on either stator row provide useful signatures (Figures 57(a) through (d)). However, when rotating stall occurs first on the downstream stator row (stator row 5), the sensors mounted on stator row 4 do not provide as clear a first indication of rotating stall (Figure 47(f)).

Other than the elimination of the outer wall static pressure Sensors 8 and 9, it is difficult to eliminate completely the other sensor configurations solely on the basis of inspection of the photographic records. Even one of the poorer configurations for detecting small amplitude rotating stall on the stators (for example, Sensor 6) might prove acceptable for use with the rotating stall control while at the same time be much easier to install and maintain in an engine than another configuration. The rotating stall control system tests were conducted with samples of both of the above types of sensor configurations.

## B. DESCRIPTION OF ROTATING STALL CONTROL

An electro-hydraulic feed-back control system was designed to meet the previously discussed requirements for a rotating stall control system. The input to the control system is the unsteady pressure signal (or signals) produced by the sensors described in the previous section. The output of the control is a mechanical operation on some variable geometry feature of the compressor to be controlled. In the current work, the variable geometry is the stagger angle of the stators in the Calspan/Air Force Rotating Annular Cascade Facility.

The control system was developed in two phases. The control system was designed and fabricated and tested on a non-rotating blade set in the annular cascade. These tests were conducted on a two blade row configuration consisting of Stator Set No. 5 and the guide vanes. Stator Set No. 5 was commanded and controlled and the guide vanes were used independently to established desired inlet conditions. Based upon the results of these tests a slight modification was made to the control system to improve the operation of the system. The original control system will be described and discussed first since it is somewhat simpler than the final version. The final version will then be described and discussed.

The signal conditioning and processing subsystem of the original design of the rotating stall control is shown in block diagram form in Figure 58. The signals at various places or stages in the circuit are shown schematically on the right hand side of the figure. In operation the system performs as follows:

- 1) A time varying electrical signal is obtained from the pressure transducer on the rotating stall sensor. (Stage 1)
- 2) This signal is bandpass-filtered to remove steady state and low frequency variations (which are not associated with rotating stall) and high frequency contaminants such as instrument noise and blade passage effects. Both corners of the passband are adjustable. (Stage 2)
- 3) The bandpass signal is then processed in an absolute value circuit (rectified) to generate a d. c. signal proportional to the pressure signal. This unit performs a rectification function, delivering a d. c. output with superposed a. c. components. (Stage 3)
- 4) The rectified signal is then input to a voltage comparator circuit. The comparator produces two output signals. The first signal, Stage 4, is obtained by comparing the rectified input signal with an adjustable d. c. reference level. Only that portion of rectified signal which exceeds the reference level is passed.

The second comparator output signal, Stage 5, controls an electronic gate. This signal activates the gate whenever the input signal exceeds the reference level. The gate has been included in the circuit to ensure that the next component of the circuit, the integrator, is referenced to zero voltage when the input signal is below the reference level.

- 5) The output from the gate is fed into an integrator. The integrator gain and decay rate are independently adjustable. The integrator output is then a signal which is obtained by integrating only that portion of the original pressure signal whose absolute value exceeds the reference level.
- 6) The output of the integrator, Stage 6, is summed in opposition with the command position signal, Stage 7. The output of the summer is fed to the servo which acts to move the stator vanes away from the stall condition (reduce angle of attack). When the vanes reduce angle of attack the original pressure signal should fall below the reference level causing the input to the integrator to drop to zero. The output voltage of the integrator then decays at a preselected, but adjustable, rate. When this signal, Stage 6, decreases sufficiently, the original command signal, Stage 7, then resumes control allowing the vanes to move towards their original position.

The control system as described above was given preliminary tests on the stationary hub configuration of the annular cascade. The results of these tests were reported in the 8th Quarterly Progress Report (CAL Report MK-2932-A-8) and will not be repeated here. The overall conclusion from these preliminary tests was that the control system performs very well in the annular cascade if the integrator decay time constant is set to large values. However operation of the control system with a long decay time constant will cause the stators to overshoot when the primary engine controls command a change from a stator stagger angle inside the rotating stall boundary to one closer to the boundary or outside of the boundary. Under this condition

the undecayed portion of the stall control signal will reinforce the engine control signal. Long decay time constants will increase the magnitude and duration of the overshoot.

In order to alleviate the above problem, the control system was modified so that it operates with two time constants, that is with a long decay time constant in the presence of rotating stall and with a short time constant once it has disappeared for a specified short period. Also a summing amplifier was added to the system to permit tests that monitor signals from more than one sensor. Separate gain controls were provided for each input to the summing amplifier. The block flow diagram for the two time constant system is shown in Figure 59 and is described below. The electronics control panel for the system is shown in Figure 60.

In the previous single time constant system the integrator decay time constant is fixed by a resistor in parallel with the integrator feedback capacitor. Since the gate removes the input signal from the integrator when the pressure signal is below the reference level, the integrator output voltage begins to decay at a slow rate (i. e., long time constant).

The revised circuitry consists of an electronic switch, an adjustable time delay circuit and a variable resistor that results in a short time constant when connected in parallel with the integrator feedback capacitor. The circuitry is designed to produce a short time constant when the electronic switch is closed and a long time constant when the switch is open. Stall pressures in excess of the reference level cause the electronic switch to open and thereby establish the long time constant. The long time constant is maintained as long as the stall pressure signal is in excess of the reference level. If the stall pressure signal falls below the reference level, the integrator is switched back to the short time constant after a specific but adjustable time delay. Thus the system selects the fast recovery time (short time constant) only if the pressure signal remains below the reference level longer than the delay time. The delay time,  $\Delta$ , is adjustable from 0.2 to 2.0 seconds and the short time constant is adjustable from 1.0 to 10.0 seconds. The long time

constant is adjustable to values in excess of 100.0 seconds.

The summing amplifier on the input to the system is also shown in Figure 59. This amplifier sums pressure signals, at appropriate gains, from different sensors to form one composite stall pressure signal. This permits tests which monitor various locations in the compressor. It is probable that for many applications, a composite signal obtained in this way will provide too much background noise. Therefore, for future work, it is planned to duplicate all components of the circuit up to the amplitude comparator for each input pressure signal. This will eliminate the background noise buildup.

An electro-hydraulic servo positions the stators in the rotating stall control system. The servo consists of a flow control valve, a feedback potentiometer and a linear actuator. The linear actuator is of the balanced piston type (equal area on each side of piston) with an effective area of  $0.2 \text{ in}^2$  and a stroke of 1.0 inch. The valve is a Moog Series 3 Flow Control Valve and provides a maximum flow of  $26 \text{ in}^3/\text{sec}$  at a supply pressure of 3000 psi and zero load pressure. A Computer Instruments Model 111 Infinite Resolution Plastic Film Potentiometer measures the actuator position. The servo was designed to meet design velocity and acceleration limits ( $62.5 \text{ in}/\text{sec}$  and  $3 \times 10^4 \text{ in}/\text{sec}^2$ , respectively) at a supply pressure of 1000 psi. However, the servo can be operated safely to pressures of 3000 psi. Figure 61 is a photograph of the servo assembly.

The servo loop gain (velocity constant) is  $300 \text{ sec}^{-1}$ . When used to drive the two stator rows in the tests of the rotating stall control system, this gain resulted in a closed loop corner frequency (down 3 db.) of 48 Hertz. The servo was stable and well behaved at this gain. It did not require velocity or acceleration feedback to improve the damping characteristics.

During the tests, a small hydraulic power supply was used to drive the servo on the rotating stall control. The hydraulic power supply consisted of a  $6 \text{ in}^3/\text{sec}$  fixed displacement pump, an unloading valve set to unload at

1200 psi and a 1 gallon accumulator. With this system, the hydraulic supply pressure was maintained between 1000 and 1200 psi. This was adequate for all tests which were conducted. No oil or overheating problems were encountered during operating periods up to 8 hours in length.

Photographs of the installation of the rotating stall control system mounted on the rotating annular cascade are shown in Figures 62 and 63. The results of the tests of this system are presented in the following sub-section.

### C. TESTS OF ROTATING STALL CONTROL SYSTEM

The rotating stall control system was tested on the same configuration of the CALSPAN/AIR FORCE Rotating Annular Cascade Facility that was used for the sensor investigation (Figure 53). A brief description of the annular cascade geometry is presented in Section IV-A and a view of the hydraulic actuator and the mechanical linkages to stator rows 4 and 5 is given in Figure 63.

The operation of the control system has been described in detail in Section IV-B and will not be repeated here. However, it is worth recalling that the system was designed and constructed so that several of the functions could be varied in order to optimize the performance. The three variable portions of the system considered during these tests were:

- 1) Detector reference level. This sets the pressure transducer signal level which must be exceeded to provide control operation.
- 2) Integrator gain. This in combination with 1) and 3) governs the rate and degree of control which is obtained.
- 3) Integrator decay time constants. These control the rate at which the control circuit signals decay so that the stator vanes can return to their original position.

The overall performance of the control system depends on the setting of these three control functions.

In operation on a compressor, the rotating stall control system would normally be used to override the primary engine control command signals. In this prototype control system, the primary engine control command signal is simulated so that the stator vanes can be ordered to take any arbitrary position in the absence of rotating stall. The presence of rotating stall then causes the stall control system to override the primary command signal.

Preliminary tests of the control system were performed prior to the main body of the tests in order to select values for the integrator decay time constants. The results of the preliminary tests were not recorded. However, on the basis of these tests, the two time constants for the integrator decay rate were chosen as 107 seconds for the long decay time which operates in the presence of rotating stall and 5.8 seconds for the short time constant which operates after rotating stall has disappeared for a specified time,  $\Delta$ . In addition, the delay time,  $\Delta$ , was set at approximately 1 second. These time constants and delay times were held fixed for the results reported in the following paragraphs.

Before proceeding into the presentation of the results, some general comments which apply to all of the data will be made. In the process of testing the control system, over 400 data records were generated. For the sake of clarity and conciseness, not all of these records will be presented. However, those records that are presented are representative of all of the data. In all of the figures which are presented (Figures 64 through 69), two recorded traces are shown for each data run. The upper trace on each record is the detector pressure signal. This signal is obtained from the various sensors and may be a single sensor output or a combined output from two sensors. The method by which the detector pressure signal is generated is listed on each figure. The lower trace on each record is the stagger angle,  $\delta_{SM_4}$ , of stator row 4. The scale factor for the stagger angle record is 2.4 degrees per major division. As noted on each figure, the top line of the stagger angle record corresponds to  $\delta_{SM_4} = 29.8$  degrees and the bottom line to  $\delta_{SM_4} = 53.8$  degrees. Since stator rows 4 and 5 are linked together,



the lower trace is also indicative of the stagger angle of stator row 5, although the numerical value for stator row 5 is different. The relationship between the stagger angles of stator rows 4 and 5 has been explained in Section IV-A.

In each of Figures 64 through 69, stator row 4 was set at a stagger angle of 29.8 degrees via the primary command signal before the rotating stall control was actuated and would return to that position if the control is turned off or if rotating stall disappears because of a change in inlet conditions or rotor rpm. The control forces the stators to take up a new position near the inception boundary for rotating stall and to remain at this position. However the final mean position and the amplitude and rate at which the stators "hunt" about the mean position depend upon the detector reference level, the integrator gain, and the distance which the stators are required to back off (increase their stagger angle) to approach the inception boundary. The back-off distance is large for most of the results presented and thus represent a severe test of the control.

In addition to the influence of the above control generated variables, the hunting behavior of the control is accentuated when rotating stall inception occurs at a smaller stator stagger angle than that which is required to eliminate it. Under these hysteretic conditions, a poor choice of detector reference level can cause unacceptable amplitude variations in the controlled stagger angle on the stators. However, as will be seen, proper choice of the detector reference level eliminates this excessive hunting.

The results of the control system tests will be presented in three steps. First some records will be presented to illustrate the separate effects of detector reference level and of integrator gain on the performance of the control system. Following this is a discussion of the steady state performance of the control system, that is operation of the control when it is required to prevent rotating stall over continuous long periods of time. Finally the transient performance of the control system during the sudden occurrence of large amplitude rotating stall is presented.

The first set of rotating stall control records, Figure 64, were obtained using two sensors to generate the detector pressure signal. It is composed of the sum of the signal from Sensor 5 (outer wall 1/4 chord static pressure on the suction surface of stator row 4) plus 23 percent of the signal from Sensor 7 (outer wall static pressure at the rotor 1/4 chord axial location). This combination was made in an attempt to provide satisfactory control action under all inlet conditions (settings of the guide vane stagger angle). Later tests with single sensors proved that the combination possessed no particular advantages. However, the results are representative of the effect of detector reference level and integrator gain and thus will be used to illustrate these effects. Note that the units used to describe the integrator gain and the detector reference level do not correspond directly to physical units. They are read from the settings of linear potentiometers on the face of the control cabinet.

Figure 64(a) is a result for the case when the control action is negligible and rotating stall is occurring. It was obtained by setting the detector reference level at its upper limit. It is presented to provide a reference for the detector pressure signal amplitude when the control is essentially inoperative. Run 26 on Figure 64(a) was taken with a very low chart speed and run 27 with a higher chart speed. In each case, the time scale is shown on the traces.

Figures 64(b) and (c) show the operation of the rotating stall control with different combinations of integrator gain and detector reference level. On each set of dual records, the integrator gain is varied, while separate sets of records are presented for different detector reference levels. It is apparent from the records that the integrator gain has very little effect on the mean stator stagger angle that the control selects. On the other hand, increasing the detector reference level allows the compressor to come closer to rotating stall inception. In fact, for this case, increasing the detector reference level above a value of 70 allows short bursts of large amplitude rotating stall to occur. This causes hunting in the controlled stator

stagger angle. As the detector reference level is increased even further, the interval between bursts of rotating stall becomes smaller. The excessive degree of hunting shown for detector reference levels above 70 is caused by hysteresis in the conditions for which large amplitude rotating stall first starts and when it dies out. This is eliminated when the detector reference level is set just low enough (70 for this case) to prevent initiation of large amplitude rotating stall.

The chart speed in Figure 64(b) and (c) is too slow to illustrate the primary effect of integrator gain, that is the increased speed of response of the control system as this gain is increased. This effect is illustrated in Figure 65 which, except for a higher chart speed, is a repeat of the upper record of Figure 64(c). In this figure the detector reference level is held constant at 90 so that bursts of rotating stall occur at frequent intervals. (This is not a desirable condition and would not be allowed in actual practice.) The control response to these bursts and the effect of the response on the duration of the bursts can be seen in the figure. For each integrator gain, two bursts of rotating stall are shown in order to illustrate the repeatability of the control response. It is evident in Figure 65 that increasing the integrator gain increases the overall speed of response of the control. The increased overall response speed results from the fact that the amount of correction from individual stall cells increases as the integrator gain is increased. Thus with high integrator gains it takes fewer stall cells to provide full corrective action, and the overall response time to full correction is decreased.

The operation of the two time constant system in the integrator circuit is also apparent in Figure 65. Note that following the final cell in each burst of rotating stall, the stator stagger angle remains nearly fixed for approximately one second and then begins to increase. In the time in which the stators remain nearly fixed, the long decay time constant (107 seconds) is in effect. After this time, the control switches to the short time constant (5.8 seconds), and the stator stagger angle begins to increase. Note also that there is no measurable delay in the initial response of the control when

rotating stall first starts.

Following the tests to determine the effect of integrator gain and detector reference level on the performance of the control system for one sensor combination, additional tests were performed using other sensors. For these later tests, the integrator gain was kept at a value of 800. This is high enough to ensure rapid control response (Figure 65(b)) without using the full capacity of the control system which is reached at a gain of 1000.

A total of three different sensors were tested at four different inlet conditions (guide vane stagger angles,  $\delta_{GV} = 24.5, 32.5, 40.5$  and  $48.5$  degrees) and with stator row 5 both loaded and unloaded. These sensors are as follows:

- 1) Sensor 2, mid-annulus total pressure on leading edge of stator row 5.
- 2) Sensor 7, outer wall static pressure at the rotor 1/4 chord axial location.
- 3) Sensor 6, outer wall 1/4 chord static pressure on the suction surface of stator row 5.

These sensors were chosen for testing beyond that afforded in the sensor investigation of Section IV-A because they appeared to provide certain desirable features. Sensor 2 generated the largest amplitude pressure fluctuations during the presence of rotating stall. Sensors 6 and 7, while generating smaller fluctuating signals during rotating stall, have the advantage that they would be easier to install and maintain than Sensor 7.

The procedure used in testing a particular sensor-control system combination is as follows. A preliminary survey was made to determine approximately the range of detector reference levels required to just barely prevent repeated occurrence of rotating stall. This survey included all four guide vane stagger angles (inlet conditions) which were used in the tests.

Once this detector reference level range was selected, control performance was recorded for fine increments of reference level in this range and larger increments elsewhere. These tests were recorded at a slow chart speed for periods usually exceeding 30 seconds. They were used to assess the degree of hunting of the control at different detector reference levels and if possible to select one particular reference level which appeared suitable for controlling rotating stall under all inlet conditions.

The criterion used in selecting the most favorable detector reference level is that it should prevent repeated occurrence of large amplitude rotating stall under all inlet conditions while at the same time it should not require the stators to back off more than is necessary. In practice it has been found that the best detector reference level for this purpose is one which allows an occasional burst of small amplitude rotating stall under conditions which would normally cause continuous occurrence of large amplitude rotating stall.

Figure 66 presents a complete set of records obtained with Sensor 2 and with stator row 5 loaded. Each of Figures 66 (a) through (d) present results for different guide vane stagger angles. In each figure, the detector reference level is increased progressively. A reference record with the control essentially inoperative is included in each figure for the purpose of comparison.

Inspection of Figure 66 shows that even when rotating stall is completely eliminated (low detector reference levels), there is a certain amount of hunting in the control action on the stator blades. However, the rate and amplitude of the hunting for detector reference levels below that which prevents frequent occurrence of rotating stall (about 220 for this case) is considered to be acceptable for an override type of control. It should be recalled that these records represent a severe test of the control system because they are designed to investigate a continuous condition which should occur only transiently in practice. That is, the primary engine control has commanded the compressor to operate continuously in a region well beyond the rotating

stall boundary and the rotating stall control is required to override this primary control on a continuous basis. No compressor would be designed to operate continuously in this fashion. Additional tests that were performed, but not shown here, indicated that hunting is reduced when a stator stagger angle closer to, but still beyond the rotating stall boundary, is commanded.

With the above comments in mind, it is concluded that Sensor 2 when operated at a detector level of 200 or 220 on the control system provides satisfactory control of rotating stall in the test rig under continuously adverse conditions. Similar tests with Sensors 6 and 7 also indicated satisfactory performance but at different settings of the detector reference level for the best result. Figures 67 and 68 show the results obtained with these two sensors for the inlet condition ( $\delta_{GV} = 24.5$  degrees) which generated the largest amplitude rotating stall when the rotating stall control was inoperative. These figures should be compared to Figure 66(a). Based on inspection of Figures 67 and 68 and the remainder of the test series for Sensors 6 and 7 it was concluded that the best detector level for Sensor 6 is between 240 and 270 and for Sensor 7 between 220 and 240.

Following the tests for continuous control operation under adverse conditions, each sensor-control combination was tested for its transient response during rotor accelerations. The integrator gain on the control was set at 800 and the detector reference level was set for the best value as determined in the previous tests. The guide vanes in the annular cascade were set to provide inlet conditions which generate a continuous large amplitude rotating stall ( $\delta_{GV} = 24.5$  degrees) at a rotor speed of 1250 rpm. The tests were initiated at a rotor speed of 1000 rpm where rotating stall is absent and then the rotor was accelerated rapidly to approximately 1250 rpm.

Figures 69 (a through c) show the results of these tests. In each case, two sets of records are shown. The lower set is a reference which shows the sensor signal when the acceleration is performed without action by the rotating stall control system. The upper records show a similar acceleration with the control operating. All three of the reference (no control)

cases show the initiation and development of a continuous large amplitude rotating stall. There are some differences in these reference cases. The differences in final form of the sensor signals are due to the different types of sensors which were used. In addition there appear to be differences in the length of time required to reach these final forms. Figures 66(a) and (c) show extremes in the required development time. The reason for this is not apparent since all of the accelerations were performed on the same configuration of the annular cascade under roughly identical conditions. However, it is believed that the apparent differences in rotating stall development are caused by differences in the flow development rather than by differences in the sensor responses. In any event, the apparent development time differences in the reference cases in no way detract from the results of the transient performance tests with the control in action.

All three of the sensor-control combinations provide full control action within approximately 300 milliseconds of rotating stall inception and limit the rotating stall to a maximum of 5 moderately sized stall cells. The best performance is exhibited by Sensor 2 (Figure 69(a)) with approximately 200 milliseconds and perhaps 3 fragmented stall cells required for full control action. However, it is believed that all three results show completely satisfactory transient response. These results combined with those of the steady state control tests presented earlier, indicate that the rotating stall control developed during this program shows great potential for providing stall control capability in an operational compressor.

#### D. CONCLUDING REMARKS

A prototype rotating stall control system for axial flow compressors has been developed and tested in the Calspan/Air Force Rotating Annular Cascade Facility. The control is an electro-hydraulic feed-back control system. The input to the control is an unsteady pressure signal produced by sensors mounted within the compressor to detect the presence of rotating stall. The output is a mechanical operation on some variable geometry

feature of the compressor to be controlled. In the annular cascade, the variable geometry was the stagger angles of the stator rows.

The control system was tested for steady state performance under conditions in which the uncontrolled compressor would remain well beyond the rotating stall inception boundary. It was also tested for transient performance during sudden accelerations from conditions without rotating stall to conditions where large amplitude rotating stall would normally occur.

The performance of the control system appears to be very satisfactory under both the steady state and the transient conditions. Thus it is concluded that the rotating stall control shows great promise and should be tested in an operational compressor which contains the required variable geometry features.



## SECTION V

### SUMMARY AND CONCLUSIONS

A combined experimental and theoretical research program on rotating stall in axial flow compressors has been conducted. In addition, a prototype rotating stall control system was developed and tested.

The experimental research included experiments designed to determine the effects of blade chord and of blade row rotation, per se, on the inception and properties of rotating stall. Flow properties, prior to and during rotating stall, were measured in sufficient detail to serve as a guide in developing the theory and to use in correlations. The experimental results did not indicate consistent trends with either blade chord or blade rotation. Stability of the flow through a blade row was also investigated experimentally by measuring the damping of disturbances introduced into the flow. The results of this investigation were more qualitative than quantitative, but definite reductions in the damping factors were detected prior to the inception of steady rotating stall. This would indicate that a stability theory based on small disturbances should be applicable to predicting the inception of rotating stall.

The appropriate stability theory was concurrently developed. It uses an incompressible two-dimensional finite thickness actuator representation of the blade row and requires the mean steady blade row loss and turning performance as inputs. A single blade-row version and a two blade-row version of the theory were developed. The neutral stability boundary predicted by the theory correlates well with the experimentally determined boundary for rotating stall inception. The theory indicates that the mechanism controlling the stability of a given flow configuration is the unsteady vorticity shed into the blade wakes by the variation of loss along the cascade axis. Within this context the slope of the curve of blade row losses as a function of inlet swirl is the most important blade-row aerodynamic characteristic influencing the inception of rotating stall. The two blade-row version of the theory indicates that blade

row interference is the mechanism controlling the number of stall cells that form at inception. Moreover, for the high hub-to-tip ratio configurations investigated in the experiments, the three-dimensional effects may be accounted for by radially averaging the flow quantities and their changes through the blade row.

The combination of the results from the theoretical and experimental studies indicate that the effects of blade chord and blade row rotation on rotating stall may be explained through the influence of these parameters on the mean steady turning and loss performance of the blade row. It would appear that this conclusion may be generalized to indicate that the effects of any of the pertinent compressor geometrical parameters on rotating stall may be similarly explained. In this context the ability to predict the inception of rotating stall depends upon the ability to predict the mean steady turning and loss performance of a blade row or on the availability of the pertinent experimental data.

A prototype rotating stall control system was developed and tested on a low speed compressor stage. This was done in conjunction with an experimental investigation to determine the best sensor configuration to determine incipient rotating stall in a compressor. Tests on the complete control system indicate that there are several sensor configurations that result in a satisfactory system. For these configurations it was possible to keep the compressor stage out of stall in the presence of a primary engine control that was calling for the stage to operate continuously beyond the rotating stall boundary. Moreover, transient performance during sudden acceleration, from conditions without rotating stall to conditions where large amplitude rotating stall would normally occur, showed rapid control response which limited the rotating stall to as few as three small fragmented cells. Based on these tests it can be concluded that the control system has definite potential for application to a full-scale compressor.

## APPENDIX A

### EXPERIMENTAL INVESTIGATION OF THE STABILITY OF FLOW THROUGH A BLADE ROW

Most of the theoretical studies of rotating stall which have been performed at Calspan have assumed that a stability analysis linearized on the basis of small disturbances in the flow is adequate to predict the conditions necessary for inception of rotating stall. Within this framework, the actual rotating stall which occurs in a compressor is viewed as a result of disturbances which have grown because of the instability of the flow. The stall acts in a nonlinear fashion to limit the magnitude of the disturbances to a finite value. Another and opposing viewpoint is that the actual stalling of the blades is a necessary part of the phenomenon of rotating stall and not simply the limiting result of a flow instability brought about by other parameters. Since these two views require different approaches to the study of rotating stall, it would be invaluable if some experimental evidence could be generated to substantiate one or the other viewpoint. Hence an experimental investigation was undertaken to measure the damping characteristics of controlled disturbances introduced into the flow between stator blades in the Calspan/Air Force Annular Cascade. The aim was to attempt to determine the stability of the flow through a blade row in a fashion analogous to the experimental investigation of boundary layer stability reported in Reference 13. Before proceeding with a description of the experiments, a brief outline of the general principle involved in the measurements will be presented.

In the small disturbance stability theory, solutions to the linearized Euler equations are assumed which have the form,  $\Psi = \phi(\chi, r) e^{j(n\theta + ct)}$  where:

$(\chi, r, \theta)$  = Cylindrical coordinate system with  $\chi$  as axial,  $r$  as radial, and  $\theta$  as angular coordinates

$c$  = Complex angular frequency

$j$  =  $\sqrt{-1}$

$n$  = Angular wave number

$\phi$  = Function of  $\chi$  and  $r$

$\Psi$  = Stream function

These solutions are investigated for stability when combined with additional equations which describe the matching of the flow across a mathematical model of a blade row. In the solution for the stream function,  $\Psi$ , only the real part is to be considered. The velocity disturbance solutions have the same general form. The quantity  $C$  is complex and can be written,  $C = C_R + j C_I$ . With this representation,  $\Psi = \phi(\chi, r) e^{-C_I t} e^{j(n\theta + C_R t)}$ . This expression represents a wave travelling in the  $\theta$  direction with angular velocity  $\frac{-C_R}{n}$  radians per second and wavelength  $\frac{2\pi}{n}$  radians, which is damped exponentially in time with a damping constant,  $C_I$ .

If the small disturbance theory is applicable to rotating stall, then the damping constant,  $C_I$ , should approach zero as the steady flow conditions approach the experimentally measured inception boundary for rotating stall.

The damping constant can be determined experimentally by generating a small amplitude periodic disturbance at one point and measuring the root mean square value (or peak to peak amplitude) at two different values of  $\theta$  with  $\chi, r$  fixed. If we let a bar over a quantity represent the root mean square value (with respect to time) then it can be shown that (as in Reference 13)

$$\frac{\bar{\Psi}(\theta + \Delta\theta)}{\bar{\Psi}(\theta)} = e^{-C_I \Delta t} \quad (A-1)$$

or

$$C_I = -\frac{1}{\Delta t} \ln \left( \frac{\bar{\Psi}(\theta + \Delta\theta)}{\bar{\Psi}(\theta)} \right) \quad (A-2)$$

where  $\Delta t$  is the time required for the wave to travel the distance  $\Delta\theta$ . For use in Equation (A-2),  $\bar{\Psi}(\theta)$  may be any flow quantity proportional to unsteady velocity. Thus, this equation can be evaluated experimentally by recording simultaneously the velocity signals from two hot wires located at fixed  $\chi$  and  $r$  and two different values of  $\theta$ . The amplitudes of the velocity signals give  $\bar{\Psi}$  and  $\Delta t$  is found from the phase shift between the two signals.

In the damping investigation of the current program, a small flat plate rotating about a radial line was used as the disturbance generator. The plate was located in the stator blade row midway between two of the fifth-stage J79 stator blades (Stator Set No. 1). A sketch of the plate is shown in Fig. 70. The flat plate was driven by a variable speed Heller Electric Motor and Controller Unit (Model T260) capable of rotating the plate up to 2000 rpm.

Provision was made to allow for a second rotating plate located at a slightly different circumferential location. The two plates could be connected by a drive shaft to rotate at identical speeds. The geometric angular relationship between the plates was adjustable. In this way a two point exciting disturbance, with adjustable phase angle, was available for the damping investigation in case single point excitation did not provide conclusive results. The disturbance generator drive mounted on the outside of the annular cascade is shown in Fig. 71.

Modifications were made to the outer casing of the annular cascade to provide suitable traversing mounts for hot-wire probes. One mount was constructed upstream and one downstream of the fifth stage stator row. These mounts allowed independent circumferential traverses (in the  $\theta$  direction) of two hot-wire probes at the same axial location. Independent circumferential adjustment of each probe was believed to be necessary because the signal amplitude detected by the probe would depend on the geometric location of the probe with respect to the nearest blades as well as with respect to the signal generator. The localized effect of the nearby blades can be essentially cancelled if both probes are located in a similar position with respect to the nearest blades.

In some preliminary experiments, the velocity disturbances generated upstream of the stators were studied with two single hot-wire systems which had been accurately linearized and calibrated. It was found that the upstream velocity disturbances generated by the rotating plate were so small that they were masked by the background turbulence level in the flow at the

measuring stations. This was the case even after filtering the velocity signals with low pass filters to remove a large portion of the turbulent fluctuations. It was possible to detect rotating stall from the upstream velocity signals although even these signals were relatively small near inception. Since the region of primary interest was near inception, it was concluded that the hot-wire equipment would not provide useable data. No attempt was made to use hot-wire equipment downstream of the stators because previous experience had indicated that the presence of the stator blade wakes made the flow even more turbulent.

At this point in the investigation, it was decided that the best way to obtain an indication of the damping in the blade row would be to use pressure taps on the suction surface of the stator blades as detectors. Previous experience in measuring the properties of rotating stall had indicated that a pressure tap situated on the quarter chord of a stator blade at mid-annulus would provide the cleanest signal for the flow disturbances in the blade row. As expected, the signals from the pressure tapped stator blades were a considerable improvement over the hot-wire data. However, even with these cleaner signals, it was extremely difficult to obtain records which were useful for investigating the damping behavior in the flow. In gathering the data which finally were obtained, a succession of combinations of disturbance generator and detector locations were used. These combinations are shown in Fig. 72 and are designated by a configuration number.

Configurations 1 and 2 did not provide any quantitative information because in each case, the signal at the pressure tap farthest removed from the disturbance generator was too small. Each of Configurations 3 through 6 provided some useful information, although even here a portion of the information was more in the nature of general observations rather than quantitative data. The general behavior will now be discussed prior to presentation of quantitative data.

The first observation is common to all configurations. It is extremely difficult to obtain synchronization between rotating stall and the

artificially generated disturbances. Rotating stall does not "lock in" to the frequency of the disturbance when the disturbance frequency is brought close to that of the rotating stall. This is true even for those cases where the disturbance amplitude was larger than that of the rotating stall as well as for Configuration 4 where both frequency and phase at two different points were adjusted to correspond to spontaneous rotating stall. Apparently, once continuous rotating stall occurs, its properties are not measurably influenced by the presence of artificial excitation at one or two discrete points along the blade row.

In contrast to the above, if the rotating stall is not well established, that is, if flow conditions are near the inception point and rotating stall is intermittent, then it is sometimes possible to stop rotating stall through deliberately mismatching the artificial disturbance and rotating stall frequencies. In fact, a stationary plate held perpendicular to the blade passage is also effective in delaying the inception of rotating stall. The latter effect is not new. It is similar to the delay in inception experienced when one or two blades in a row are set at stagger angles which differ from the remainder of the row.

The experiments using the two disturbance generators of Configuration 4 were undertaken because there was a possibility that excitation at a single point was not sufficient to excite the traveling wave modes of interest to a measurable degree under conditions where the damping of these modes is high. The tests on Configurations 1 through 3 had shown that for almost all flow conditions the damping was very high. Thus, it was hoped that the two-point excitation would be more successful in exciting the desired traveling wave modes. A series of tests were performed in which both the frequency (angular velocity) and the relative phase (geometric angular relationship) were varied to correspond to the frequency and phase of naturally occurring rotating stall near the inception point. Comparison of the results of these tests with those from the single generator tests of Configuration 3 for identical flow conditions showed that two point excitation provided no measurable improvement over single point excitation.

The tests with Configurations 5 and 6 were performed to investigate the effect of disturbance amplitude on the measurements. In Configurations 2, 3, and 4 the amplitude of the artificial disturbance detected with the pressure transducer nearest to a generator was often larger than that detected during rotating stall. (The disturbances generated in Configuration 1 were too small to be of use.) The disturbances detected in Configuration 5 were very small, as in Configuration 1. With Configuration 6, the artificial disturbances were significantly smaller than rotating stall but large enough to provide some records which were suitable for analysis to obtain damping values. Comparison of the records with similar data from Configuration 3 suggested that the disturbance amplitude does not greatly affect the damping, at least over the range tested.

As previously mentioned it was initially intended that velocity measurements obtained with hot wires would be used in conjunction with Equation (A-2) to determine the damping constant. However, when it became necessary to use the quarter-chord pressure measurements, the applicability of Equation (A-2) became questionable. Although the linear theory would indicate that the unsteady pressures are linearly related to the unsteady velocities, the past experimental experience with the precursor signals provided by the quarter chord pressure taps would indicate that this is not the case. It is felt that the quarter-chord pressure taps would not give such clear precursor signals of rotating stall if they did not amplify the unsteadiness in the flow in a nonlinear fashion. However, because of the logarithmic dependence shown in Equation (A-2), the nonlinearities in the pressure signals probably do not greatly affect the form of the result. For instance, note that if the pressure signal is proportional to the unsteady velocity raised to the power  $m$ , the only change required in Equation (A-2) is that the right hand side be multiplied by  $m$ .

It was not feasible to determine accurately the pressure-velocity relationship of the experimental setup. In view of this, it was decided to treat the pressure measurements as though they were linearly related to the velocity. It is realized that this treatment may lead to quantitative errors



in the results but the qualitative behavior should still be correct. In actual practice, the data obtained in the experiments were reduced by applying Equation (A-2) in the form,

$$c_r = - \frac{1}{\Delta t} \ln \left( \frac{P(\theta + \Delta\theta)}{P(\theta)} \right)$$

where peak-to-peak amplitudes were used for the values of  $P$ . These amplitudes were obtained by averaging over several cycles on the photographically recorded time histories of oscilloscope traces that included signals from both quarter-chord pressure taps. The  $\Delta t$  was obtained from the same photos by measuring the time phase shift between the two signals.

The useable data that were reduced in this fashion are shown in Figures 73(a) through 73(d). Where possible, the corresponding two blade row theoretical estimates for the damping factor are included. In order to obtain useable signals from the detector farthest away from the disturbance generator, it was necessary to locate this second detector close to the first detector. This in turn reduced the time lag,  $\Delta t$ , between the detector signals and consequently made accurate measurement of  $\Delta t$  difficult. The cases with high damping, and in particular, the case shown in Figure 73(d), were the worst in this respect. However, the trends shown by the data in each figure appear to be consistent, with relatively little scatter.

Inspection of Figures 73(a) through (d) shows that, as required by the theory, all of the experimental data indicate a decrease in damping as the rotating stall inception boundary is approached. Moreover, for the case where the pressure signal indicated turbulent flow well in advance of a distinguishable rotating stall inception point, both the theory and the experiments show a gradual decrease in damping as the inception point is approached, and the damping values are not large. (Figure 73(a)). For those cases where the pressure signals were "clean" prior to inception, the measured damping is very high and the transition from stable to unstable conditions occurs rapidly (Figures 73(c) and (d)). This also is in agreement with the theory, although the quantitative comparison in Figure 73(d) is not as good. (The theory could not be applied to the case shown

in Figure 73(c) because experimental loss data were not available). The results presented in Figure 73(b) is an intermediate case between the two extremes mentioned above. Here the measured damping is not large but the transition near inception is more rapid than that observed in Figure 73(a).

Keeping in mind the qualitative nature of the comparison between theory and experiment, it can be said that the agreement between theory and experiment is satisfactory. Moreover, as noted previously, all of the measurements show a decrease in damping as rotating stall is approached. The above observations, along with the good correlation between theory and experiment for rotating stall inception which has been demonstrated in the main body of this report, lead to the conclusion that a small disturbance stability theory is applicable to the prediction of rotating stall inception.

## APPENDIX B

### DETAILED DEVELOPMENT OF TWO BLADE ROW ROTATING STALL STABILITY THEORY

The flow configuration for the two blade row model is shown in Figure 50. Each blade row is modeled by a finite thickness actuator sheet as it was in the single blade row theory. No lag times were assumed in any of the actuator characteristics. A stream function  $\psi_i$  is defined in each flow region such that  $u_i = \frac{\partial \psi_i}{\partial y}$  and  $w_i = -\frac{\partial \psi_i}{\partial x}$ . The  $\psi_i$  are then of the form

$$\psi_i = \phi_i(x) e^{j(ct + ny/r)}$$

and

$$\phi_i = A_i e^{-nx/r} + B_i e^{nx/r} + D_i e^{-jnx/r \left( \frac{cr}{nU_0} + S_i \right)}$$

There are then nine constants to be determined. The requirements of bounded flow disturbances at upstream and downstream infinity and no vorticity in the flow ahead of the first blade row result in

$$A_0 = D_0 = B_2 = 0 \quad (\text{B-1})$$

Then the disturbance velocities become

$$u_0 = j \frac{n}{r} B_0 \exp \left\{ \frac{nx}{r} + j \left( ct + \frac{ny}{r} \right) \right\} \quad (\text{B-2a})$$

$$w_0 = -B_0 \frac{n}{r} \exp \left\{ \frac{nx}{r} + j \left( ct + \frac{ny}{r} \right) \right\} \quad (\text{B-2b})$$

$$u_1 = A_1 j \frac{n}{r} \exp \left\{ -\frac{nx}{r} + j \left( ct + \frac{ny}{r} \right) \right\} + B_1 j \frac{n}{r} \exp \left\{ \frac{nx}{r} + j \left( ct + \frac{ny}{r} \right) \right\} \\ + D_1 j \frac{n}{r} \exp \left\{ -j \frac{nx}{r} \left( \frac{cr}{nU_0} + S_1 \right) + j \left( ct + \frac{ny}{r} \right) \right\} \quad (\text{B-2c})$$

$$w_1 = A_1 \frac{n}{r} \exp \left\{ -\frac{nx}{r} + j \left( ct + \frac{ny}{r} \right) \right\} - B_1 \frac{n}{r} \exp \left\{ \frac{nx}{r} + j \left( ct + \frac{ny}{r} \right) \right\} \\ + D_1 j \frac{n}{r} \left( \frac{cr}{nU_0} + S_1 \right) \exp \left\{ -j \frac{nx}{r} \left( \frac{cr}{nU_0} + S_1 \right) + j \left( ct + \frac{ny}{r} \right) \right\} \quad (\text{B-2d})$$

$$u_2 = A_2 j \frac{n}{r} \exp \left\{ -\frac{nx}{r} + j \left( ct + \frac{ny}{r} \right) \right\} \quad (\text{B-2e})$$

$$+ D_2 j \frac{n}{r} \exp \left\{ -j \frac{nx}{r} \left( \frac{cr}{nU_0} + S_2 \right) + j \left( ct + \frac{ny}{r} \right) \right\}$$

$$\omega_2 = A_2 \frac{n}{r} \exp \left\{ -\frac{nx}{r} + j \left( ct + \frac{ny}{r} \right) \right\} \quad (\text{B-2f})$$

$$+ D_1 j \frac{n}{r} \left( \frac{cr}{nU_0} + S_2 \right) \exp \left\{ -j \frac{nx}{r} \left( \frac{cr}{nU_0} + S_2 \right) + j \left( ct + \frac{ny}{r} \right) \right\}$$

The remaining six unknowns are determined by the application of the following three matching conditions at each actuator:

- 1) Conservation of mass flow
- 2) Vorticity compatibility
- 3) Flow deflection relation

The general conservation of mass matching condition for the  $i^{\text{th}}$  actuator is expressed by

$$u_{o_{i-1}}(x_{o_{i-1}}, y_{o_{i-1}}, t_0) = u_{o_i}(x_{o_i}, y_{o_i}, t_0) \quad (\text{B-3})$$

where  $x_{o_{i-1}}$  is the leading edge of the actuator and  $x_{o_i}$  is the trailing edge of the  $i^{\text{th}}$  actuator. The general vorticity compatibility relation for the  $i^{\text{th}}$  actuator is expressed by

$$\begin{aligned} \frac{\partial}{\partial t_0} (\omega_{o_i} - \omega_{o_{i-1}}) - \alpha_i \sec \delta_i \frac{\partial^2 u_{o_{i-1}}}{\partial t_0 \partial y_0} + U_0 (n_{o_i} - n_{o_{i-1}}) \\ = \frac{\partial}{\partial y_0} \left\{ \frac{1}{2} X_i \left[ (U_{o_{i-1}} + u_{o_{i-1}})^2 + (W_{o_{i-1}} + \omega_{o_{i-1}})^2 \right] \right\} \end{aligned} \quad (\text{B-4})$$

where all quantities subscripted with  $i-1$  are evaluated at  $x_{o_{i-1}}$ , and all quantities subscripted with  $i$  are evaluated at  $x_{o_i}$ . Also  $\alpha_i$  and  $\delta_i$  are the chord and stagger angle of the  $i^{\text{th}}$  blade row, respectively. The general flow deflection relation at each actuator is given by

$$\omega_{o_i} - \delta_i u_{o_i} = g_i (\omega_{o_{i-1}} - \delta_{i-1} u_{o_{i-1}}) \quad (\text{B-5})$$

and where

$$q_i = \frac{\partial S_i}{\partial S_{i-1}}$$

Equation B-5 is also evaluated in the same manner as the previous one.

Combining Equations (B-2), (B-3), (B-4), and (B-5), the following homogeneous system is obtained for the unknowns:

$$\begin{bmatrix} a_{11} \\ a_{12} \\ a_{13} \\ a_{14} \\ a_{15} \\ a_{16} \end{bmatrix} \begin{bmatrix} B_0 \\ A_1 \\ B_1 \\ D_1 \\ A_2 \\ D_2 \end{bmatrix} = 0 \quad (\text{B-6})$$

The  $a_{ij}$  matrix is a six by six with the following elements ( $i$  - row index,  $j$  - column index):

$$a_{11} = 1$$

$$a_{12} = -e^{Q_1}$$

$$a_{13} = -e^{Q_2}$$

$$a_{14} = -e^{Q_3}$$

$$a_{15} = 0$$

$$a_{16} = 0$$

$$a_{21} = 0$$

$$a_{22} = e^{-Tn/r}$$

$$a_{23} = e^{Tn/r}$$

$$a_{24} = e^{-\frac{nT}{r}(k+S_1)}$$

$$a_{25} = -e^{P_1}$$

$$a_{26} = -e^{P_3}$$

$$a_{31} = -j(1+q_1)(k+\bar{\Omega}_1) - \frac{j}{2}(1+d_0^2)(1+jd_0)X'_1 - X_1(1+jd_0)$$

$$a_{32} = -j(k+\bar{\Omega}_1)e^{Q_1}$$

$$a_{33} = j(k+\bar{\Omega}_1)e^{Q_2}$$

$$a_{34} = -[1+d_1(k+S_1)]e^{Q_1}$$

$$a_{35} = 0$$

$$a_{36} = 0$$

$$a_{41} = 0$$

$$a_{42} = \left\{ j(1-q_2)(k+\bar{\Omega}_2) + \frac{j}{2}(1+d_1^{+2})X'_2(1-jd_1^+) - X_2(1-jd_1^+) \right\} e^{-\frac{nT}{r}}$$

$$a_{43} = \left\{ -j(1+q_2)(k+\bar{\Omega}_2) - \frac{j}{2}(1+d_1^{+2})X'_2(1+jd_1^+) - X_2(1+jd_1^+) \right\} e^{\frac{nT}{r}}$$

$$a_{44} = \left\{ -(k+S_1) \left[ \frac{1}{2}(1+d_1^{+2})X'_2 + d_1^+(X_2-1) \right] - jq_2(k+\bar{\Omega}_2) + 1 - X_2 + \frac{1}{2}d_1^+(1+d_1^{+2})X'_2 \right\} e^{-j\frac{nT}{r}(k+S_1)}$$

$$a_{45} = -j(k+\bar{\Omega}_2)e^{P_1}$$

$$a_{46} = -\left\{ 1+d_2^+(k+S_2) \right\} e^{P_3}$$

$$a_{51} = q_1(1+jd_0)$$

$$a_{52} = (1-jd_1)e^{Q_1}$$

$$a_{53} = -(1+jd_1)e^{Q_2}$$

$$a_{54} = j(k+\bar{\Omega}_1)e^{Q_3}$$

$$a_{55} = 0$$

$$a_{56} = 0$$

$$\begin{aligned}
a_{61} &= 0 \\
a_{62} &= -q_2 (1 - j S_1^+) e^{-\frac{nT}{r}} \\
a_{63} &= q_2 (1 + j S_1^+) e^{\frac{nT}{r}} \\
a_{64} &= -q_2 j (\kappa + \bar{\Omega}_2) e^{-j \frac{nT}{r} (\kappa + S_1)} \\
a_{65} &= (1 - j S_2^+) e^{P_1} \\
a_{66} &= j (\kappa + \bar{\Omega}_2) e^{P_2}
\end{aligned}$$

where

$$\begin{aligned}
Q_1 &= -\frac{nd_1}{r} \cos \delta_1 + j \frac{nd_1}{r} \sin \delta_1 \\
Q_2 &= \frac{nd_1}{r} \cos \delta_1 + j \frac{nd_1}{r} \sin \delta_1 \\
Q_3 &= j \frac{nd_1}{r} \sin \delta_1 - j \frac{nd_1}{r} \cos \delta_1 (y + S_1) \\
P_1 &= -\frac{nd_2}{r} \cos \delta_2 + j \frac{nd_2}{r} \sin \delta_2 \\
P_3 &= j \frac{nd_2}{r} \sin \delta_2 - j \frac{nd_2}{r} \cos \delta_2 (y + S_2)
\end{aligned}$$

This system has a nontrivial solution when the characteristic determinant is zero, i. e.,

$$|a_{ij}| = 0 \quad (\text{B-7})$$

One root may be determined by inspection as  $\kappa = -S_2 - j$  which is the counterpart of the previously encountered zero amplitude root. This has been factored out of Equation (B-7) and the remaining expression is

$$m_{31} n_{31} e^{\frac{-n}{r}(T-x_1)} + m_{32} n_{32} e^{\frac{n}{r}(T-x_1)} + m_{33} n_{33} e^{-j \frac{n}{r}(T-x_1)(\kappa + S_1)} = 0 \quad (\text{B-8})$$

where the  $m_{3i} n_{3i}$  are polynomials in the unknown  $\kappa$ , namely

$$m_{31} = b_{11} (k + \bar{\Omega}_2) + b_{21}$$

$$b_{11} = -j q_2$$

$$b_{12} = \frac{j}{2} (1 + \mathcal{S}_1^{+2}) (1 - j \mathcal{S}_1^+) X_2' - X_2 (1 - j \mathcal{S}_1^+) \\ - (1 + \mathcal{S}_2^{+2}) + q_2 (1 + j \mathcal{S}_2^+) (1 - j \mathcal{S}_1^+)$$

$$m_{32} = b_{21} (k + \bar{\Omega}_2) + b_{22}$$

$$b_{21} = -j (2 + q_2)$$

$$b_{22} = -\frac{j}{2} (1 + \mathcal{S}_1^{+2}) X_2' (1 + j \mathcal{S}_1^+) - X_2 (1 + j \mathcal{S}_1^+) \\ - q_2 (1 + j \mathcal{S}_2^+) (1 + j \mathcal{S}_1^+) - (1 + \mathcal{S}_2^{+2})$$

$$m_{33} = b_{31} (k + \bar{\Omega}_2) + b_{32}$$

$$b_{31} = -j (1 + q_2) + j q_2 (1 + j \mathcal{S}_2^+) + \mathcal{S}_1^+ \\ - \frac{j}{2} (1 + \mathcal{S}_1^{+2}) X_2' - \mathcal{S}_1^+ X_2$$

$$b_{32} = \mathcal{S}_1^{+2} - \mathcal{S}_1^{+2} X_2 + 1 - X_2 - (1 + \mathcal{S}_2^{+2})$$

$$\eta_{31} = b_{41} (k + \bar{\Omega}_1)^2 + b_{42} (k + \bar{\Omega}_1) + b_{43}$$

$$b_{41} = q_1$$



$$b_{42} = -s_1 [(1 + j s_1) - q_1 (1 + j s_0)] + \frac{1}{2} (1 + s_0^2) (1 + j s_0) X_1' \\ - j X_1 (1 + j s_0) - j (1 + j s_1) (1 + q_1) + j q_1 (1 + j s_0)$$

$$b_{43} = - (1 + s_1^2) [(1 + j s_1) - q_1 (1 + j s_0)] \\ + (1 + j s_1) \left[ -\frac{j}{2} (1 + s_0^2) (1 + j s_0) X_1' - X_1 (1 + j s_0) \right]$$

$$\eta_{32} = b_{51} (k + \bar{\Omega}_1)^2 + b_{52} (k + \bar{\Omega}_1) + b_{53}$$

$$b_{51} = -(2 + q_1)$$

$$b_{52} = -s_1 (1 - j s_1) - j (1 + q_1) (1 - j s_1) - \frac{j}{2} (1 + s_0^2) (1 + j s_0) X_1' \\ + j X_1 (1 + j s_0) + j q_1 (1 + s_0) (1 + j s_1)$$

$$b_{53} = (1 - j s_1) \left[ -\frac{j}{2} (1 + s_0^2) (1 + j s_0) X_1' - X_1 (1 + j s_0) \right] \\ - q_1 (1 + j s_0) (1 + s_1^2) - (1 - j s_1) (1 + s_1^2)$$

$$\eta_{33} = b_{61} (k + \bar{\Omega}_1) + b_{62}$$

$$b_{61} = 2j (1 + q_1) - 2s_1 \quad 2j q_1 (1 + j s_0)$$

$$b_{62} = j (1 + s_0^2) (1 + j s_0) X_1' + 2X_1 (1 + j s_0)$$

where

$$q_1 = \frac{\partial s_1}{\partial s_0}$$

$$j = \frac{\partial s_1^*}{\partial s_1}$$

$$q_1 = \frac{nd_1}{r} \sec \delta_1$$

$$q_2 = \frac{nd_2}{r} \sec \delta_2$$

$$x_1 = d_1 \cos \delta_1$$

$T$  = The distance from the leading edge of actuator 1 to the leading edge of actuator 2

$X_1$  = loss coefficient of 1st blade row

$$X'_1 = \frac{\partial X_1}{\partial \tan \beta_{0_2}}$$

$X_2$  = loss coefficient of 2nd blade row

$$X'_2 = \frac{\partial X_2}{\partial \tan \beta_{0_1}}$$

$d_1$  = chord of 1st blade row

$d_2$  = chord of 2nd blade row

$\delta_1$  = stagger angle of 1st blade row

$\delta_2$  = stagger angle of 2nd blade row

In the limit for large blade row spacing,  $T$  becomes infinite and Equation (B-8) becomes:

$$\mathcal{M}_{32} \mathcal{N}_{32} = 0$$

Comparing  $\mathcal{M}_{32}$  with Equation 29 it is seen that  $\mathcal{M}_{32} = 0$  corresponds to the characteristic equation for the second blade row in isolation. Inspection of

$\mathcal{N}_{32}$  similarly shows that  $\mathcal{N}_{32} = 0$  corresponds to the characteristic equation for the first blade row in isolation. (However, the trivial root  $k = -\delta_2 - \frac{1}{\delta_2}$  has not been factored out of this expression).

Equation (B-8) was solved numerically using a Newton-Raphson technique (Reference 14). That is an error function is formed by letting

$$F = m_{31} n_{31} e^{-\frac{n}{r}(T-x_1)} + m_{32} n_{32} e^{\frac{n}{r}(T-x_1)} + m_{33} n_{33} e^{-\frac{n}{r}(T-x_1)(k+S_1)}$$

The problem is then to find the zeros of  $F$ . This is done by expanding  $F$  in a Taylor Series about some initial guess at the solution,  $k_1$ , i. e.,

$$F(k) = F(k_1) + (k - k_1) F'(k_1)$$

where  $F' = \frac{\partial F}{\partial k}$ . Then, the next iterate is given by

$$k_2 = k_1 - \frac{F(k_1)}{F'(k_1)} \tag{B-9}$$

Then  $F(k_2)$  is calculated. The process is repeated until  $F(k_n)$  is made sufficiently small. In the present calculation, a solution was considered to be obtained when  $|F(k_n)| < 10^{-4}$ . The initial guess was usually the single blade row solution for the second of the two blade sets. For sufficiently high  $n$ , Equation (B-8) was generally found to have a root which was extremely close to this first guess. This root will be referred to as the principal root and is the solution shown plotted in all of the figures presented in this report. Additional roots will be discussed subsequently.

Because of the transcendental term in Equation (B-4), the values of the function  $F$  possess regions of high frequency oscillation in the complex  $k$  plane. In these regions, use of  $F'(k)$  in the iteration scheme, Equation (B-9), generally led to divergence of the scheme. Replacing  $F'(k)$  by its finite difference approximation was found to solve this problem and this revision to the scheme was used in all the remaining calculations. This process essentially averages the values of  $F'(k)$  in these regions.

The algebra involved in expanding the determinant in Equation (B-7) to obtain Equation (B-8) was checked by using a FORMAC program on the

Calspan IBM 370/175 Computing Machine. This also proved valuable in obtaining additional analytic solutions to Equation (B-8).

Since Equation (B-8) is transcendental, there is no theory guaranteeing the number of roots. Besides the trivial root already mentioned, two additional trivial roots have been found for the case when  $S_0 = 0$ , which is generally true. They are

$$k = \pm j - \delta,$$

Unfortunately, because of the fashion in which they satisfy the equation, no simplification of Equation (B-3) is possible. These roots were discovered by numerical investigation and then verified analytically by inputting them to the previously mentioned FORMAC program. In addition to these analytic roots, another root has been discovered by numerical exploration. It is always stable and propagates in the opposite direction to the principal root. It evidently has no physical significance and is therefore not shown in any of the figures of this report.

The preceding type of analysis may be extended to an arbitrary number of blade rows. The general characteristic determinant will be of order three times the number of blade rows and will be transcendental.

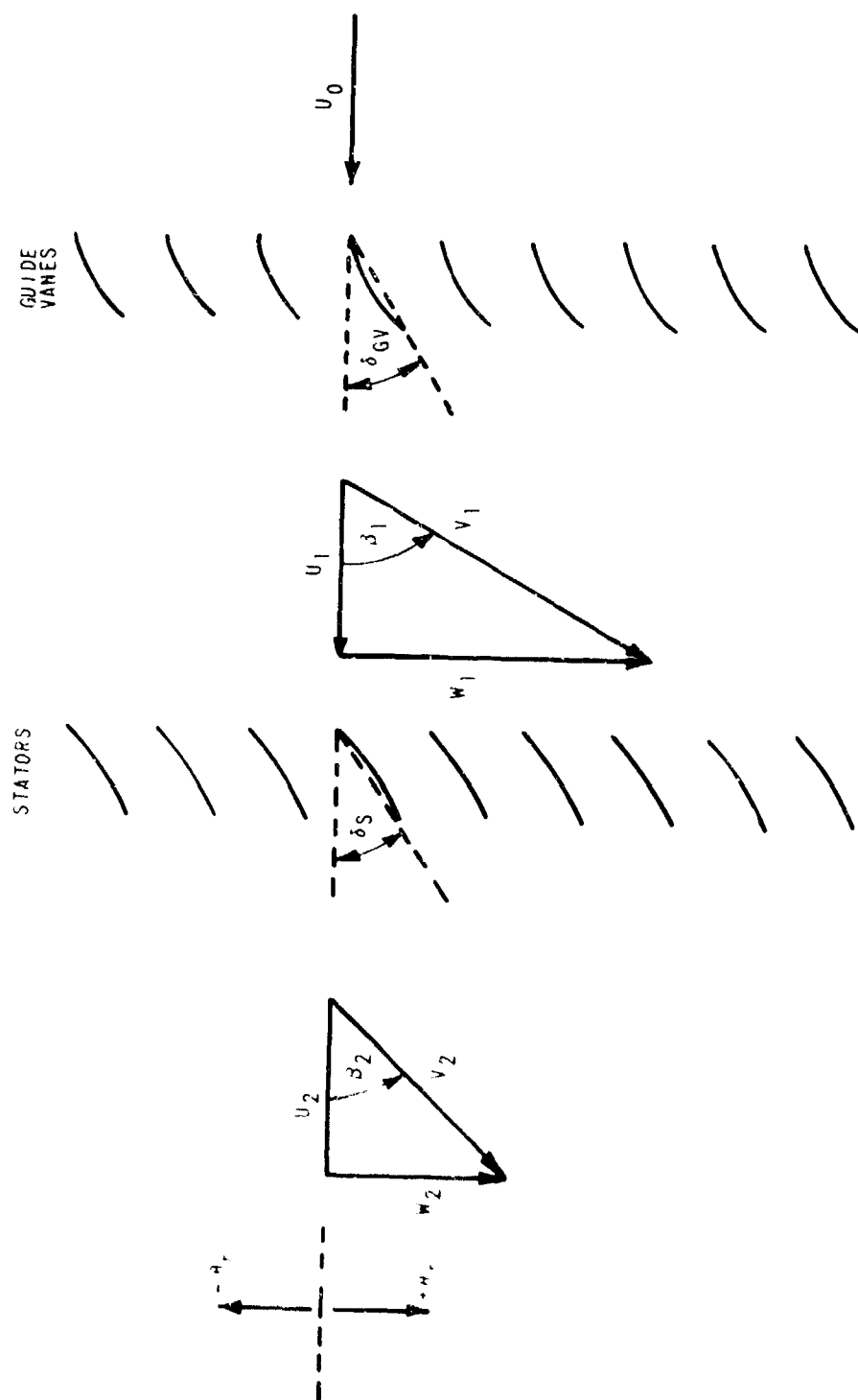


Figure 1 NOTATION FOR ANNULAR CASCADE WITH STATIONARY HUB

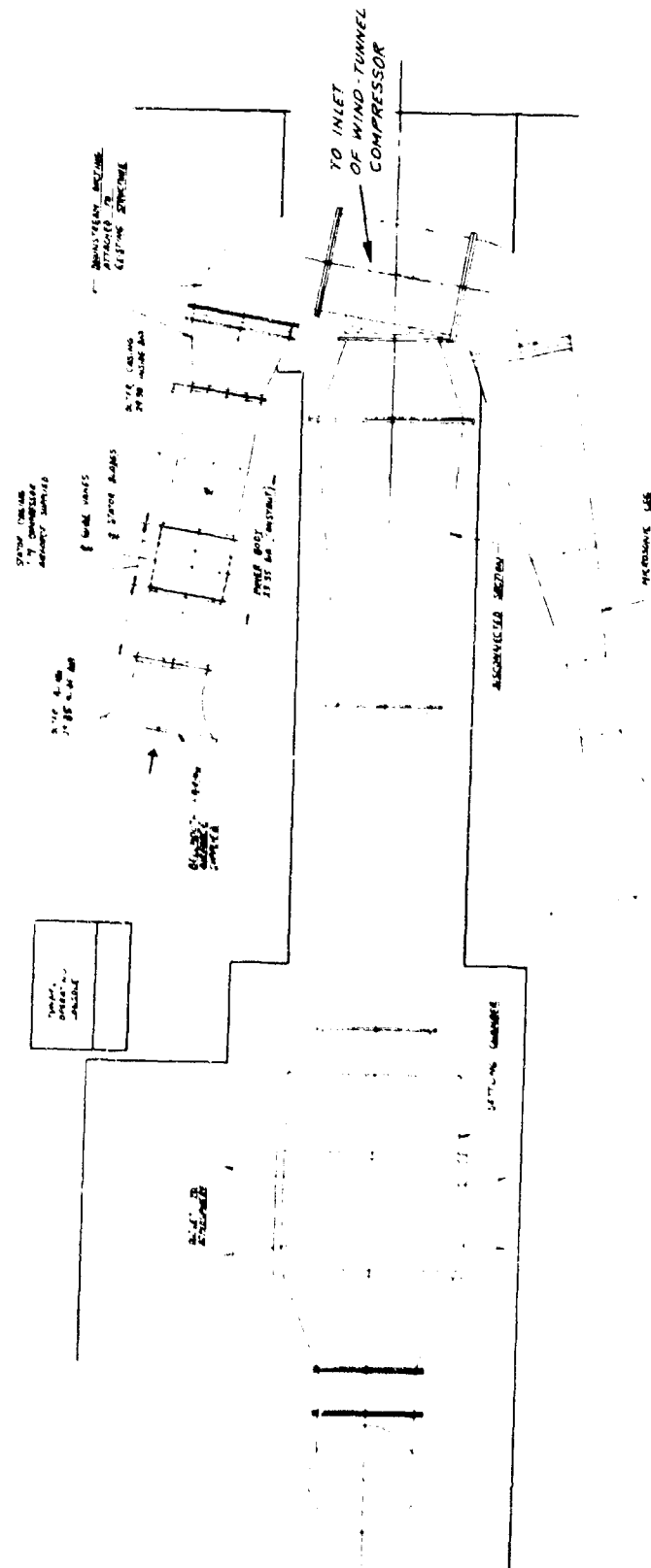


Figure 2 PLAN VIEW OF RESEARCH ANNULAR CASCADE FACILITY ATTACHED TO CALSPAN/AIR FORCE ONE-FOOT HIGH-SPEED WIND TUNNEL

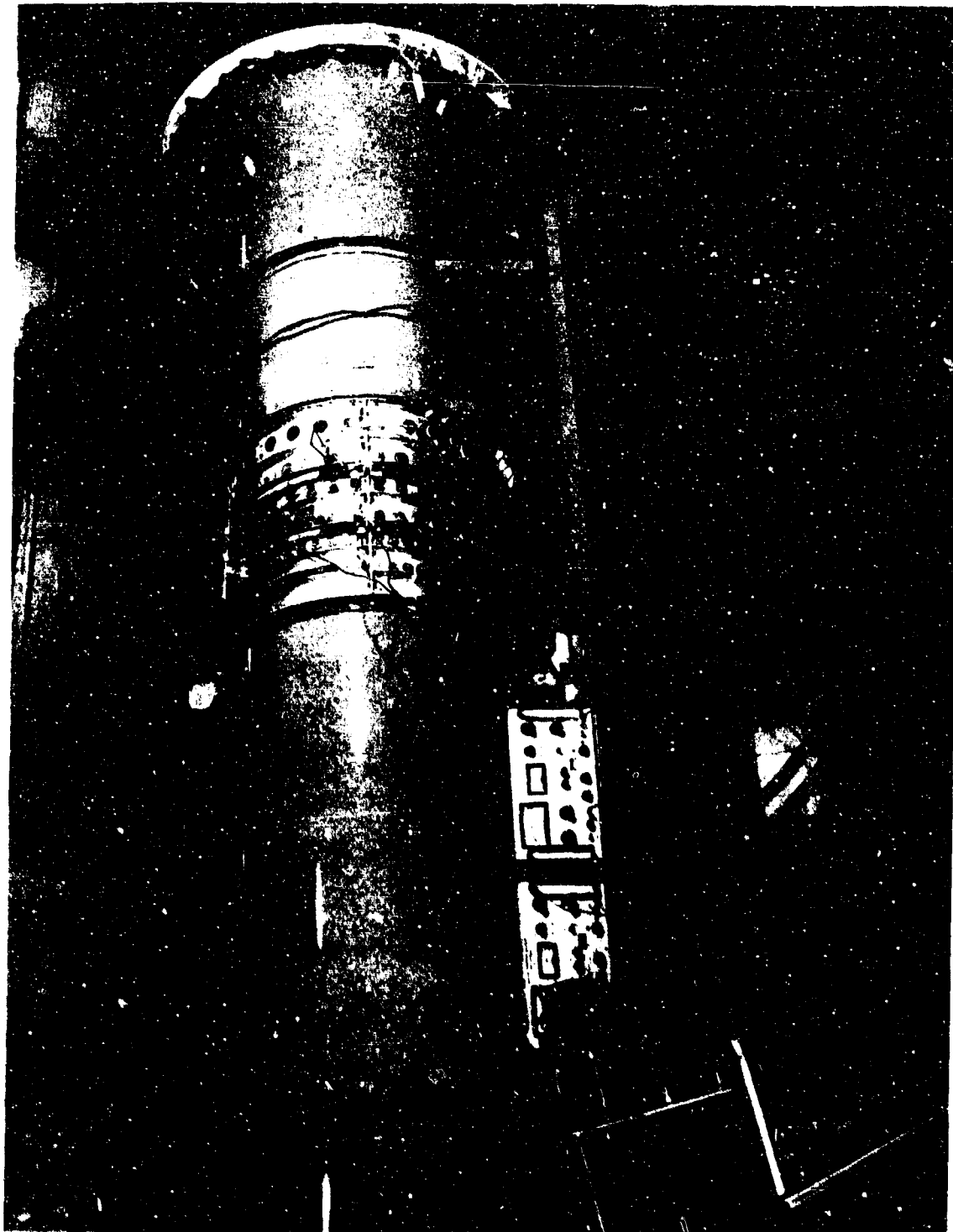


Figure 3 OVERALL VIEW OF ANNULAR CASCADE TEST SECTION

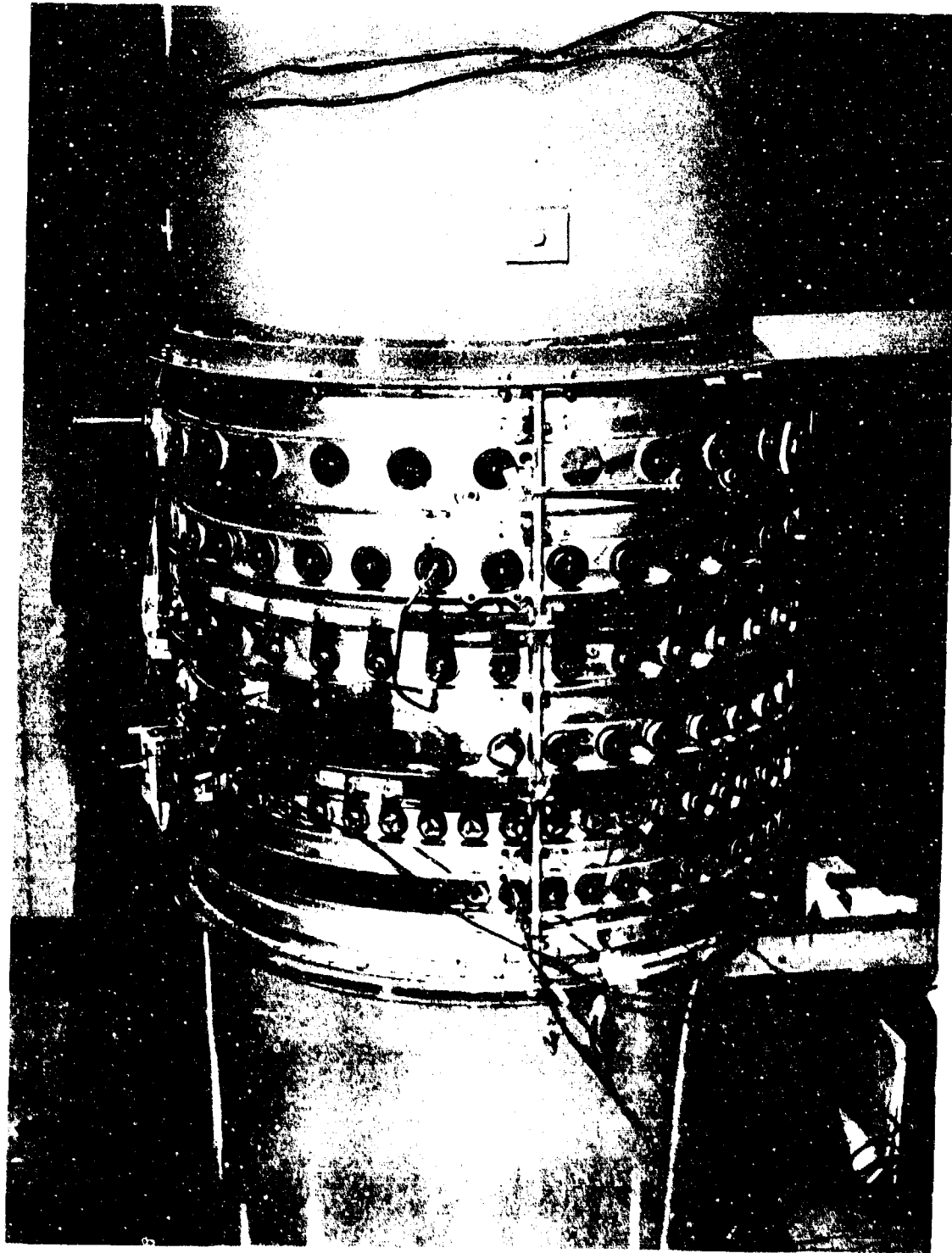


Figure 4 VIEW OF ANNULAR CASCADE TEST SECTION





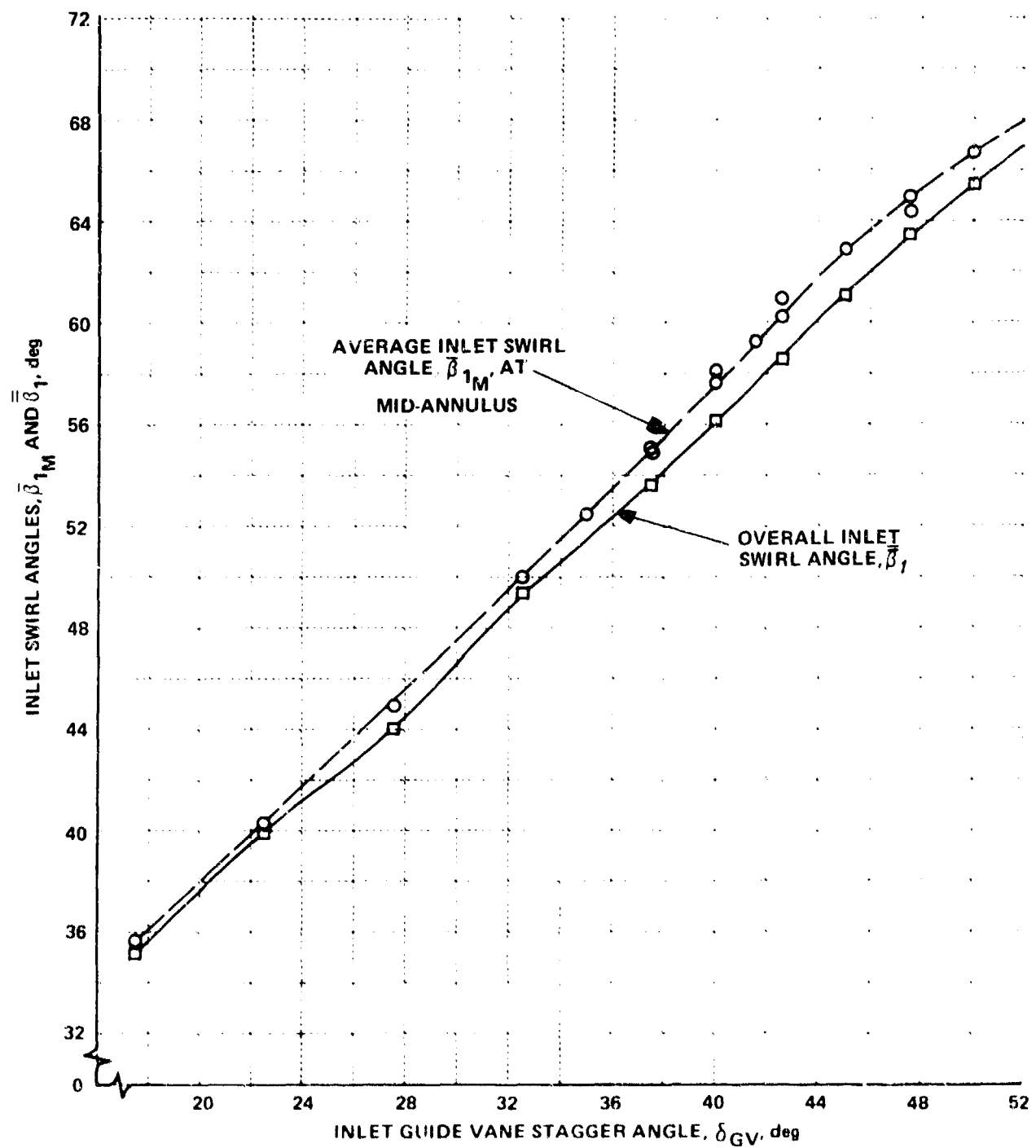


Figure 6 AVERAGE INLET SWIRL ANGLE,  $\bar{\beta}_{1M}$ , AT MID-ANNULUS AND OVERALL INLET SWIRL ANGLE,  $\bar{\beta}_1$ , AS A FUNCTION OF INLET GUIDE VANE STAGGER ANGLE

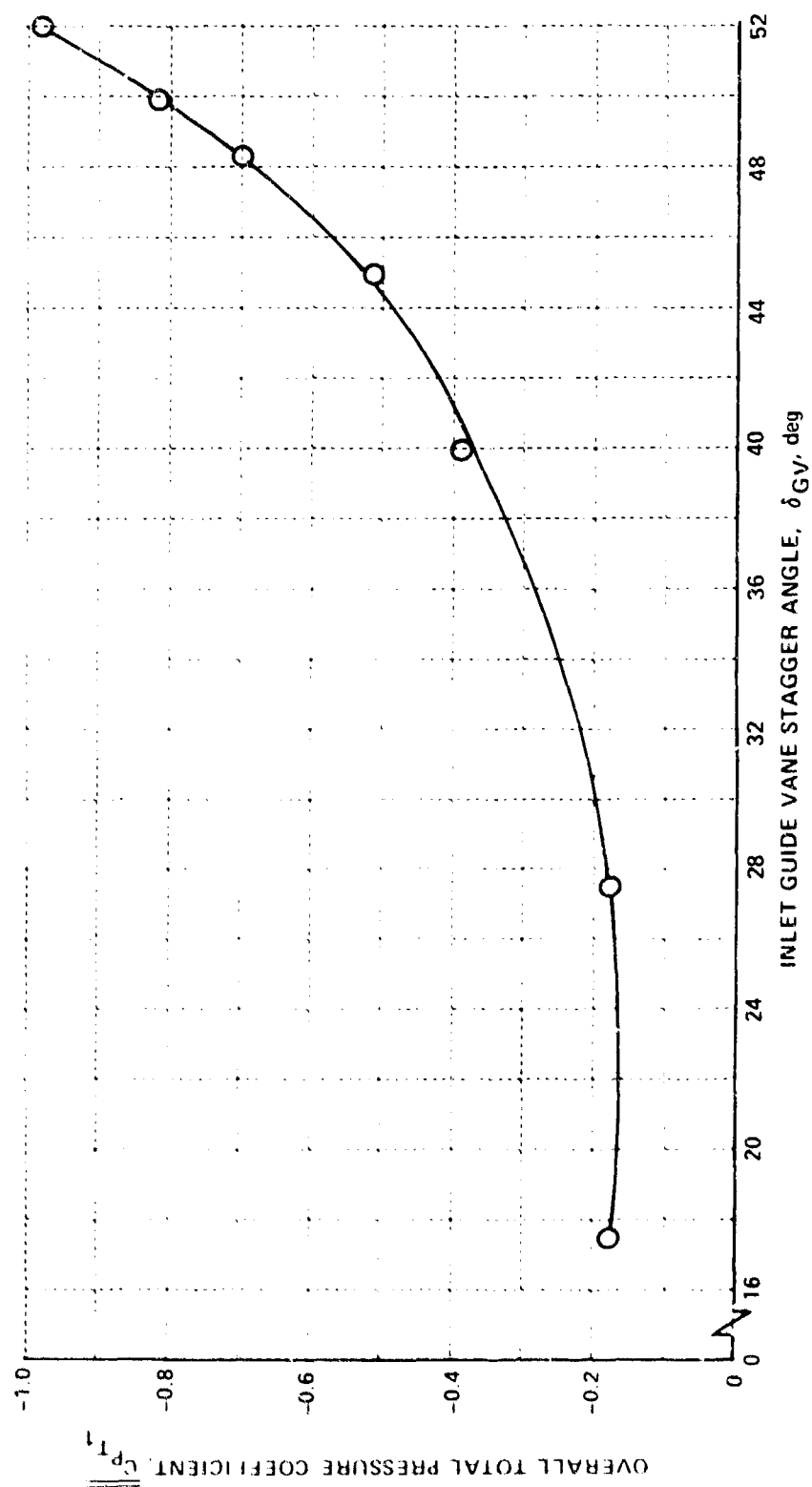


Figure 7 OVERALL TOTAL PRESSURE LOSS THROUGH INLET GUIDE VANES

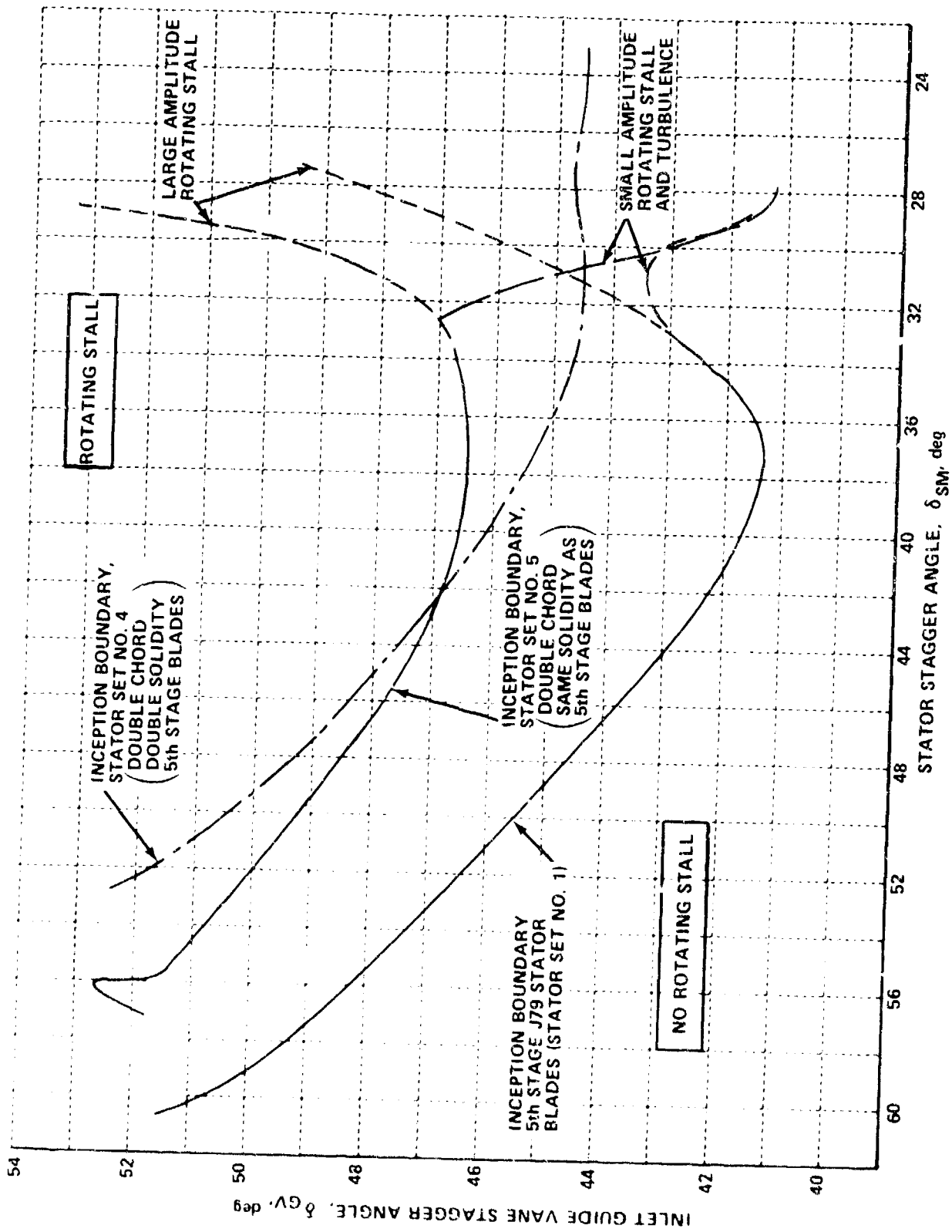


Figure 8 ROTATING STALL INCEPTION BOUNDARIES ON STATOR SETS NO. 1, 4 AND 5

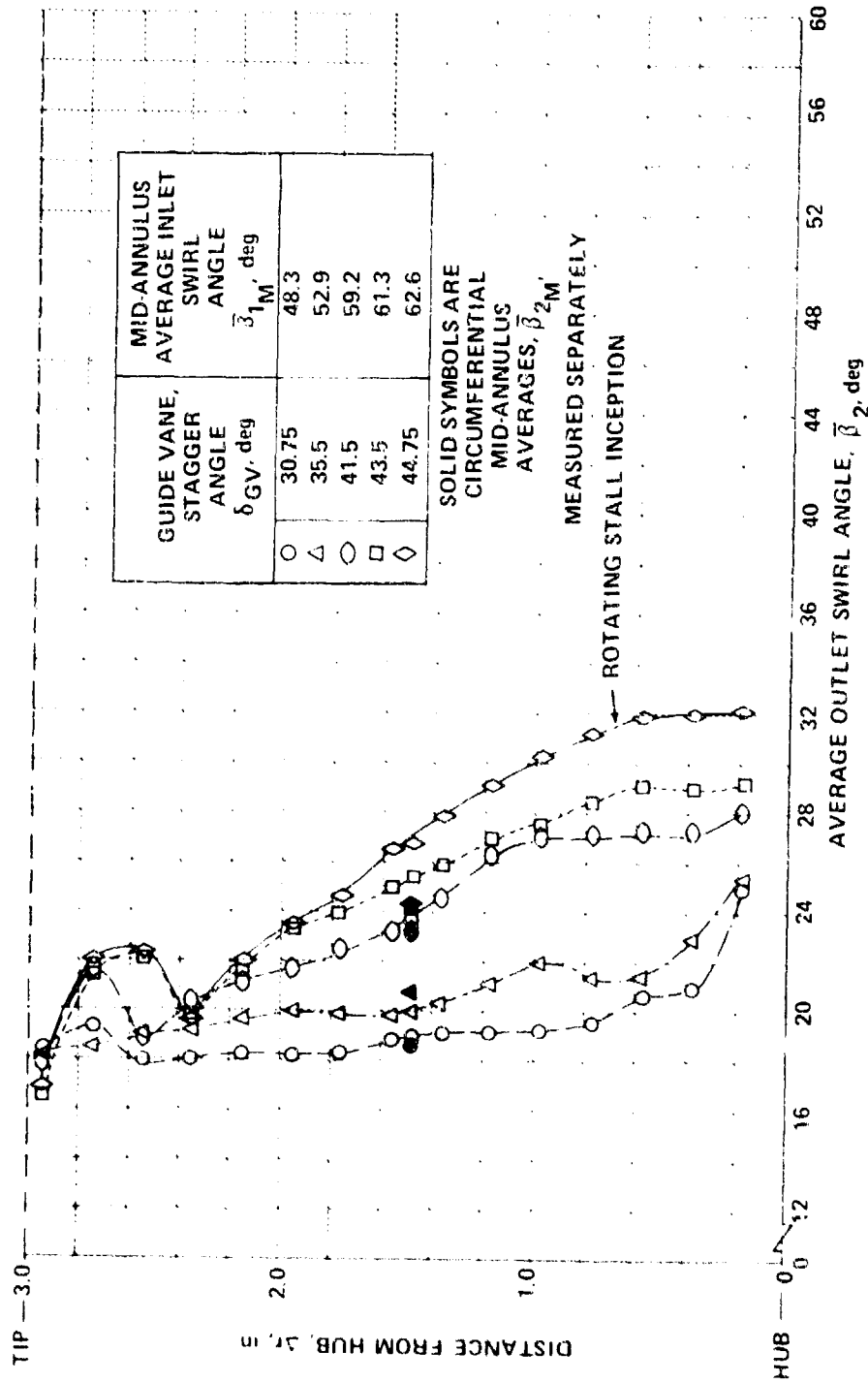


Figure 9 RADIAL DISTRIBUTIONS OF AVERAGE SWIRL ANGLE DOWNSTREAM OF STATOR SET NO. 4

(a) STATOR STAGGER ANGLE,  $\delta_{SM} = 28.2$  DEG

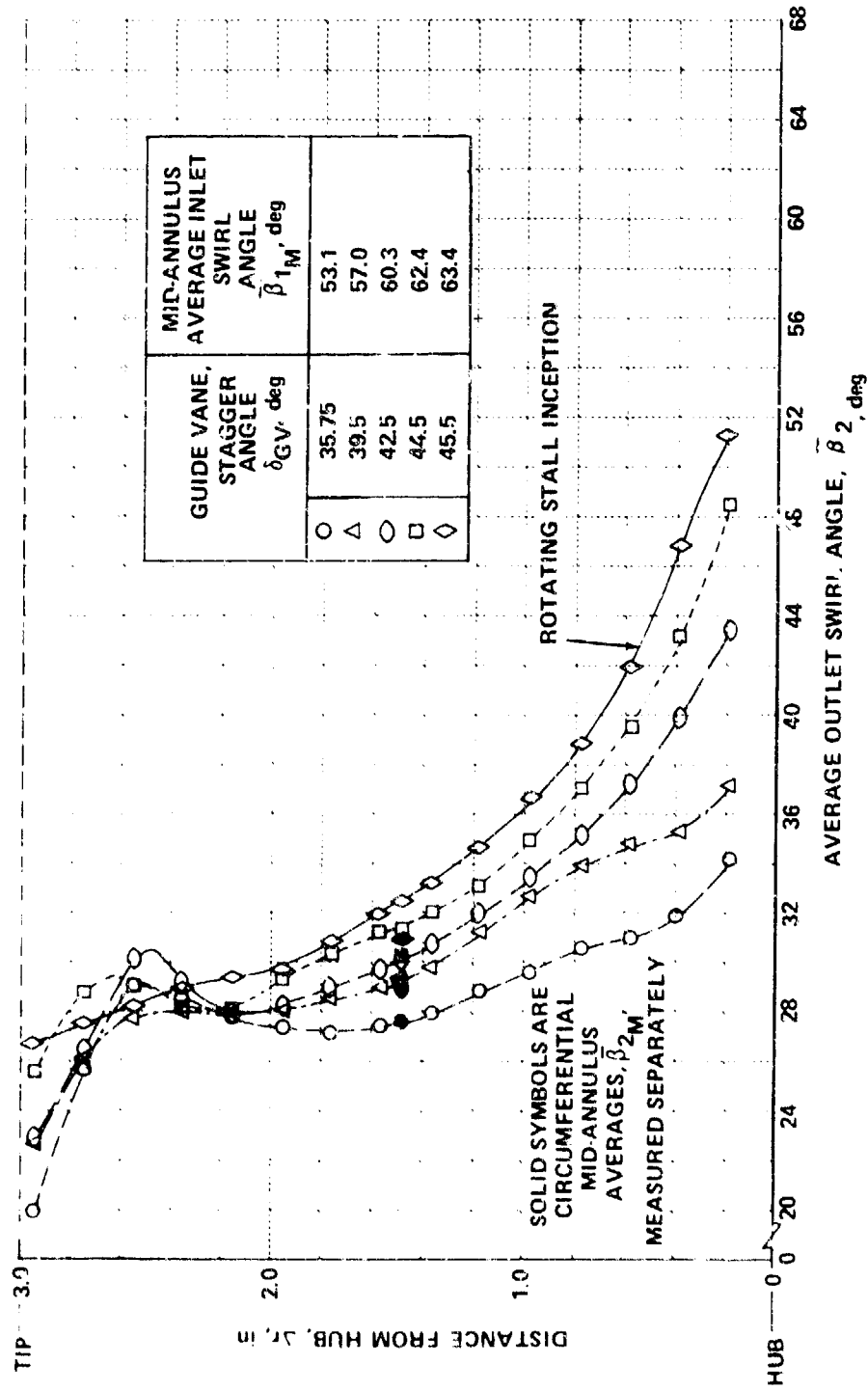


Figure 9 (Cont.) RADIAL DISTRIBUTION OF AVERAGE SWIRL ANGLE DOWNSTREAM OF STATOR SET NO. 4

(b) STATOR STAGGER ANGLE,  $\delta_{SM} = 37.2$  DEG

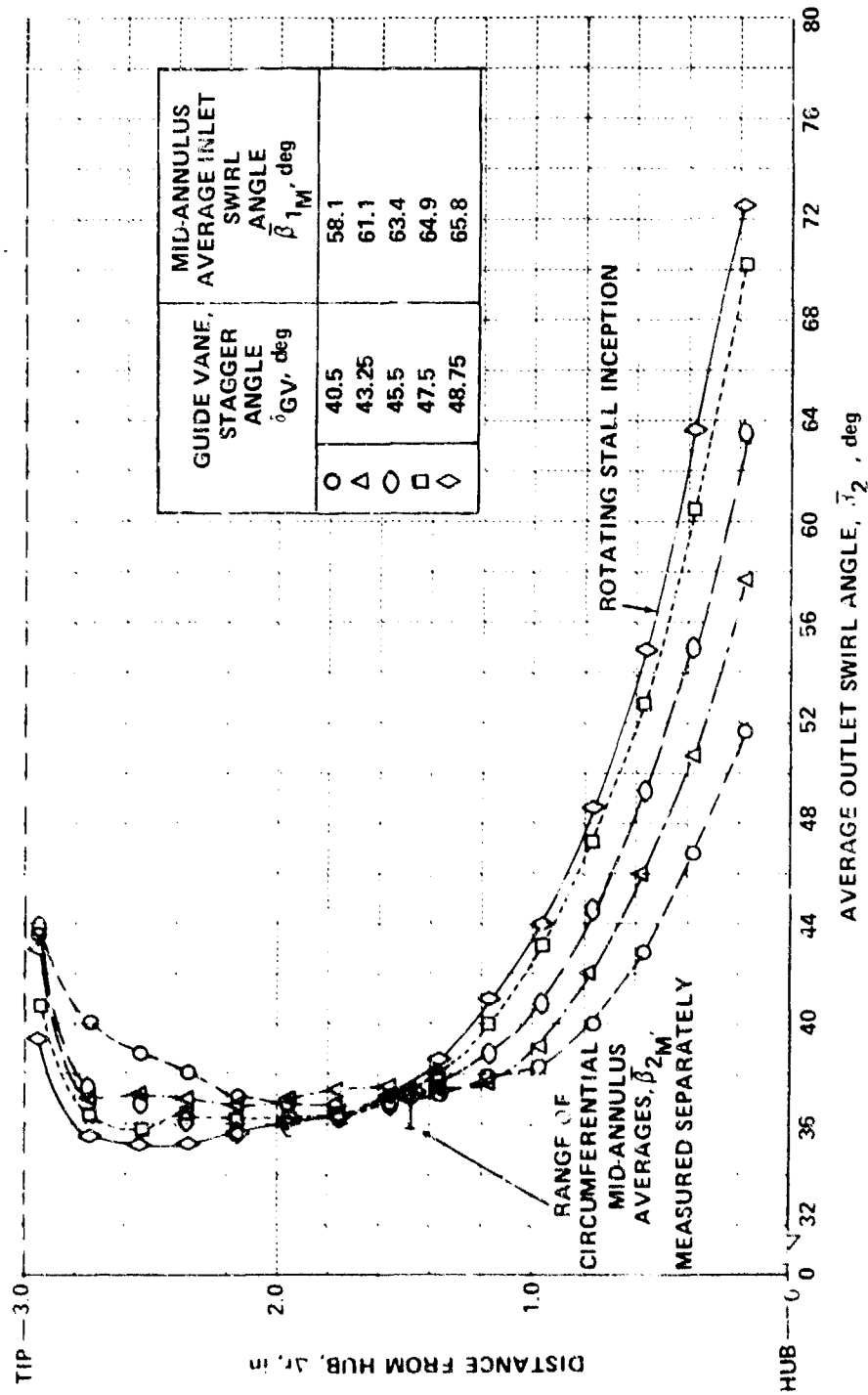


Figure 9 (Cont.) RADIAL DISTRIBUTIONS OF AVERAGE SWIRL ANGLE DOWNSTREAM OF STATOR SET NO. 4

(c) STATOR STAGGER ANGLE,  $\delta_{SM} = 47.2$  DEG

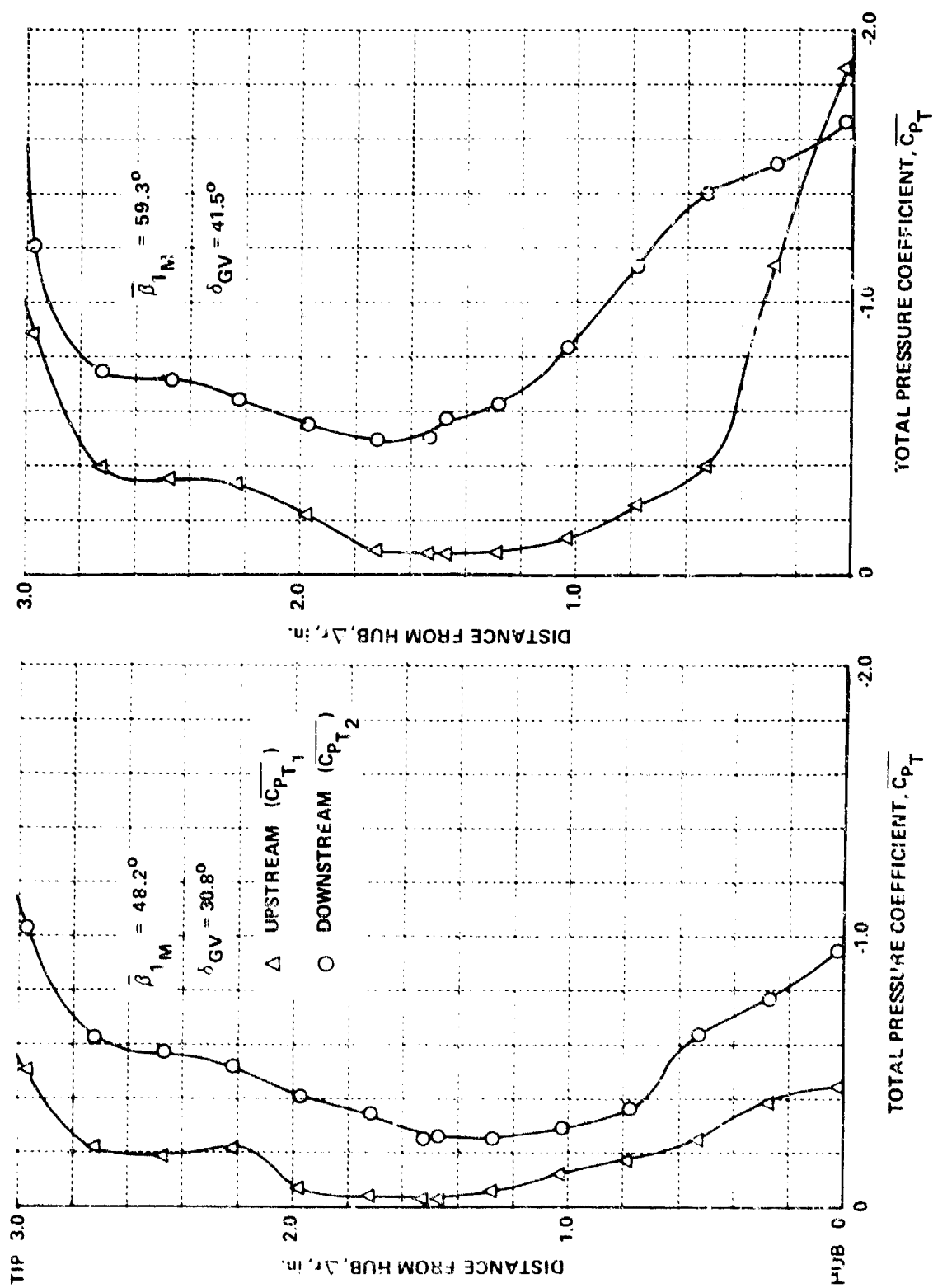


Figure 10 RADIAL DISTRIBUTION OF TOTAL PRESSURE UPSTREAM AND DOWNSTREAM OF STATOR SET NO. 4

(a) STATOR STAGGER ANGLE,  $\delta_{SM} = 28.2$  DEG (SHEET 1 OF 4)



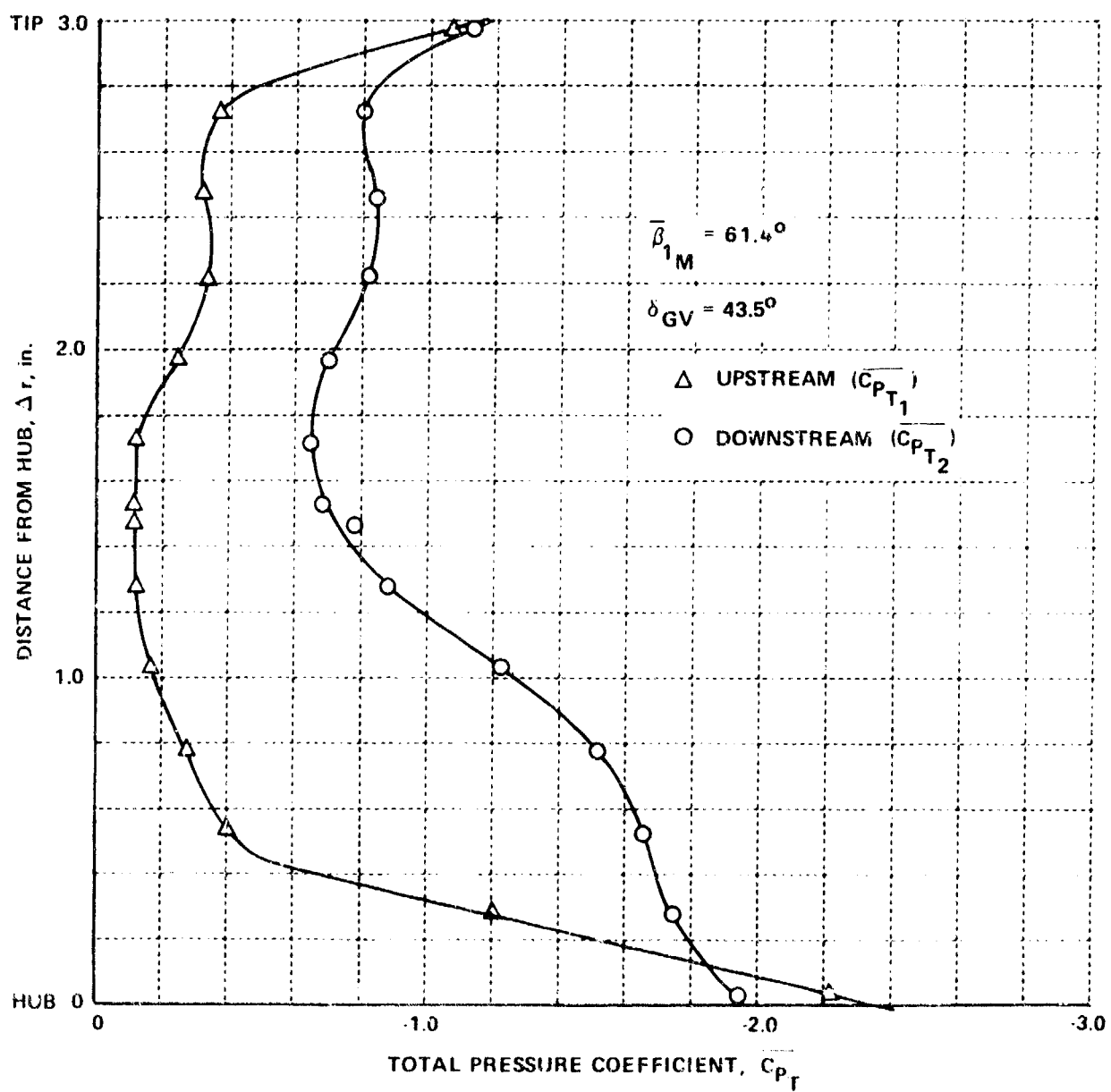


Figure 10 RADIAL DISTRIBUTION OF TOTAL PRESSURE UPSTREAM AND DOWNSTREAM OF STATOR SET NO. 4

(a) STATOR STAGGER ANGLE,  $\delta_{SM} = 28.2$  DEG (SHEET 2 OF 4)

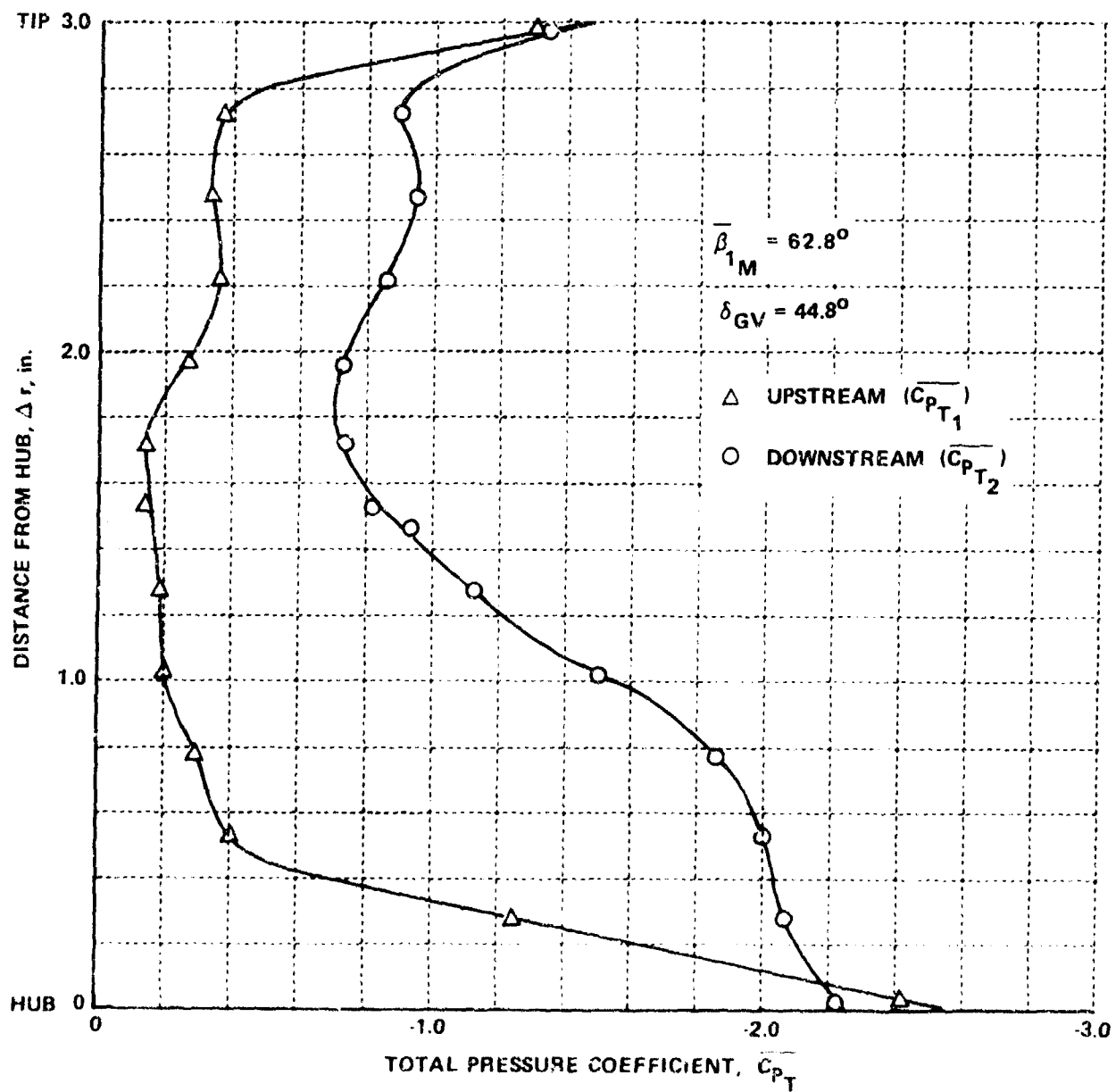


Figure 10 RADIAL DISTRIBUTION OF TOTAL PRESSURE UPSTREAM AND DOWNSTREAM OF STATOR SET NO. 4

(a) STATOR STAGGER ANGLE,  $\delta_{SM} = 28.2$  DEG (SHEET 3 OF 4)

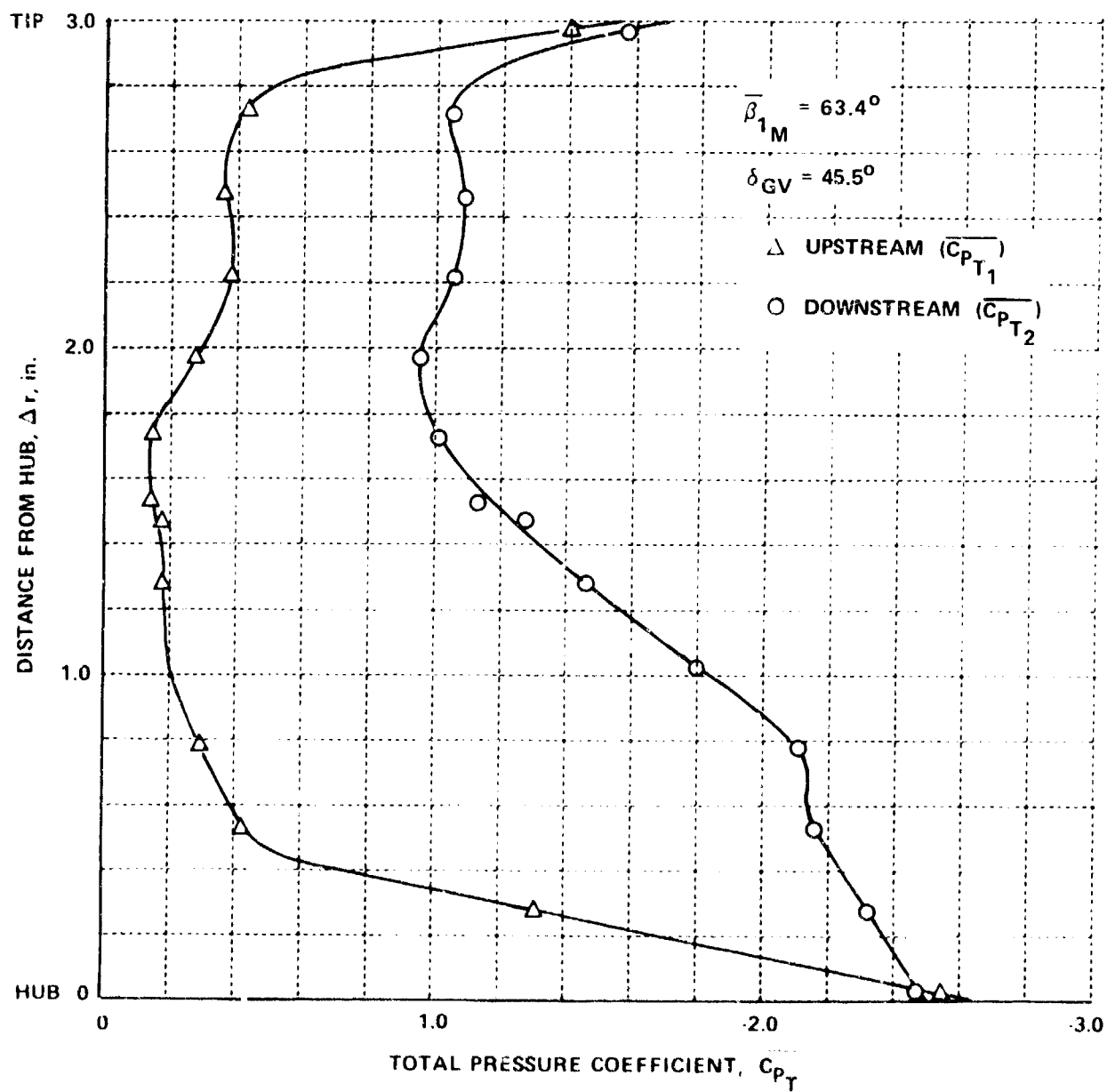
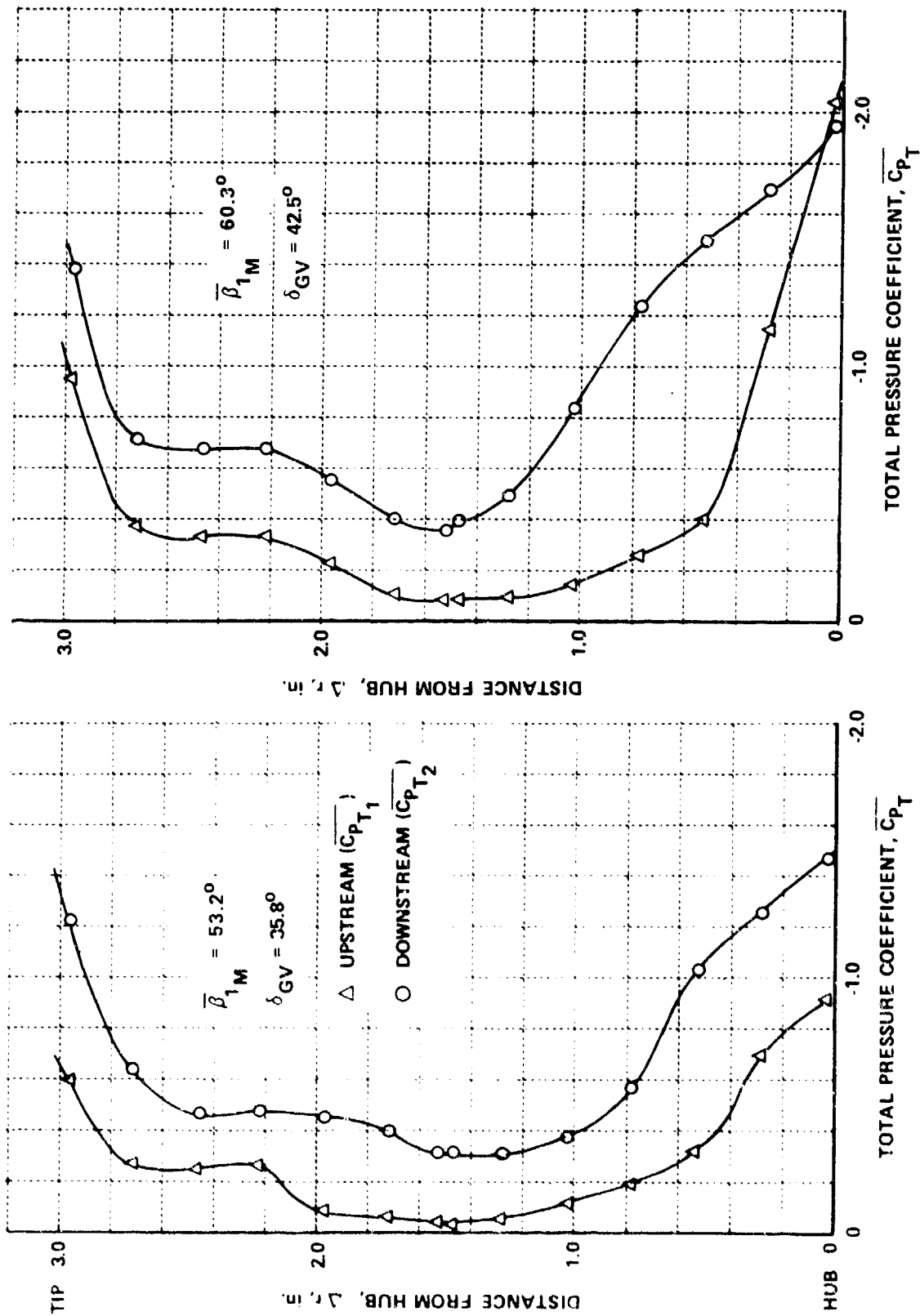


Figure 10 RADIAL DISTRIBUTION OF TOTAL PRESSURE UPSTREAM AND DOWNSTREAM OF STATOR SET NO. 4

(a) STATOR STAGGER ANGLE,  $\delta_{SM} = 28.2$  DEG (SHEET 4 OF 4)



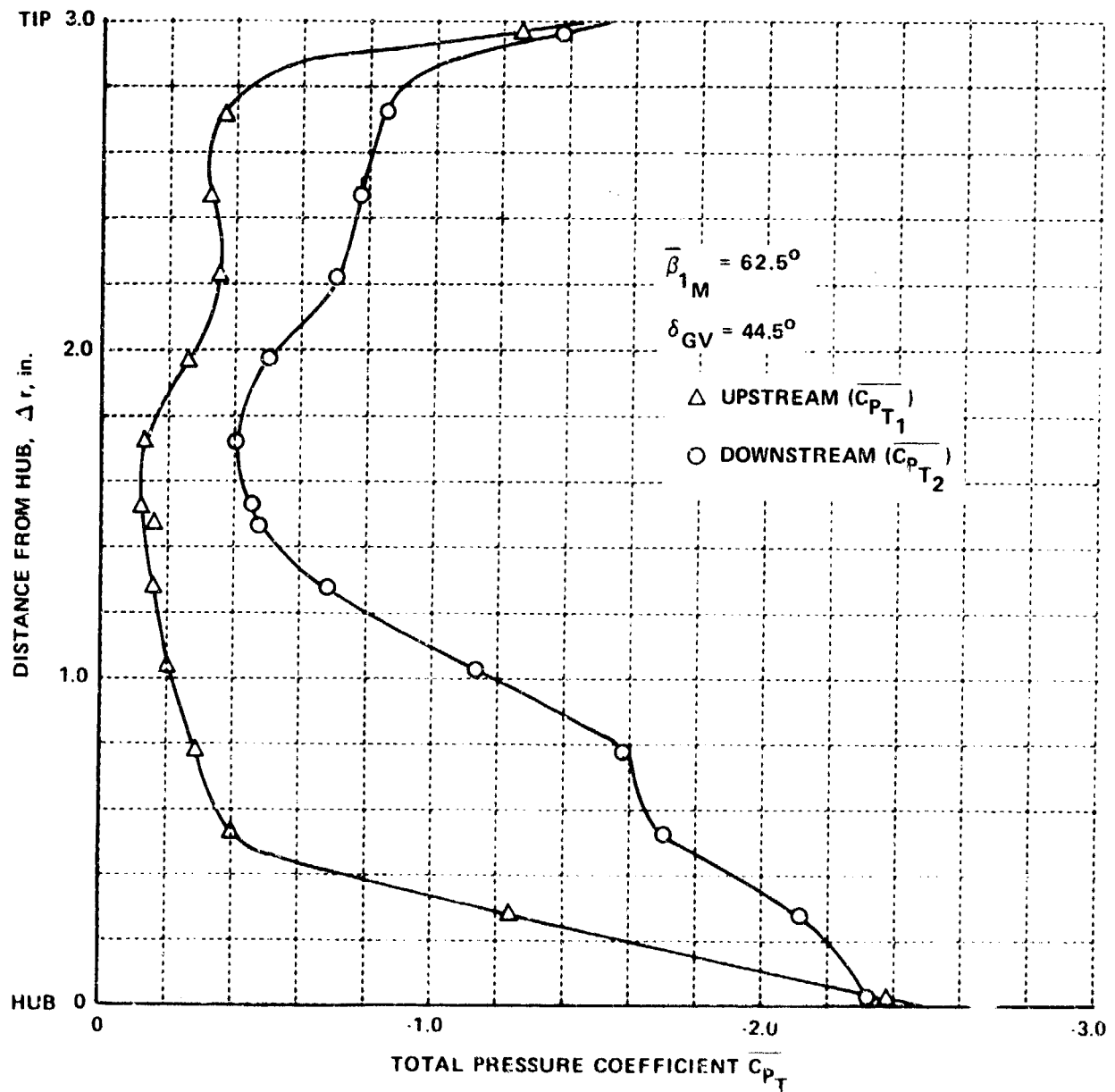


Figure 10 (Cont.) RADIAL DISTRIBUTION OF TOTAL PRESSURE UPSTREAM AND DOWNSTREAM OF STATOR SET NO. 4

(b) STATOR STAGGER ANGLE,  $\delta_{SM} = 37.2$  DEG (SHEET 2 OF 4)

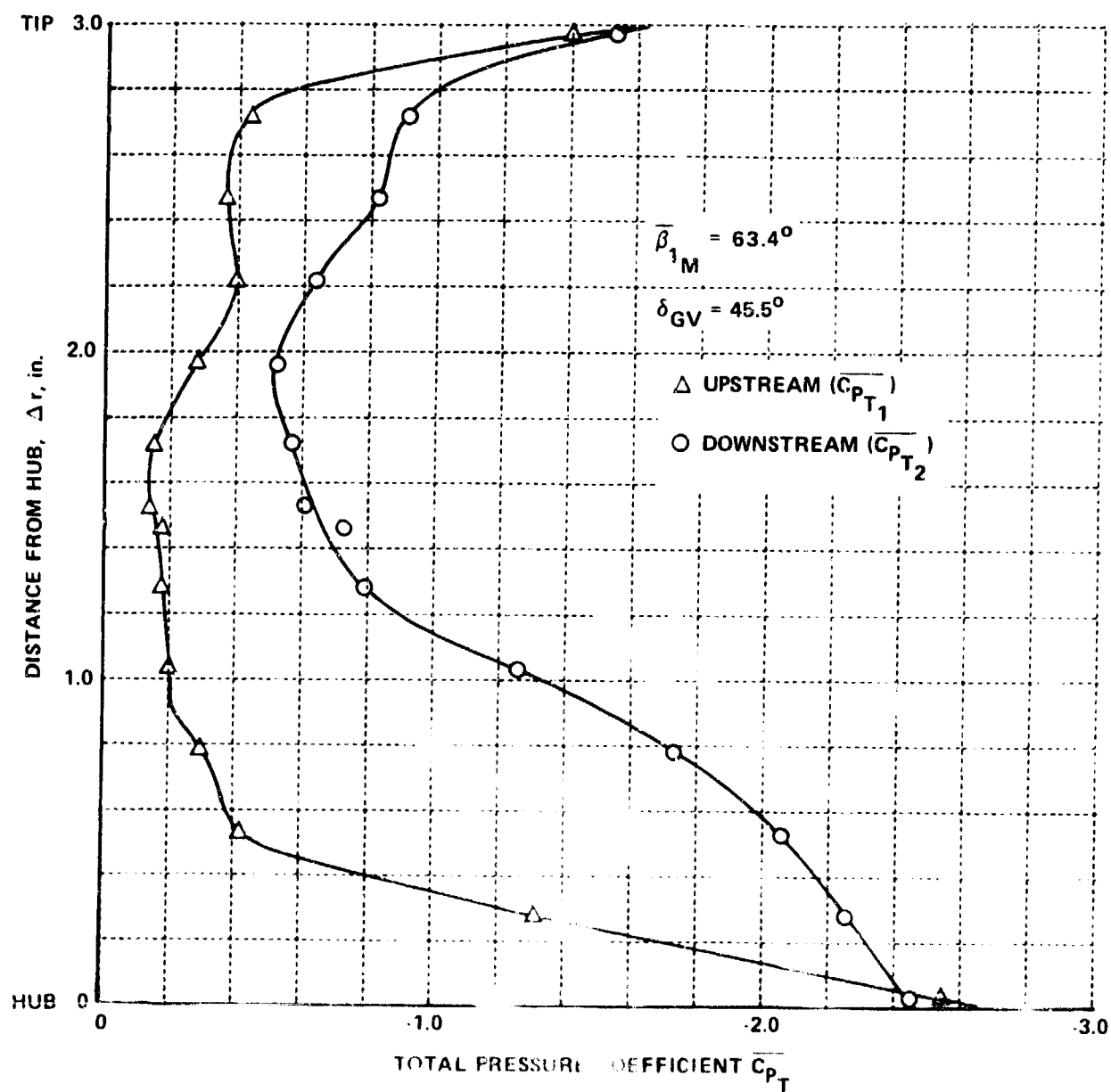


Figure 10 (Cont.) RADIAL DISTRIBUTION OF TOTAL PRESSURE UPSTREAM AND DOWNSTREAM OF STATOR SET NO. 1

(b) STATOR STAGGER ANGLE,  $\delta_{SM} = 37.2$  DEG (SHEET 3 OF 4)

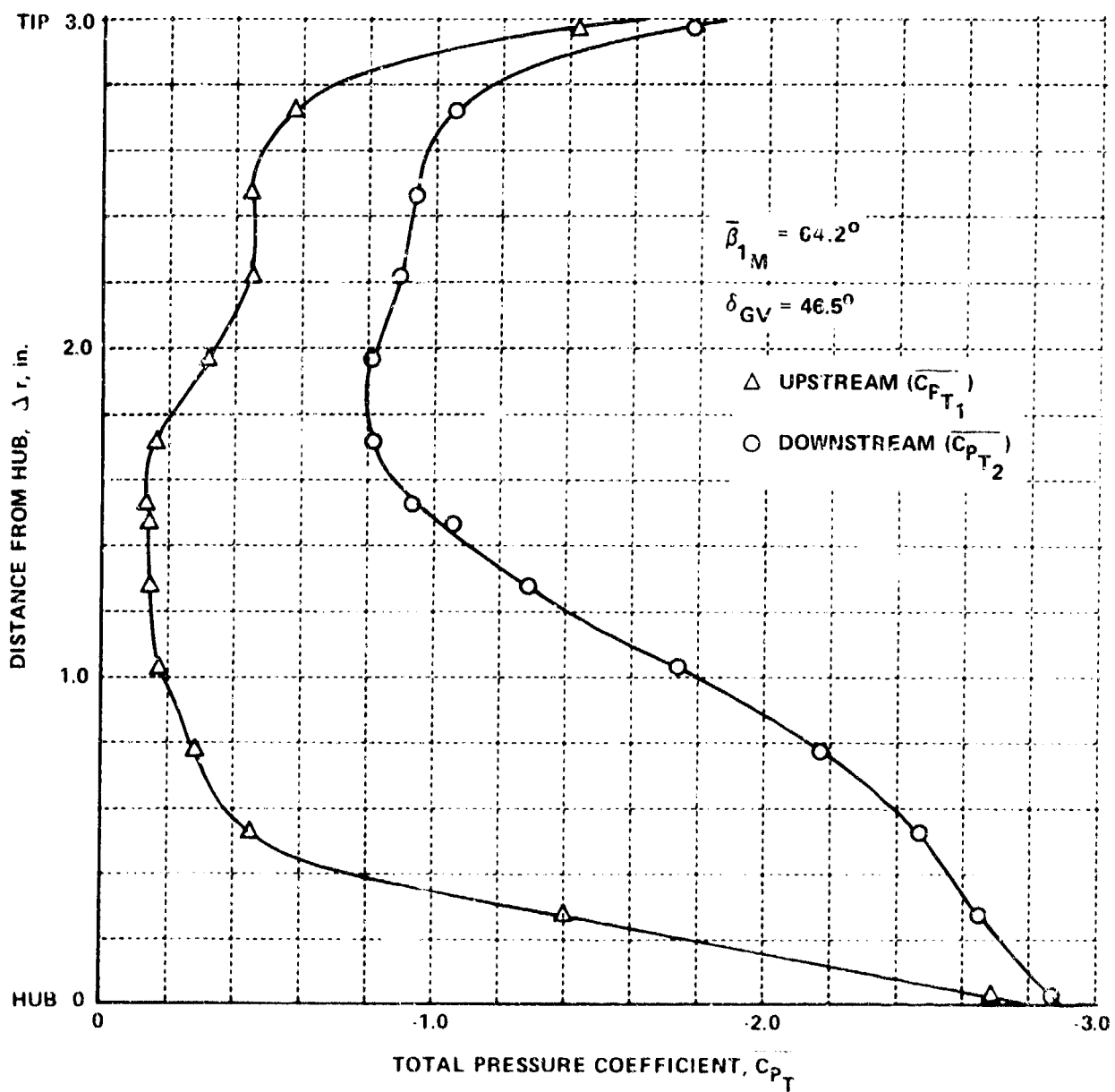


Figure 10 (Cont.) RADIAL DISTRIBUTION OF TOTAL PRESSURE UPSTREAM AND DOWNSTREAM OF STATOR SET NO. 4

(b) STATOR STAGGER ANGLE,  $\delta_{SM} = 37.2$  DEG (SHEET 4 OF 4)

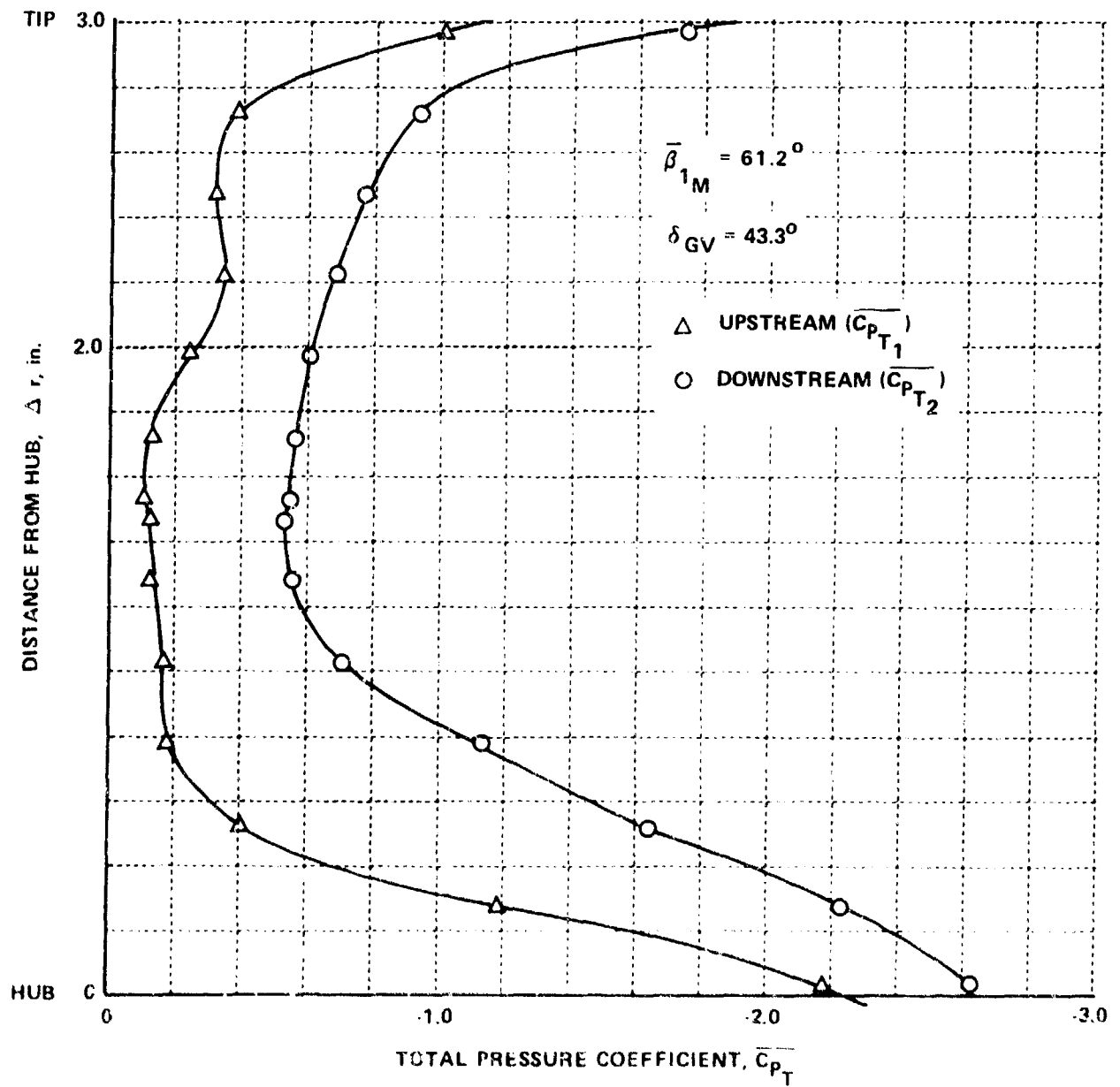


Figure 10 (Cont.) RADIAL DISTRIBUTION OF TOTAL PRESSURE UPSTREAM AND DOWNSTREAM OF STATOR SET NO. 4

(c) STATOR STAGGER ANGLE,  $\delta_{SM} = 47.2$  DEG (SHEET 1 OF 5)



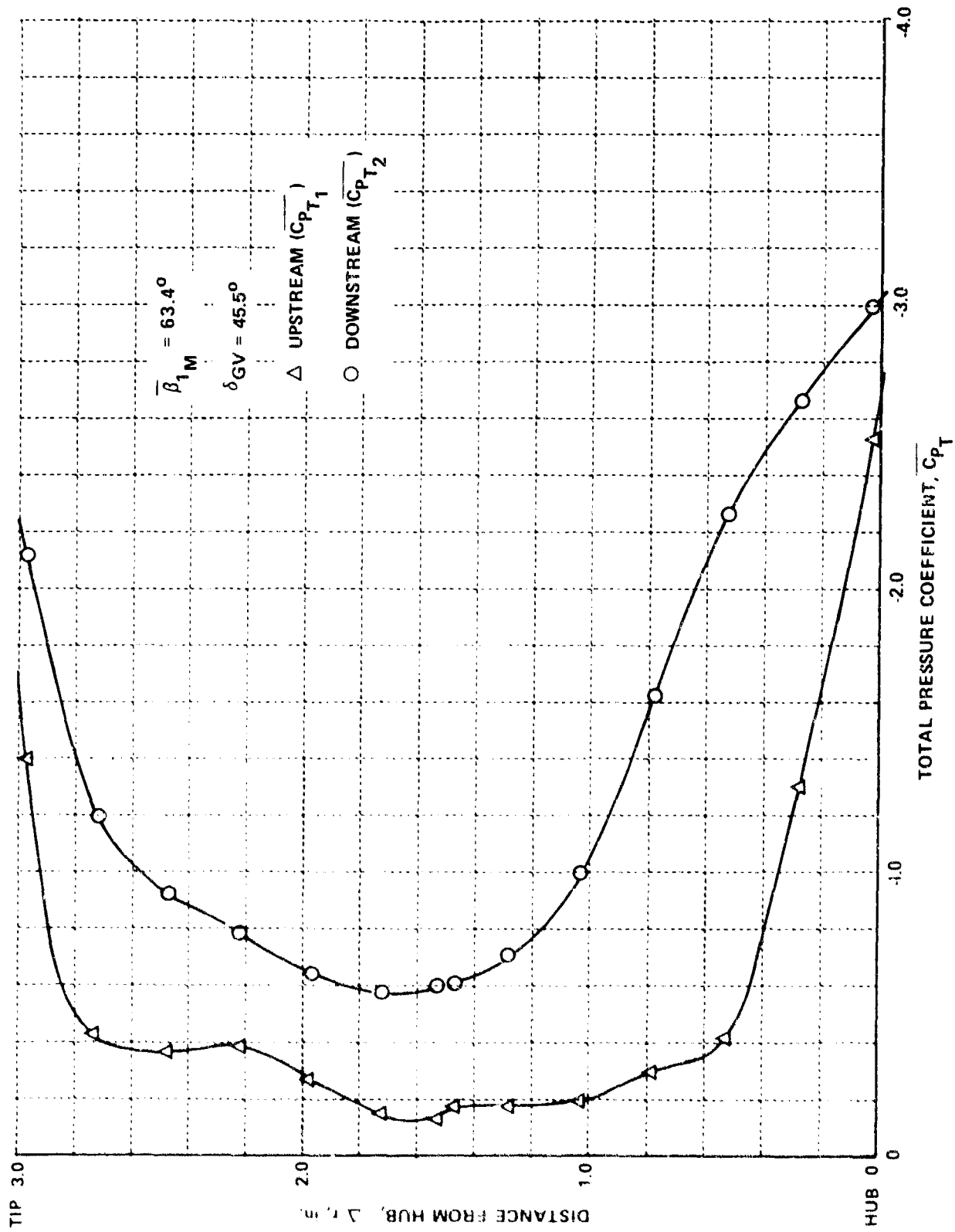


Figure 10 (Cont.) RADIAL DISTRIBUTION OF TOTAL PRESSURE UPSTREAM AND DOWNSTREAM OF STATOR SET NO. 4

(c) STATOR STAGGER ANGLE,  $\delta_{SM} = 47.2$  DEG (SHEET 2 OF 5)

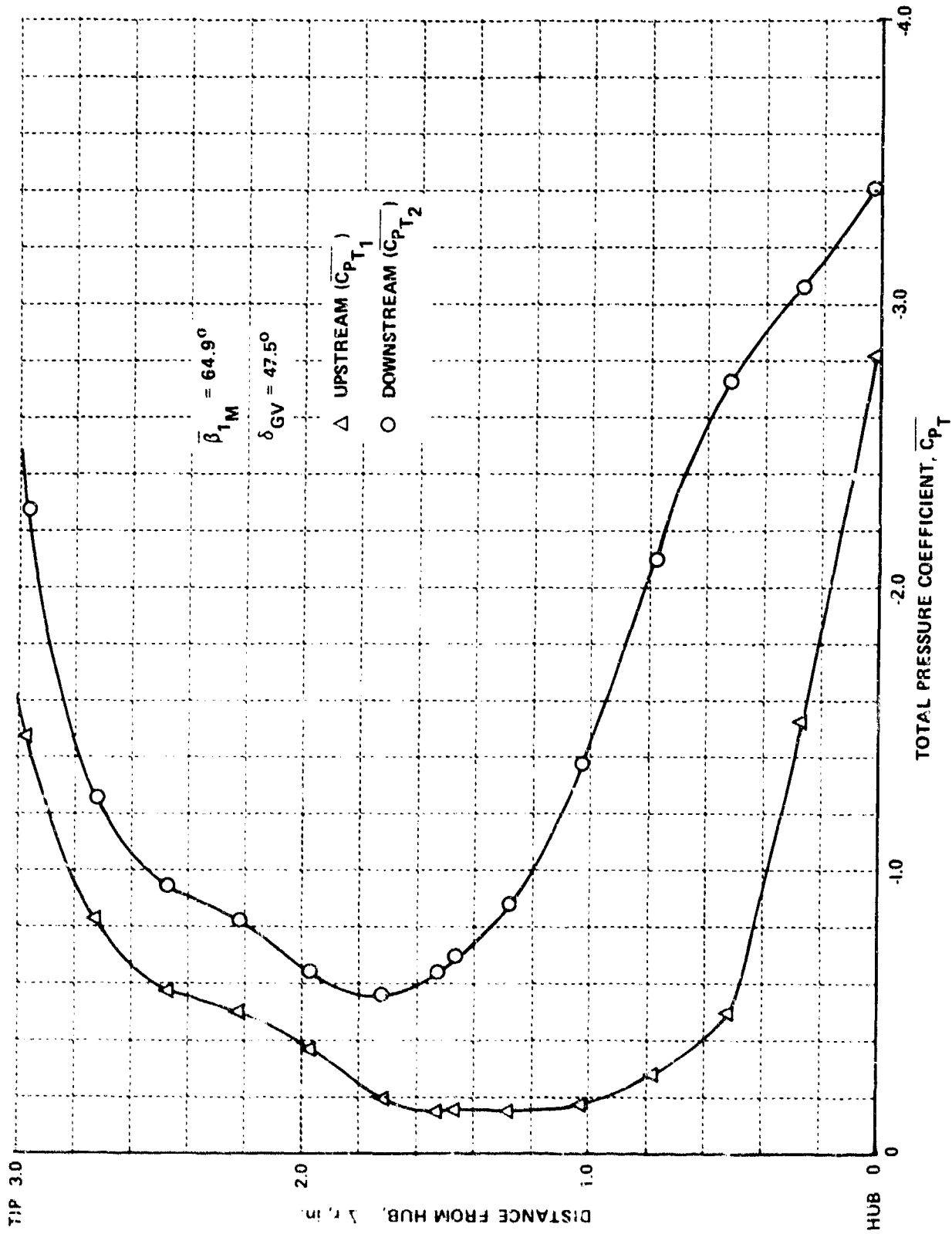


Figure 10 (Cont.) RADIAL DISTRIBUTION OF TOTAL PRESSURE UPSTREAM AND DOWNSTREAM OF STATOR SET NO. 4

(c) STATOR STAGGER ANGLE,  $\delta_{SM} = 47.2$  DEG (SHEET 3 OF 5)

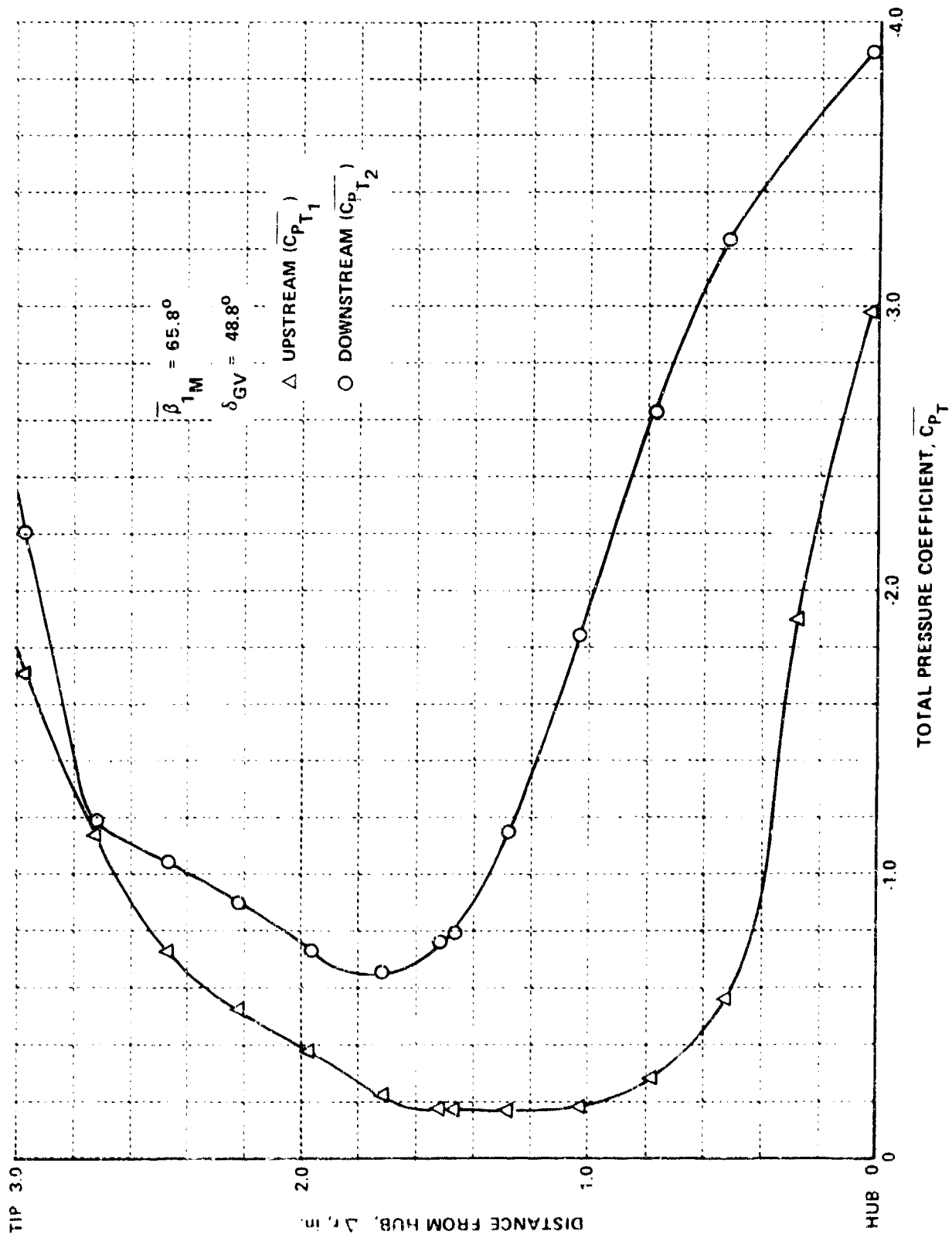


Figure 10 (Cont.) RADIAL DISTRIBUTION OF TOTAL PRESSURE UPSTREAM AND DOWNSTREAM OF STATOR SET NO. 4

(c) STATOR STAGGER ANGLE,  $\delta_{SM} = 47.2$  DEG (SHEET 4 OF 5)

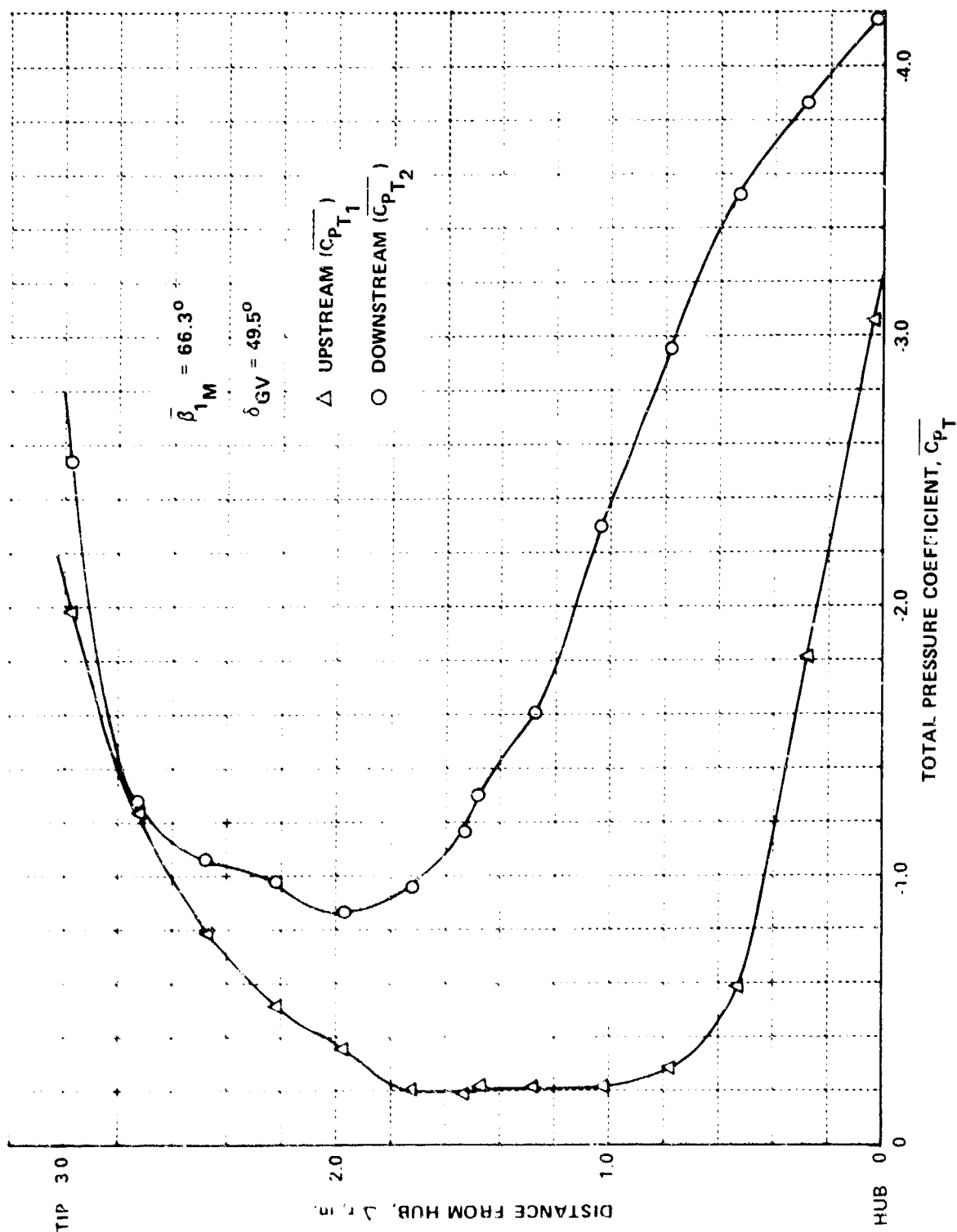


Figure 10 (Cont.) RADIAL DISTRIBUTION OF TOTAL PRESSURE UPSTREAM AND DOWNSTREAM OF STATOR SET NO. 4

(c) STATOR STAGGER ANGLE,  $\delta_{SM} = 47.2$  DEG (SHEET 5 OF 5)

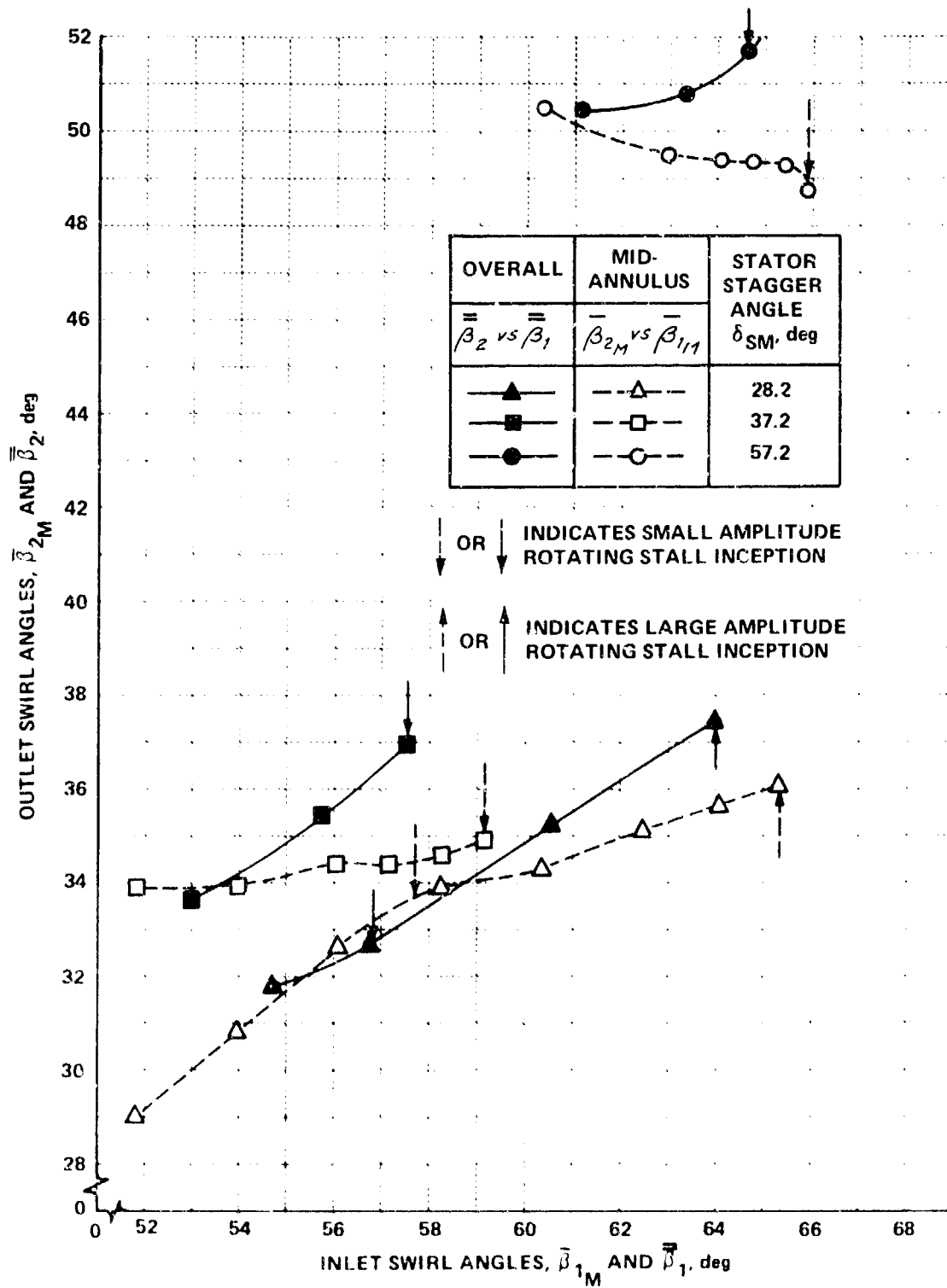


Figure 11 OVERALL AND MID-ANNULUS FLOW TURNING PERFORMANCE OF STATOR SET NO. 1

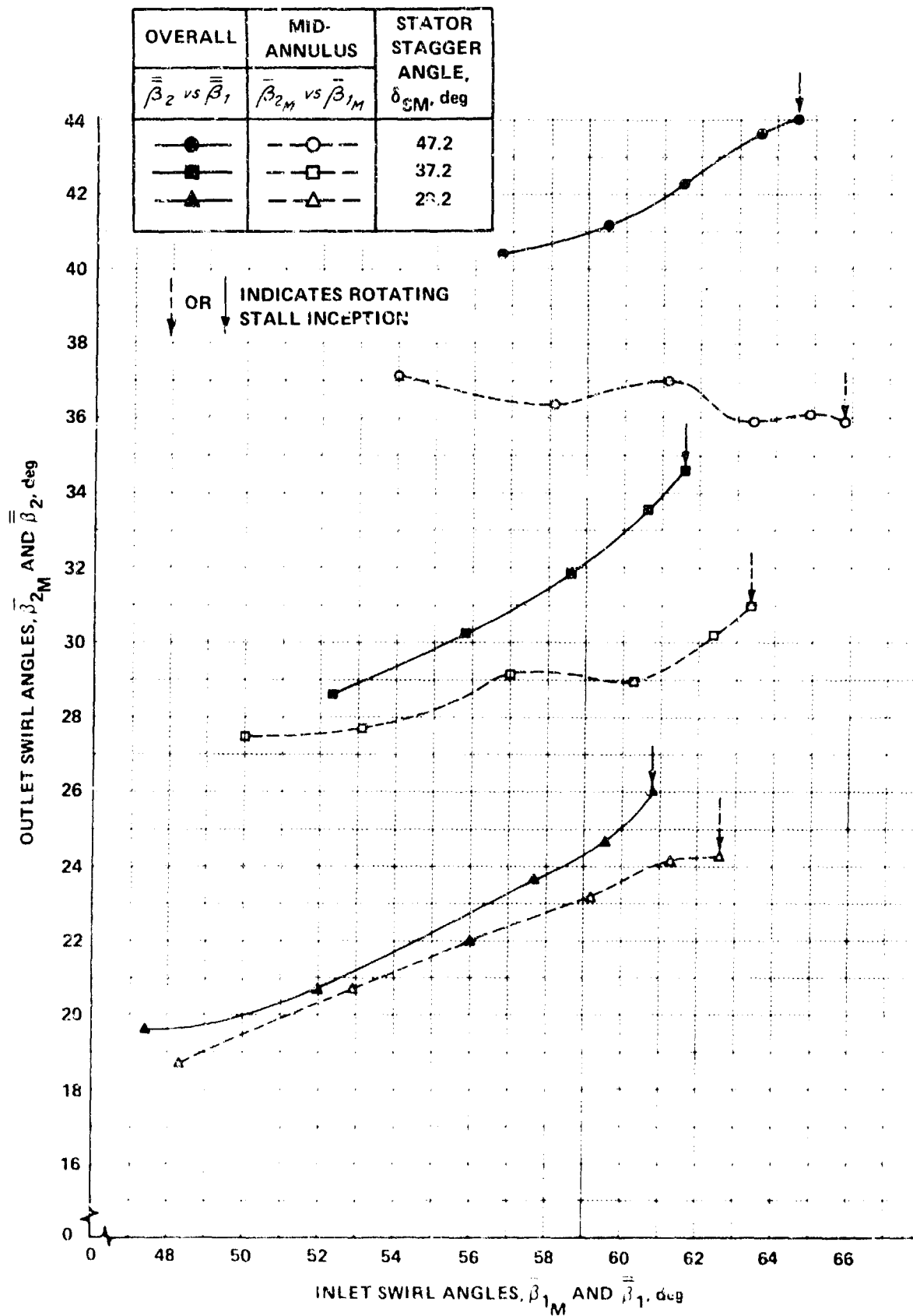


Figure 12 OVERALL AND MID-ANNULUS TURNING PERFORMANCE OF STATOR SET NO. 4.

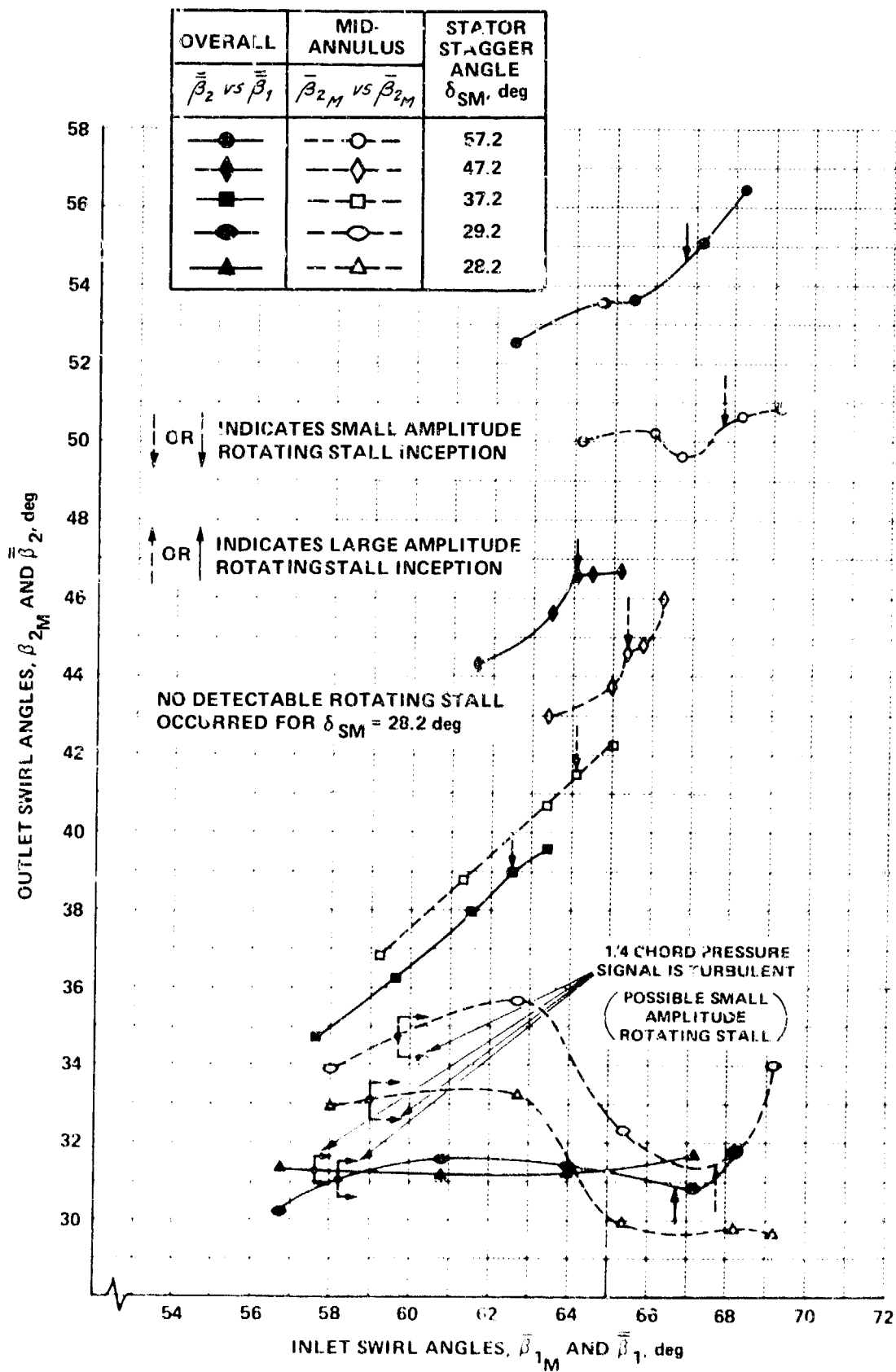


Figure 13 OVERALL AND MID-ANNULUS TURNING PERFORMANCE OF STATOR SET NO. 5

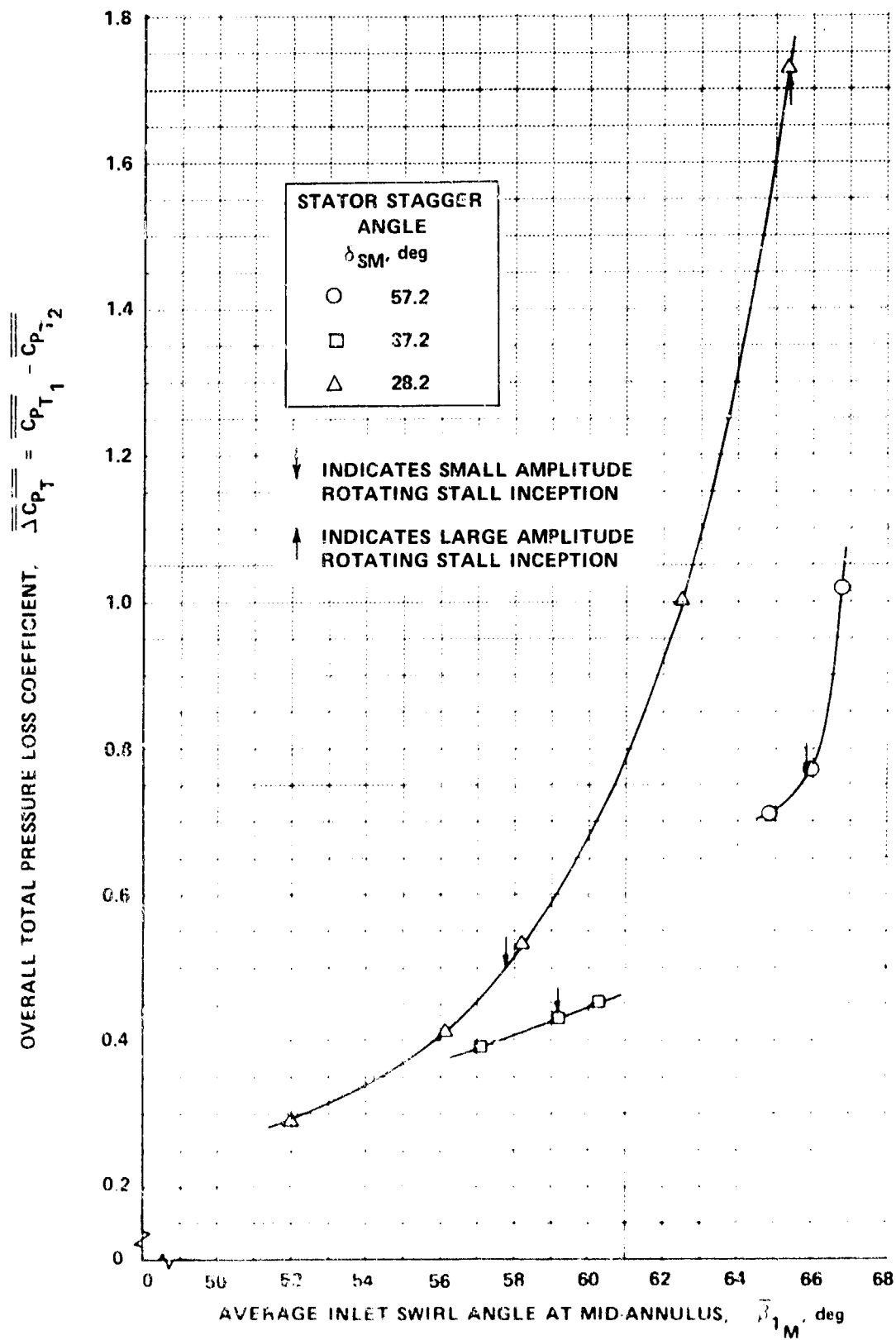


Figure 14 OVERALL TOTAL PRESSURE LOSS THROUGH STATOR SET NO. 1



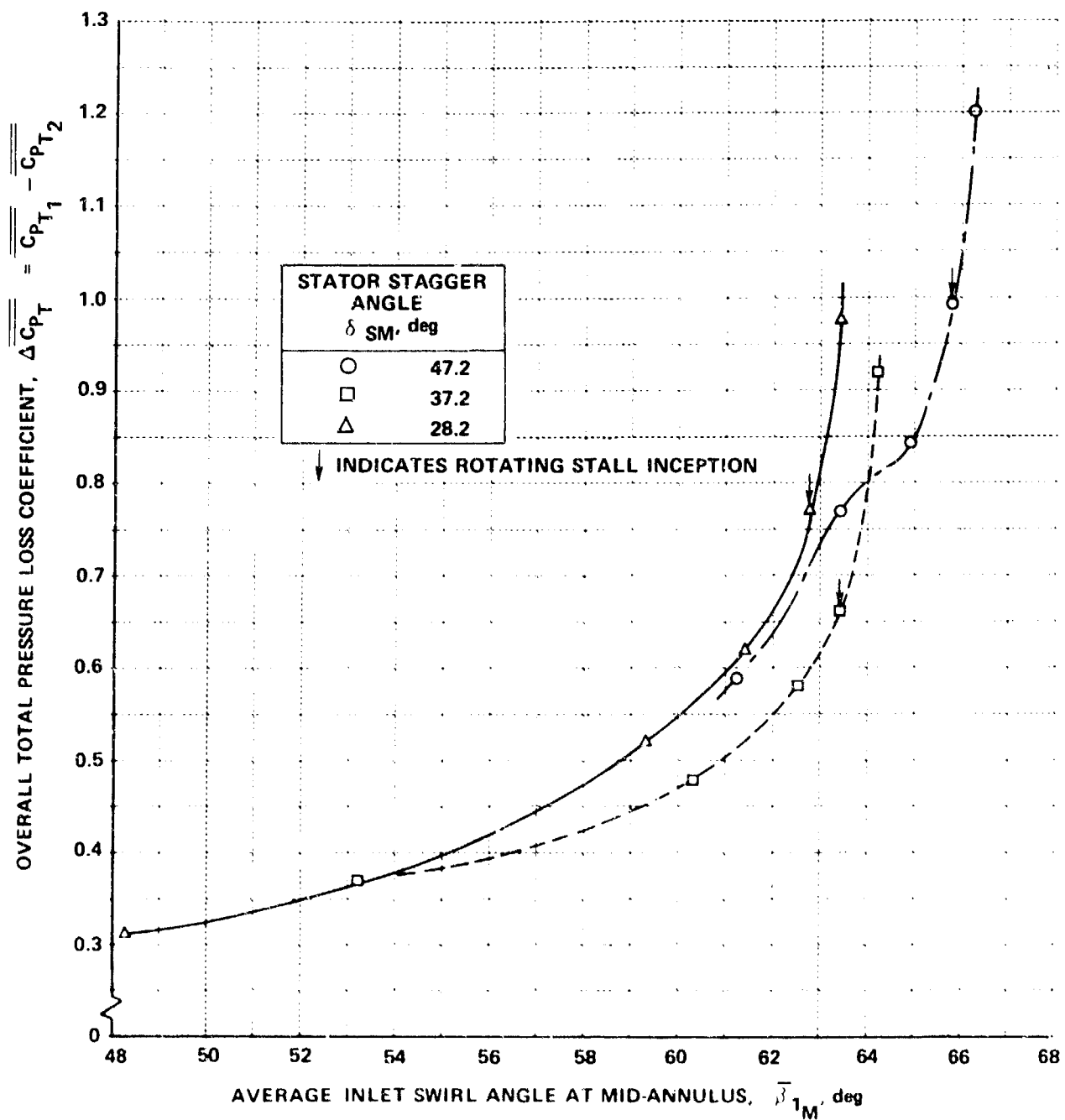


Figure 15 OVERALL TOTAL PRESSURE LOSS THROUGH STATOR SET NO. 4

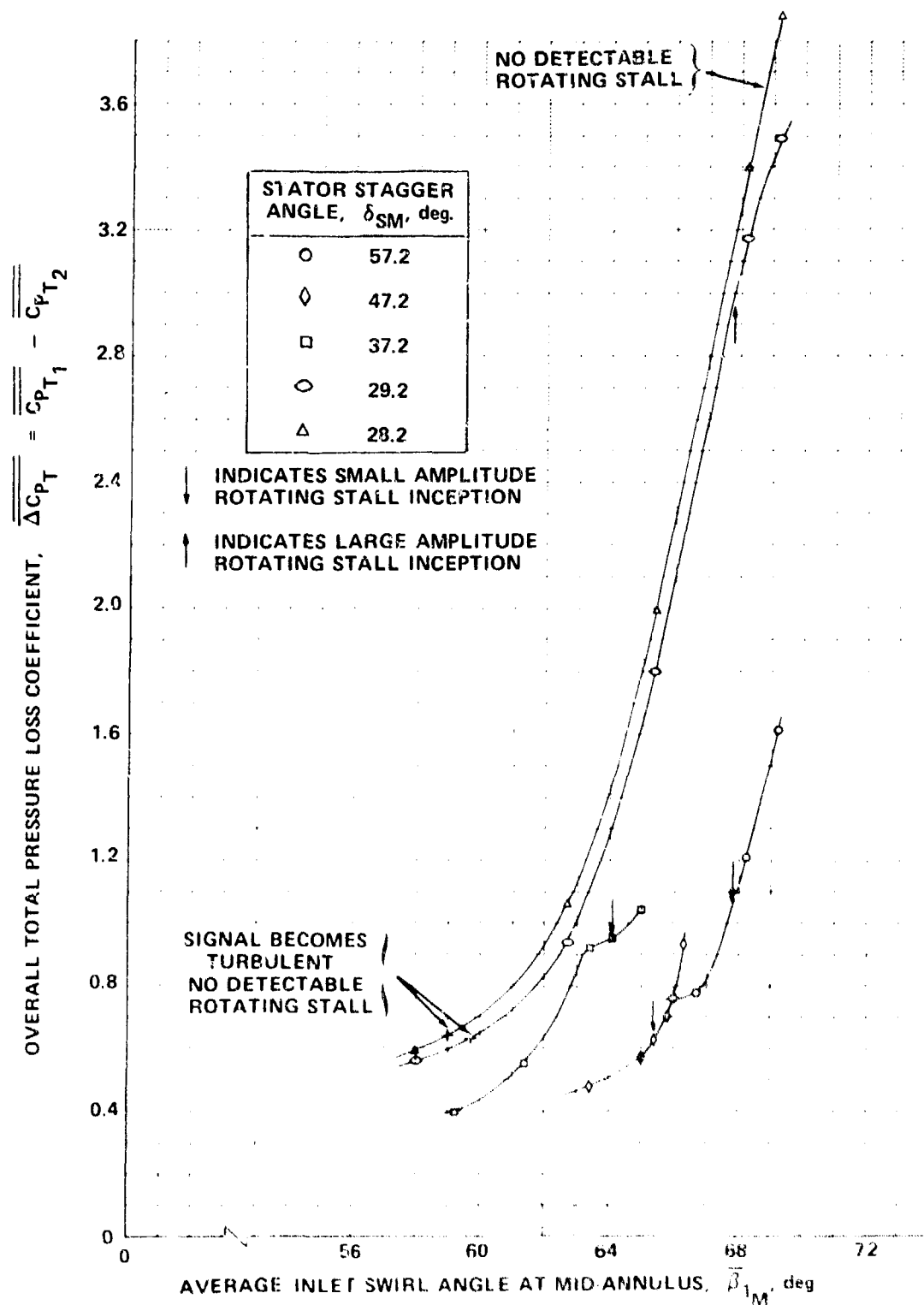
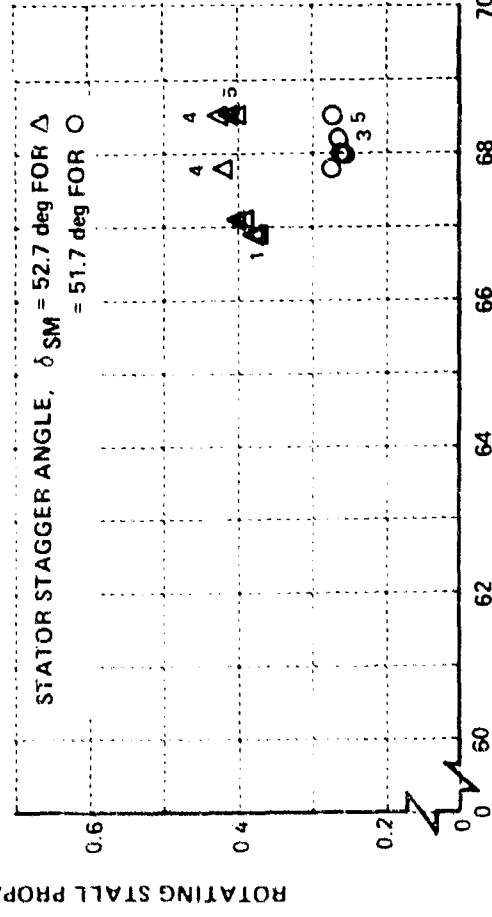
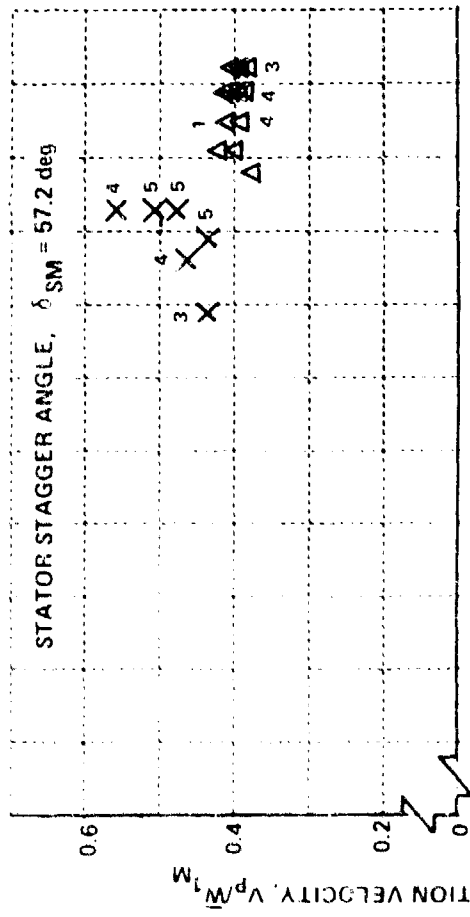


Figure 16 OVERALL TOTAL PRESSURE LOSS THROUGH STATOR SET NO. 5



STATOR SET NO.	STATOR SET NO.
X	1
O	4
$\Delta$	5

NUMBERS NEAR  
 DATA POINTS  
 INDICATE NUMBER  
 OF CELLS

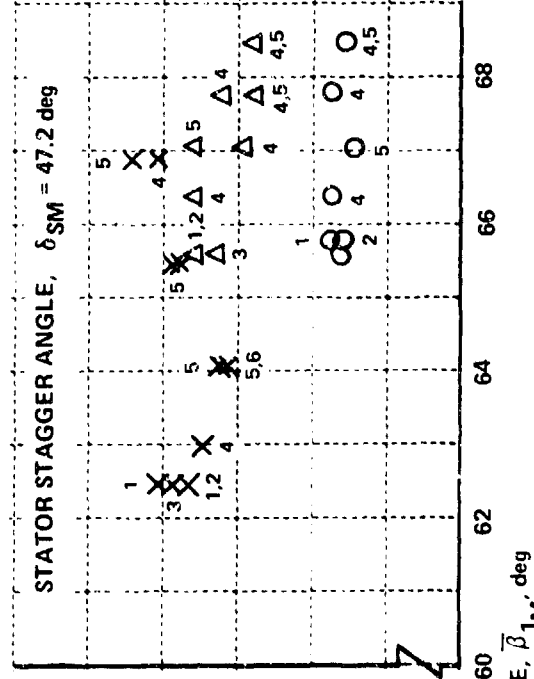


Figure 17 ROTATING STALL PROPAGATION VELOCITY AND NUMBER OF CELLS  
 ON STATOR SETS NO. 1, 4, AND 5 (SHEET 1 OF 2)

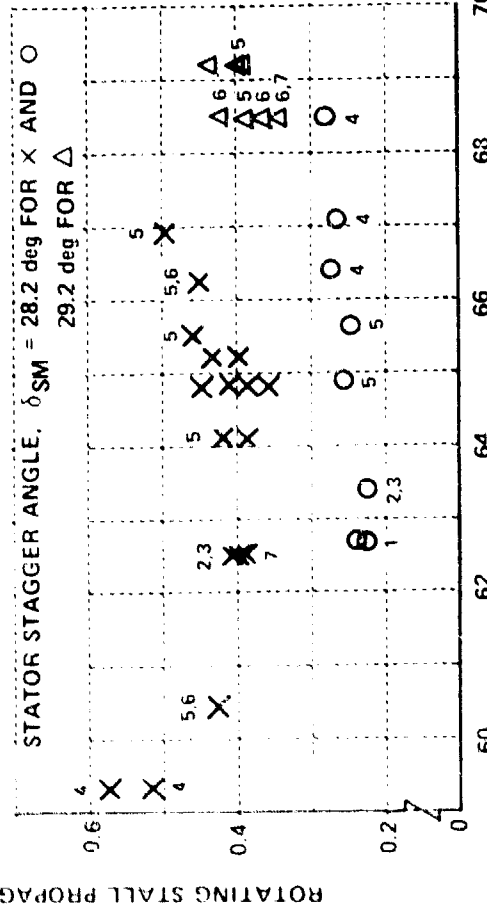
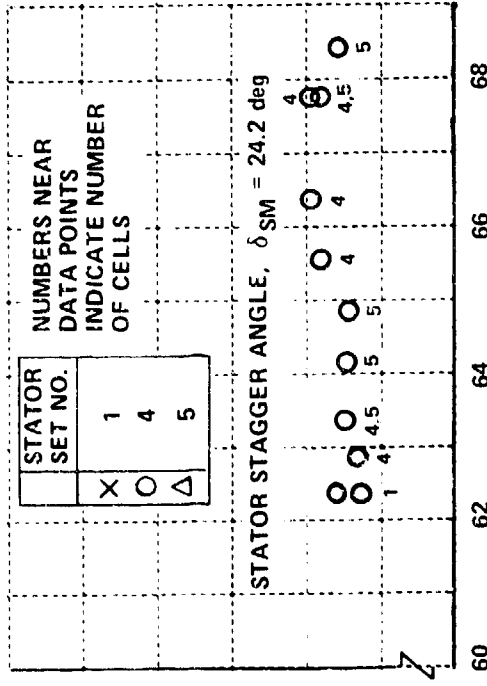
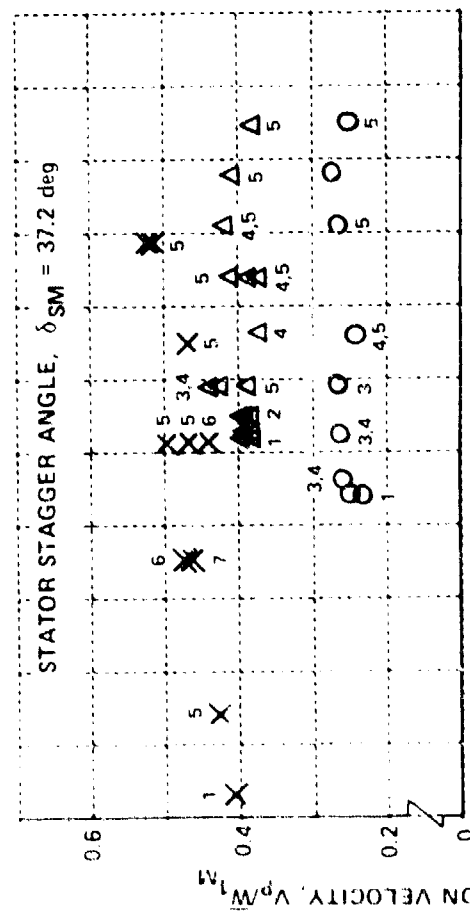
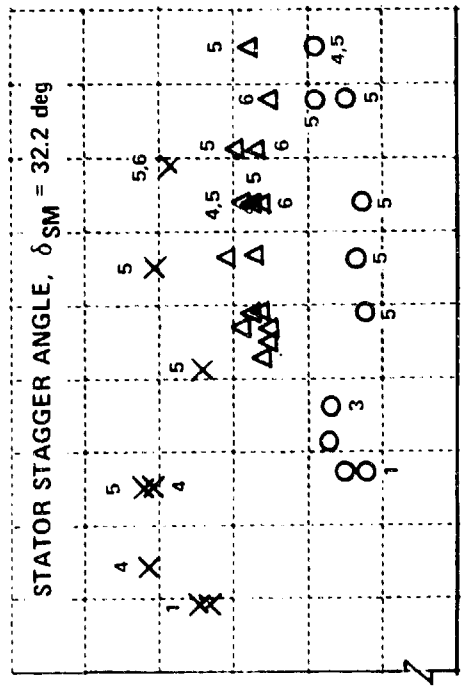


Figure 17 ROTATING STALL PROPAGATION VELOCITY AND NUMBER OF CELLS ON STATOR SETS NO. 1, 4, AND 5 (SHEET 2 OF 2)

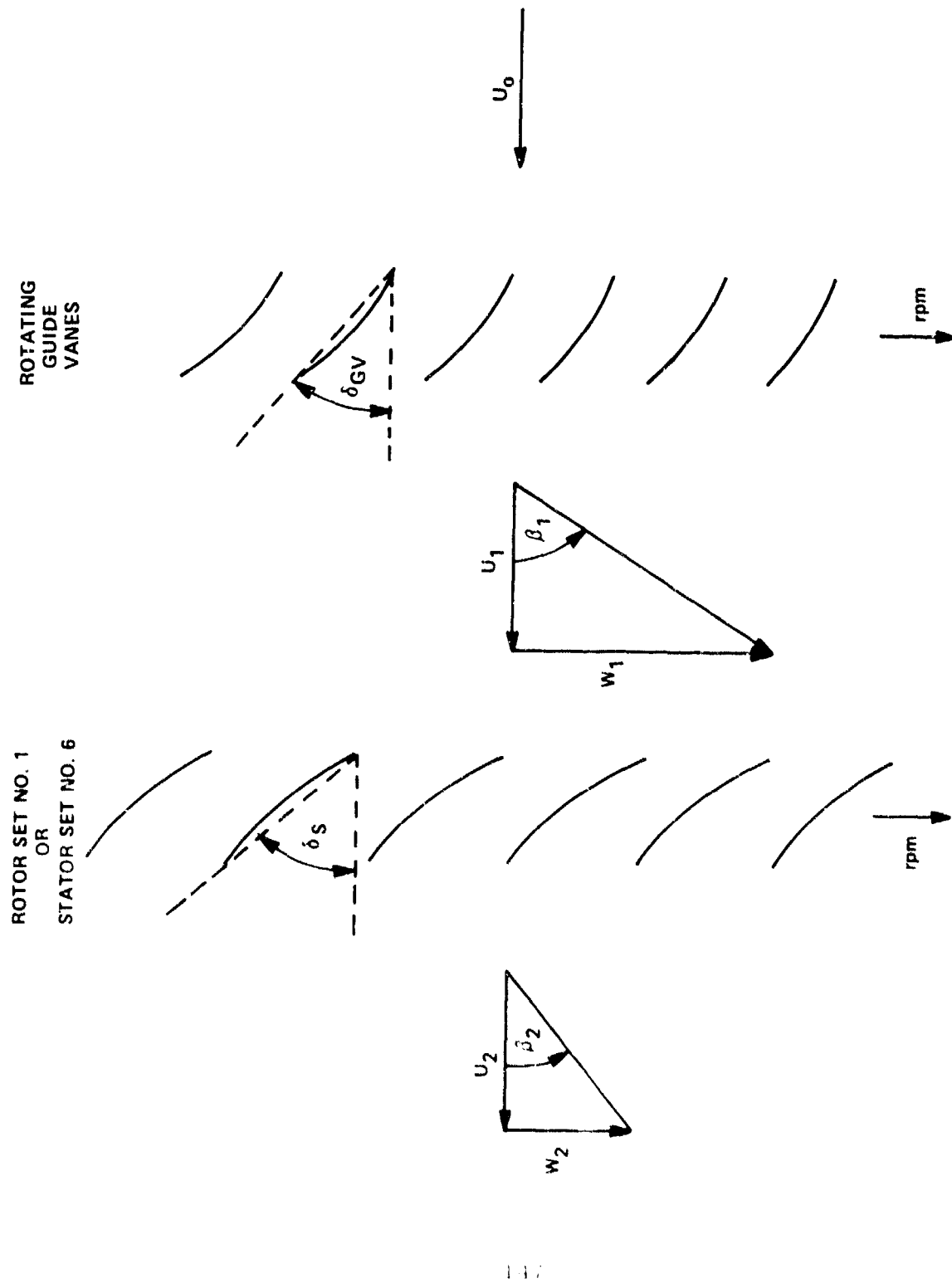


Figure 18 NOTATION FOR ANNULAR CASCADE WITH ROTATING HUB

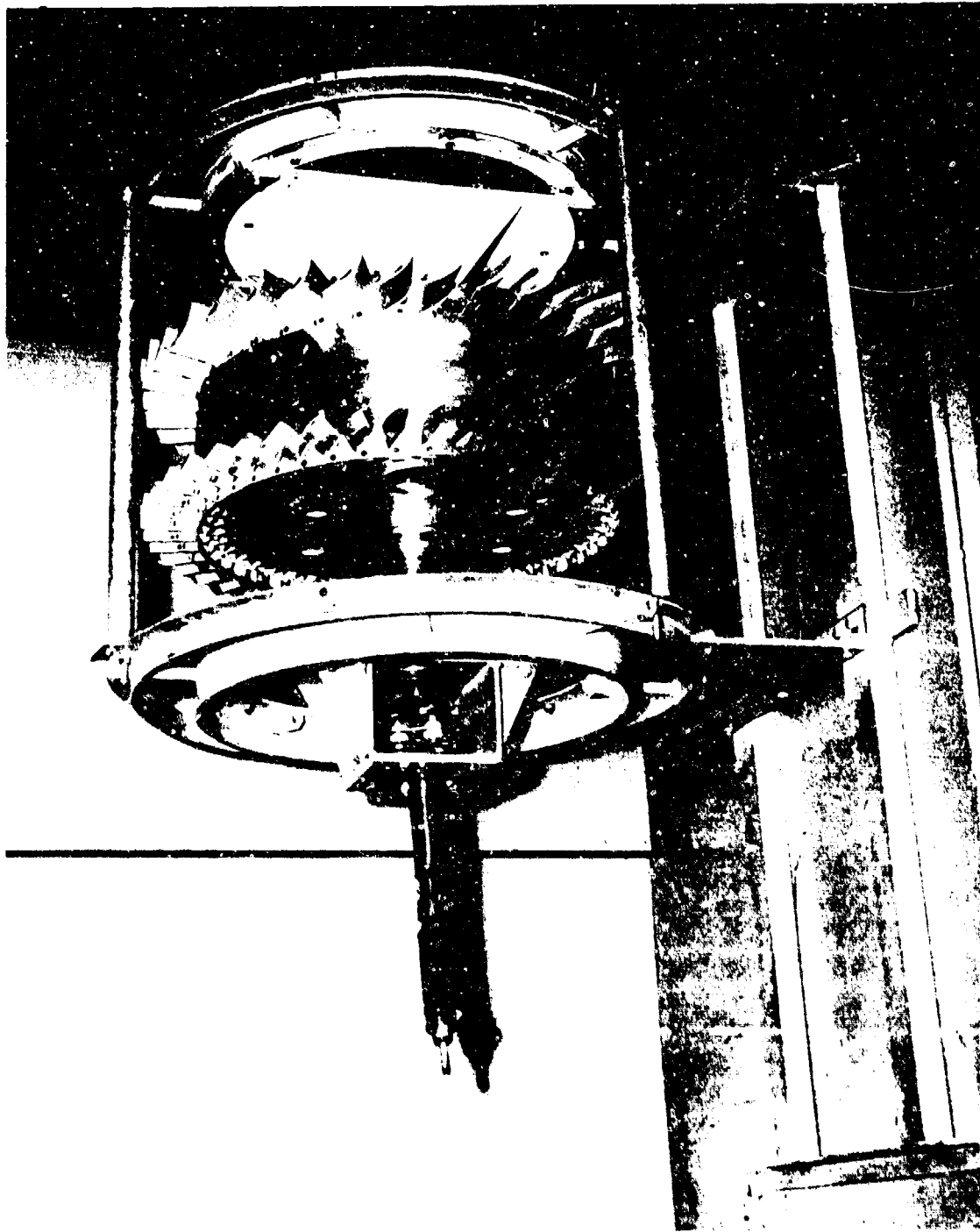


Figure 19 PARTIAL REAR VIEW OF ROTOR ASSEMBLY

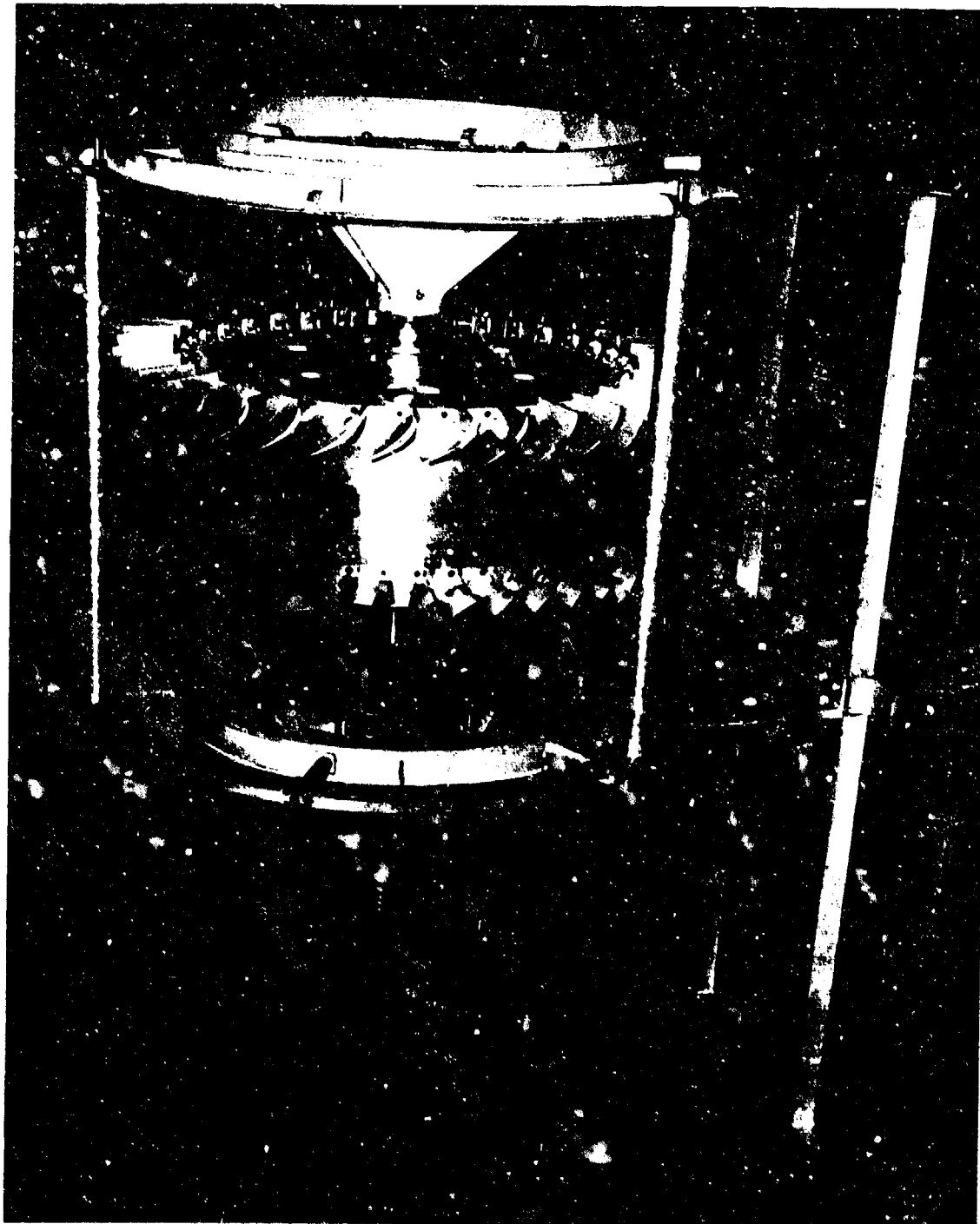


Figure 20 PARTIAL FRONT VIEW OF ROTOR ASSEMBLY









Preceding page blank

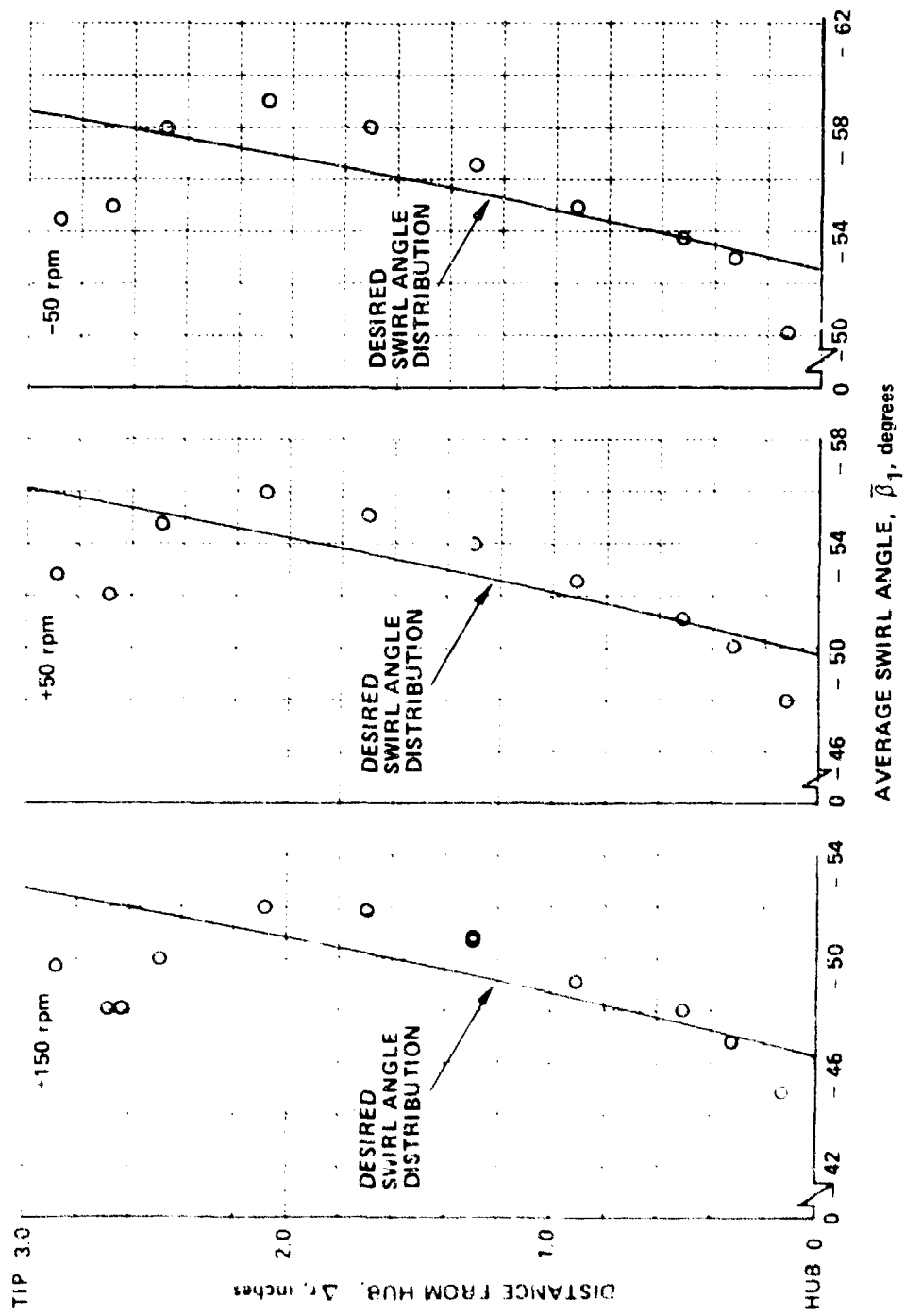


Figure 22 AVERAGE SWIRL ANGLE DISTRIBUTION ALONG A RADIUS DOWNSTREAM OF ROTATING GUIDE VANES, GUIDE VANE STAGGER ANGLE AT HUB,  $\delta_{GV} = 36.1$  DEGREES (SHEET 1 OF 2)

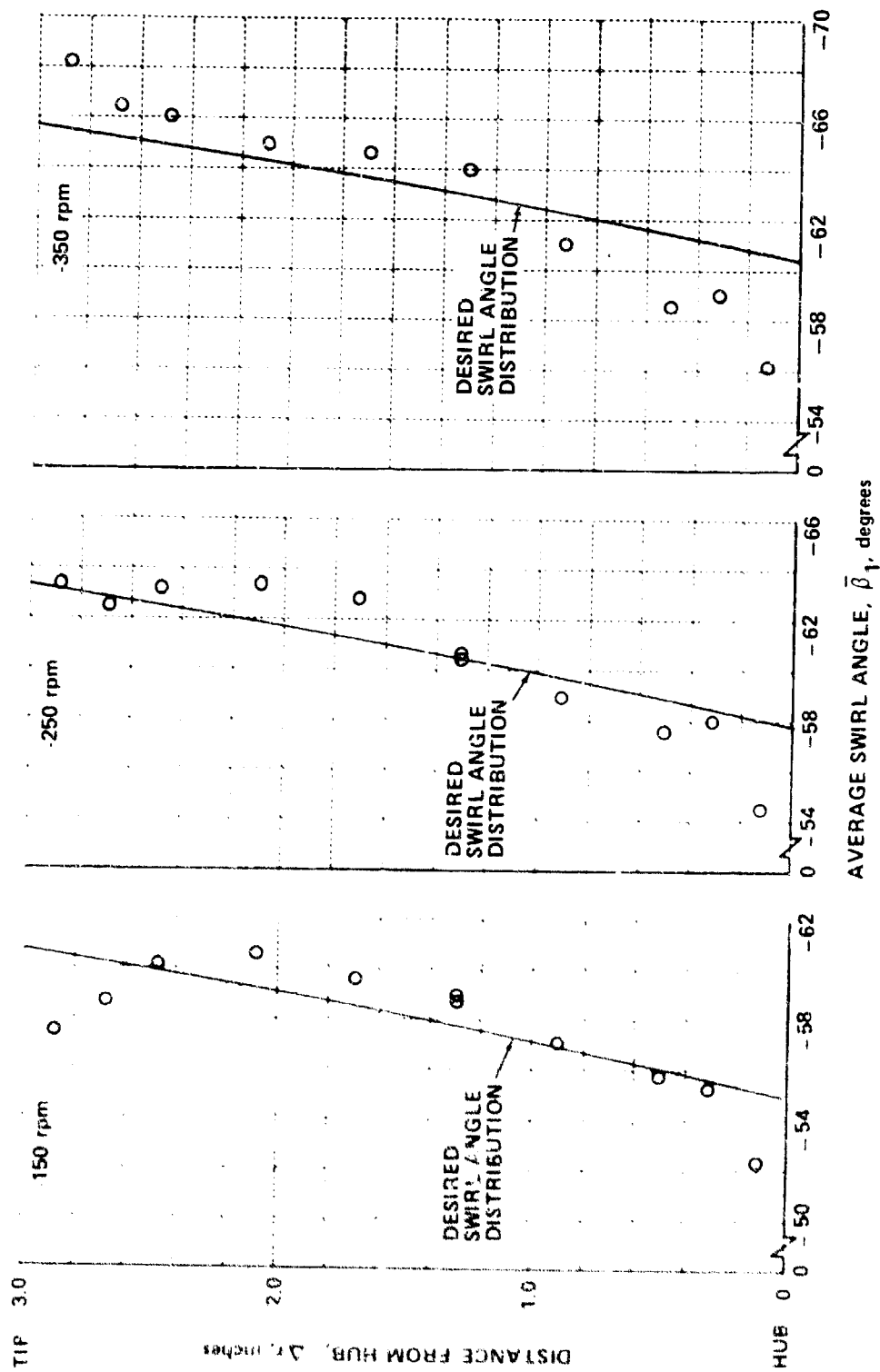


Figure 22 AVERAGE SWIRL ANGLE DISTRIBUTION ALONG A RADIUS DOWNSTREAM OF ROTATING GUIDE VANES, GUIDE VANE STAGGER ANGLE AT HUB,  $\delta_{GV} = 36.1$  DEGREES (SHEET 2 OF 2)

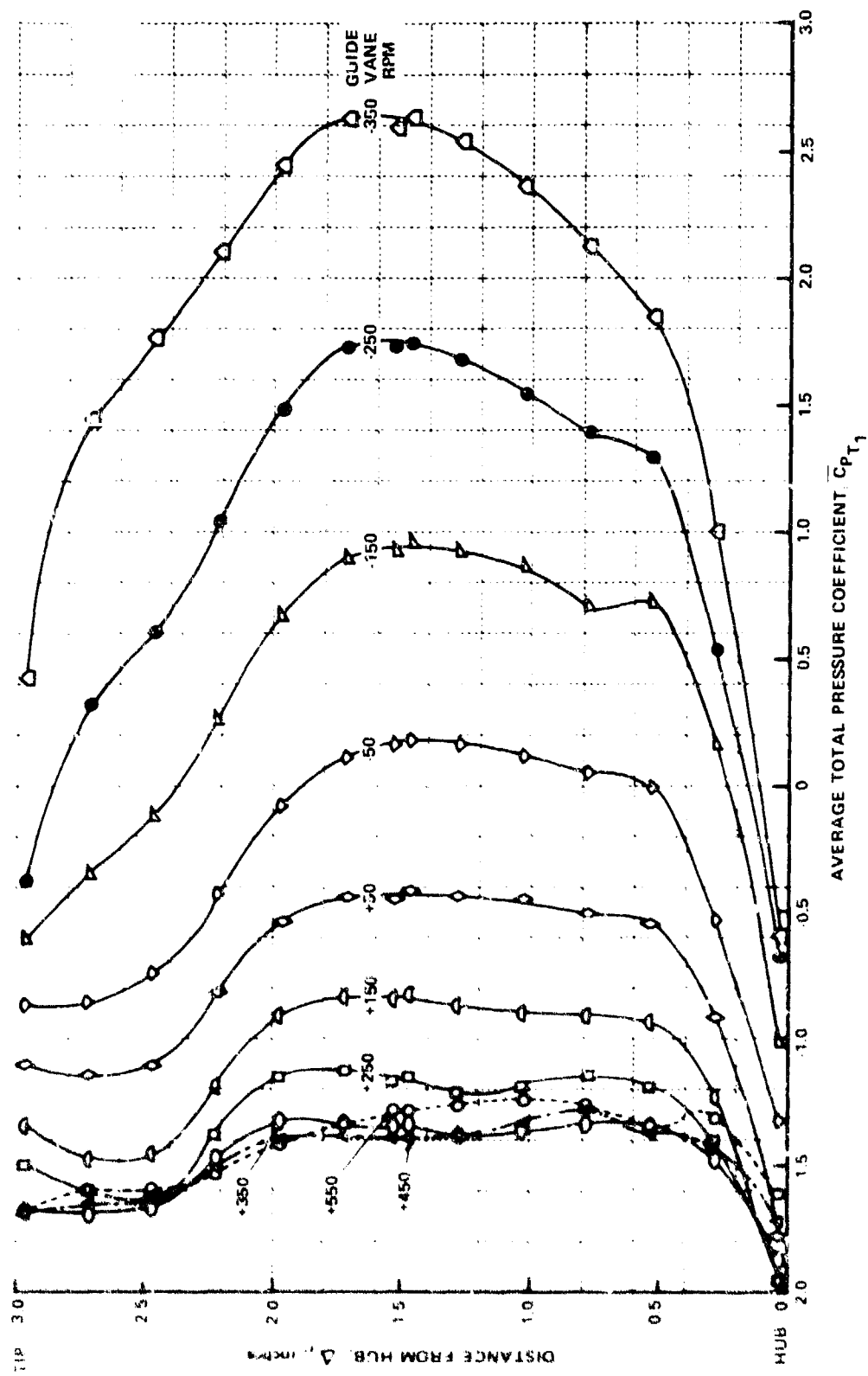


Figure 23 RADIAL DISTRIBUTION OF TOTAL PRESSURE DOWNSTREAM OF ROTATING GUIDE VANES,  
GUIDE VANE STAGGER ANGLE AT HUB,  $\delta_{GV} = 36.1$  DEGREES

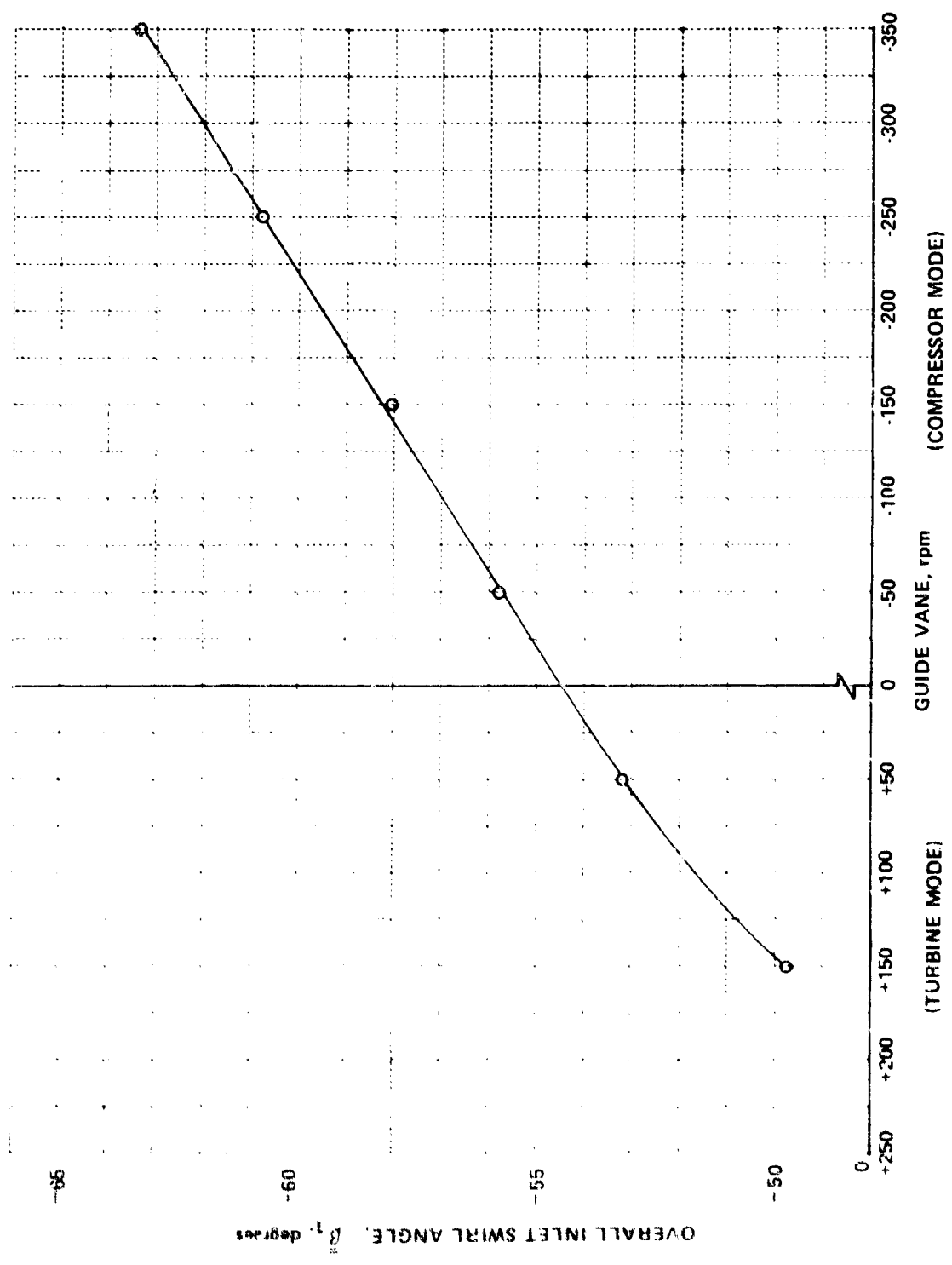


Figure 24 OVERALL INLET SWIRL ANGLE DOWNSTREAM OF ROTATING GUIDE VANES,  
 GUIDE VANE STAGGER ANGLE AT HUB,  $\delta_{GV} = 36.1$  DEGREES

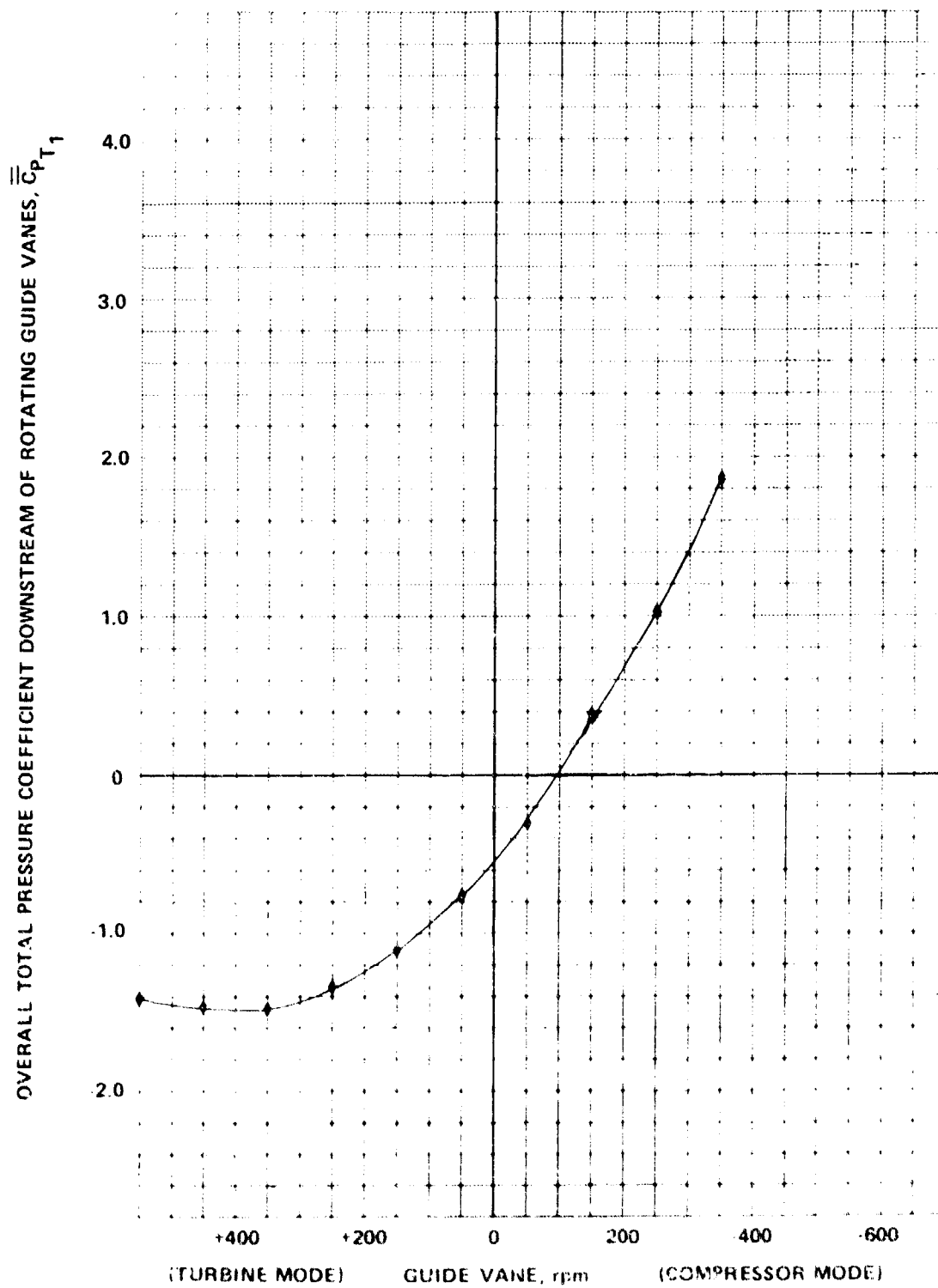


Figure 25 OVERALL TOTAL PRESSURE DOWNSTREAM OF ROTATING GUIDE VANES, GUIDE VANE STAGGER ANGLE AT HUB,  $\delta_{GV} = 36.1$  DEGREES

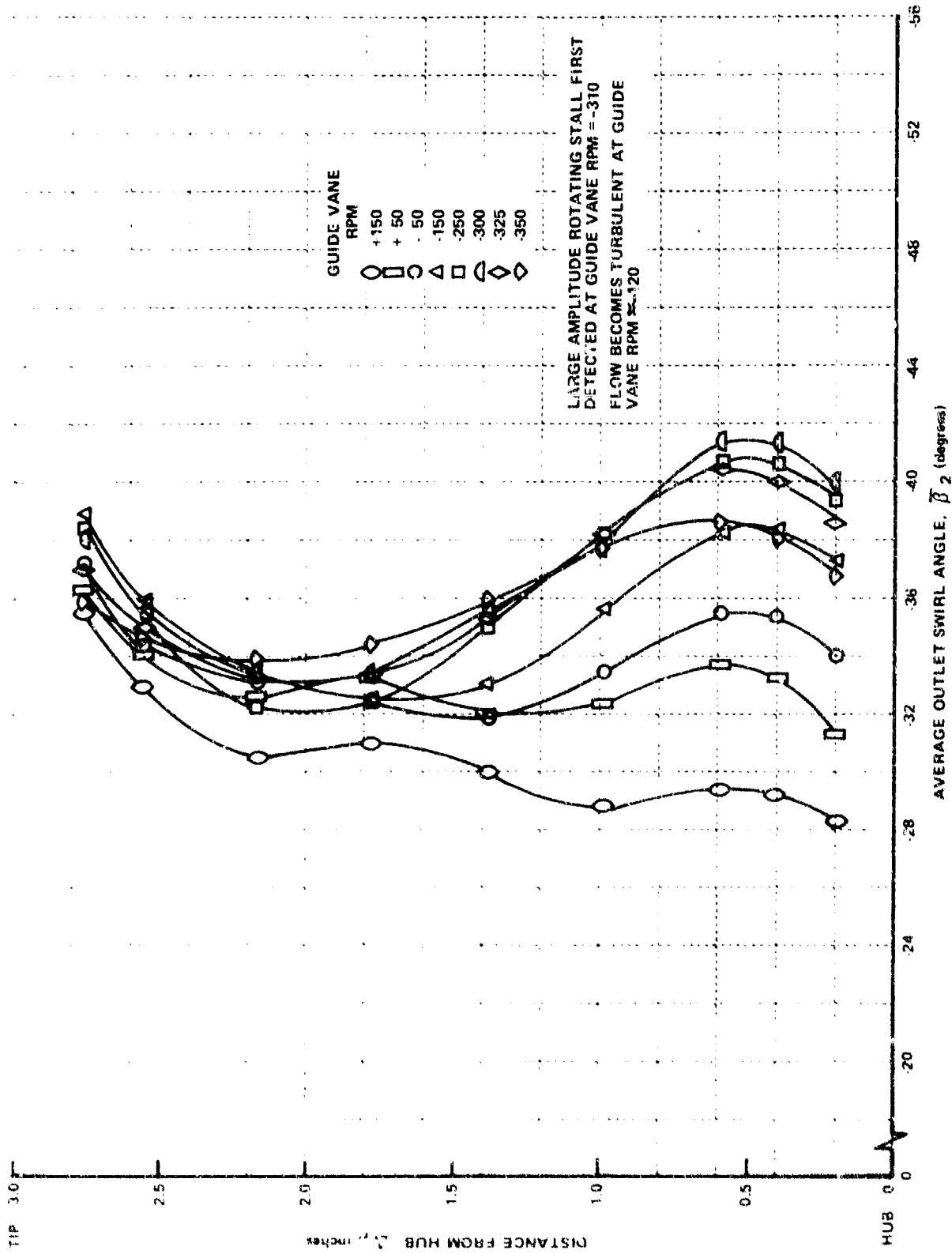


Figure 26 AVERAGE SWIRL ANGLE DISTRIBUTIONS ALONG A RADIUS DOWNSTREAM OF STATOR SET NO. 6

(a) STATOR STAGGER ANGLE,  $\delta_{SM} = 30$  DFG



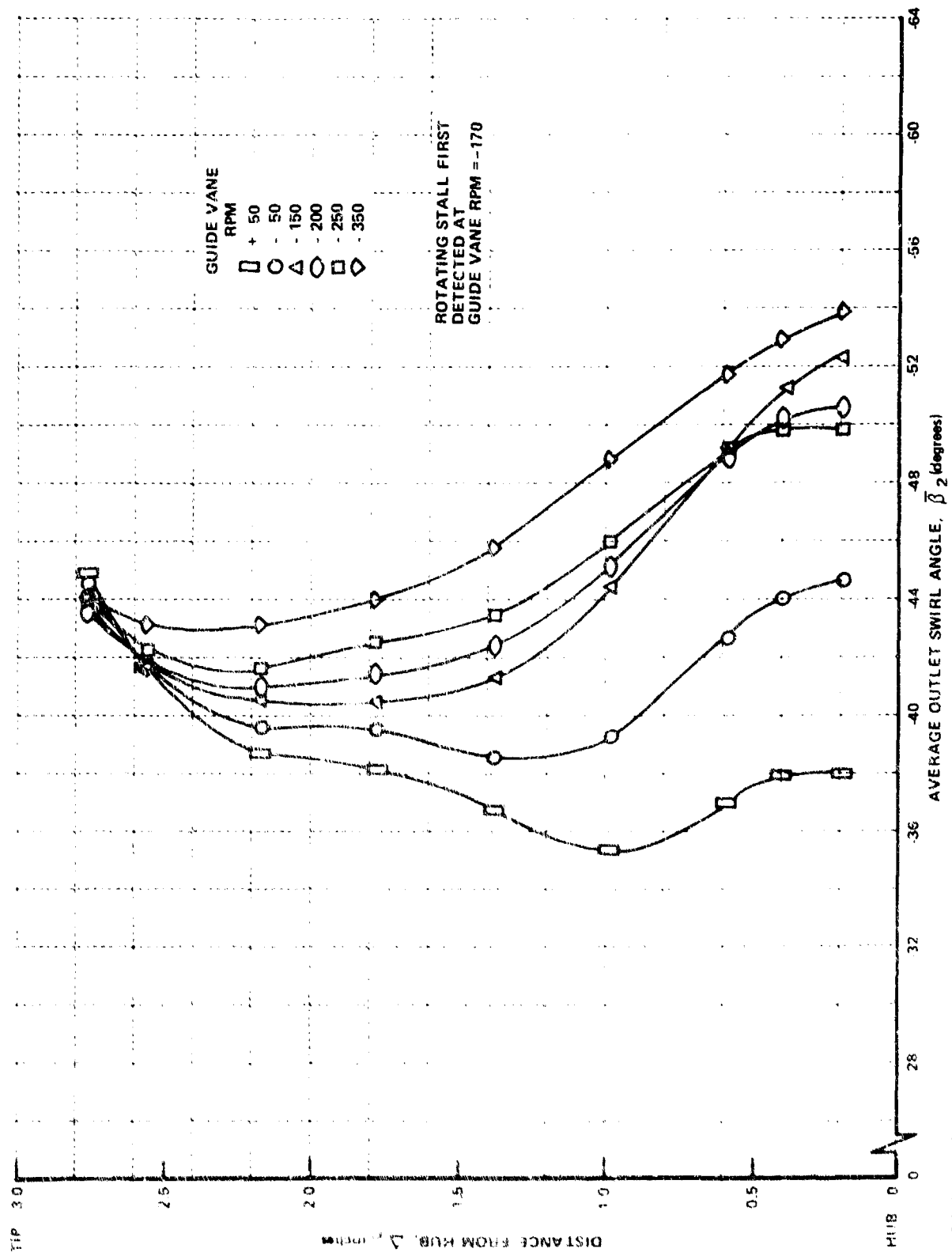


Figure 26 (Cont.) AVERAGE SWIRL ANGLE DISTRIBUTIONS ALONG A RADIUS DOWNSTREAM OF STATOR SET NO. 6

(b) STATOR STAGGER ANGLE,  $\delta_{SM} = 40$  DEG

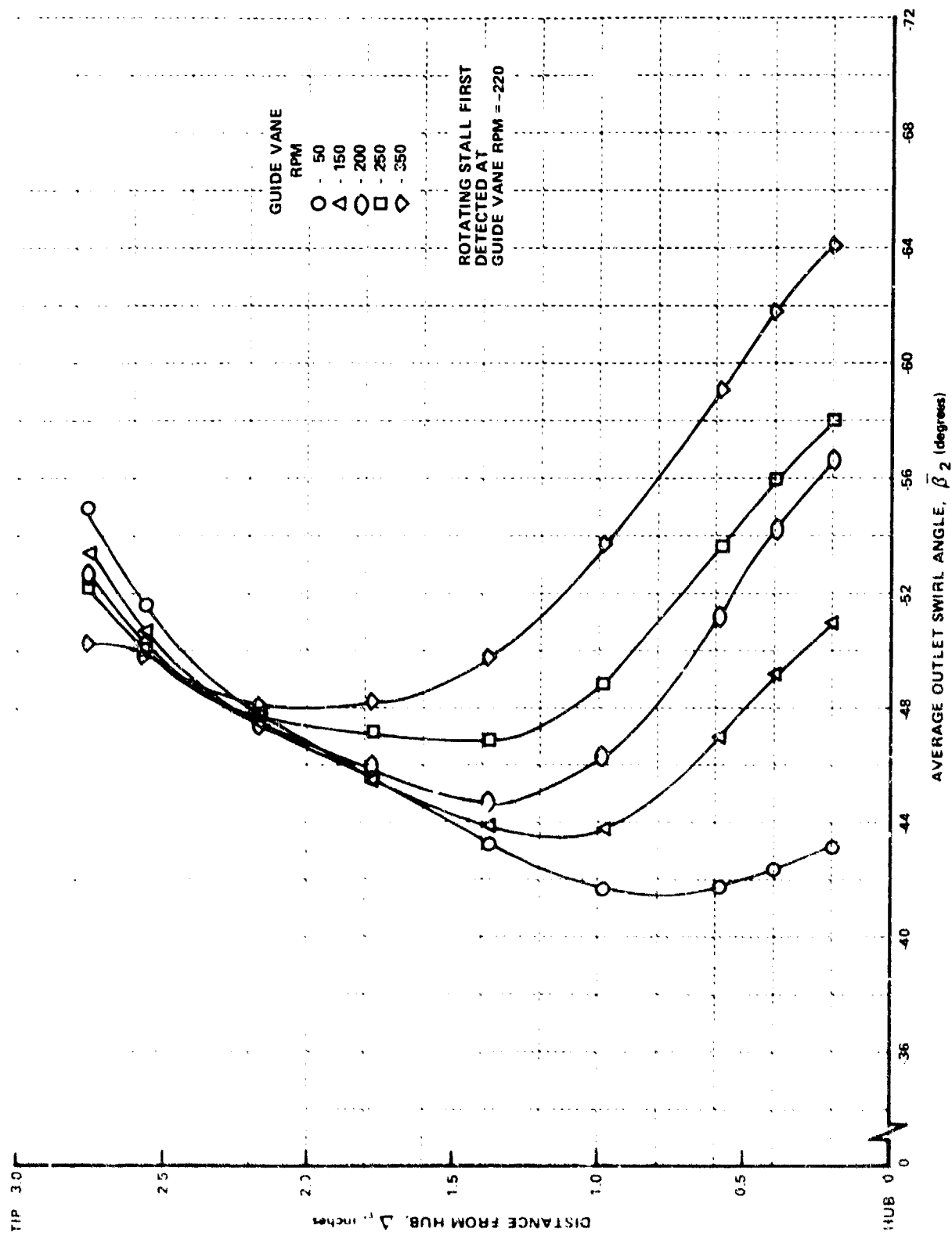


Figure 26 (Cont.) AVERAGE SWIRL ANGLE DISTRIBUTIONS ALONG A RADIUS DOWNSTREAM OF STATOR SET NO. 6

(c) STATOR STAGGER ANGLE,  $\delta_{SM} = 50$  DEG

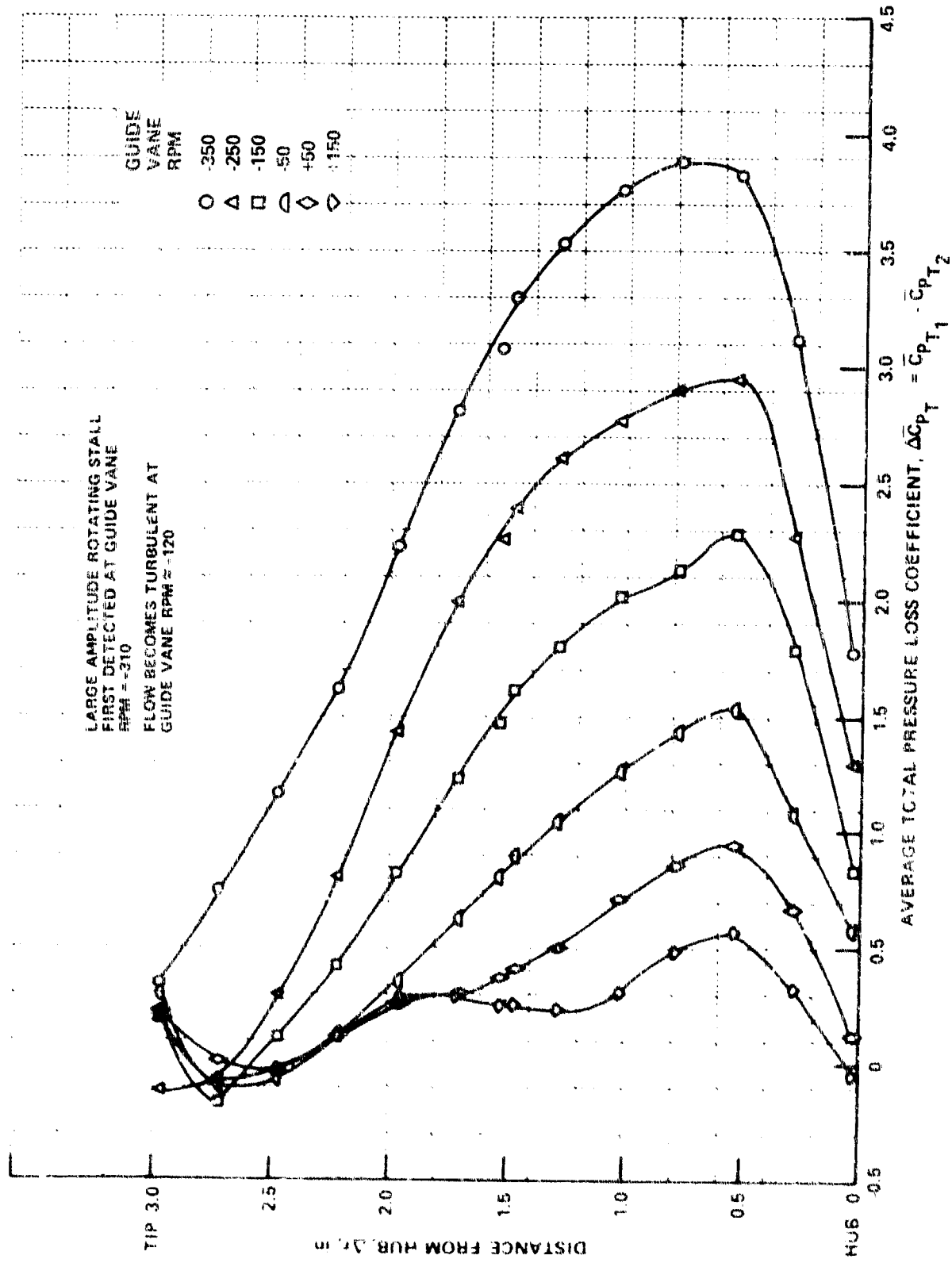


Figure 27 RADIAL DISTRIBUTIONS OF AVERAGE TOTAL PRESSURE LOSS THROUGH STATOR SET NO. 6

(a) STATOR STAGGER ANGLE,  $\delta_{SM} = 30$  DEG

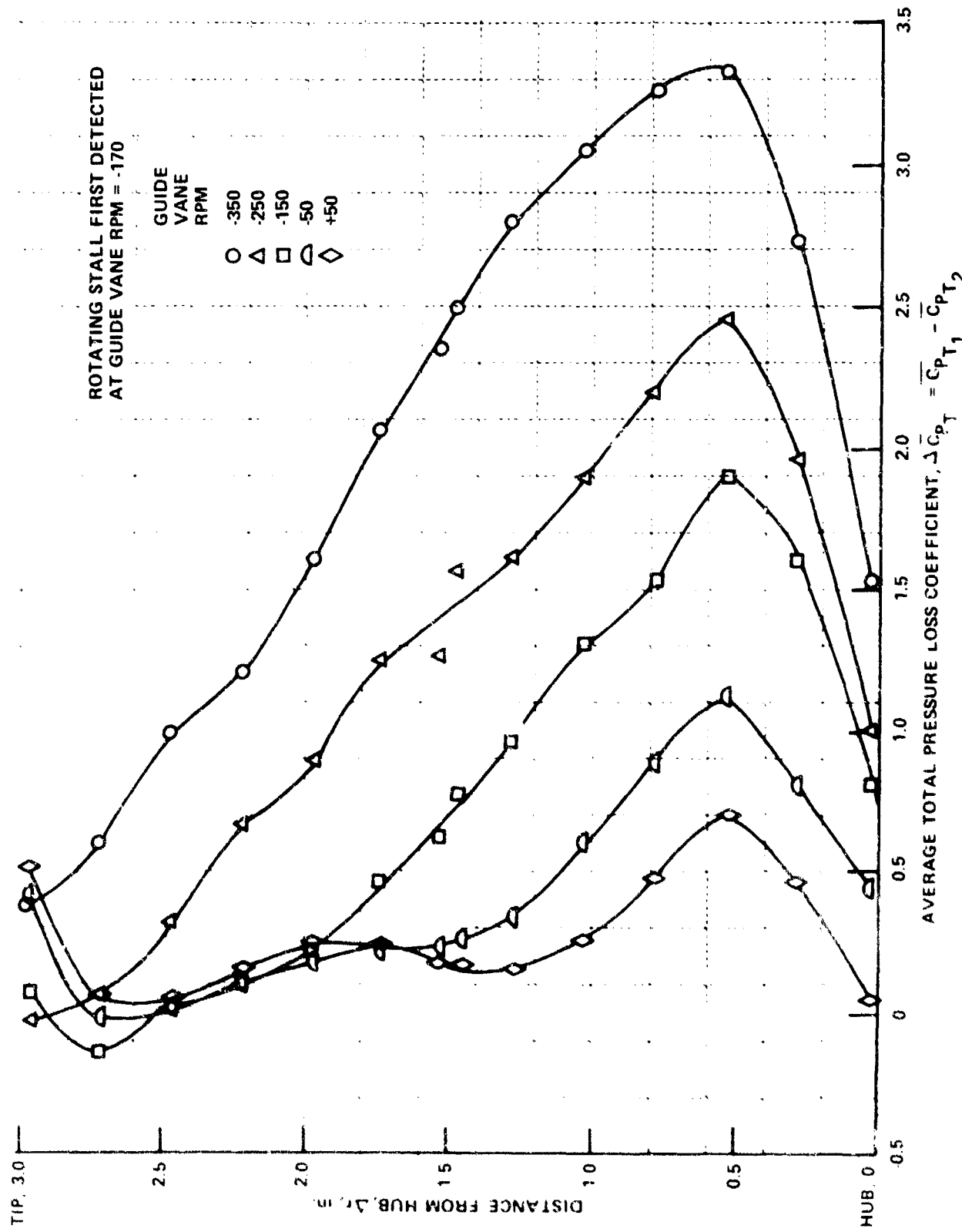


Figure 27 (Cont.) RADIAL DISTRIBUTIONS OF AVERAGE TOTAL PRESSURE LOSS THROUGH STATOR SET NO. 6

(b) STATOR STAGGER ANGLE,  $\delta_{SM} = 40$  DEG

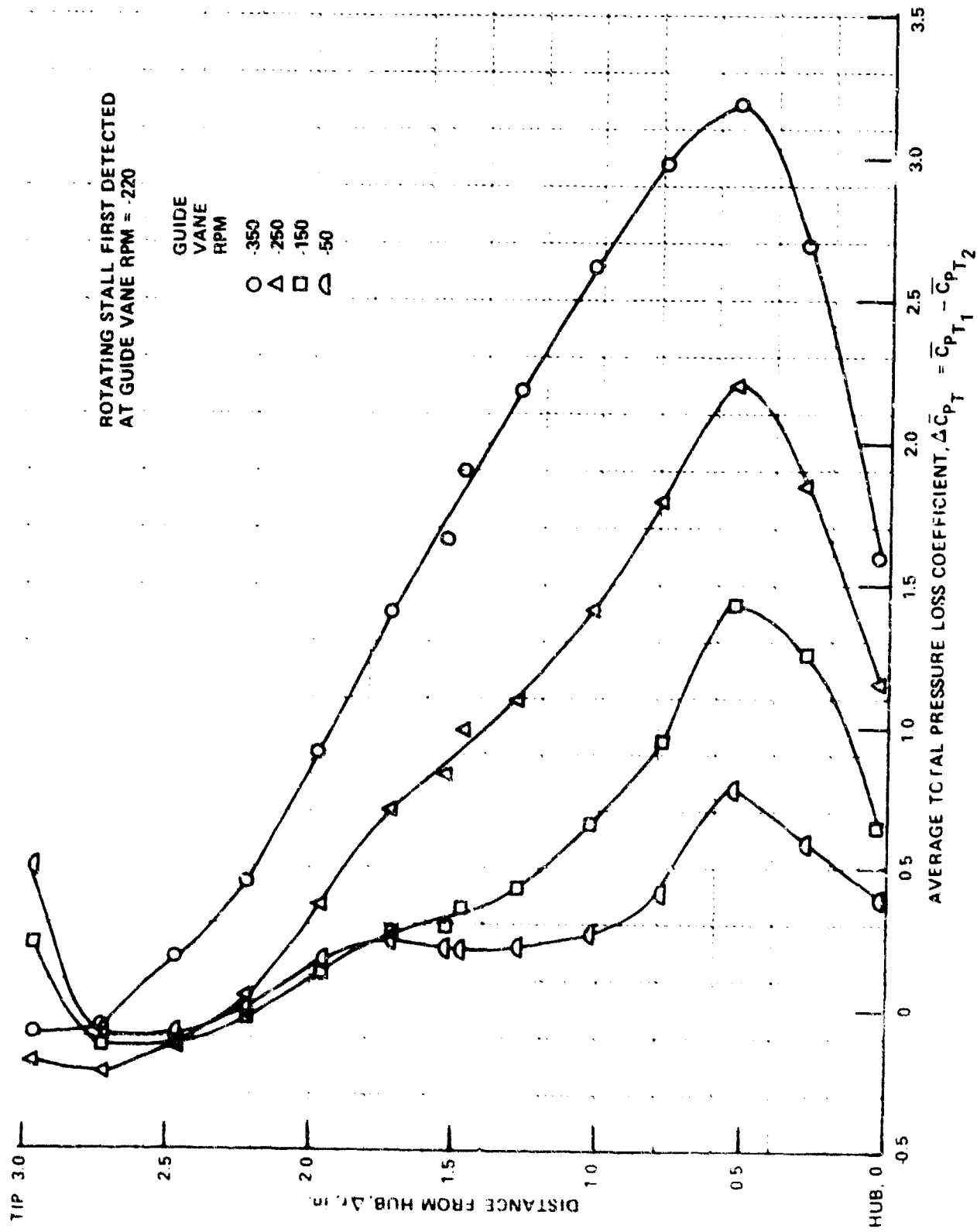


Figure 27 (Cont.) RADIAL DISTRIBUTIONS OF AVERAGE TOTAL PRESSURE LOSS THROUGH STATOR SET NO 6

(c) STATOR STAGGER ANGLE,  $\delta_{SM} = 50$  DEG

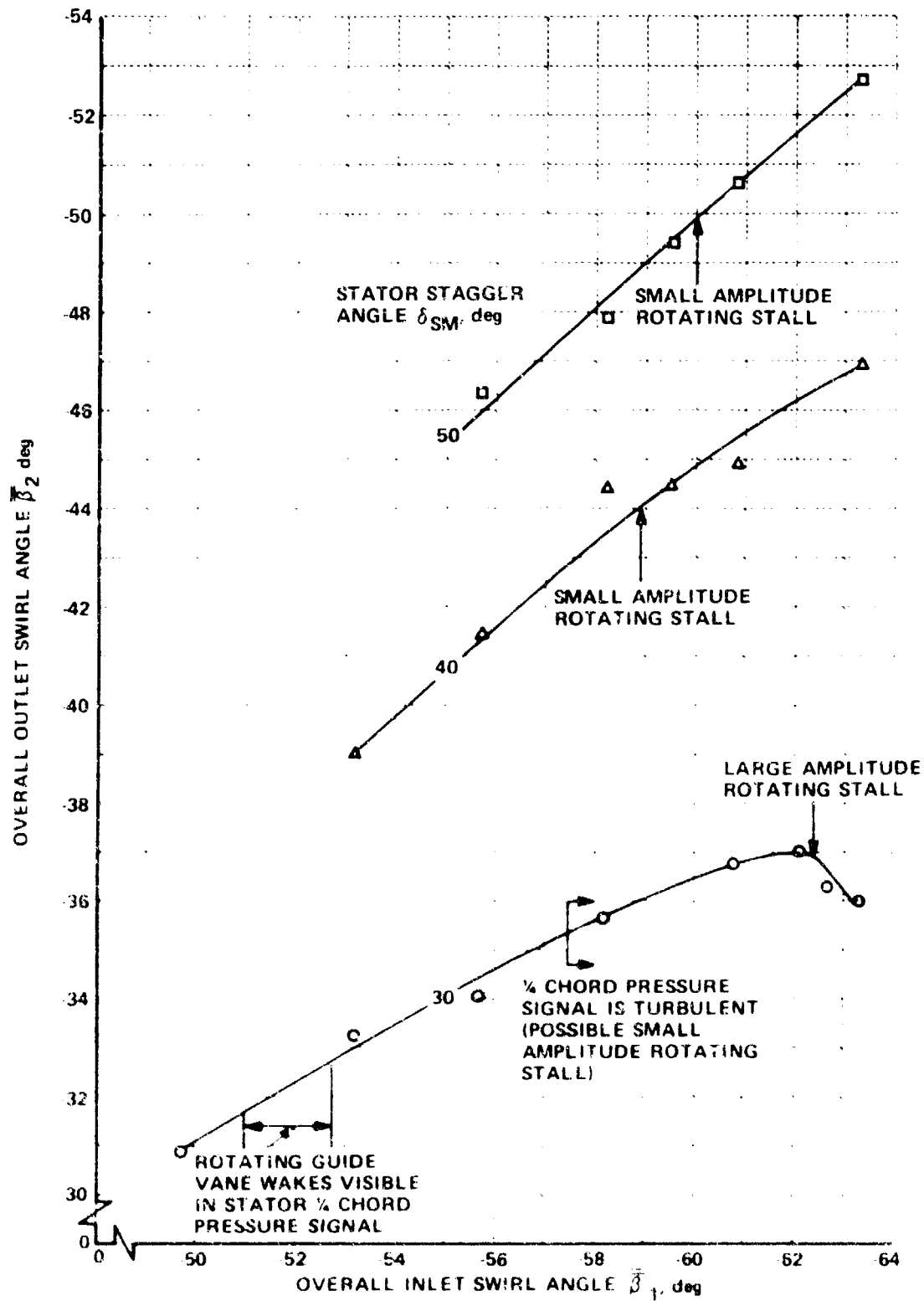


Figure 28 OVERALL FLOW TURNING PERFORMANCE OF STATOR SET NO. 6

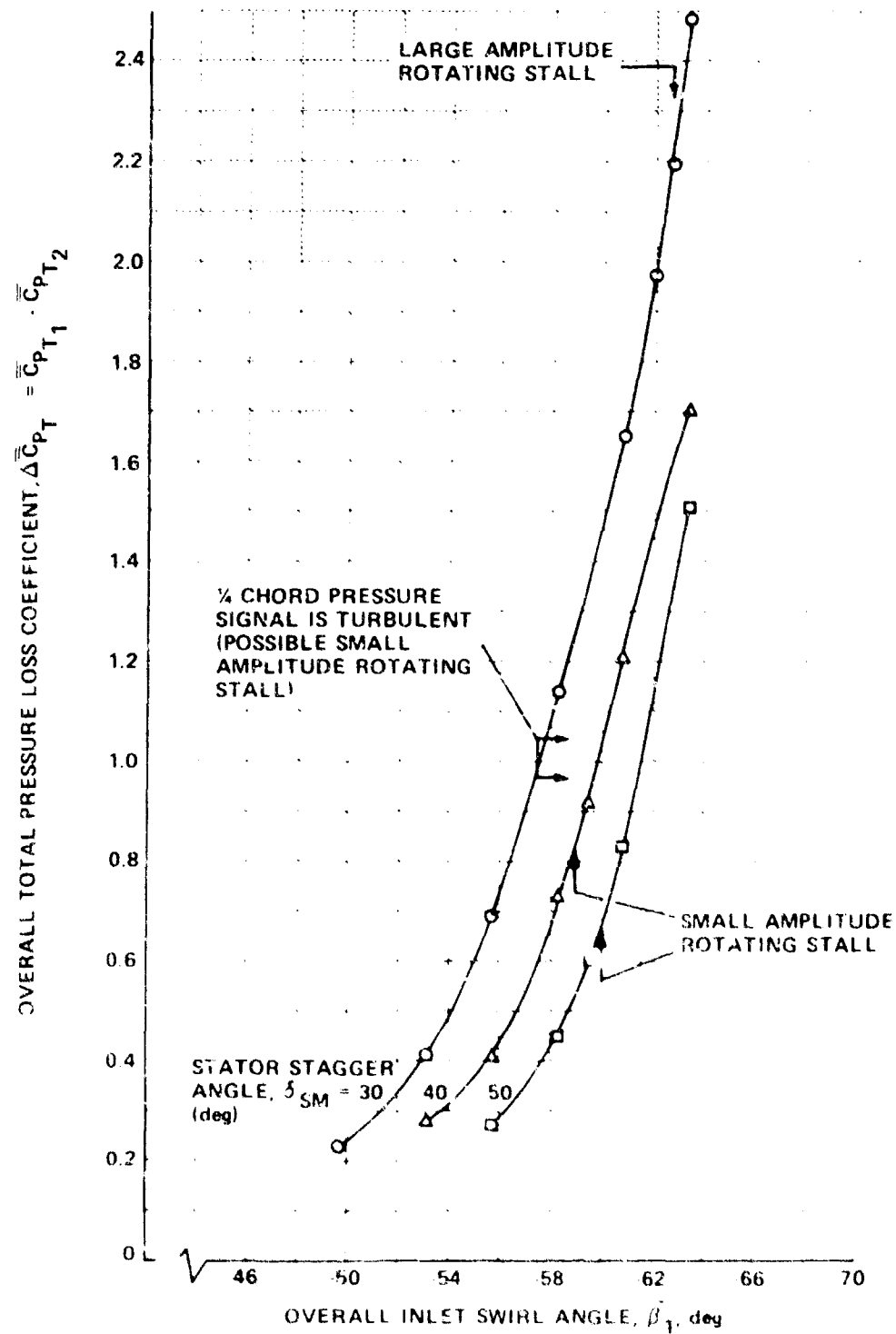


Figure 29 OVERALL TOTAL PRESSURE LOSS THROUGH STATOR SET NO. 6

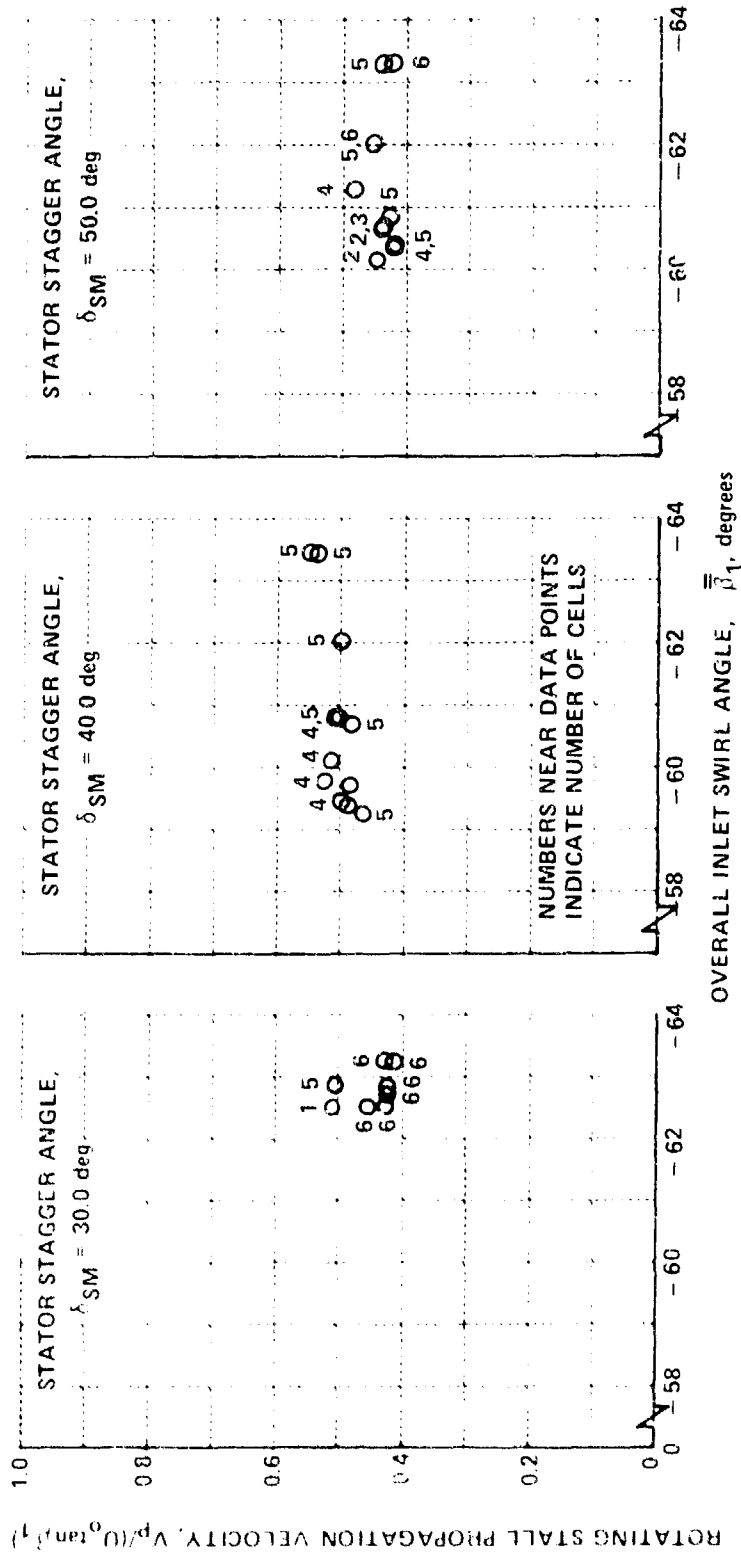


Figure 30 ROTATING STALL PROPAGATION VELOCITY AND NUMBER OF CELLS ON STATOR SET NO. 6



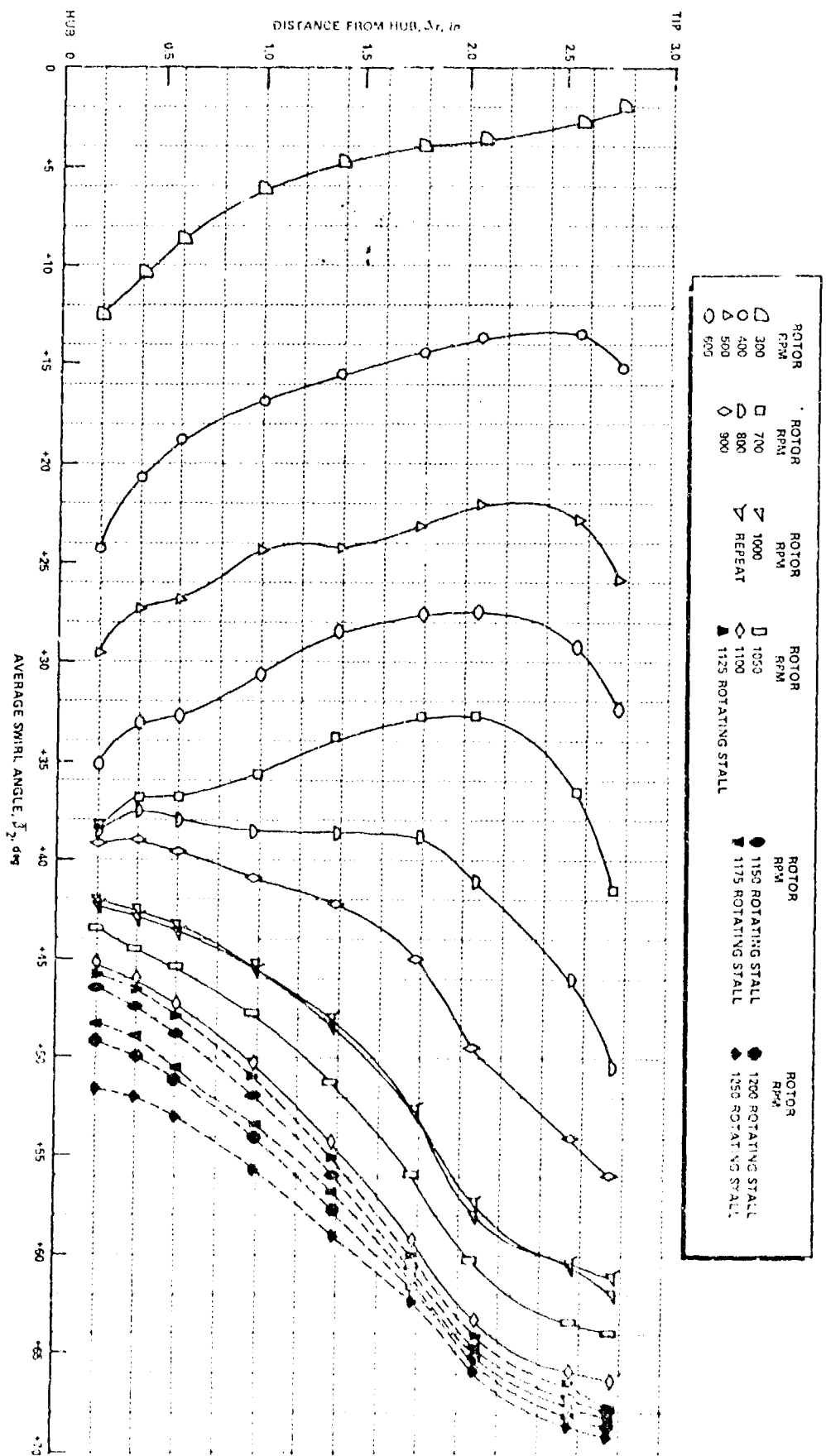


Figure 31 AVERAGE SWIRL ANGLE DISTRIBUTION ALONG A RADIUS' DOWNSTREAM OF ROTOR SET NO. 1, ABSOLUTE COORDINATE SYSTEM  
 (a) ROTOR STAGGER ANGLE,  $\delta_{RM} = 30$  DEG

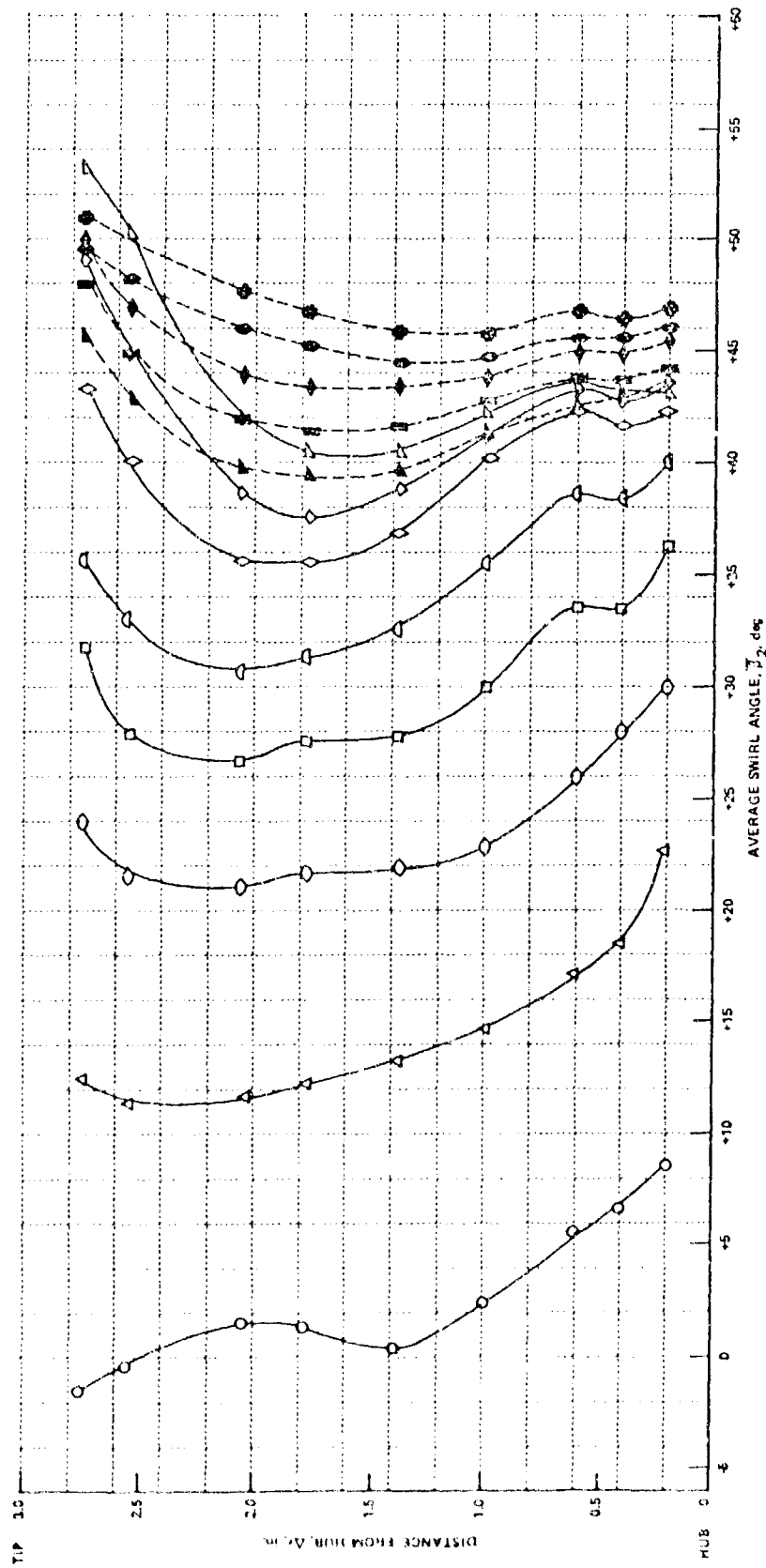
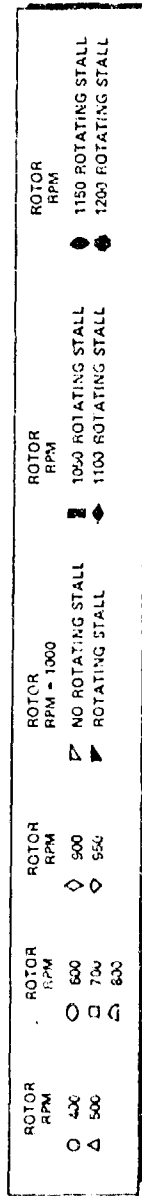


Figure 31 (Cont.) AVERAGE SWIRL ANGLE DISTRIBUTION ALONG A RADIUS DOWNSTREAM OF ROTOR SET NO. 1, ABSOLUTE COORDINATE SYSTEM

(b) ROTOR STAGGER ANGLE,  $\delta_{RM} = 40$  DEG

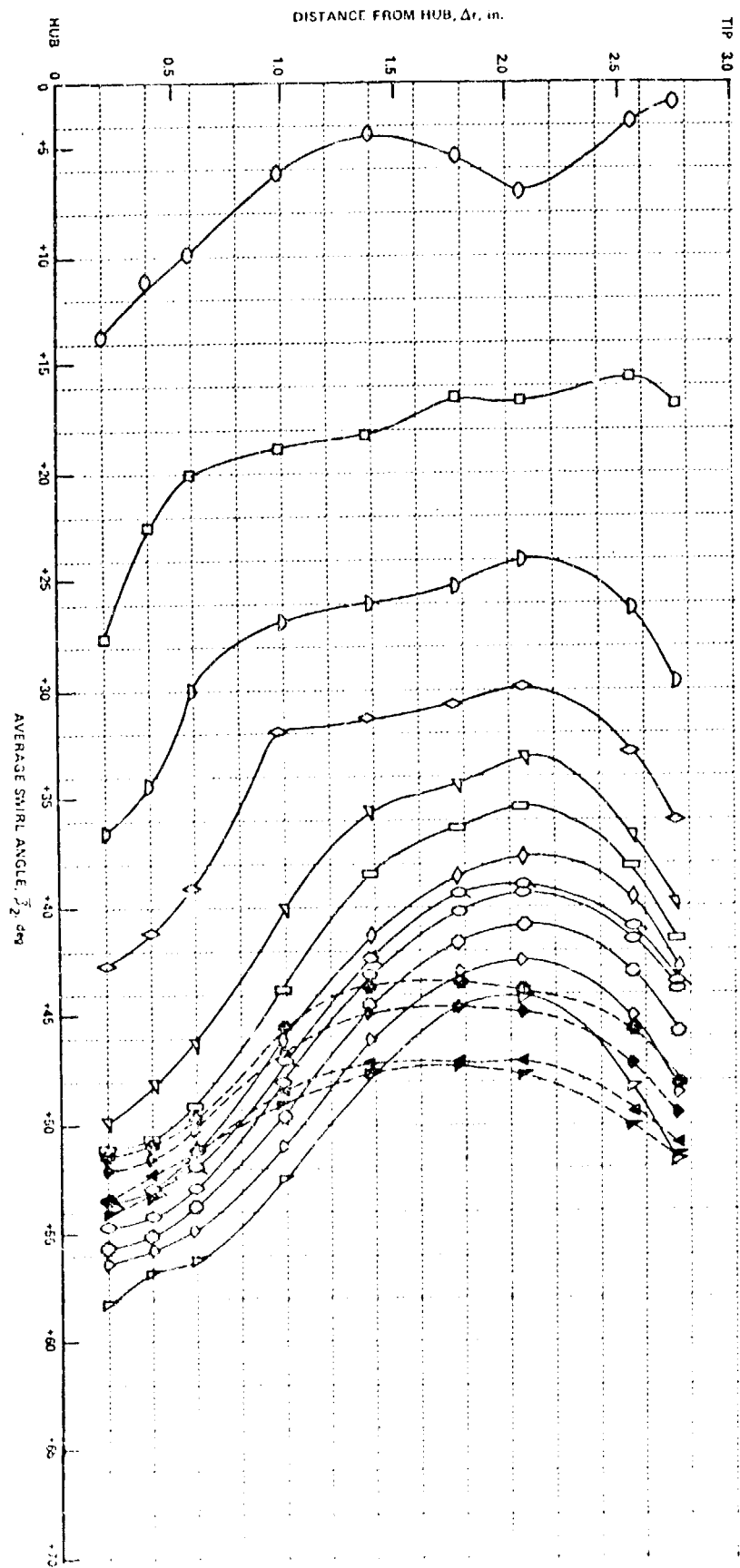


Figure 31 (Cont.) AVERAGE SWIRL ANGLE DISTRIBUTION ALONG A RADIUS DOWNSTREAM OF ROTCR SET NO. 1, ABSOLUTE COORDINATE SYSTEM  
 (e) ROTOR STAGGER ANGLE, 6 RM - 30 DEG

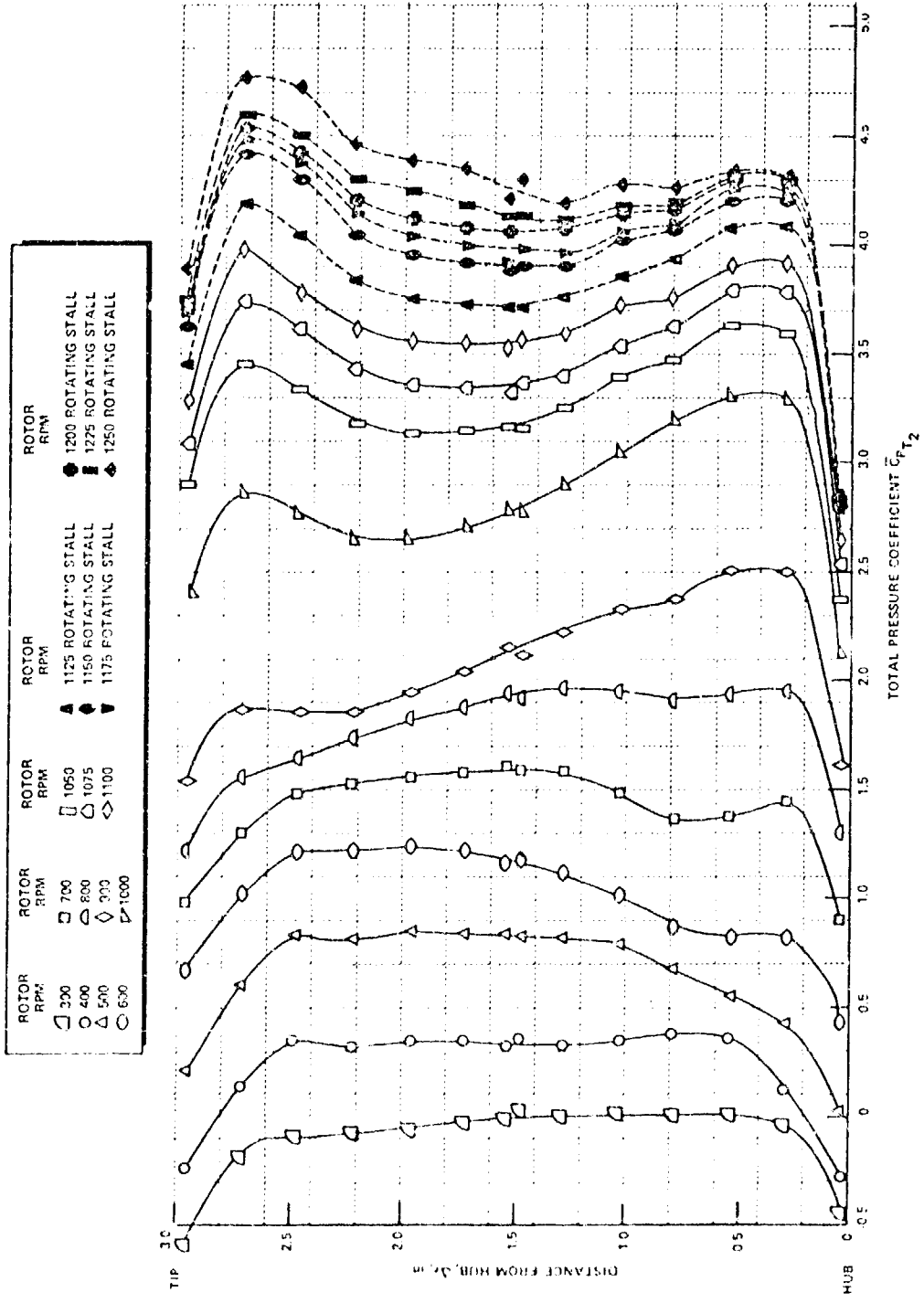


Figure 32 RADIAL DISTRIBUTIONS OF TOTAL PRESSURE DOWNSTREAM OF ROTOR SET NO. 1, ABSOLUTE COORDINATE SYSTEM

(a) ROTOR STAGGER ANGLE,  $\delta_{RM} = 30$  DEG

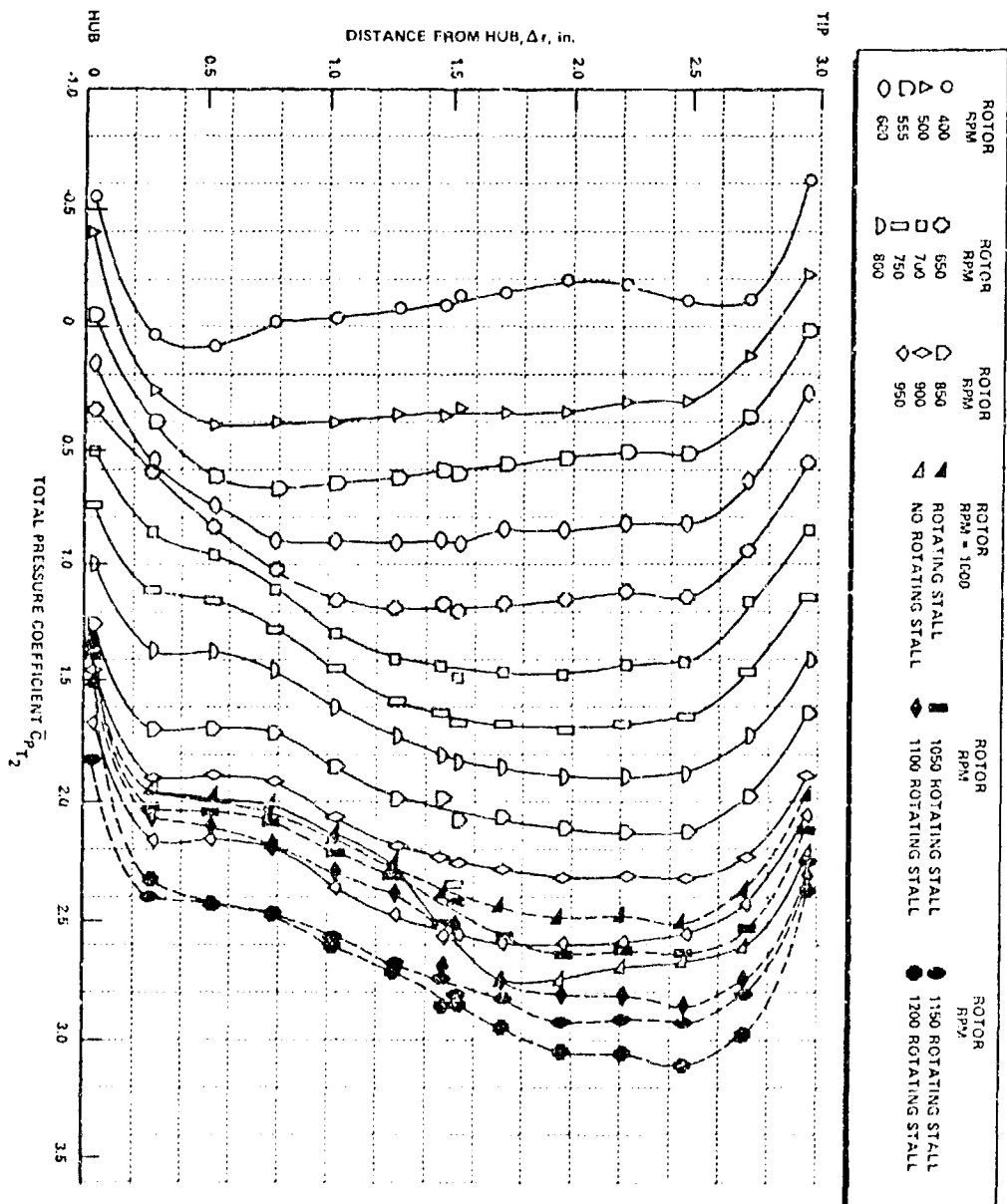


Figure 32 (Cont.) RADIAL DISTRIBUTIONS OF TOTAL PRESSURE DOWNSTREAM OF ROTOR  
 SET NO. 1, ABSOLUTE COORDINATE SYSTEM  
 (b) ROTOR STAGGER ANGLE,  $\delta_{RM} = 40$  DEG

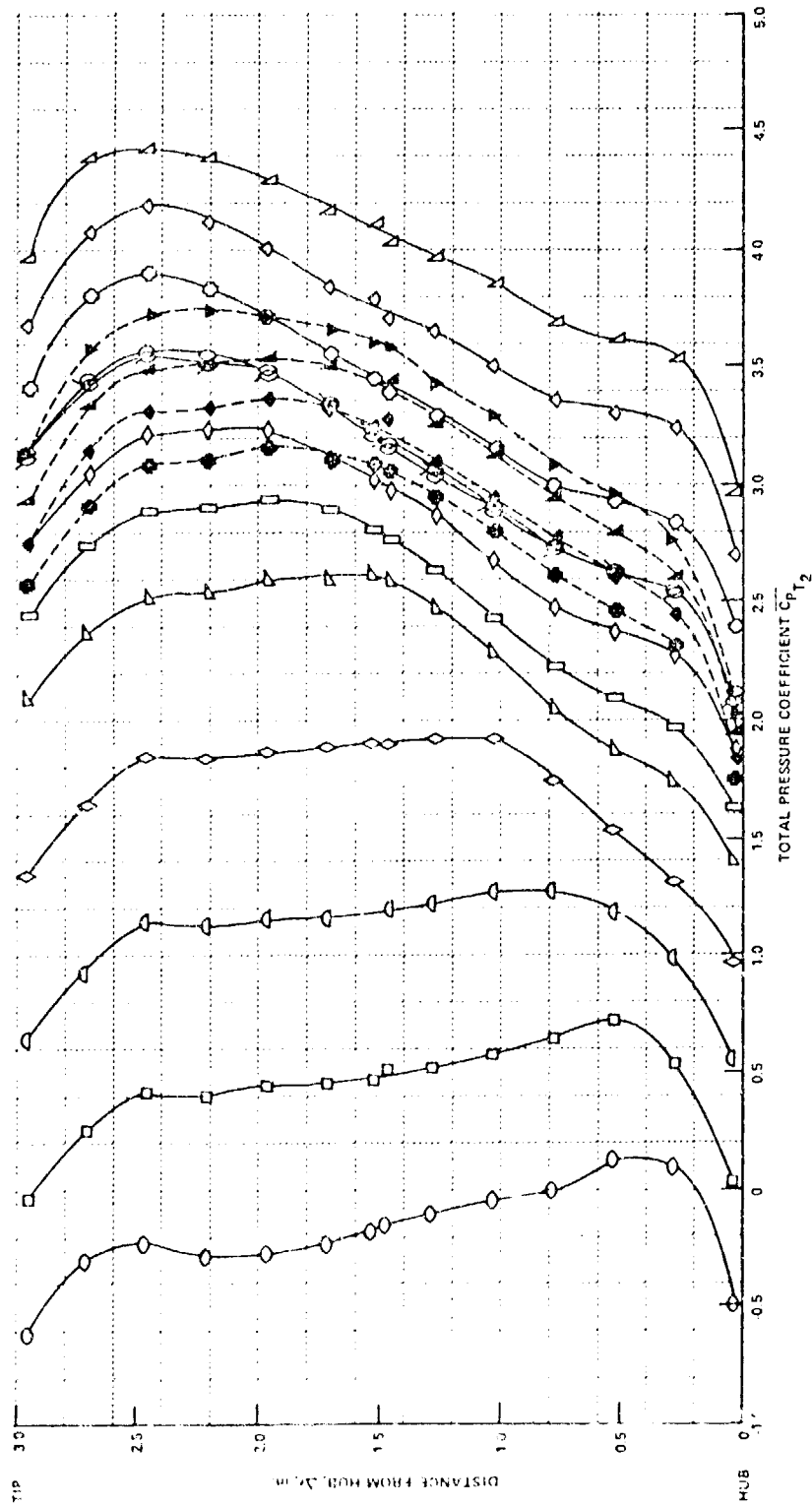
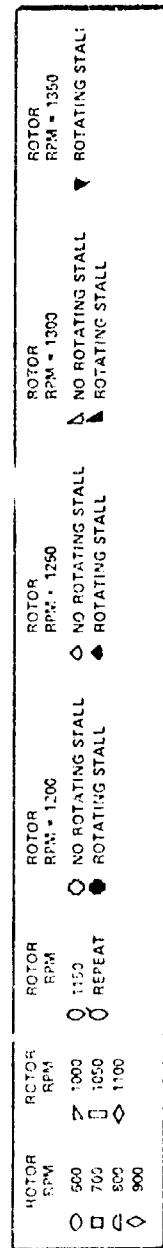


Figure 32 (Cont.) RADIAL DISTRIBUTIONS OF TOTAL PRESSURE DOWNSTREAM OF ROTOR  
SET NO. 1. ABSOLUTE COORDINATE SYSTEM

(c) ROTOR STAGGER ANGLE,  $\delta_{RM} = 50$  DEG

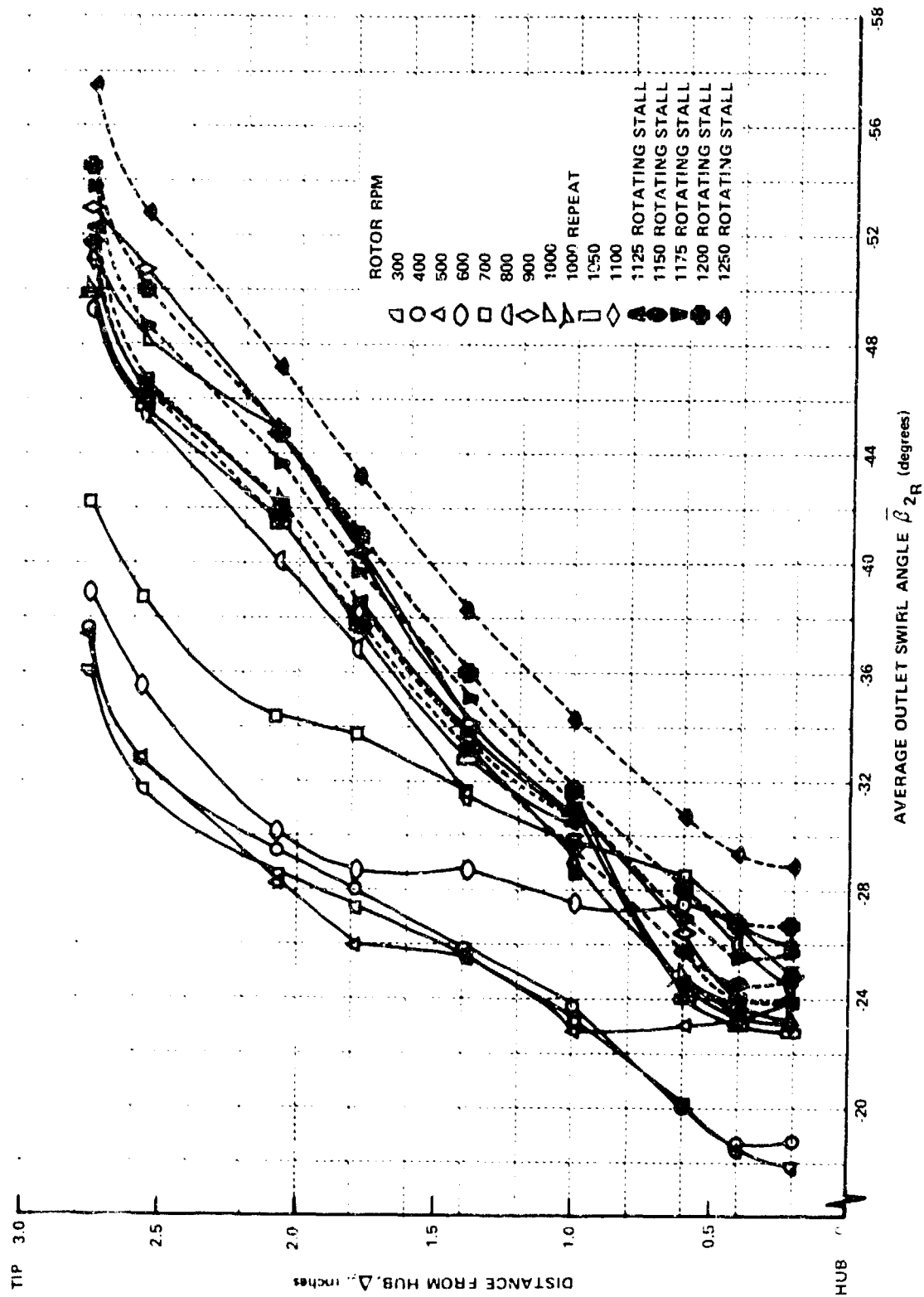


Figure 33 AVERAGE SWIRL ANGLE DISTRIBUTIONS ALONG A RADIUS DOWNSTREAM OF ROTOR NO. 1, COORDINATE SYSTEM MOVING WITH ROTOR

(a) ROTOR STATOR ANGLE,  $\delta_{RM} = 30$  DEG

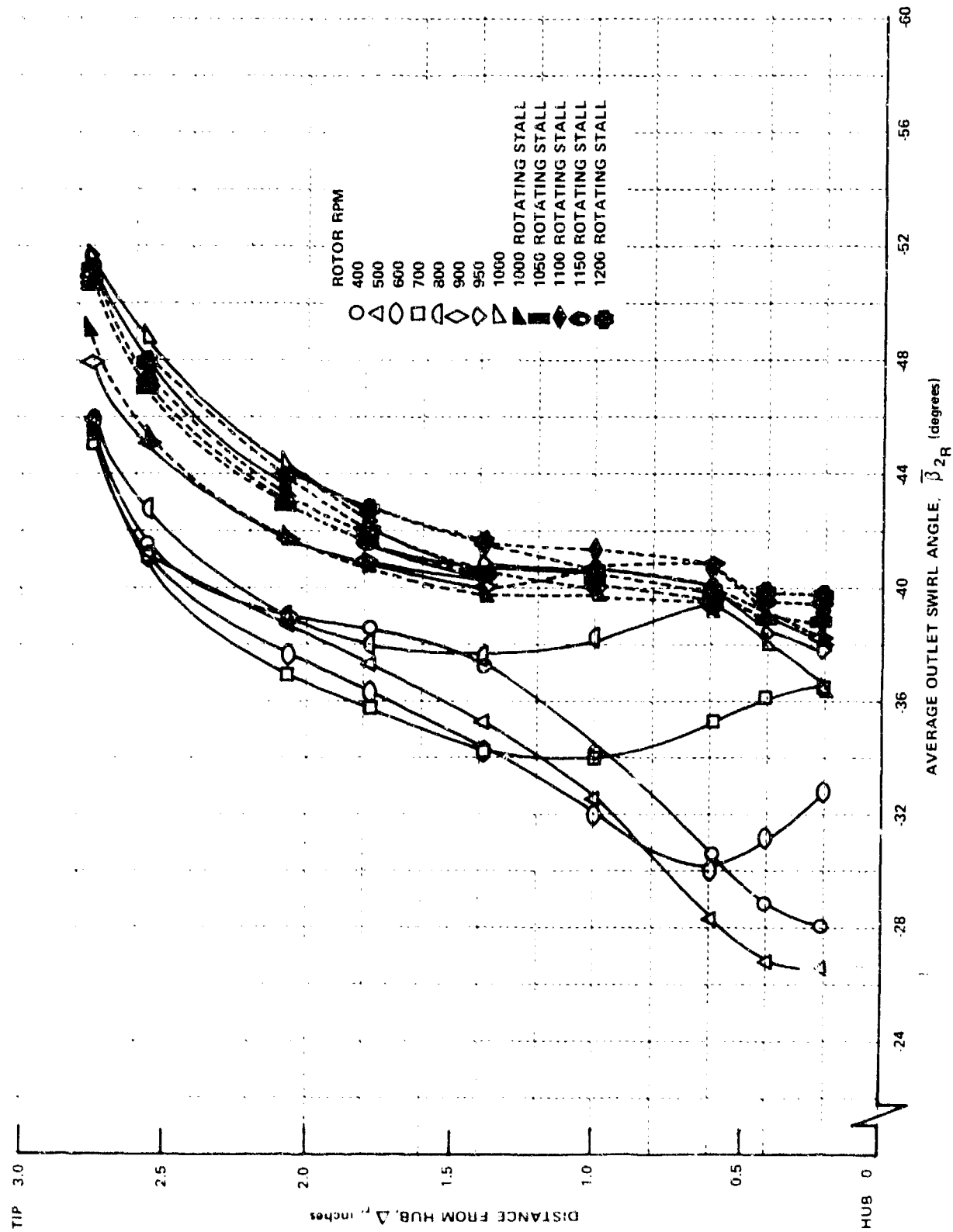


Figure 33 (Cont.) AVERAGE SWIRL ANGLE DISTRIBUTIONS ALONG A RADIUS DOWNSTREAM OF ROTOR SET NO.1,  
COORDINATE SYSTEM MOVING WITH ROTOR

(b) ROTOR STAGGER ANGLE,  $\delta_{RM} = 40$  DEG



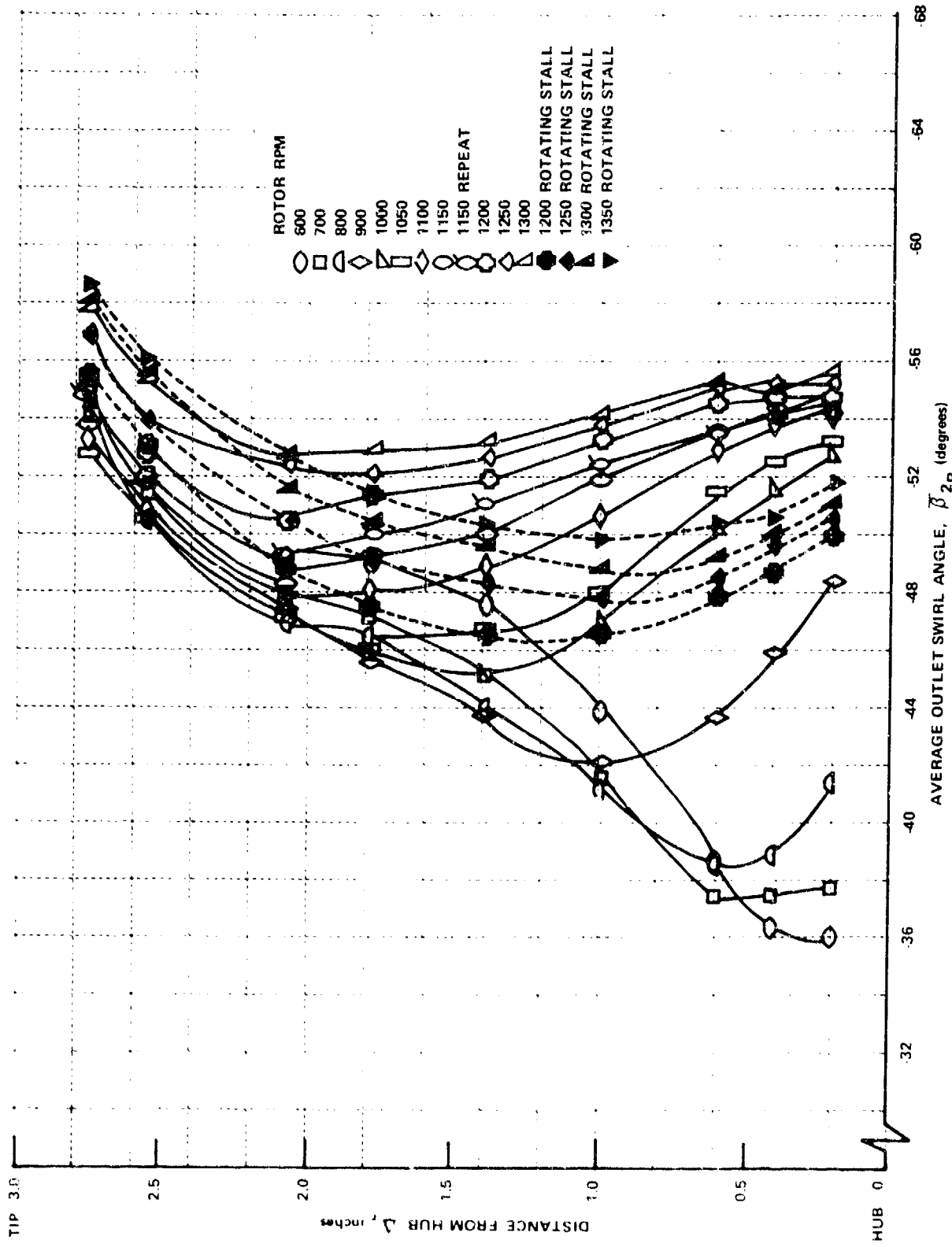


Figure 33 (Cont.) AVERAGE SWIRL ANGLE DISTRIBUTIONS ALONG A RADIUS DOWNSTREAM OF ROTOR NO. 1, COORDINATE SYSTEM MOVING WITH ROTOR

(c) ROTOR STAGGER ANGLE,  $\delta_{RM} = 50$  DEG

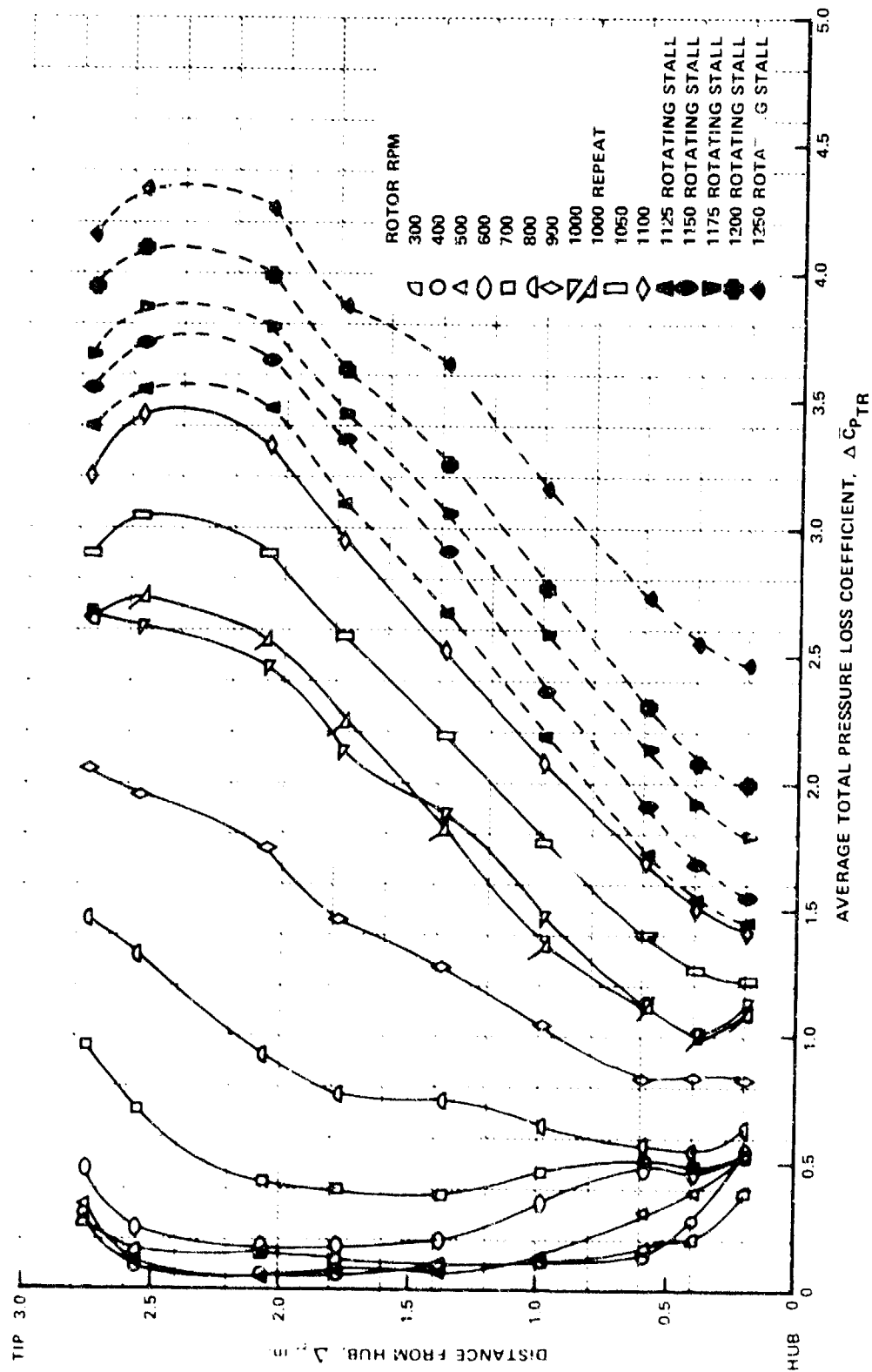


Figure 34 RADIAL DISTRIBUTIONS OF AVERAGE TOTAL PRESSURE LOSS THROUGH ROTOR SET NO. 1, COORDINATE SYSTEM MOVING WITH ROTOR

(a) ROTOR STAGGER ANGLE,  $\delta_{RM} = 30$  DEG

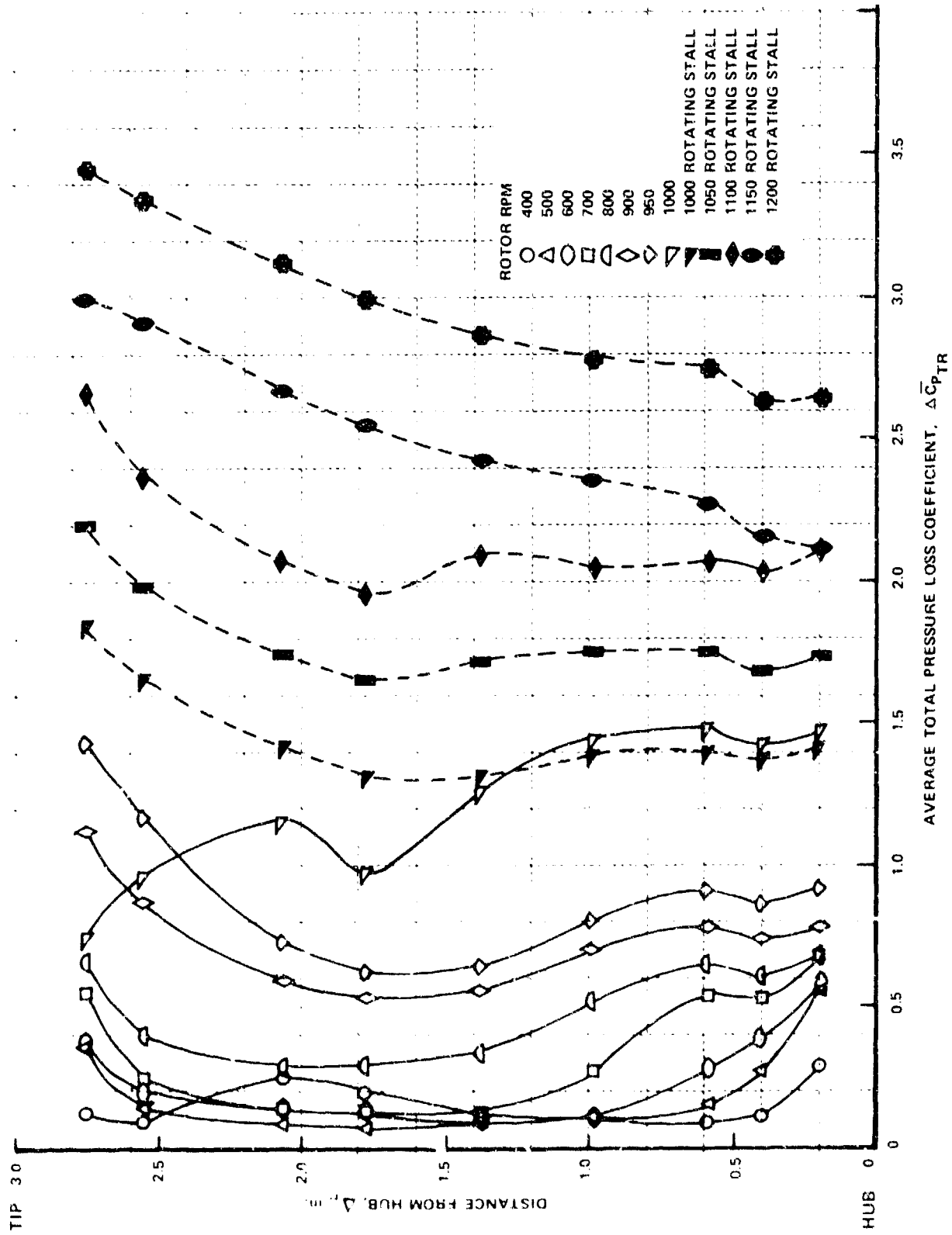


Figure 34 (Cont.) RADIAL DISTRIBUTIONS OF AVERAGE TOTAL PRESSURE LOSS THROUGH ROTOR SET NO. 1, COORDINATE SYSTEM MOVING WITH ROTOR  
 (b) ROTOR STAGGER ANGLE,  $\delta_{RM} = 40$  DEG

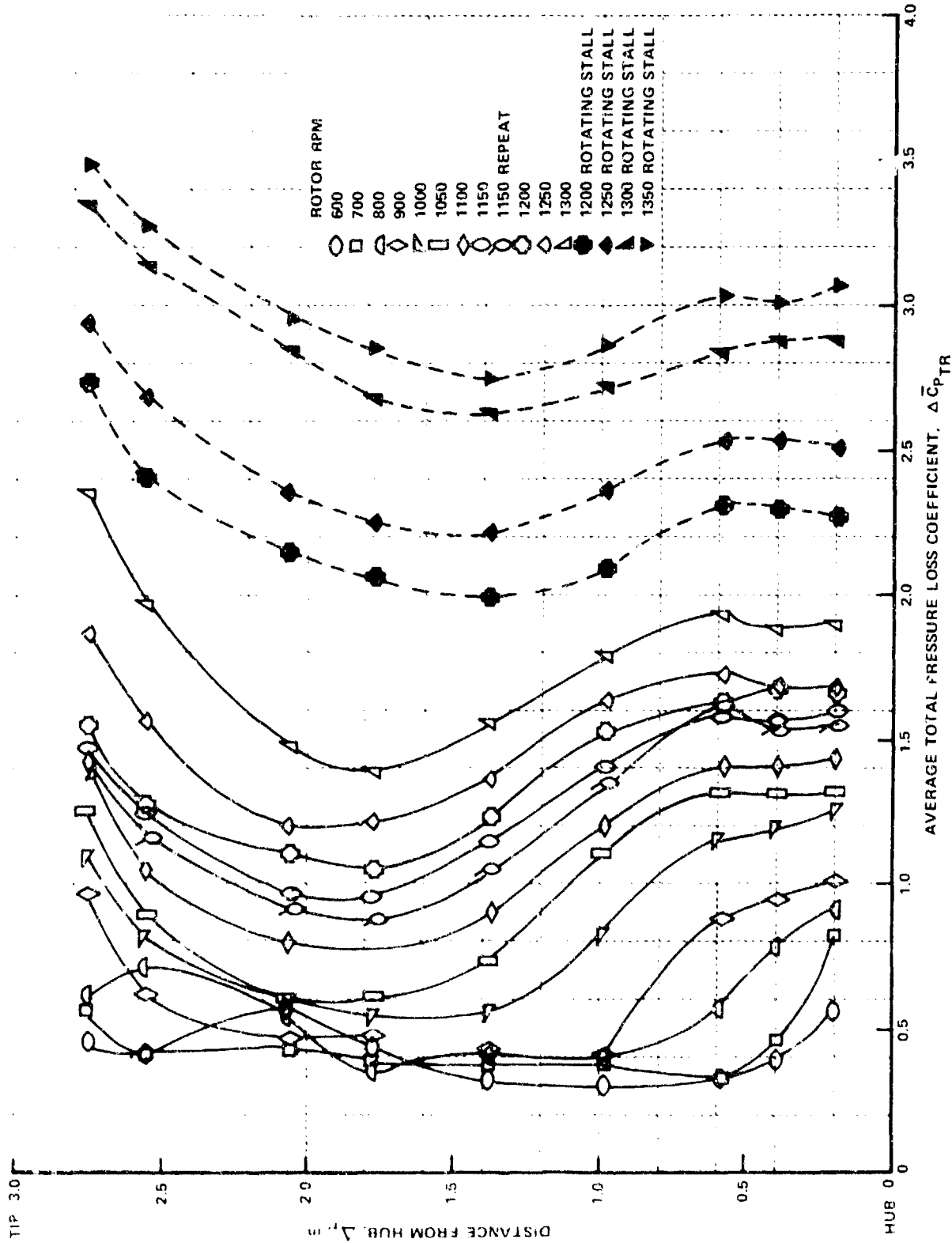


Figure 34 (Cont.) RADIAL DISTRIBUTIONS OF TOTAL PRESSURE LOSS THROUGH ROTOR SET NO. 1, COORDINATE SYSTEM MOVING WITH ROTOR

(c) ROTOR STAGGER ANGLE,  $\delta_{RM} = 50$  DEG

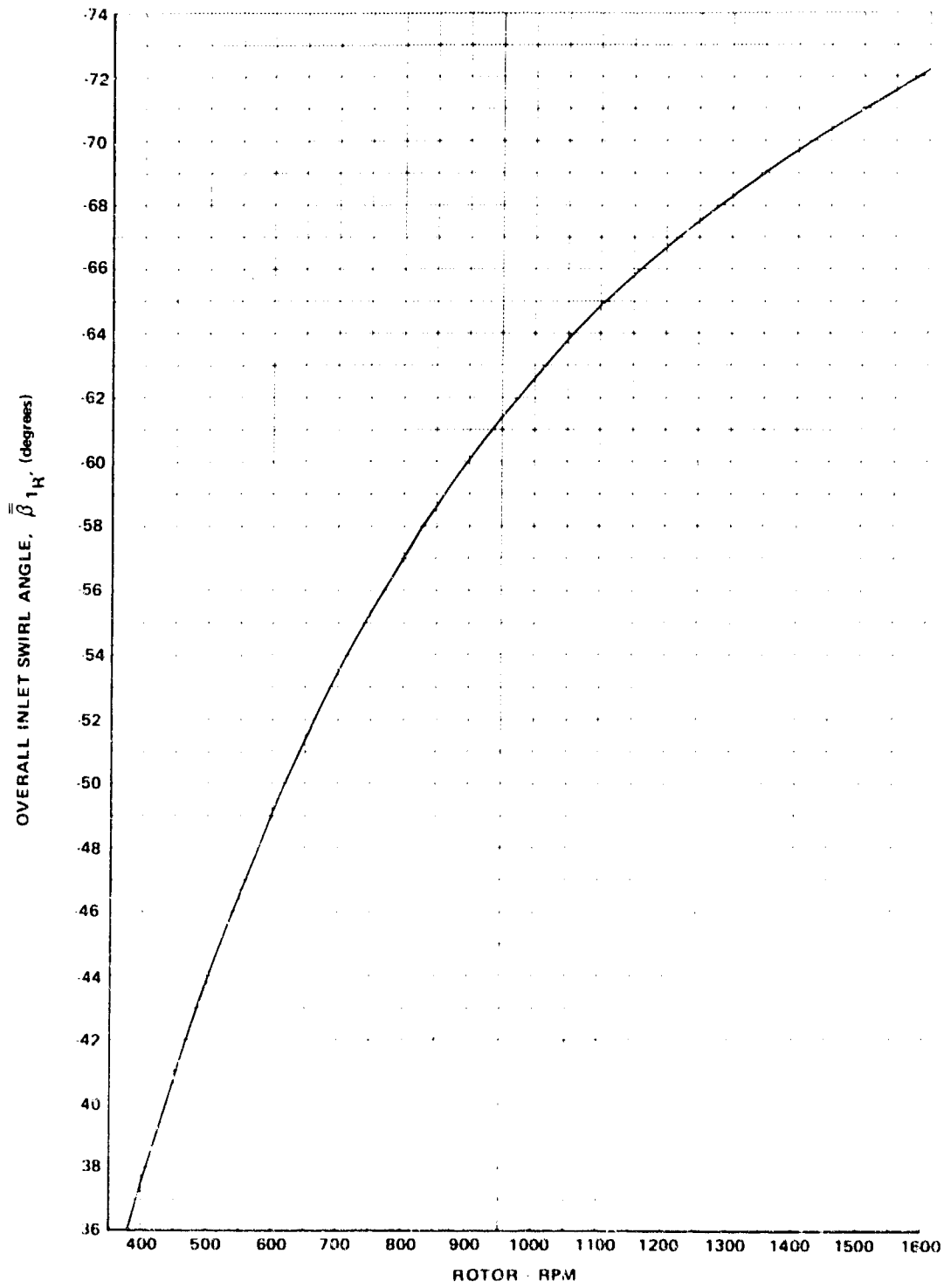


Figure 35 OVERALL INLET SWIRL ANGLE,  $\bar{\beta}_{1R}$ , RELATIVE TO ROTOR SET NO. 1, AS A FUNCTION OF ROTOR RPM

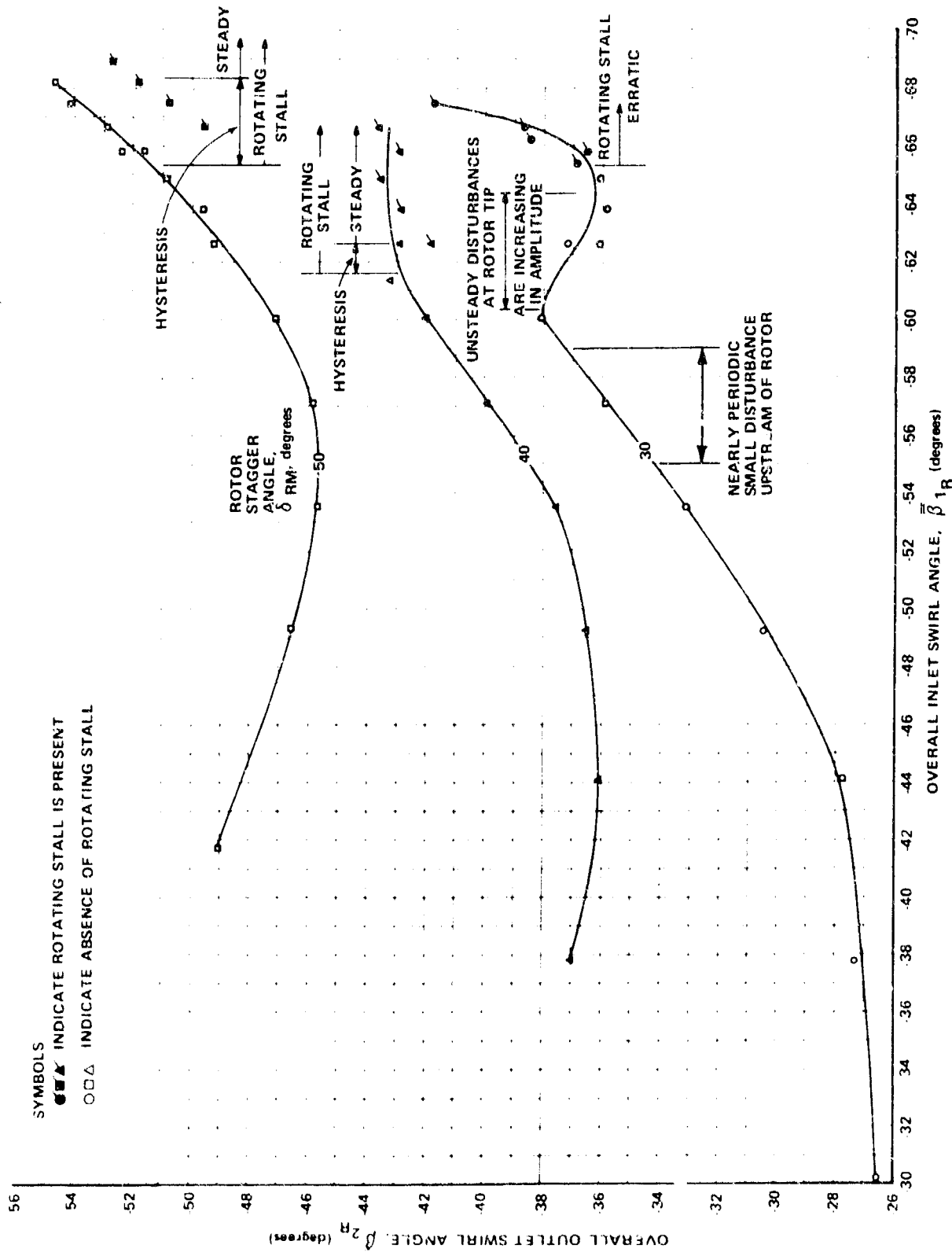


Figure 36 FLOW TURNING PERFORMANCE OF ROTOR SET NO. 1, COORDINATE SYSTEM RELATIVE TO ROTOR

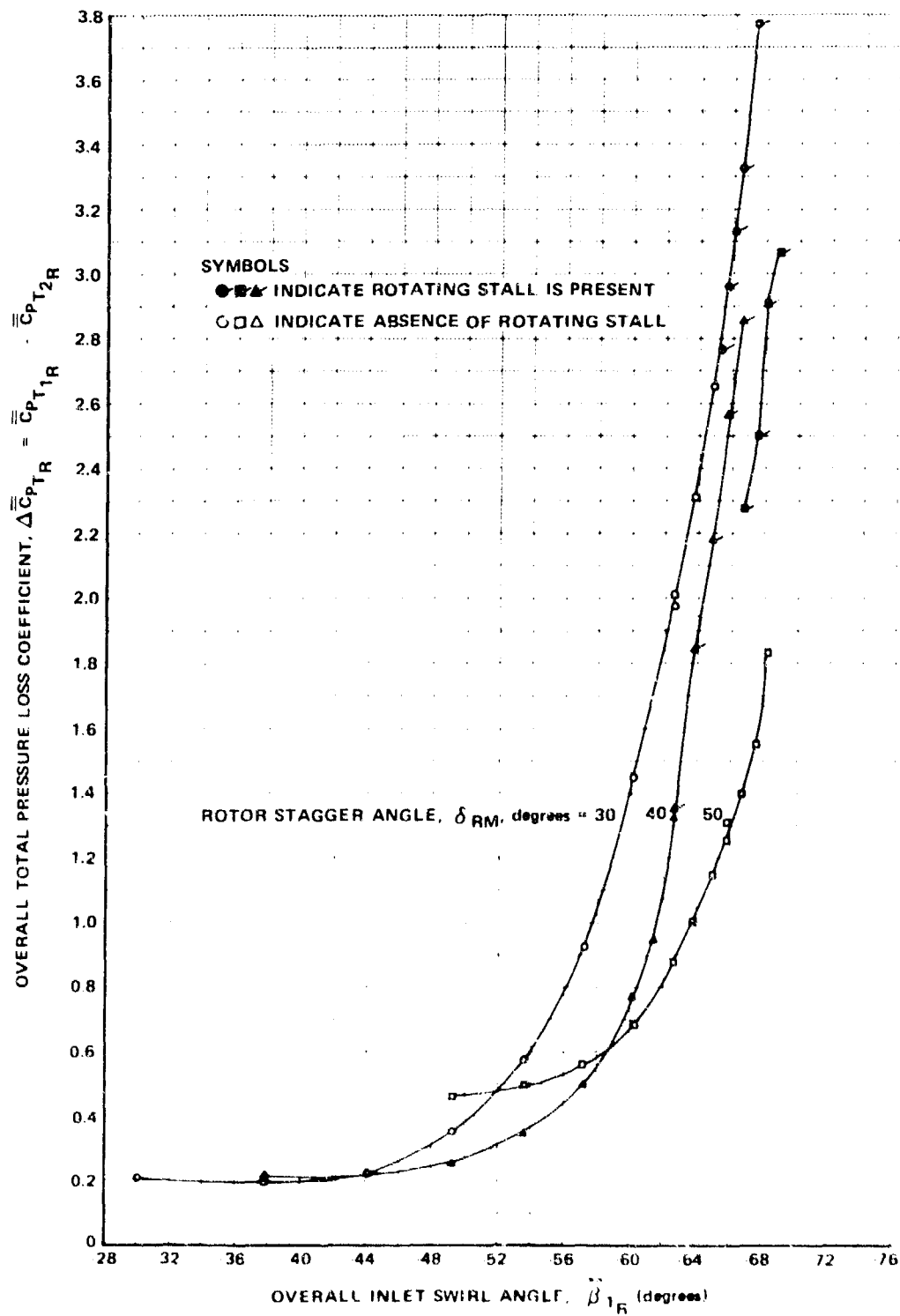


Figure 37 OVERALL TOTAL PRESSURE LOSS THROUGH ROTOR SET NO. 1, COORDINATE SYSTEM RELATIVE TO ROTOR

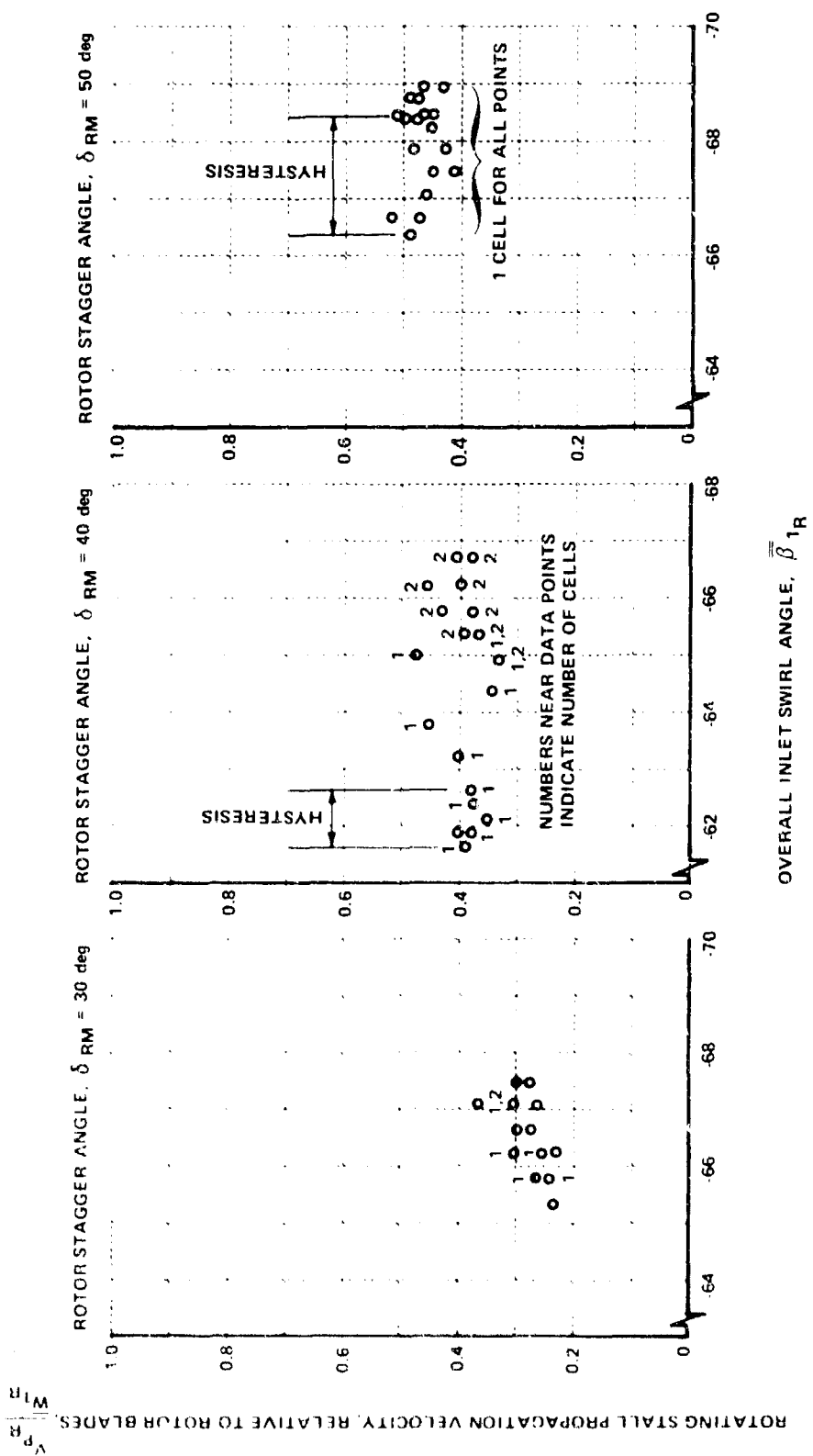


Figure 38 ROTATING STALL PROPAGATION VELOCITY AND NUMBER OF CELLS FOR ROTOR SET NO. 1, COORDINATE SYSTEM RELATIVE TO ROTOR



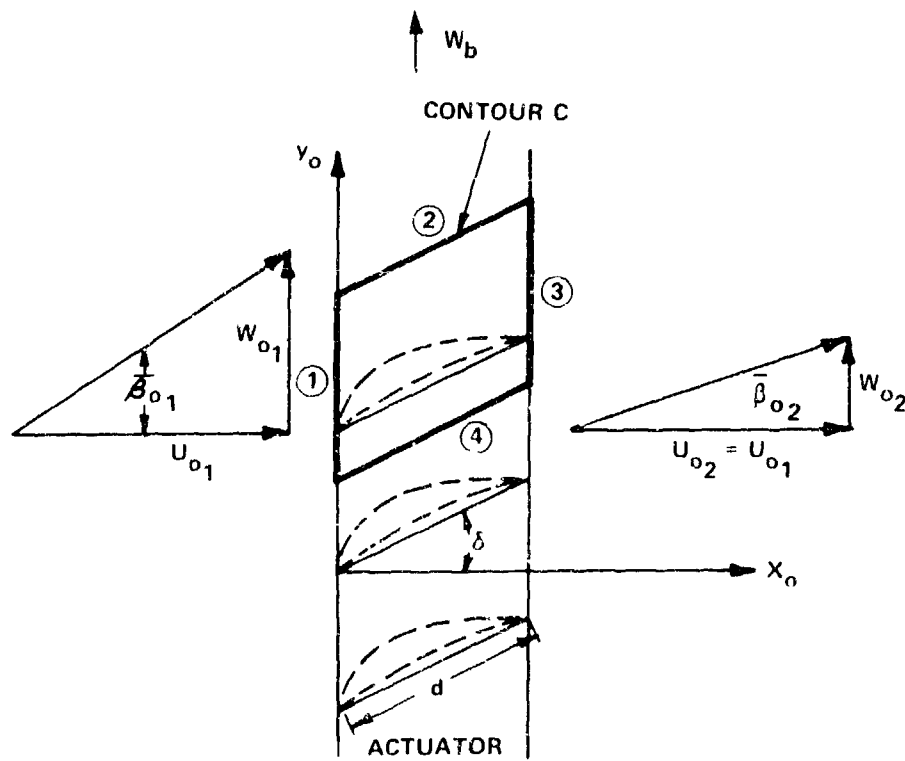


Figure 39 FINITE THICKNESS ACTUATOR MODEL FOR SINGLE BLADE ROW THEORY

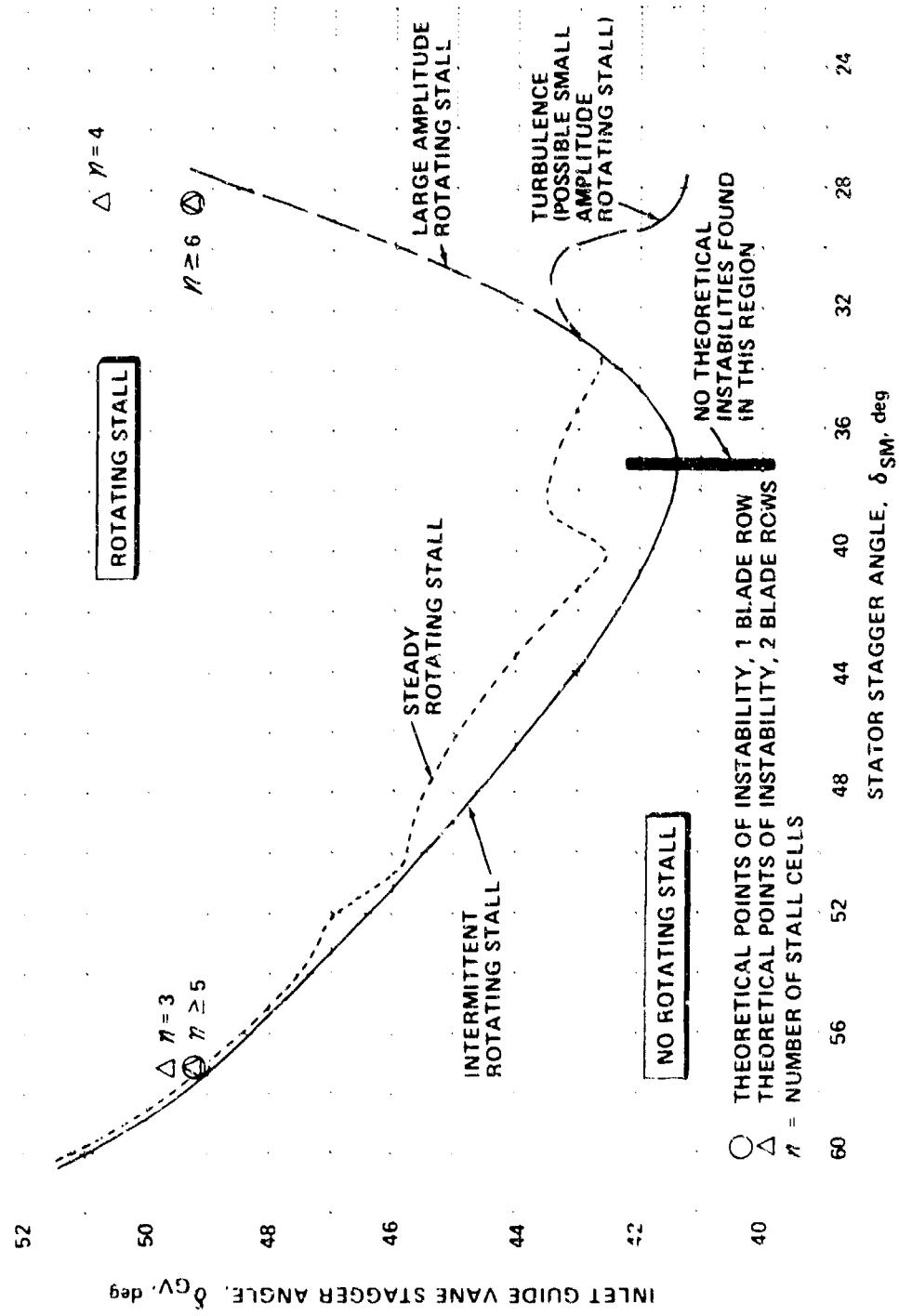
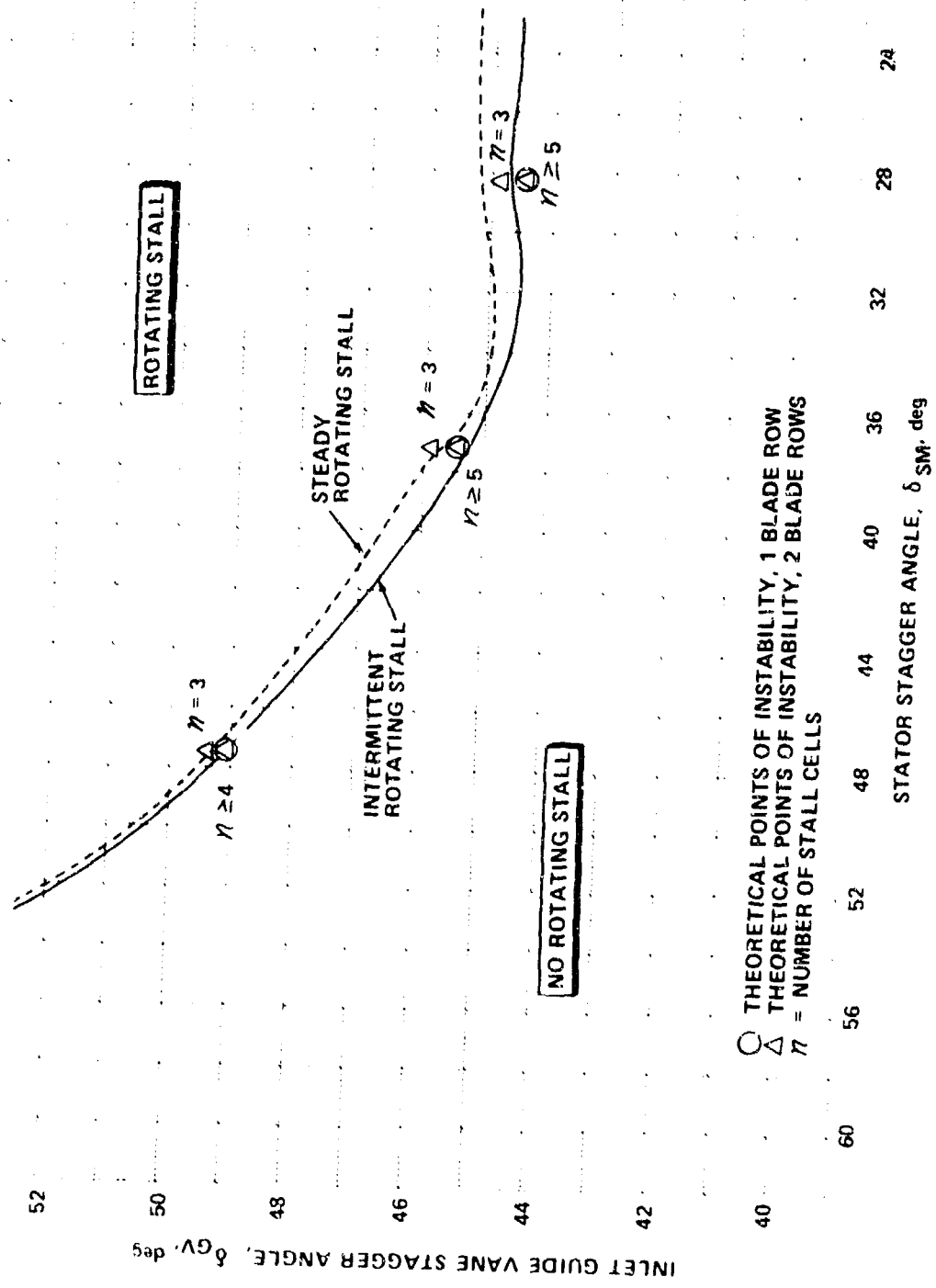


Figure 40 ROTATING STALL INCEPTION BOUNDARY ON STATOR SET NO. 1 AND COMPARISON WITH THEORY



○ THEORETICAL POINTS OF INSTABILITY, 1 BLADE ROW  
 △ THEORETICAL POINTS OF INSTABILITY, 2 BLADE ROWS  
 $n$  = NUMBER OF STALL CELLS

Figure 41 ROTATING STALL INCEPTION BOUNDARY ON STATOR SET NO. 4 AND COMPARISON WITH THEORY

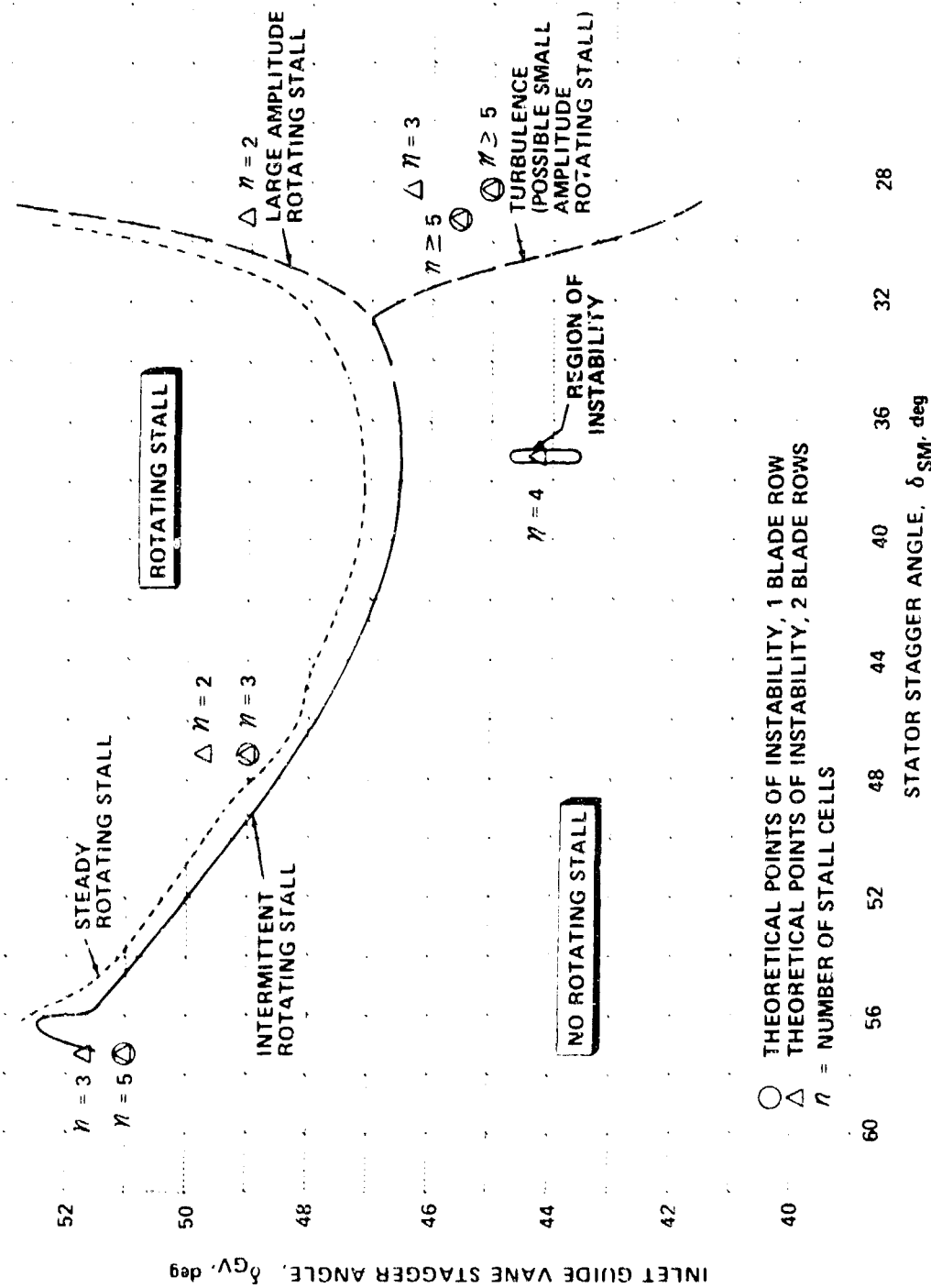


Figure 42 ROTATING STALL INCEPTION BOUNDARY ON STATOR SET NO. 5 AND COMPARISON WITH THEORY

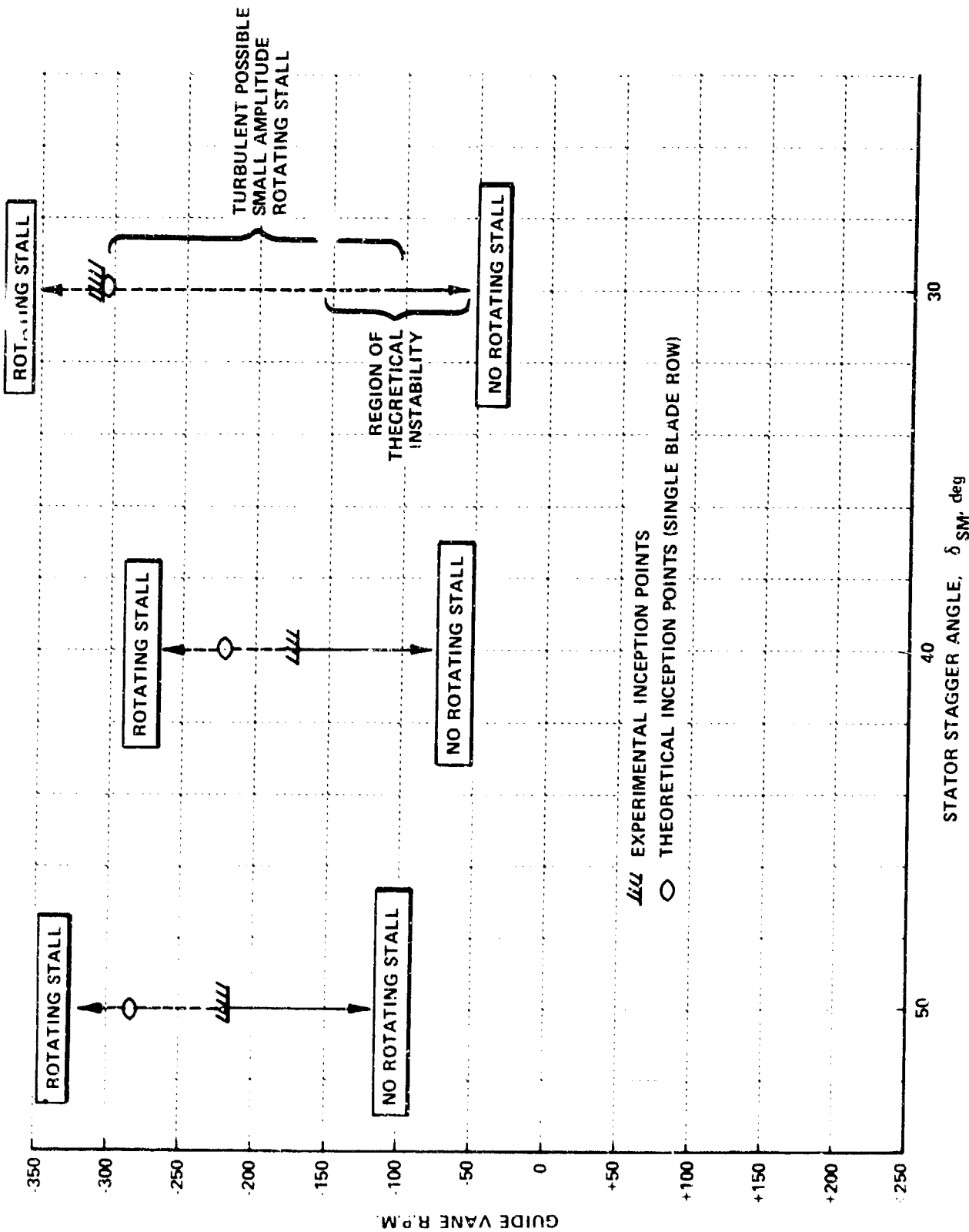


Figure 43 ROTATING STALL INCEPTION BOUNDARY ON STATOR SET NO. 6 AND COMPARISON WITH THEORY

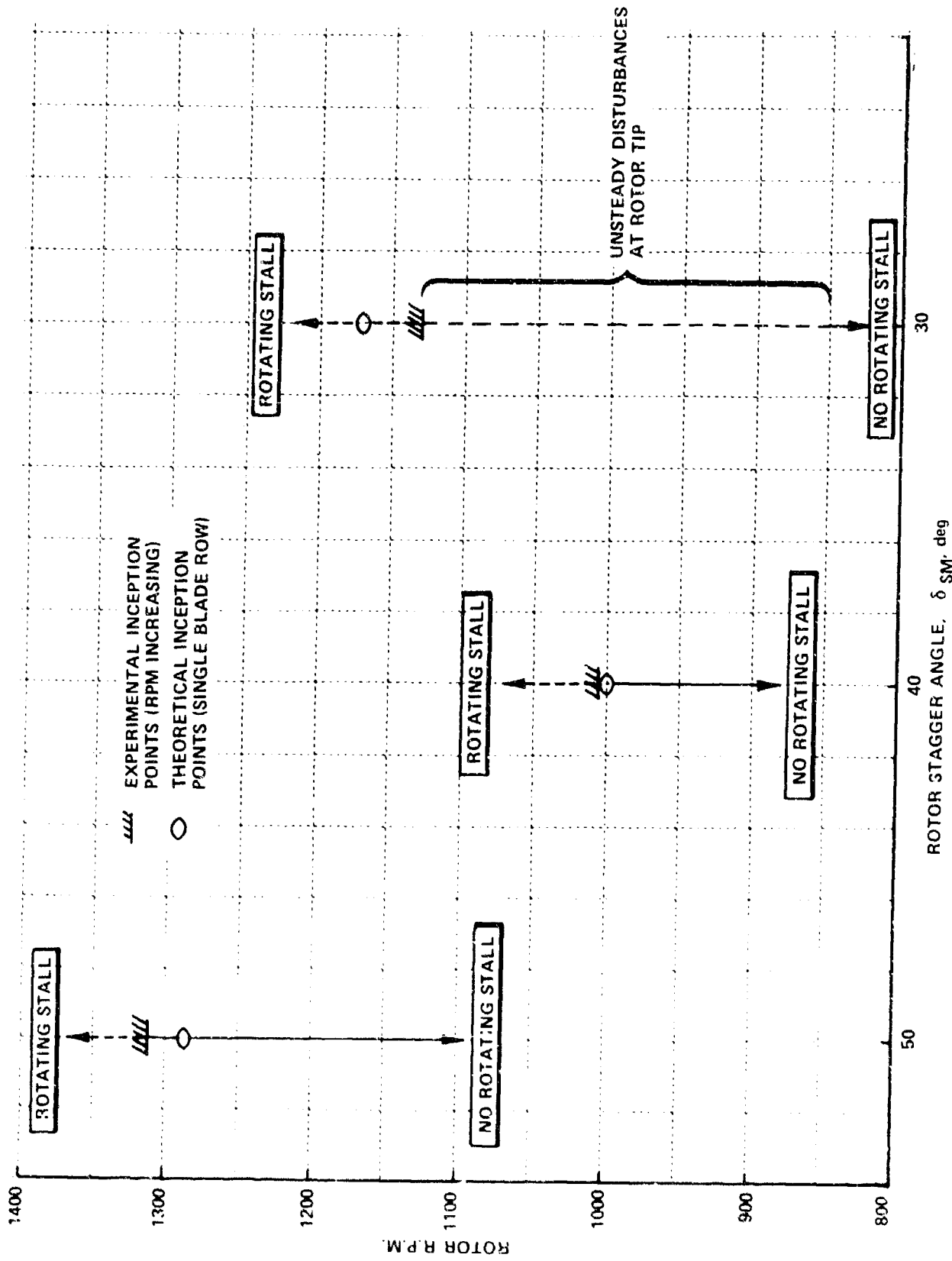


Figure 44 ROTATING STALL INCEPTION BOUNDARY ON ROTOR SET NO. 1 AND COMPARISON WITH THEORY

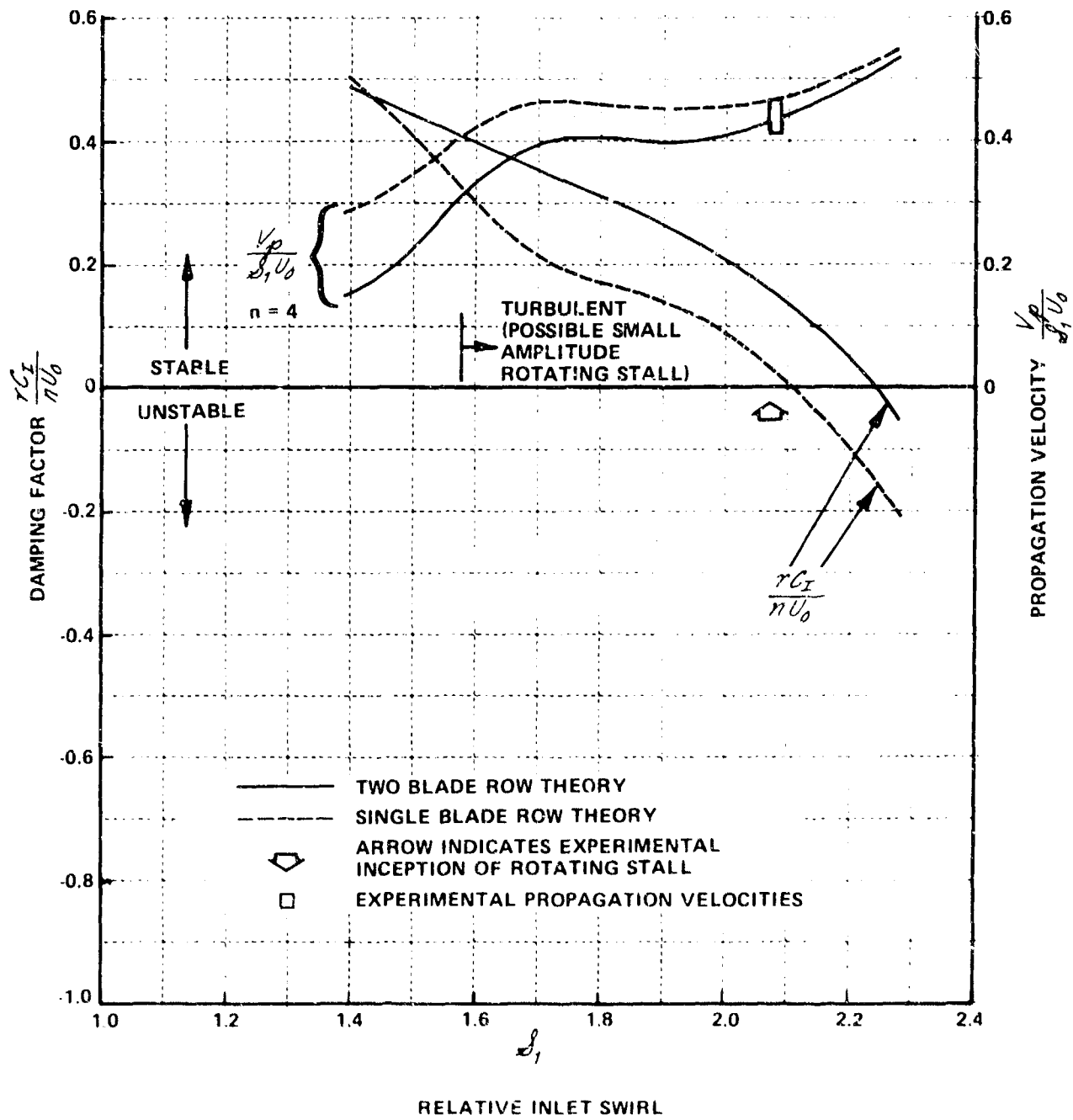


Figure 45 THEORETICAL STABILITY CHARACTERISTICS OF STATOR SET NO. 1  
 (a) STATOR STAGGER ANGLE,  $\delta_{SM} = 28.2$  DEG

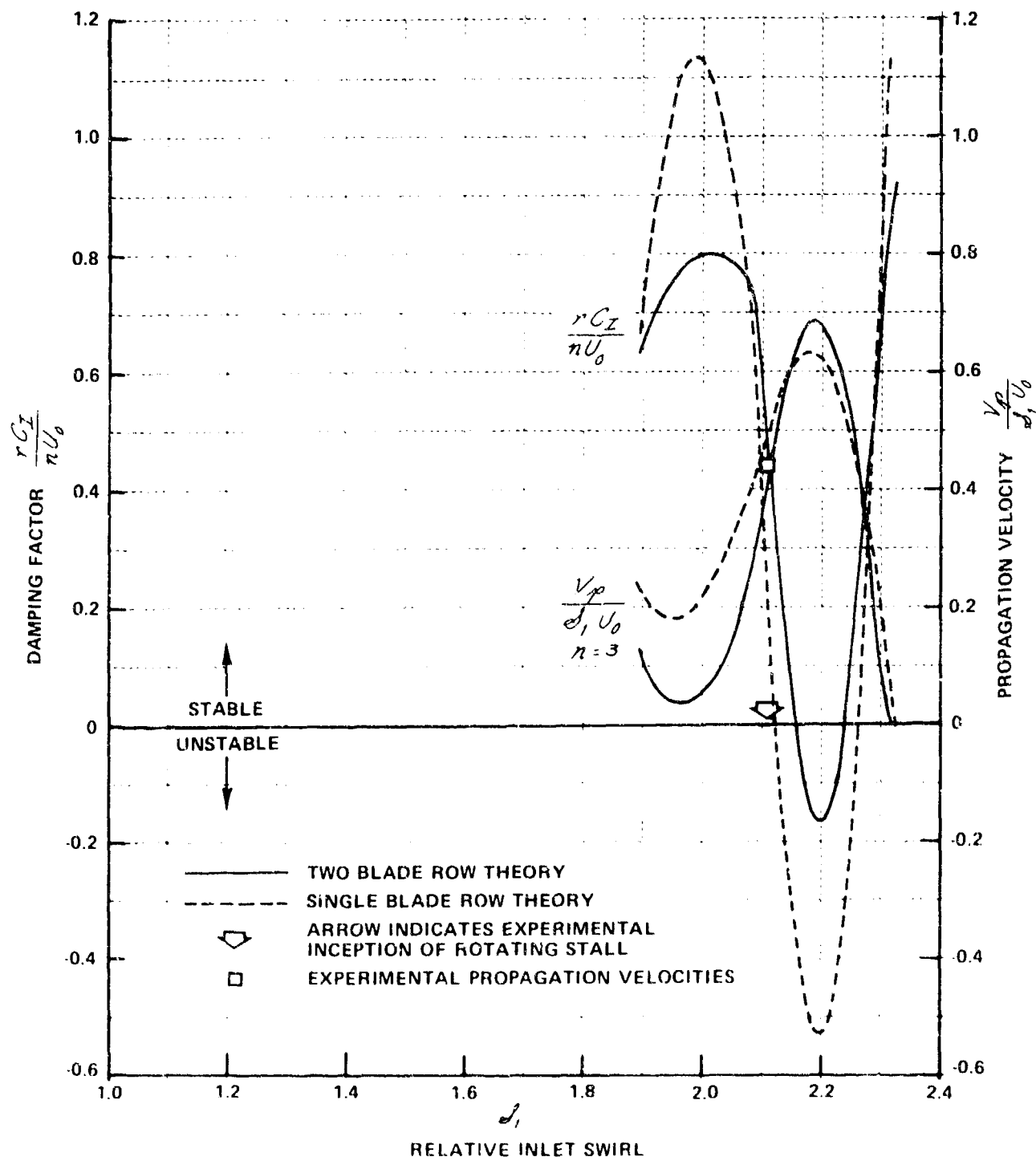


Figure 45 (Cont.) THEORETICAL STABILITY CHARACTERISTICS OF STATOR SET NO. 1  
 (b) STATOR STAGGER ANGLE,  $\delta_{SM} = 57.2$  DEG



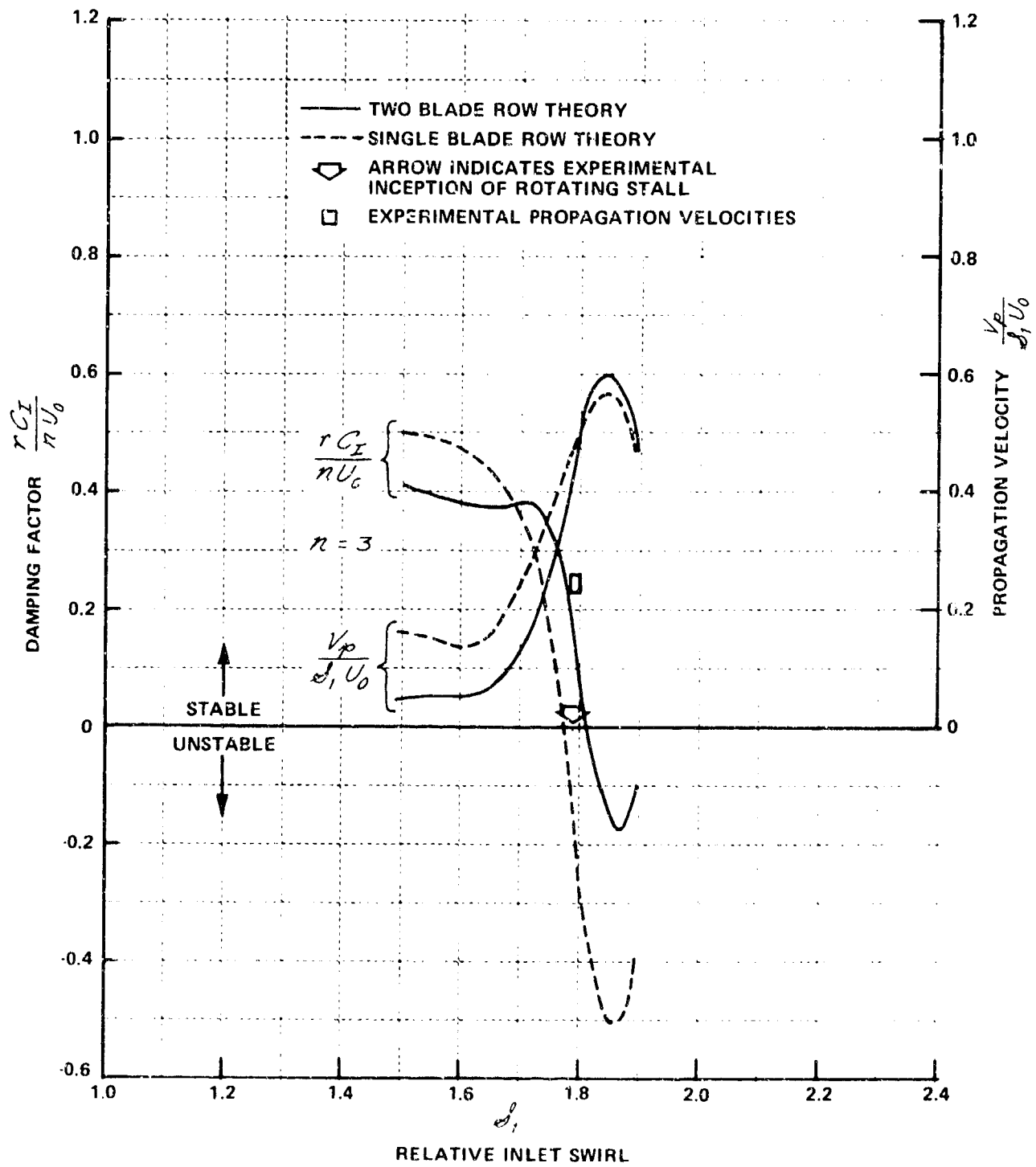


Figure 46 THEORETICAL STABILITY CHARACTERISTICS OF STATOR SET NO. 4  
 (a) STATOR STAGGER ANGLE,  $\delta_{SM} = 28.2$  DEG

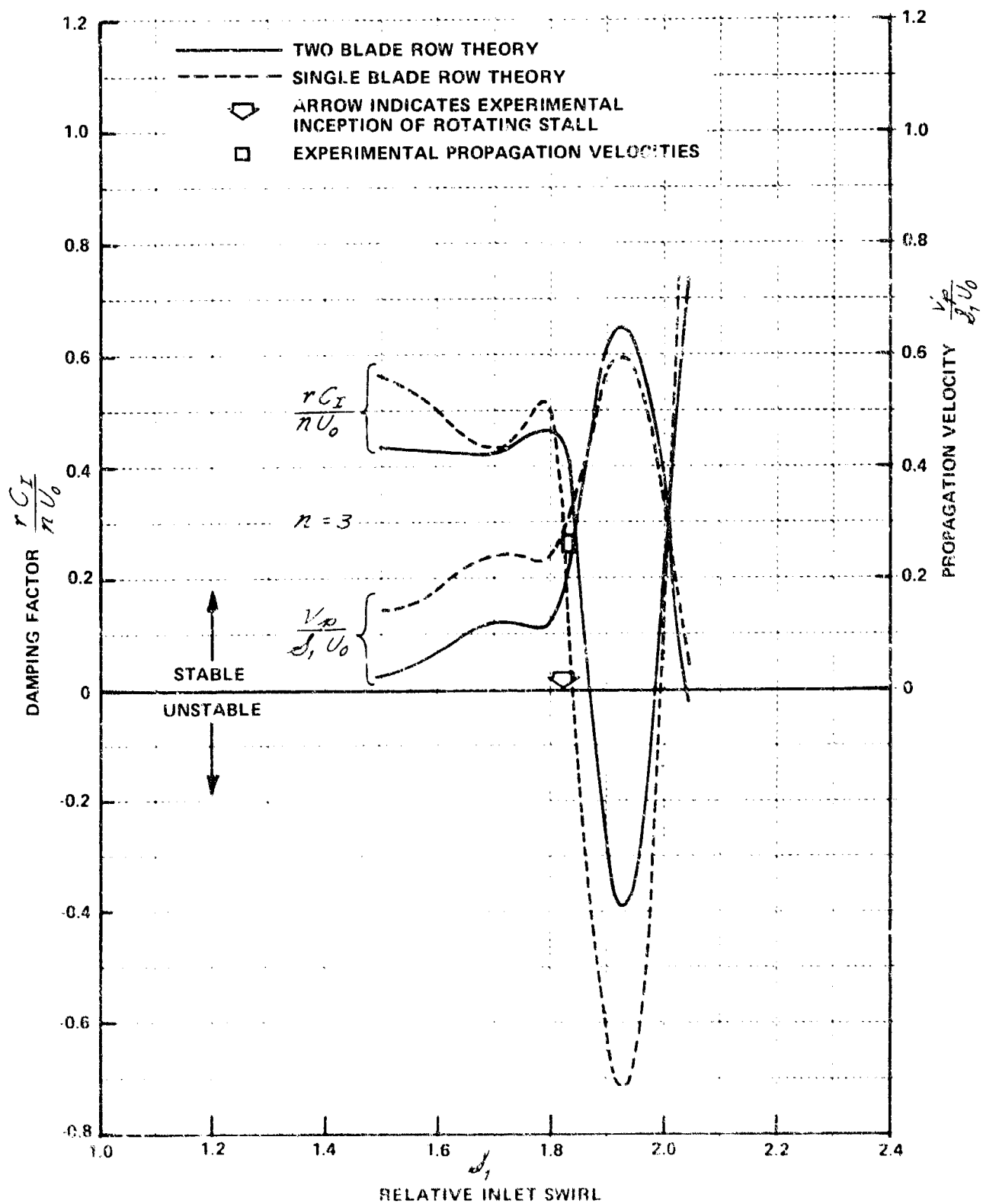


Figure 46 (Cont.) THEORETICAL STABILITY CHARACTERISTICS OF STATOR SET NO. 4  
 (b) STATOR STAGGER ANGLE,  $\delta_{SM} = 37.2$  DEG

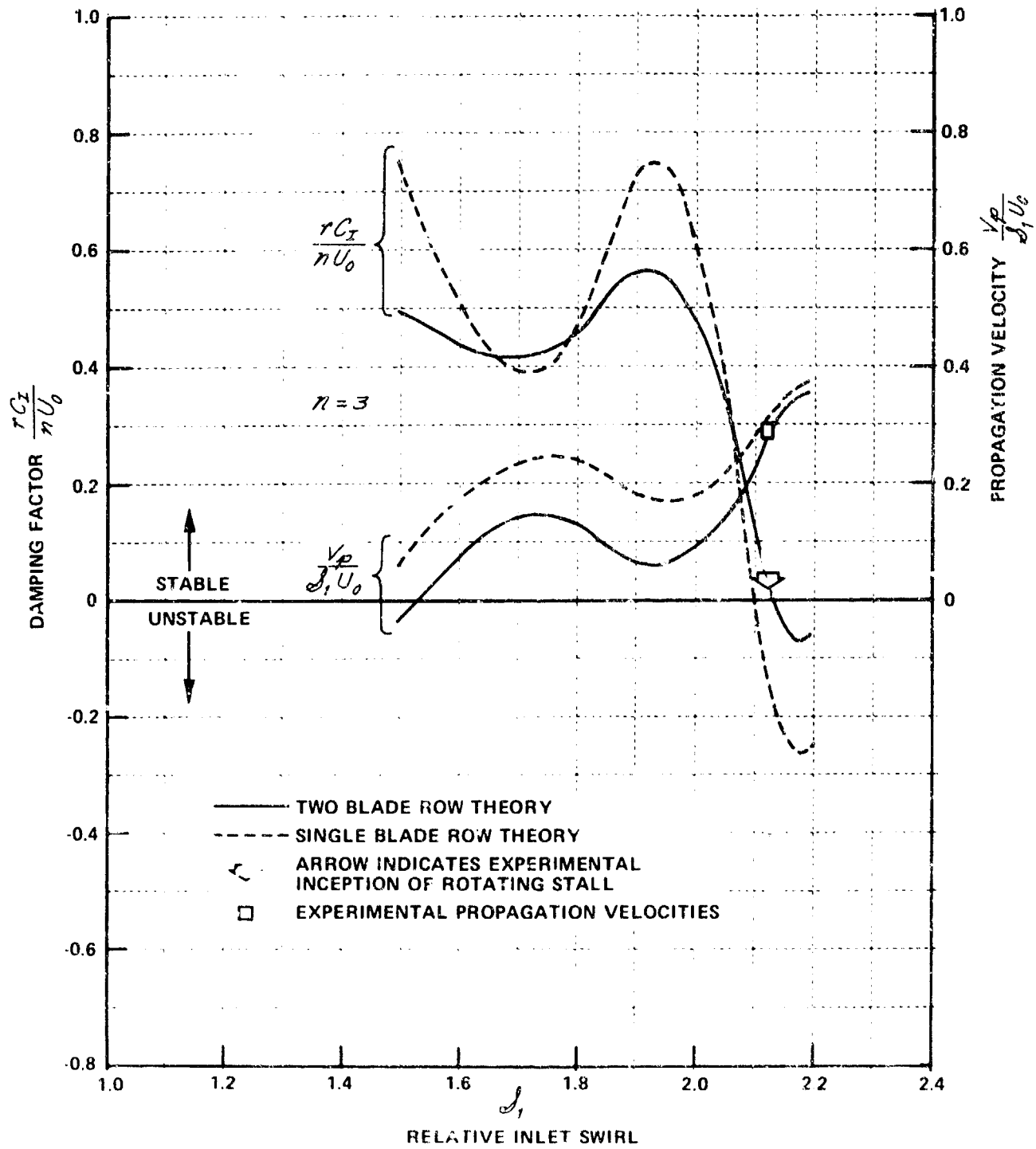


Figure 46 (Cont.) THEORETICAL STABILITY CHARACTERISTICS OF STATOR SET NO. 4  
 (c) STATOR STAGGER ANGLE,  $\delta_{SM} = 47.2$  DEG

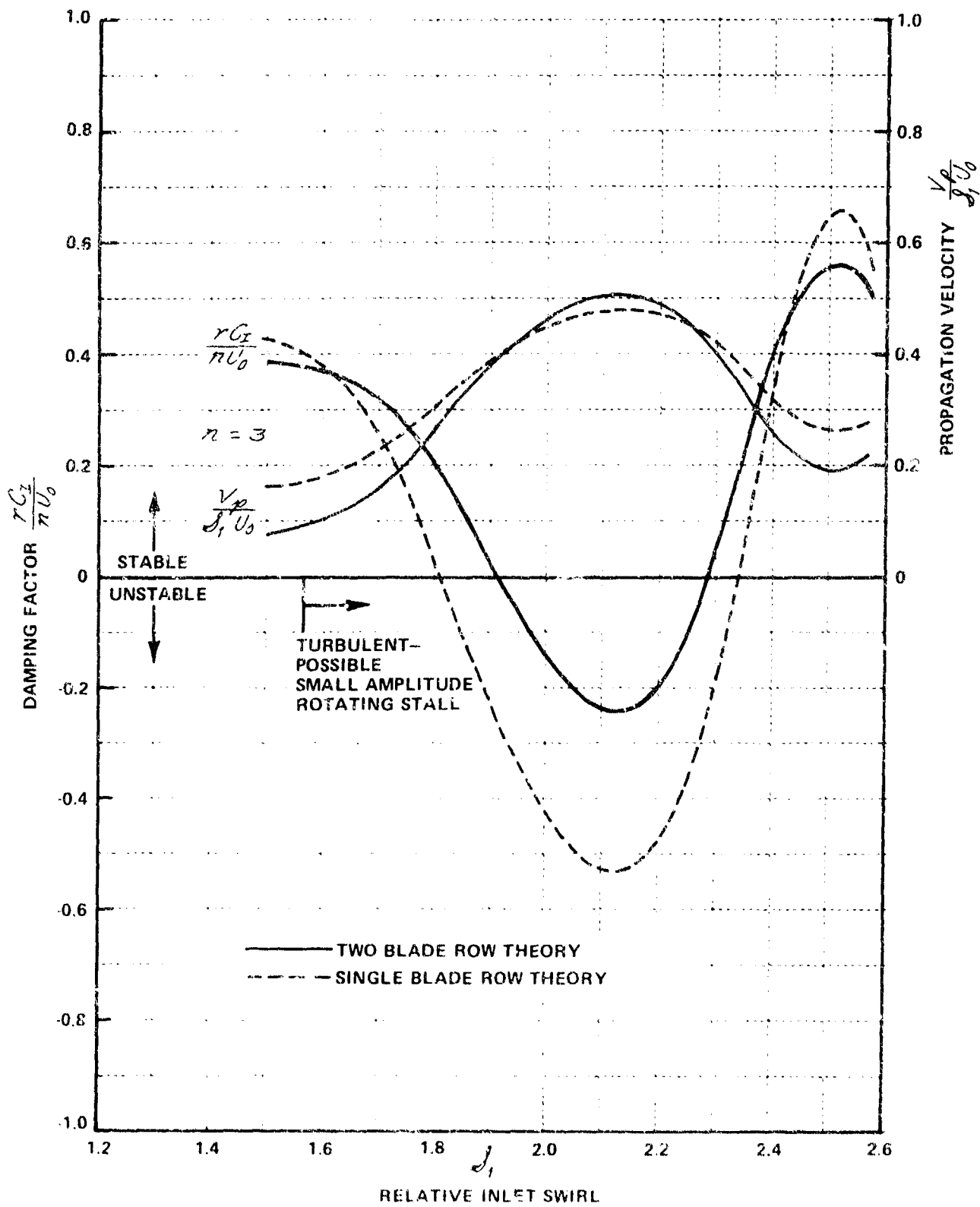


Figure 47 THEORETICAL STABILITY CHARACTERISTICS OF STATOR SET NO. 5  
 (a) STATOR STAGGER ANGLE,  $\delta_{SM} = 28.2$  DEG

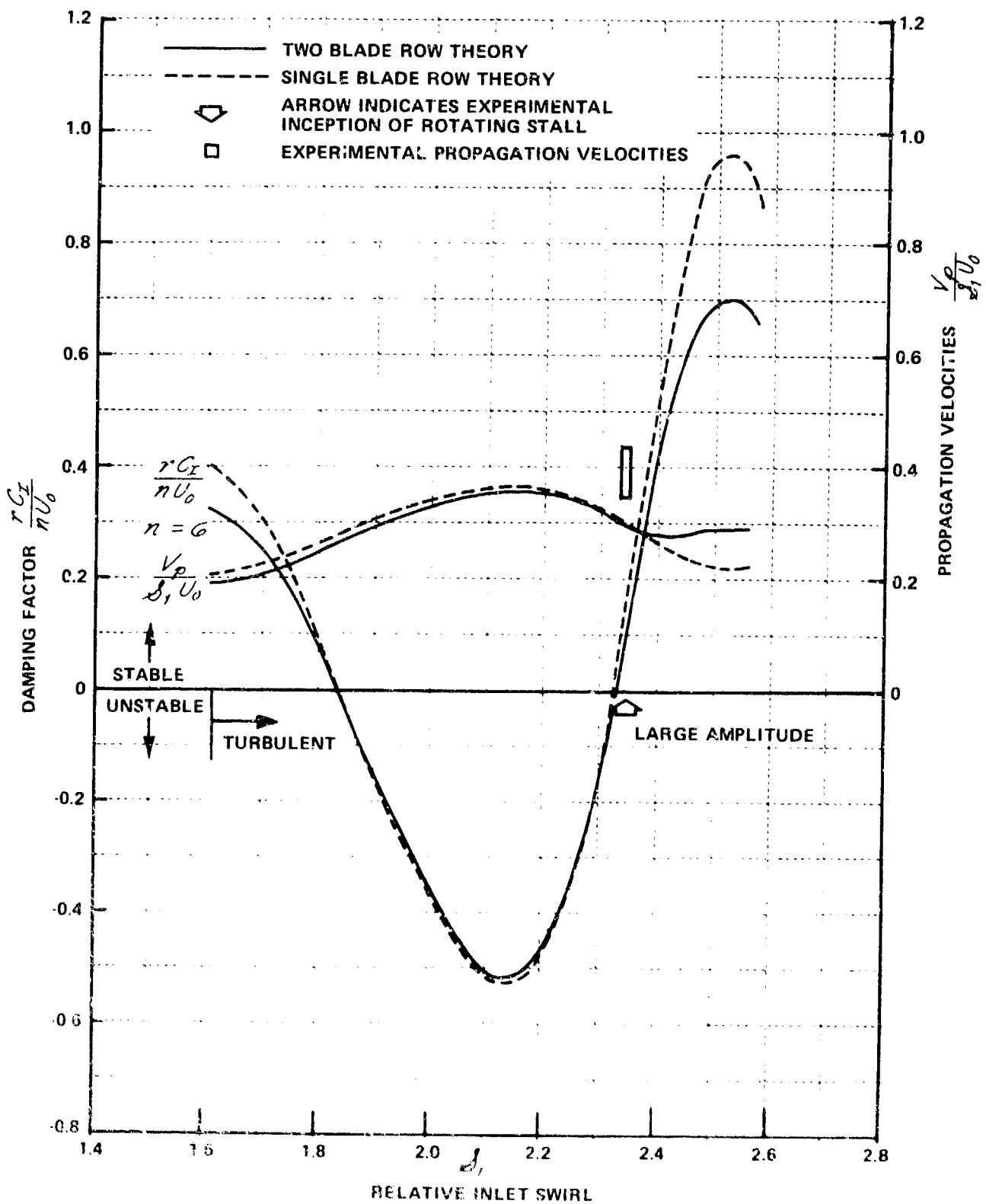


Figure 47 (Cont.) THEORETICAL STABILITY CHARACTERISTICS OF STATOR SET NO. 5  
 (b) STATOR STAGGER ANGLE,  $\delta_{SM} = 29.2$  DEG

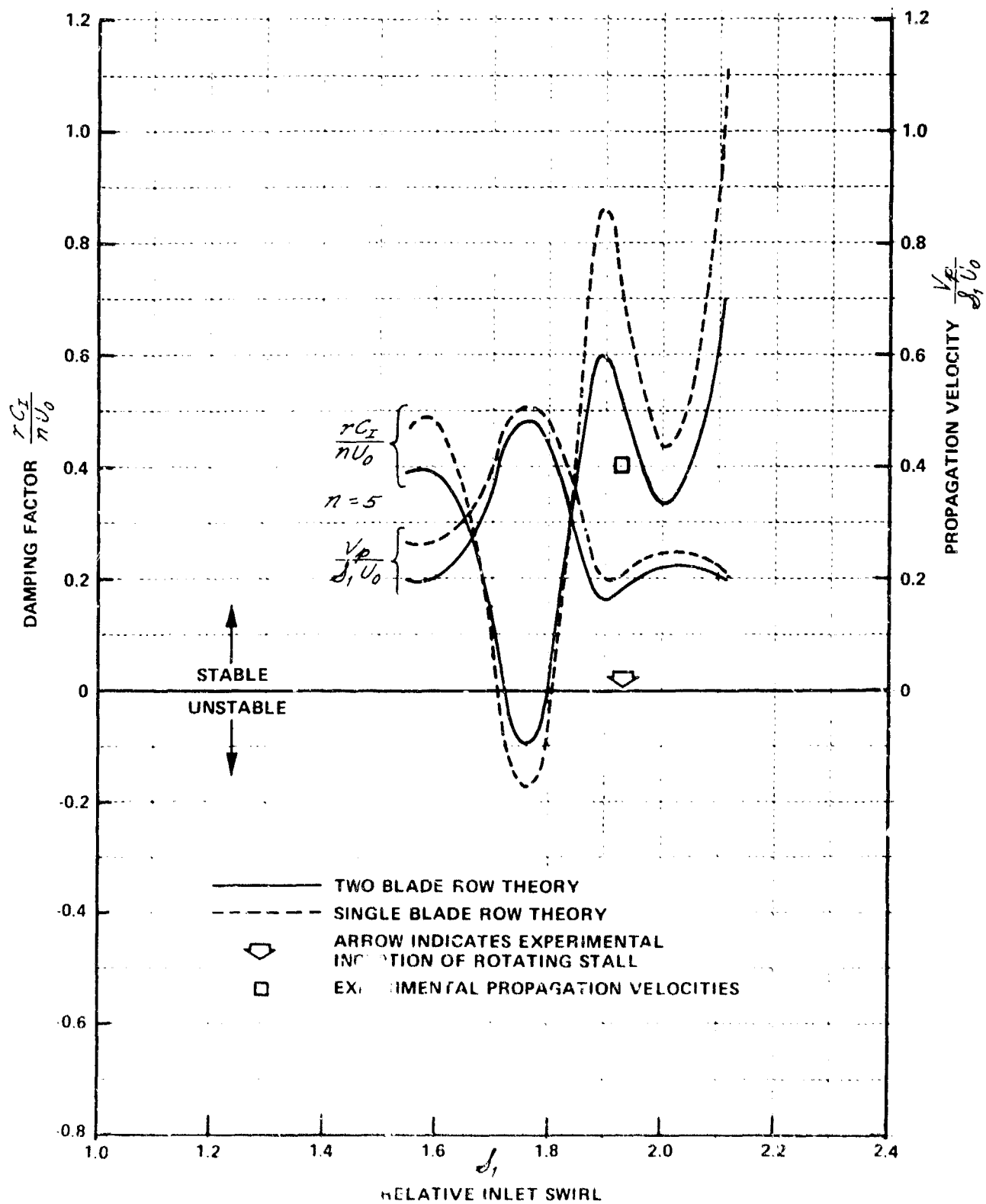


Figure 47 (Cont.) THEORETICAL STABILITY CHARACTERISTICS OF STATOR SET NO. 5  
 (c) STATOR STAGGER ANGLE,  $\delta_{SM} = 37.2$  DEG

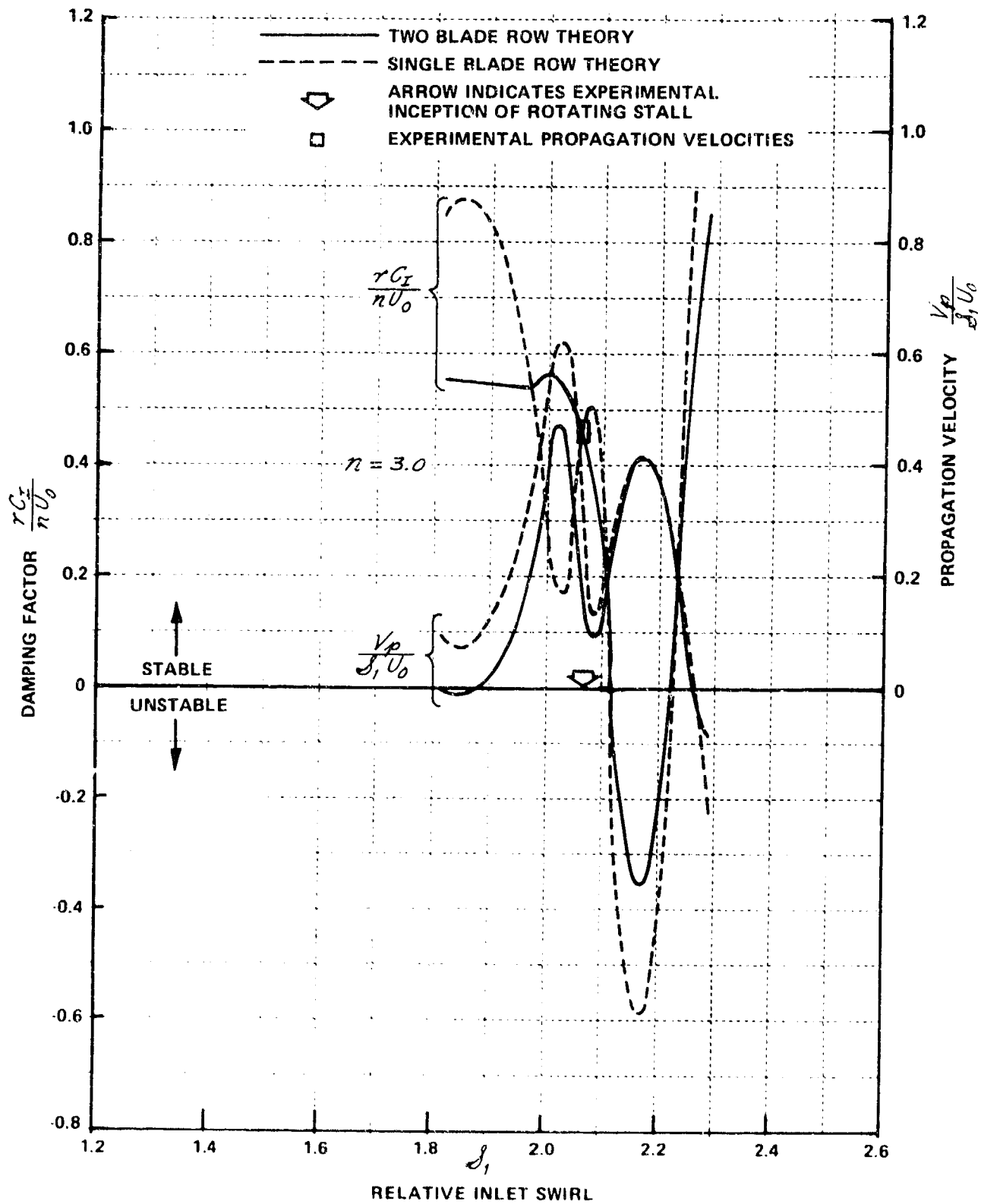


Figure 47 (Cont.) THEORETICAL STABILITY CHARACTERISTICS OF STATOR SET NO. 5  
 (d) STATOR STAGGER ANGLE,  $\delta_{SM} = 47.2$  DEG

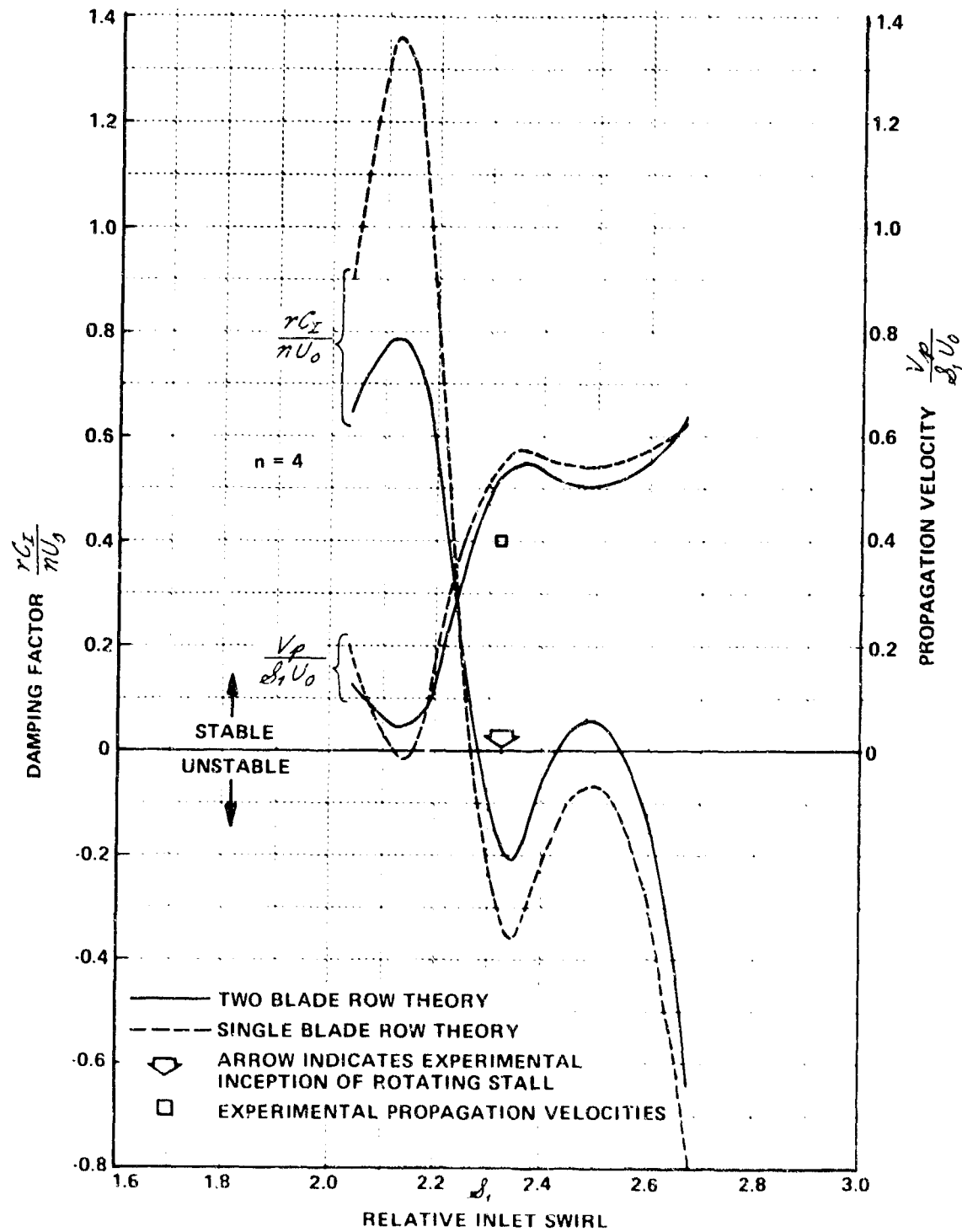


Figure 47 (Cont.) THEORETICAL STABILITY CHARACTERISTICS OF STATOR SET NO. 5  
 (e) STATOR STAGGER ANGLE,  $\delta_{SM} = 57.2$  DEG



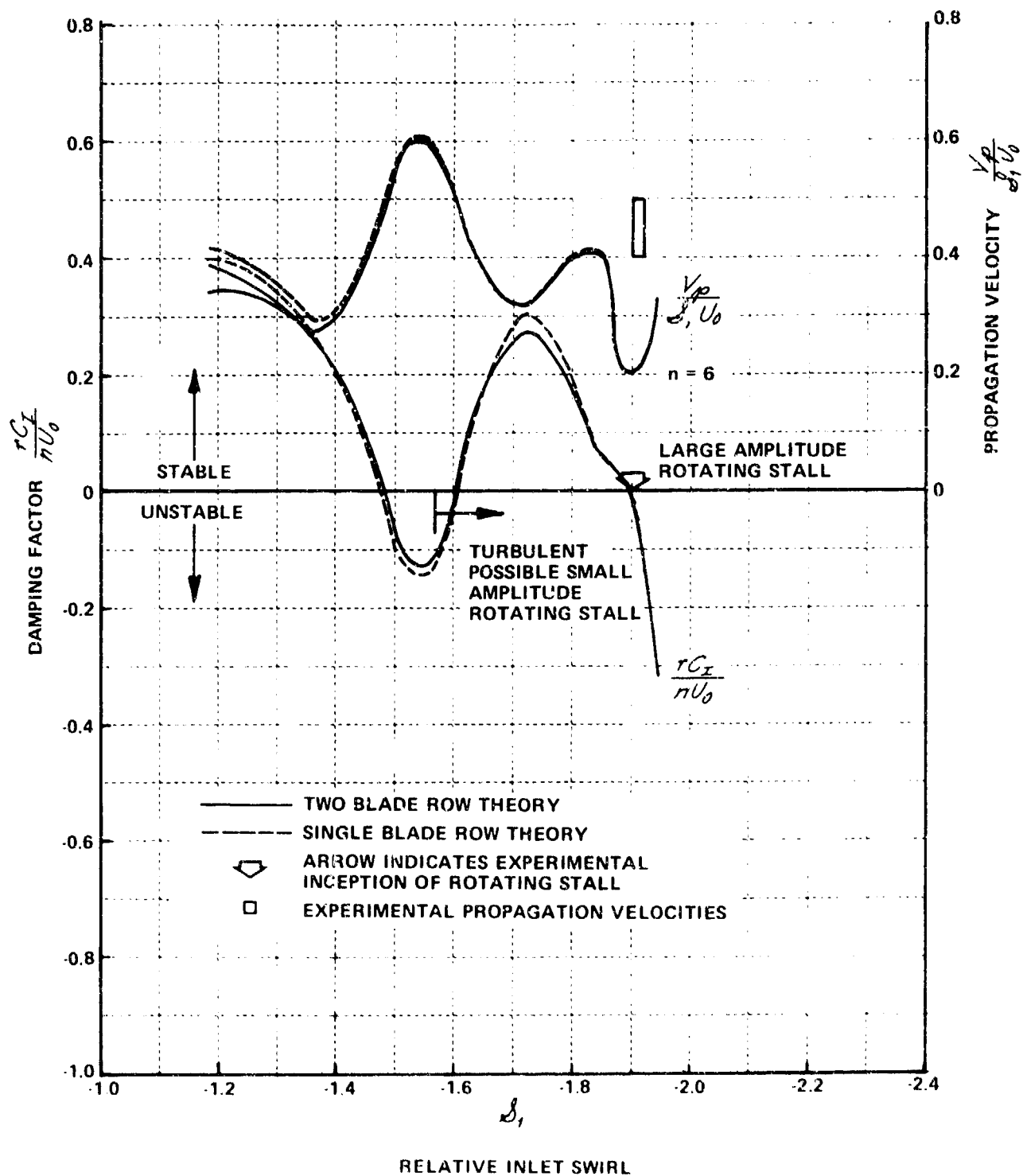


Figure 48 THEORETICAL STABILITY CHARACTERISTICS OF STATOR SET NO. 6  
 (a) STATOR STAGGER ANGLE,  $\delta_{SM} = 30$  DEG

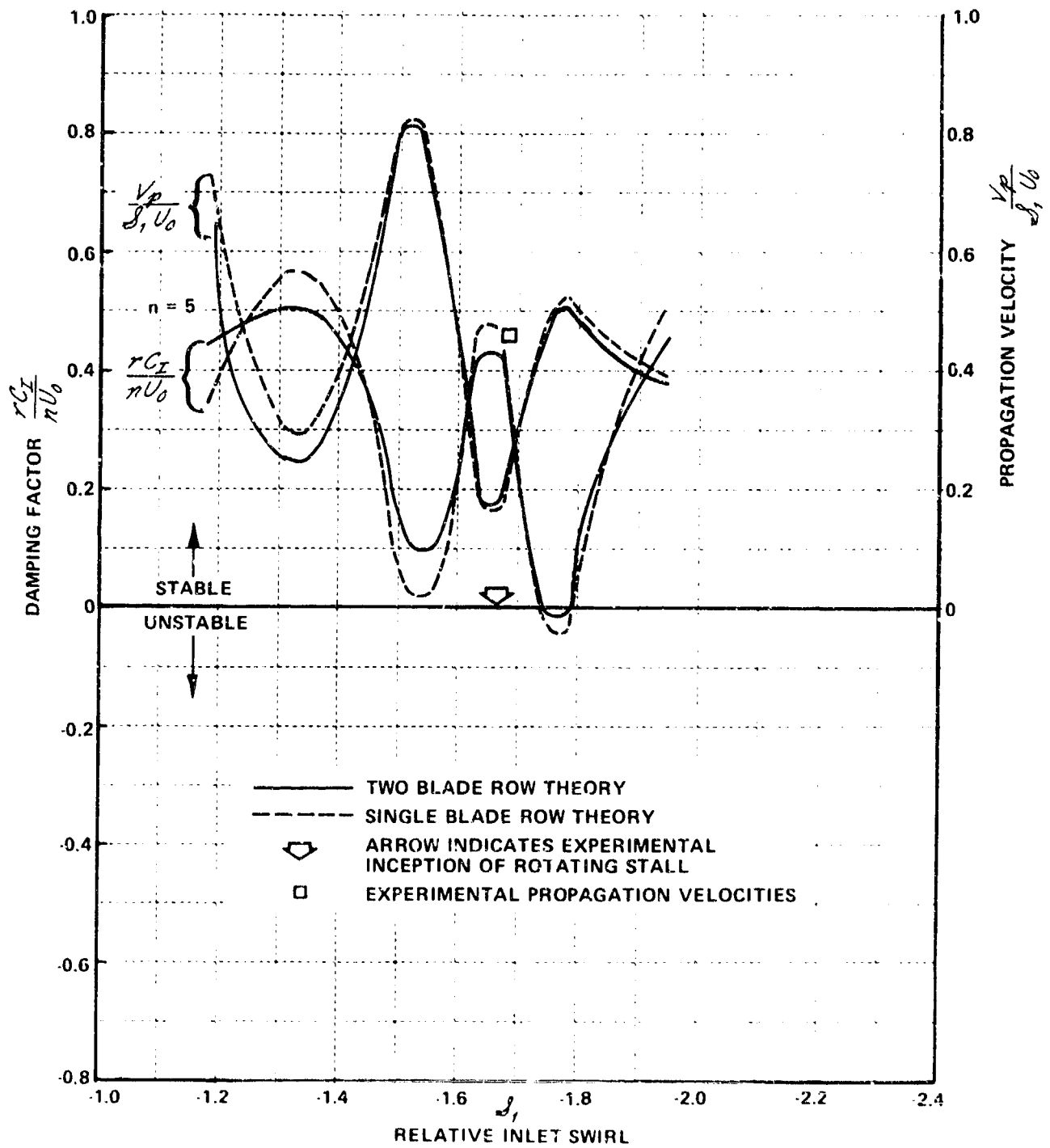


Figure 48 (Cont.) THEORETICAL STABILITY CHARACTERISTICS OF STATOR SET NO. 6  
 (b) STATOR STAGGER ANGLE,  $\delta_{SM} = 40$  DEG

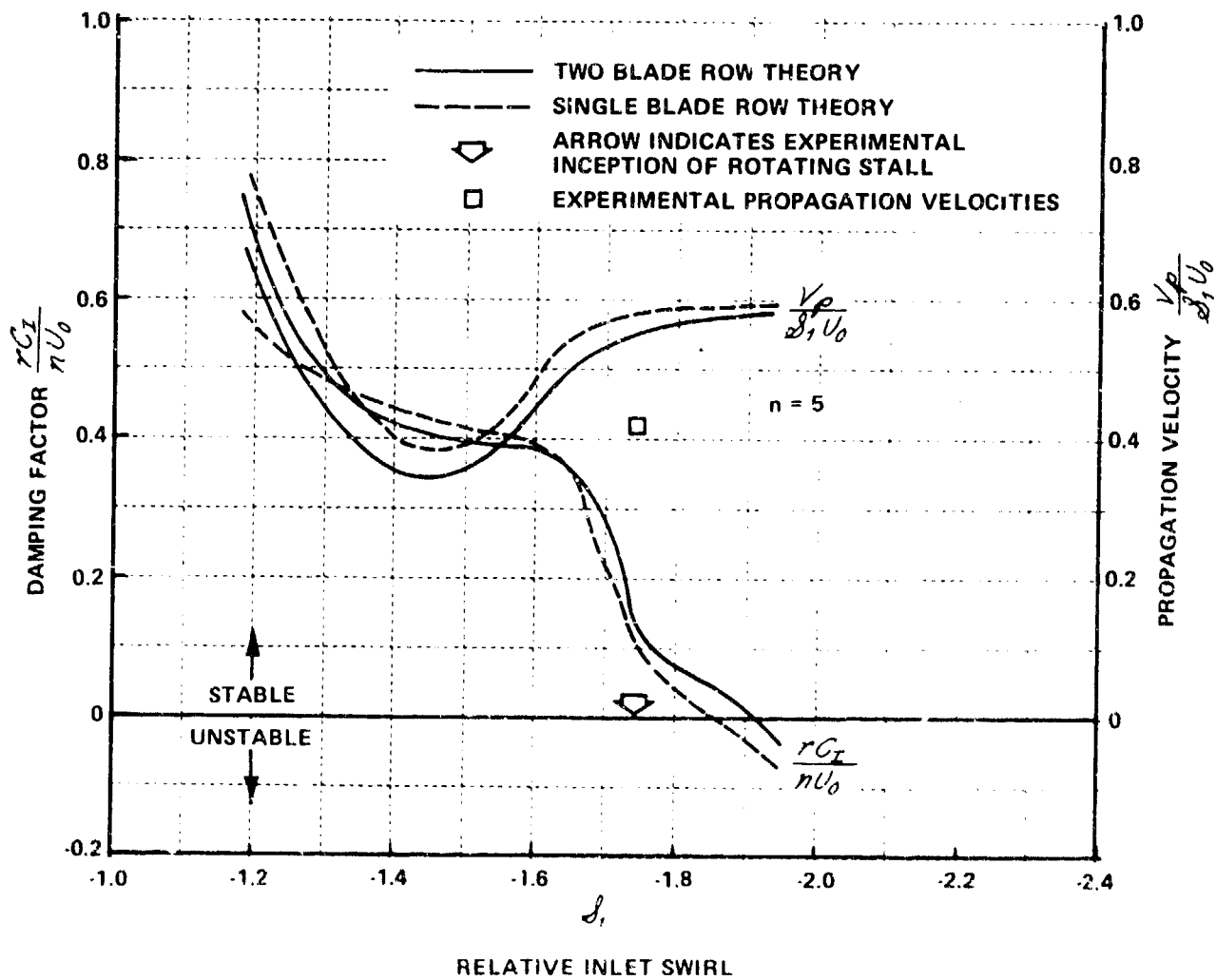


Figure 48 (Cont.) THEORETICAL STABILITY CHARACTERISTICS OF STATOR SET NO. 6  
 (c) STATOR STAGGER ANGLE,  $\delta_{SM} = 50$  DEG

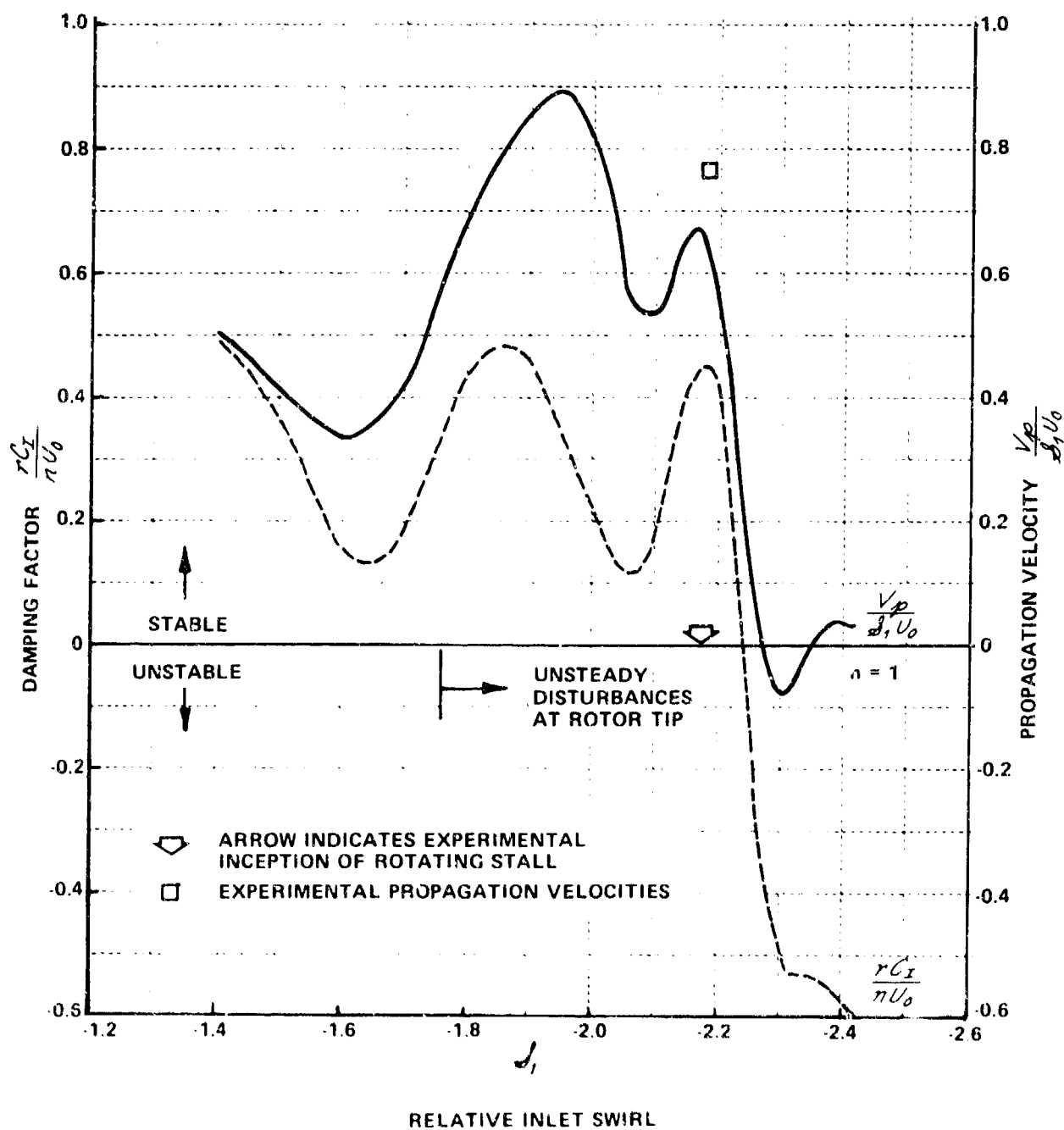


Figure 49 THEORETICAL STABILITY CHARACTERISTICS OF ROTOR SET NO. 1

(a) ROTOR STAGGER ANGLE,  $\delta_{RM} = 30$  DEG

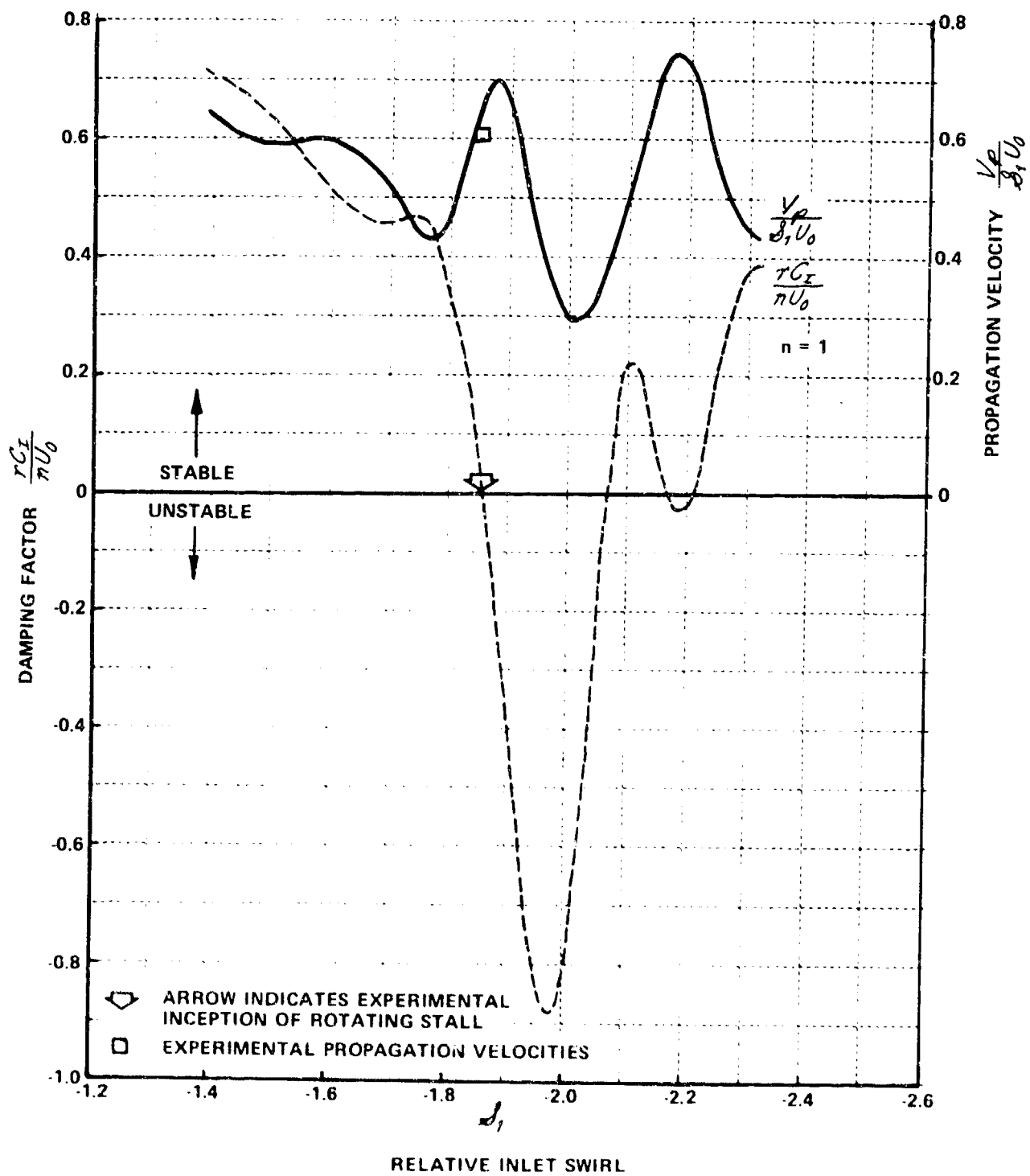


Figure 49 (Cont.) THEORETICAL STABILITY CHARACTERISTICS OF ROTOR SET NO. 1  
 (b) ROTOR STAGGER ANGLE,  $\delta_{RM} = 40$  DEG

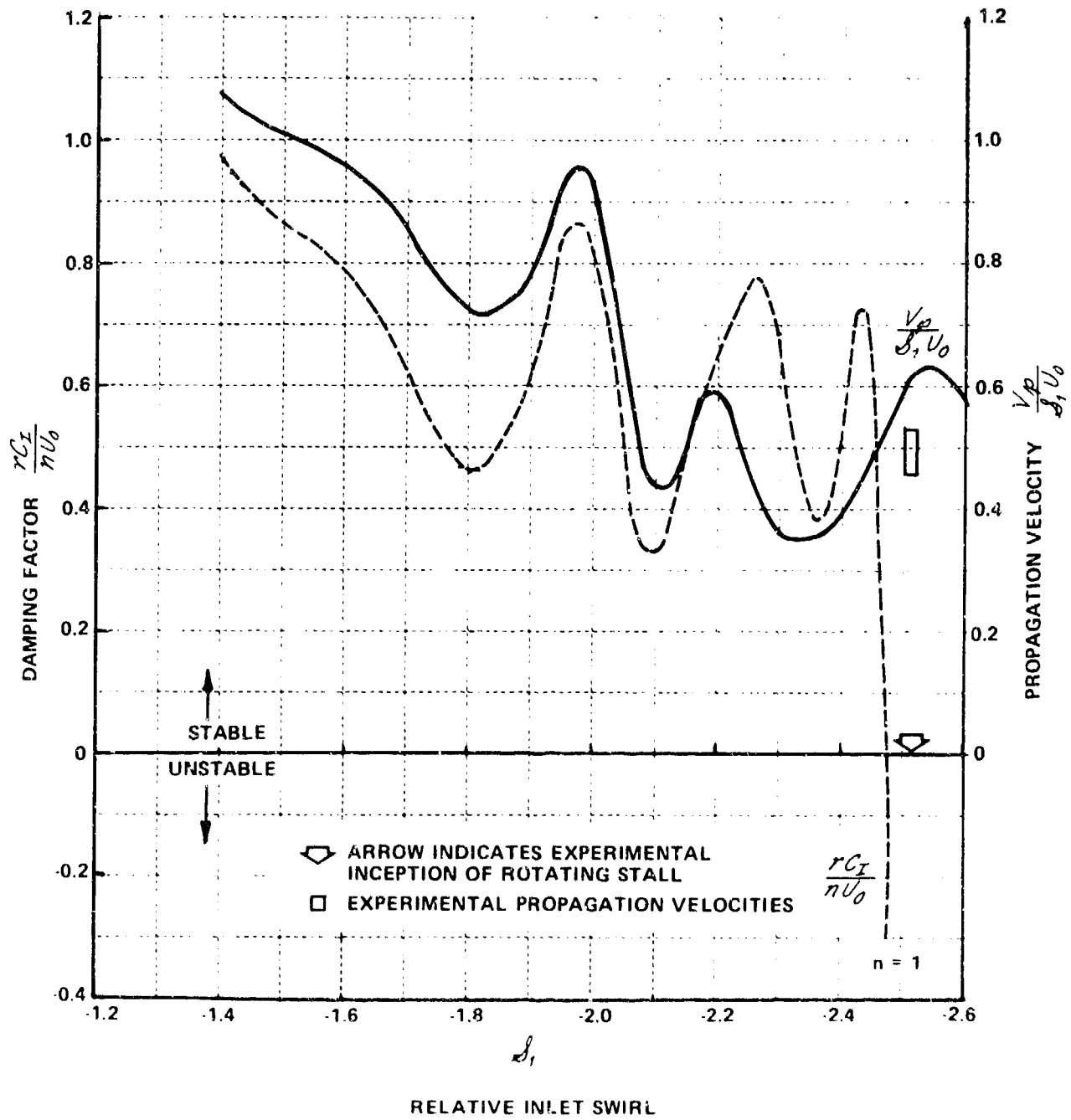


Figure 49 (Cont.) THEORETICAL STABILITY CHARACTERISTICS OF ROTOR SET NO. 1

(c) ROTOR STAGGER ANGLE,  $\delta_{RM} = 50$  DEG

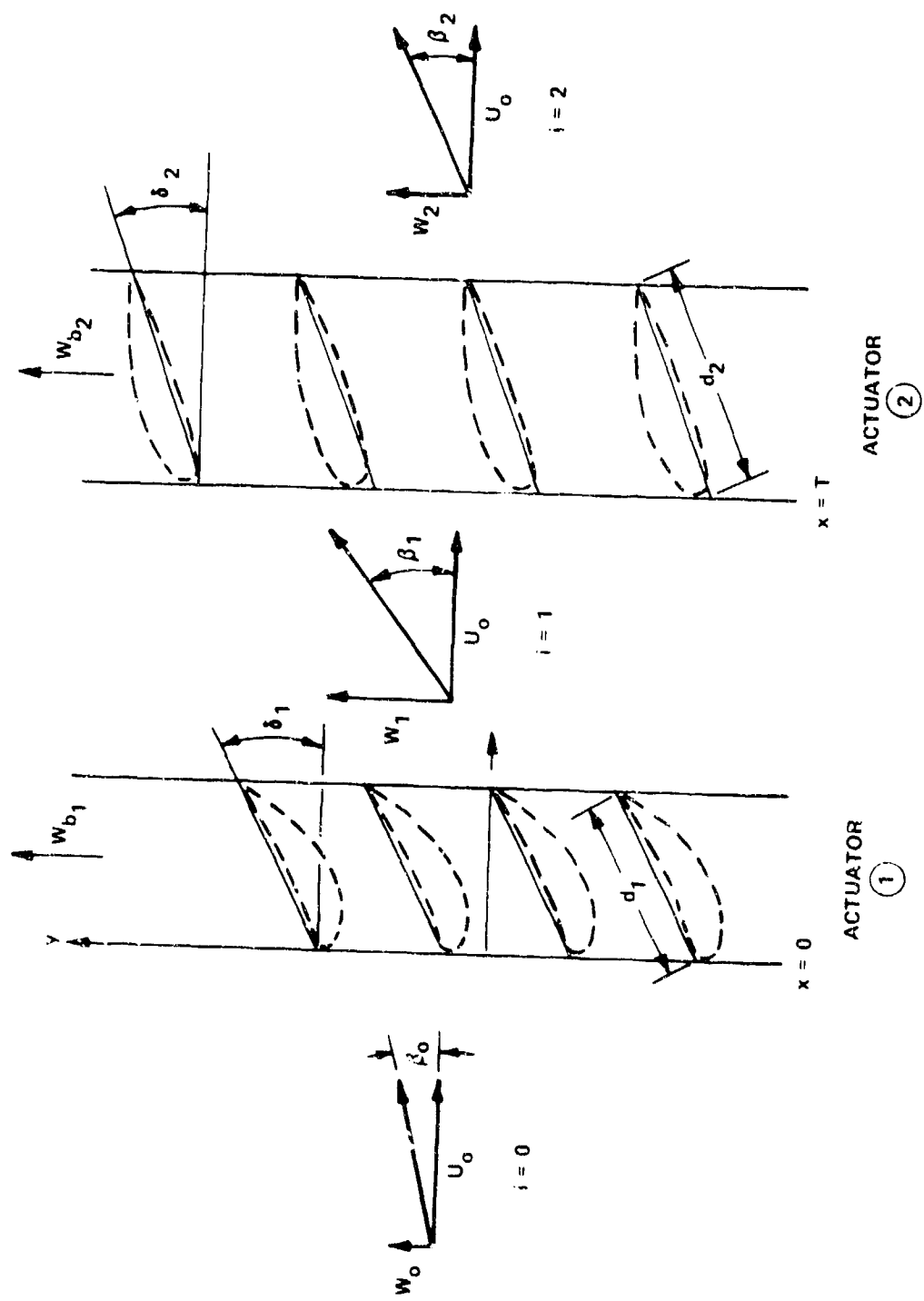


Figure 50 FINITE THICKNESS MODEL FOR TWO BLADE ROW THEORY

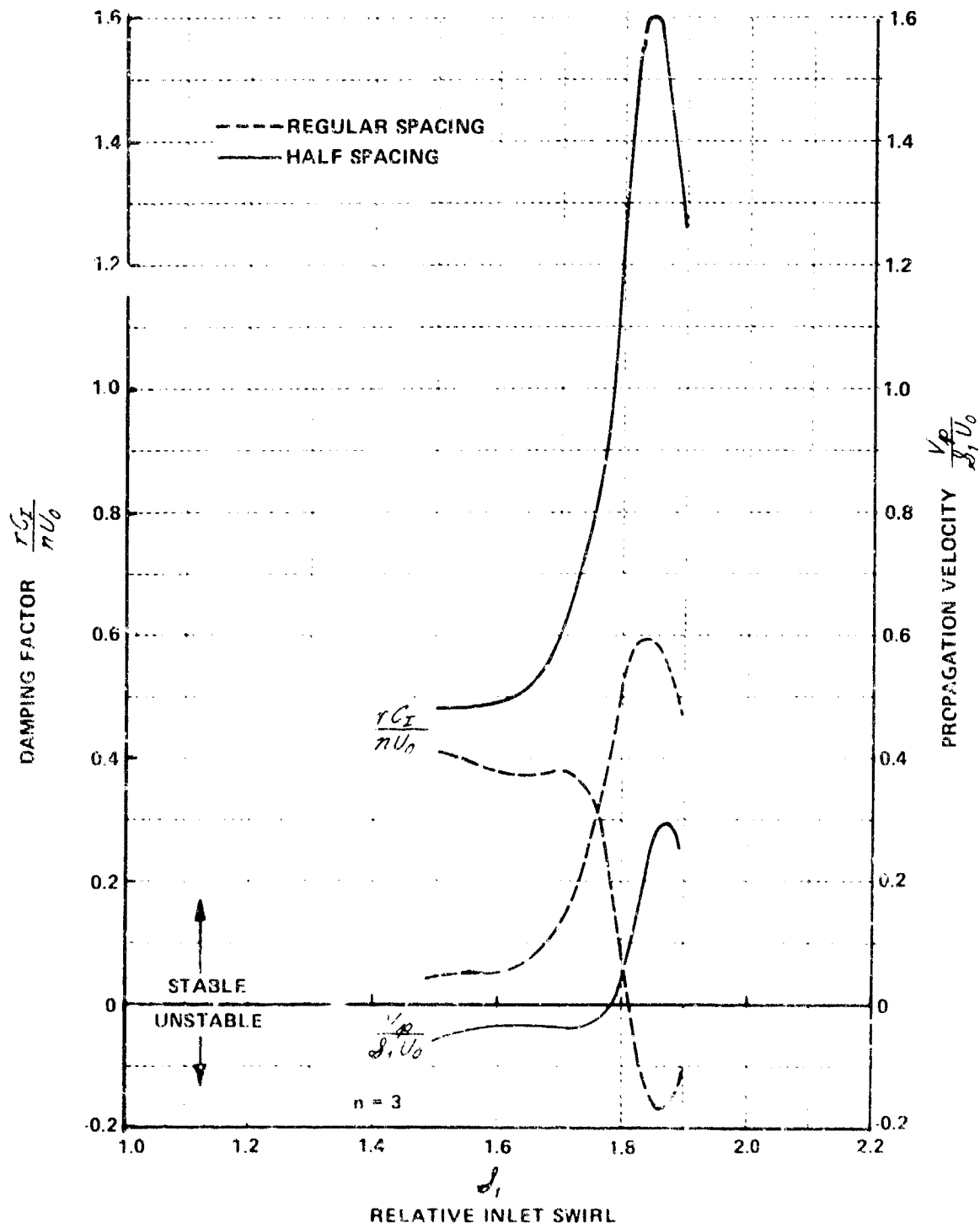


Figure 51 THEORETICAL EFFECTS OF HALVING THE BLADE ROW SPACING ON STATOR SET NO. 4

(a)  $\delta_{SM} = 28.2$  DEG,  $n = 3$



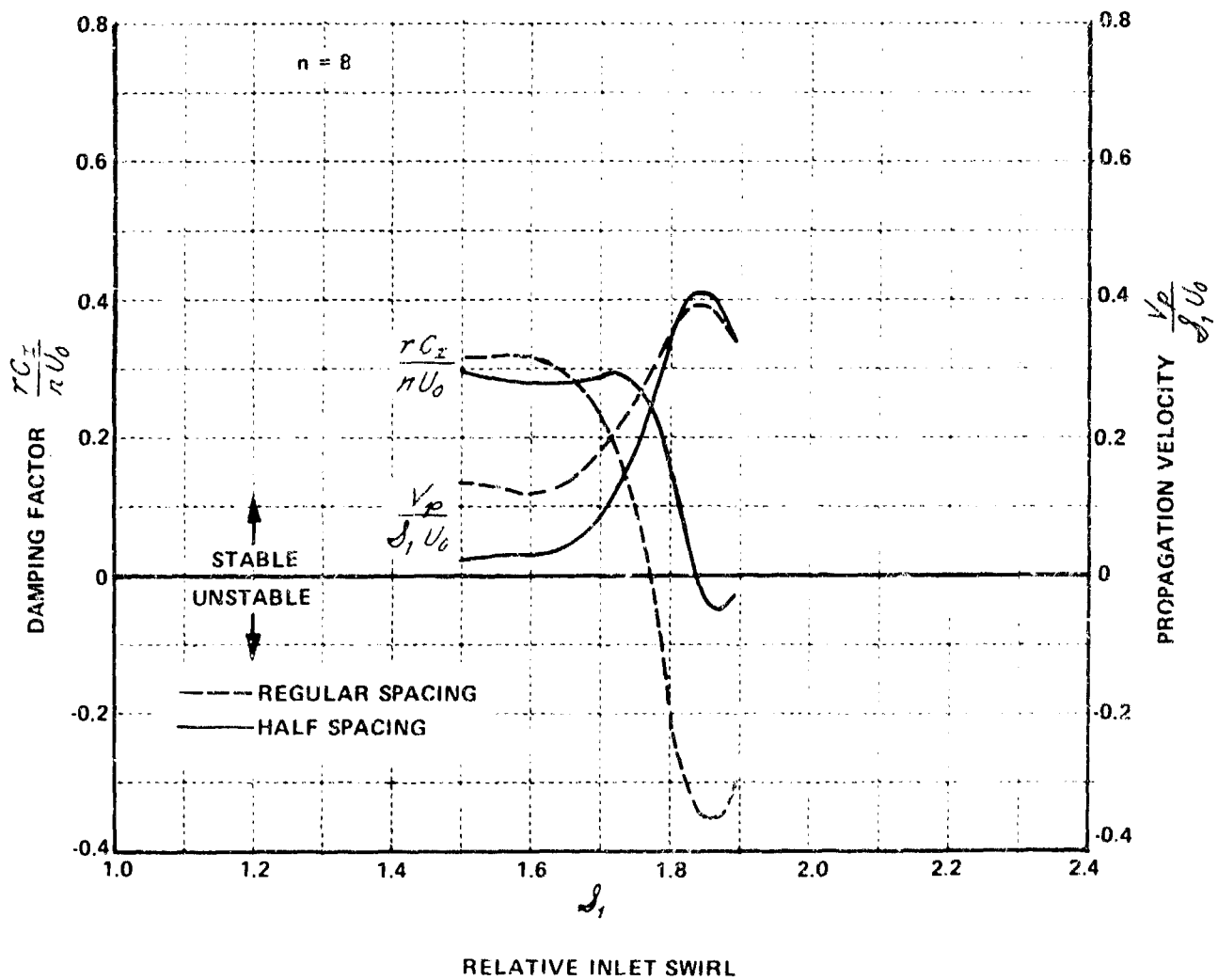


Figure 51 (Cont.) THEORETICAL EFFECTS OF HALVING THE BLADE ROW SPACING ON STATOR NO. 4

(b)  $\delta_{SM} = 28.2$  DEG,  $n = 8$

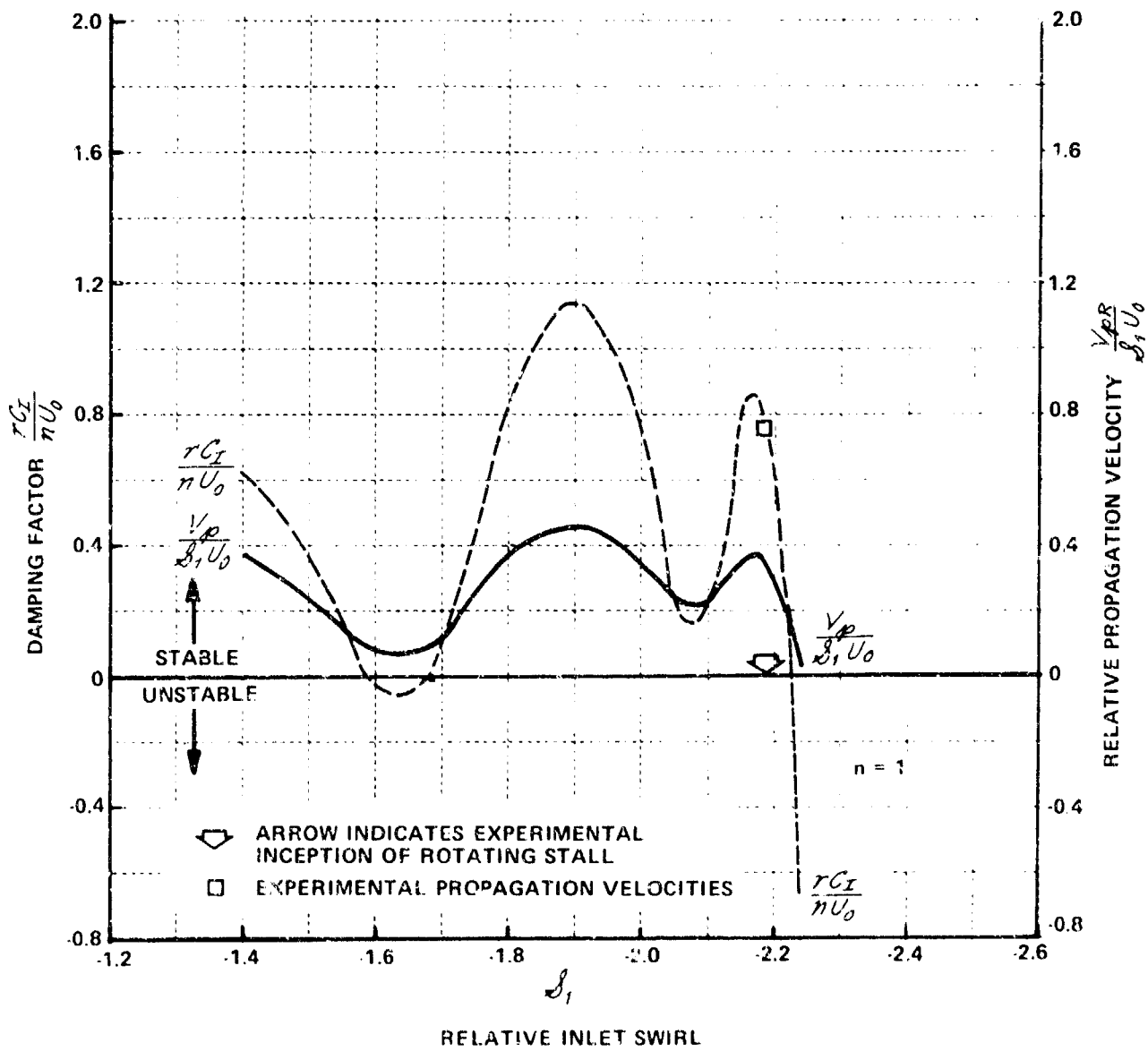


Figure 52 THEORETICAL STABILITY CHARACTERISTICS OF ROTOR SET NO. 1  
 ASSUMING CONSTANT PRESSURE JUST DOWNSTREAM OF ROTOR  
 (a) ROTOR STAGGER ANGLE,  $\delta_{RM} = 30$  DEG

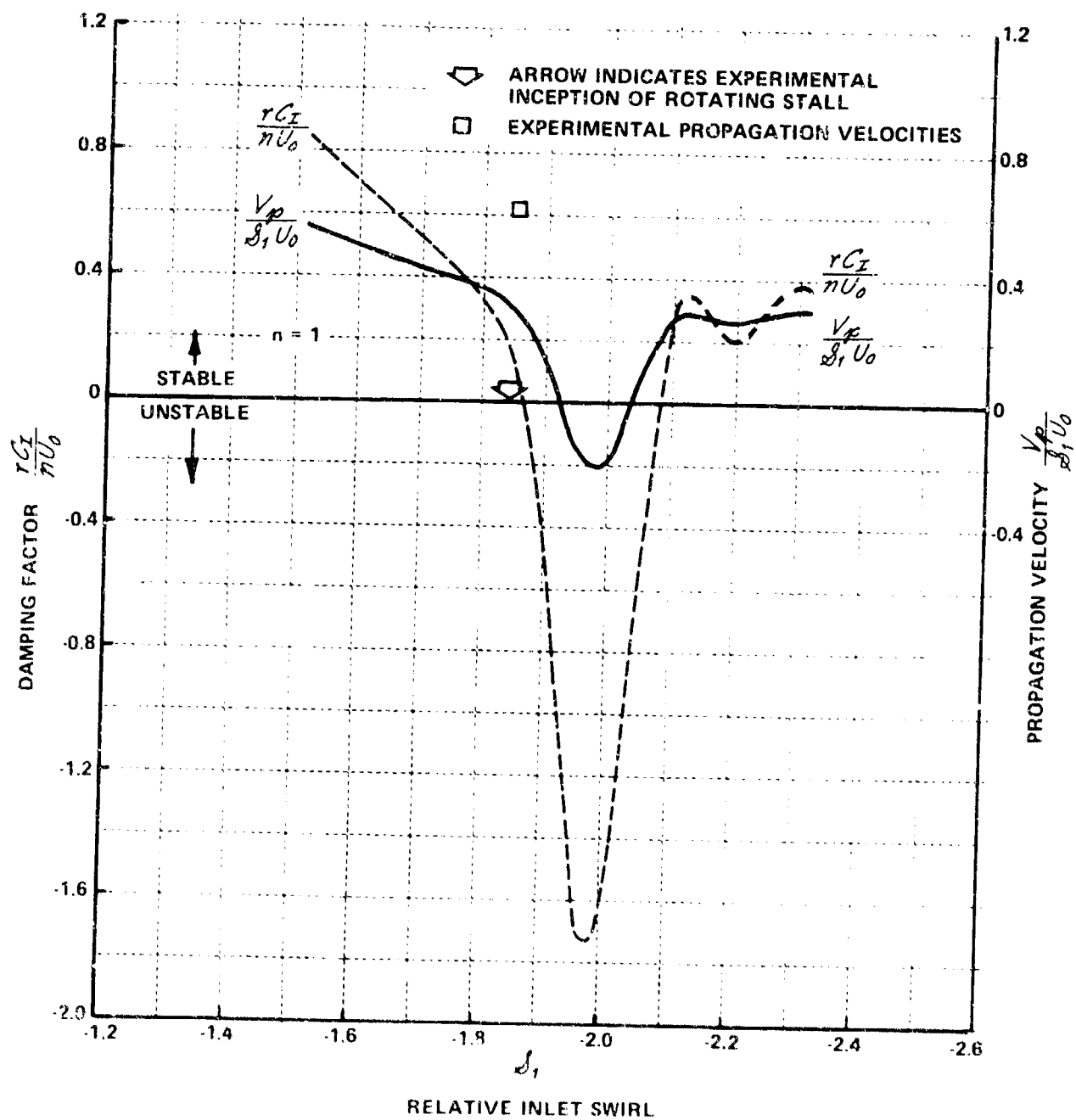


Figure 52 (Cont.) THEORETICAL STABILITY CHARACTERISTICS OF ROTOR SET NO. 1  
 ASSUMING CONSTANT PRESSURE JUST DOWNSTREAM OF THE ROTOR

(b) ROTOR STAGGER ANGLE,  $\delta_{RM} = 40$  DEG

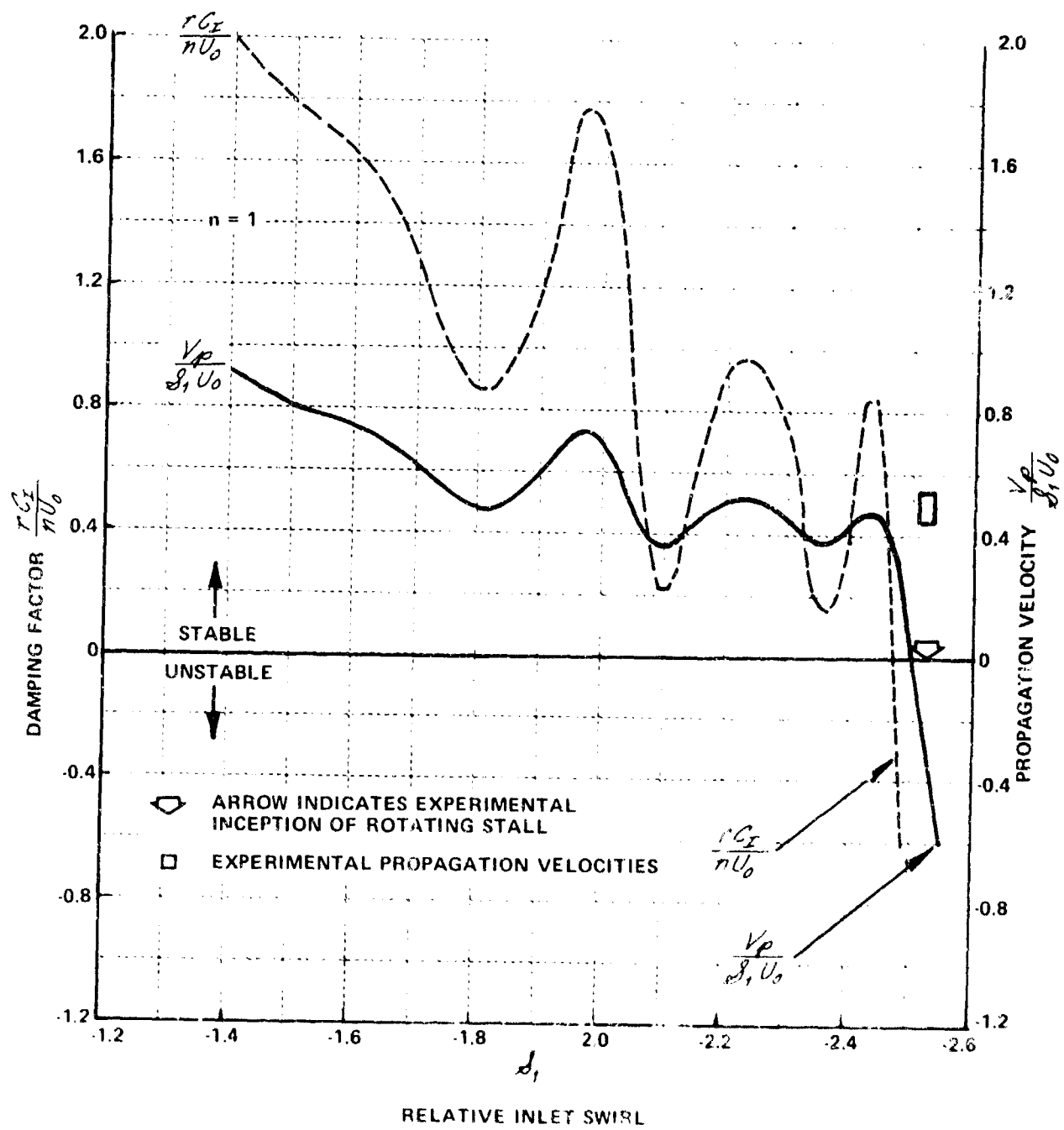


Figure 52 (Cont.) THEORETICAL STABILITY CHARACTERISTICS OF ROTOR SET NO. 1  
 ASSUMING CONSTANT PRESSURE JUST DOWNSTREAM OF ROTOR  
 (c) ROTOR STAGGER ANGLE,  $\delta_{RM} = 50$  DEG

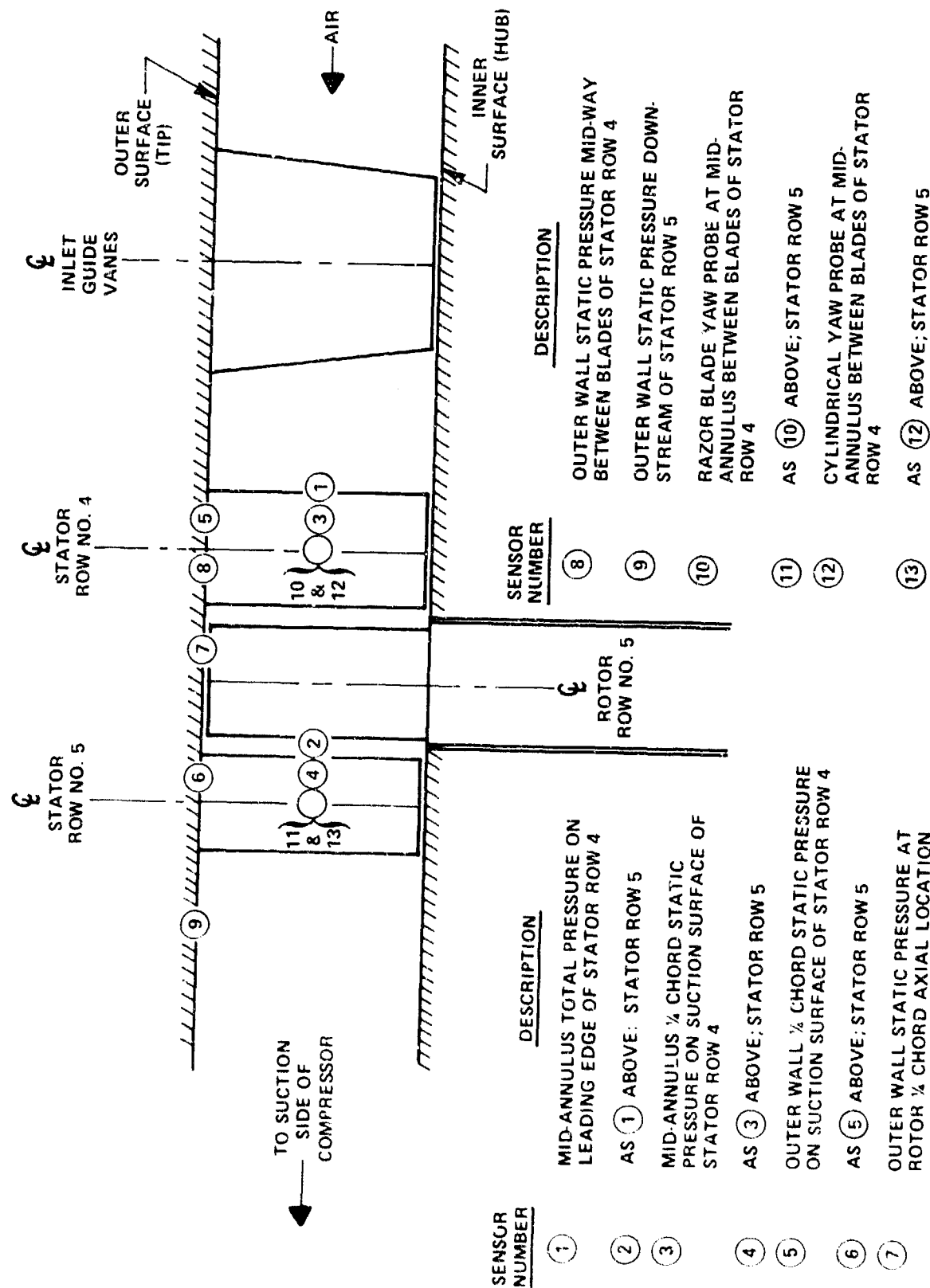


Figure 53 ANNULAR CASCADE CONFIGURATION USED TO TEST PROTOTYPE ROTATING STALL CONTROL AND SENSORS

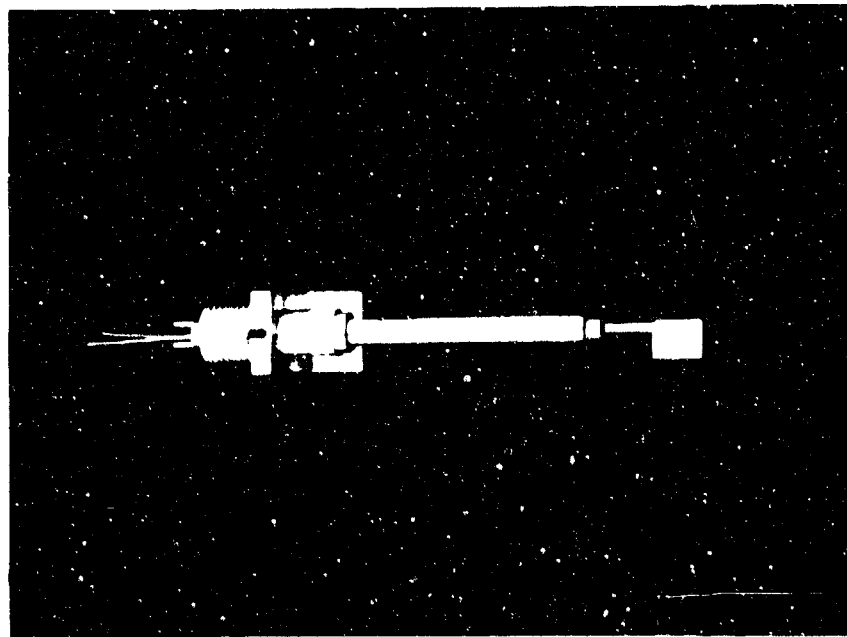
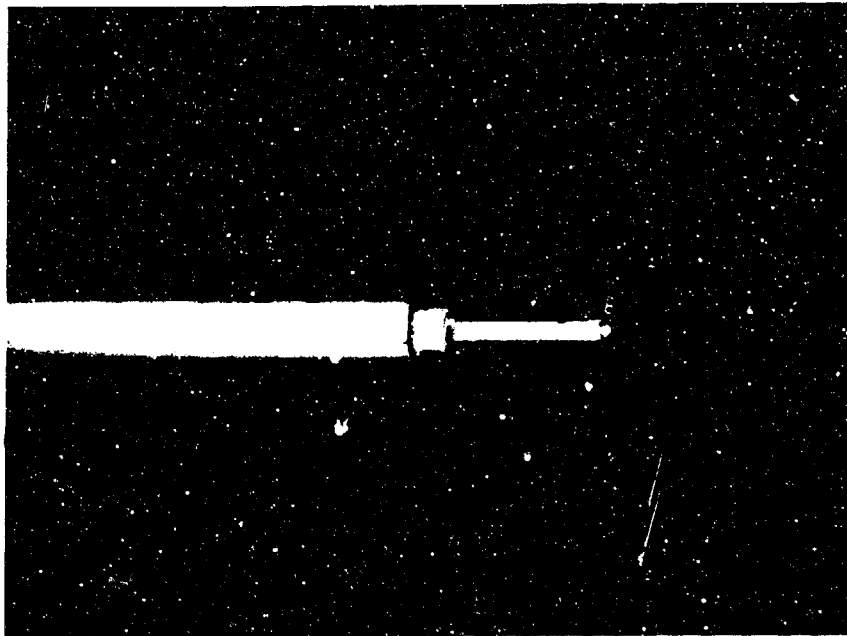


Figure 54 RAZOR BLADE YAW PROBE

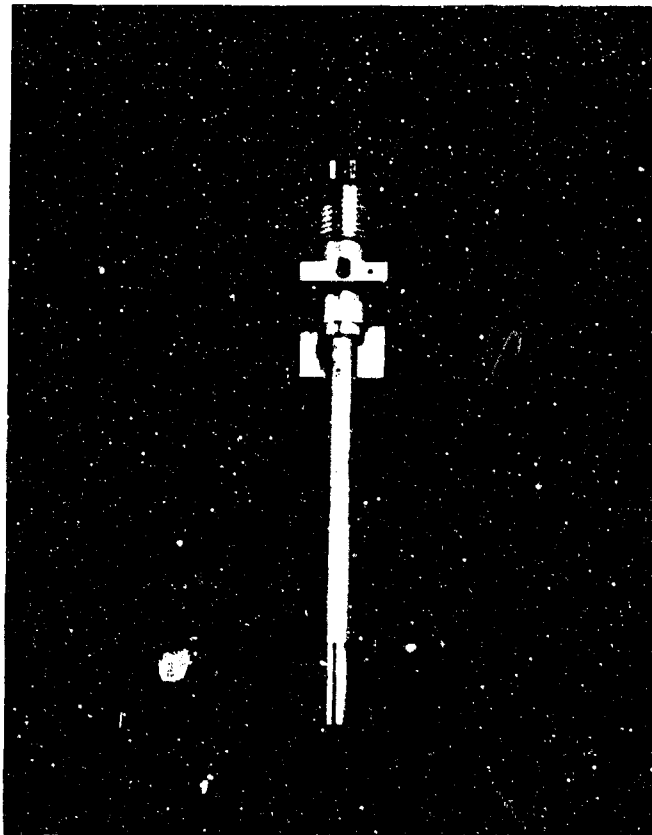


Figure 55 CYLINDRICAL YAW PROBE

RECORD      SENSOR LOCATION  
 UPPER      ⑦ ROTOR-OUTER WALL  
 LOWER      ③ MID-ANNULUS ¼ CHORD STATIC, STATOR ROW 4

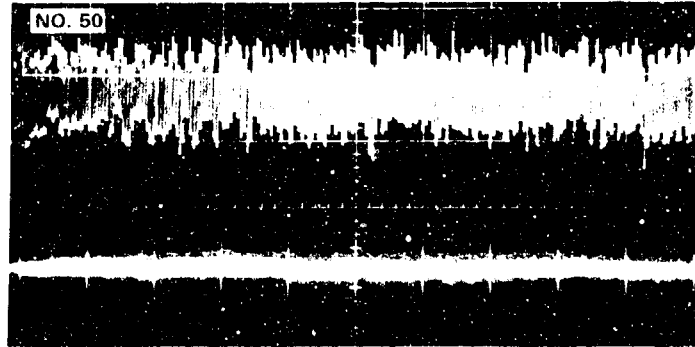
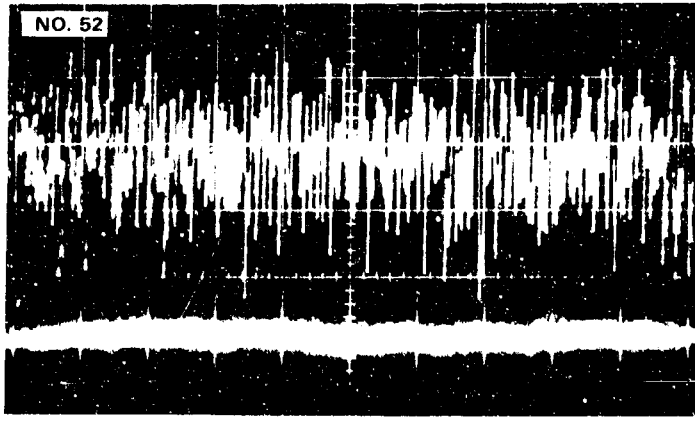
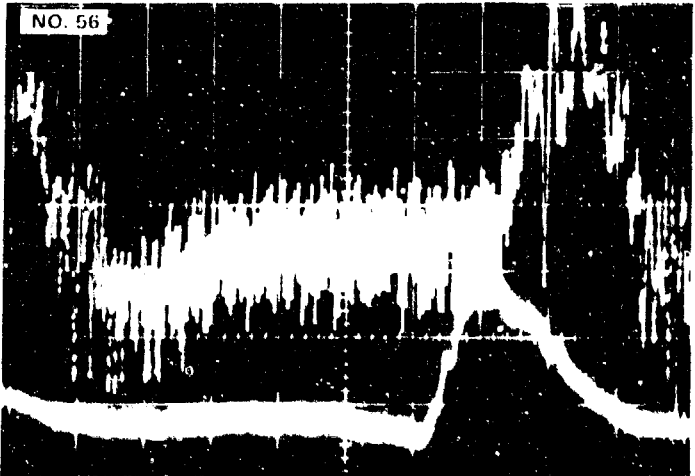
VERTICAL SENSITIVITY (mV/cm)	OSCILLOSCOPE DISPLAY FOR STATOR ROW 5 UNLOADED	MID-ANNULUS STAGGER ANGLE OF STATOR ROW 4 $\delta_{SM_4}$ (Degrees)
50		45.8
50		33.8
50		29.8

Figure 56 UNSTEADY PRESSURE RECORDS FROM VARIOUS ROTATING STALL SENSOR CONFIGURATIONS, INLET GUIDE VANE STAGGER ANGLE,  $\delta_{GV} = 24.5$  DEGREES

(a) SENSORS ⑦ AND ③, STATOR ROW 5 UNLOADED



RECORD

UPPER

LOWER

SENSOR LOCATION

① MID-ANNULUS TOTAL PRESSURE, STATOR ROW 4

⑤ OUTER WALL ¼ CHORD STATIC, STATOR ROW 4

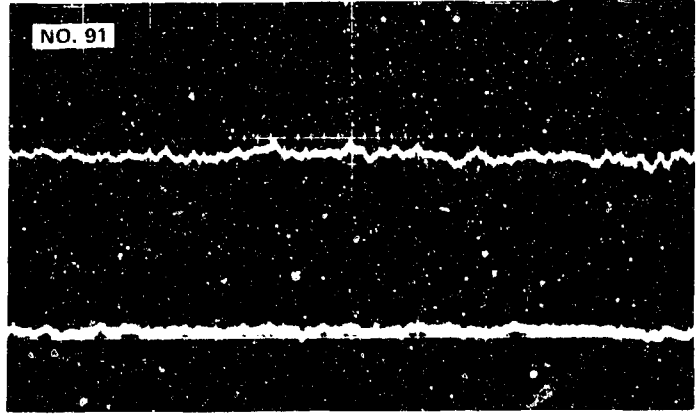
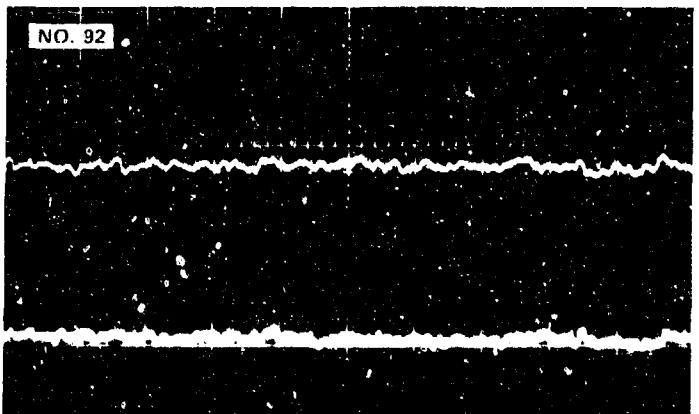
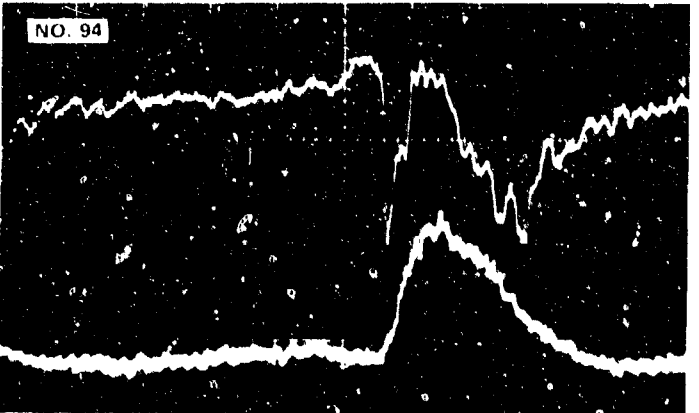
VERTICAL SENSITIVITY (mV/cm)	OSCILLOSCOPE DISPLAY FOR STATOR ROW 5 UNLOADED	MID-ANNULUS STAGGER ANGLE OF STATOR ROW 4 $\delta_{SM_4}$ (Degrees)
50		45.8
50		33.8
50		29.8

Figure 56 (Cont.) UNSTEADY PRESSURE RECORDS FROM VARIOUS ROTATING STALL SENSOR CONFIGURATIONS, INLET GUIDE VANE STAGGER ANGLE,  $\delta_{GV} = 24.5$  DEGREES

(b) SENSORS ① AND ⑤, STATOR ROW 5 UNLOADED

RECORD

UPPER

LOWER

SENSOR LOCATION

② MID-ANNULUS TOTAL PRESSURE, STATOR ROW 5

⑥ OUTER WALL ¼ CHORD STATIC, STATOR ROW 5

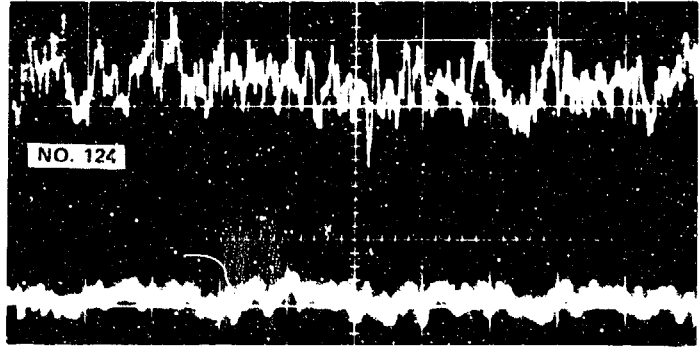
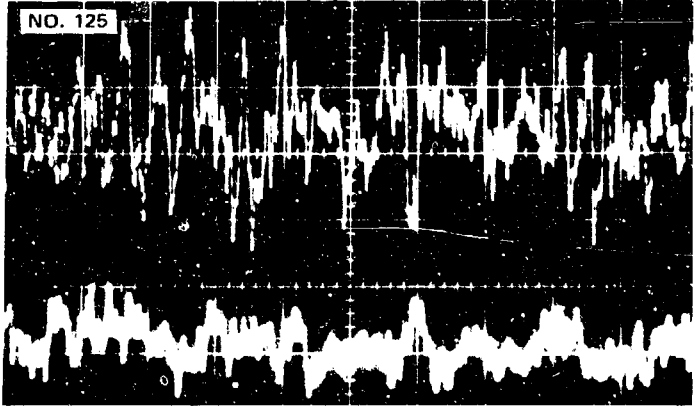
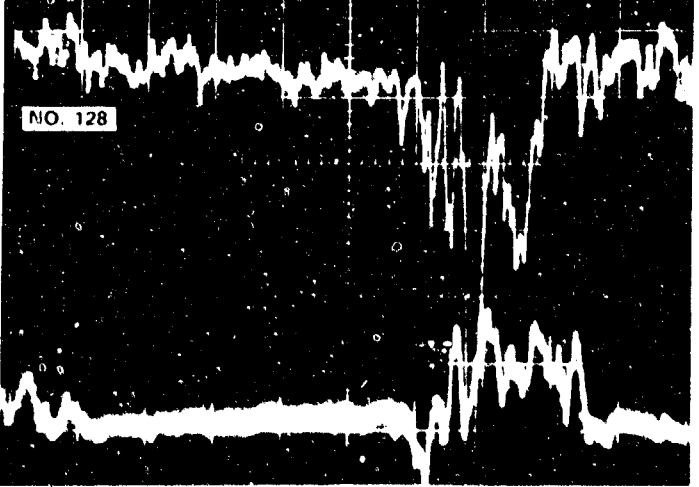
VERTICAL SENSITIVITY (mV/cm)	OSCILLOSCOPE DISPLAY FOR STATOR ROW 5 UNLOADED	MID-ANNULUS STAGGER ANGLE OF STATOR ROW 4 $\delta_{SM_4}$ (Degrees)
50		45.8
50		33.8
100		29.8

Figure 56 (Cont.) UNSTEADY PRESSURE RECORDS FROM VARIOUS ROTATING STALL SENSOR CONFIGURATIONS, INLET GUIDE VANE STAGGER ANGLE,  $\delta_{GV} = 24.5$  DEGREES

(c) SENSORS ② AND ⑥, STATOR ROW 5 UNLOADED

RECORD      SENSOR LOCATION  
 UPPER      ⑦ ROTOR-OUTER WALL  
 LOWER      ④ MID-ANNULUS ¼ CHORD STATIC, STATOR ROW 5

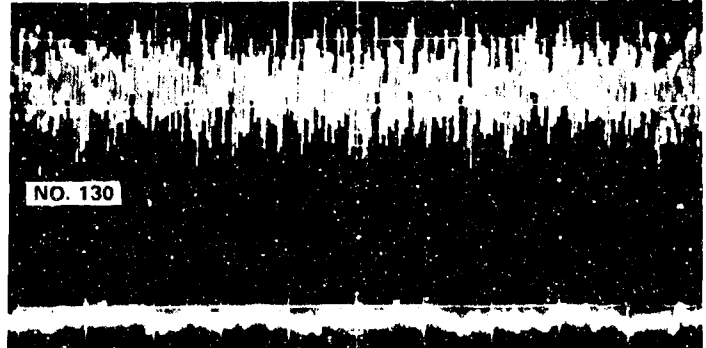
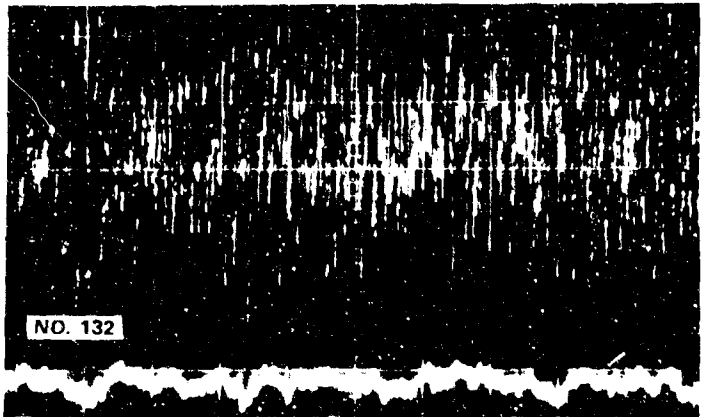
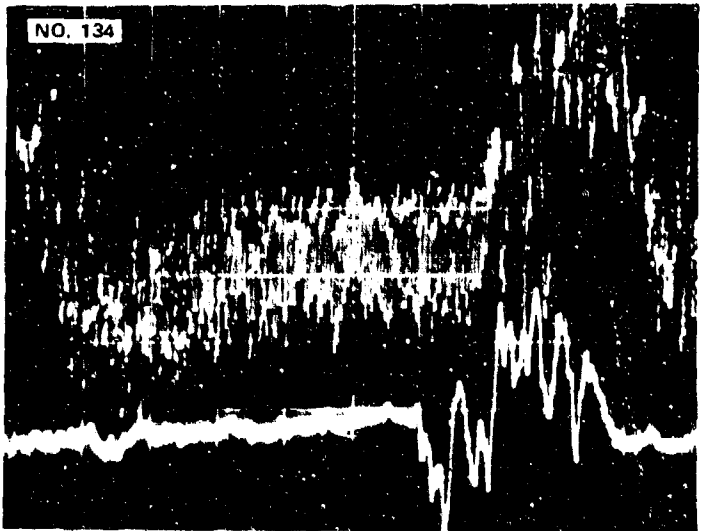
VERTICAL SENSITIVITY (mV/cm)	OSCILLOSCOPE DISPLAY FOR STATOR ROW 5 UNLOADED	MID-ANNULUS STAGGER ANGLE OF STATOR ROW 4 $\delta_{SM_4}$ (Degrees)
50		45.8
50		33.8
50		29.8

Figure 56 (Cont.) UNSTEADY PRESSURE RECORDS FROM VARIOUS ROTATING STALL SENSOR CONFIGURATIONS, INLET GUIDE VANE STAGGER ANGLE,  $\delta_{GV} = 24.5$  DEGREES

(d) SENSORS ⑦ AND ④, STATOR ROW 5 UNLOADED

RECORD  
UPPER  
LOWER

SENSOR LOCATION  
(8) OUTER WALL STATIC BETWEEN BLADES OF STATOR ROW 4  
(9) OUTER WALL STATIC DOWNSTREAM OF STATOR ROW 5

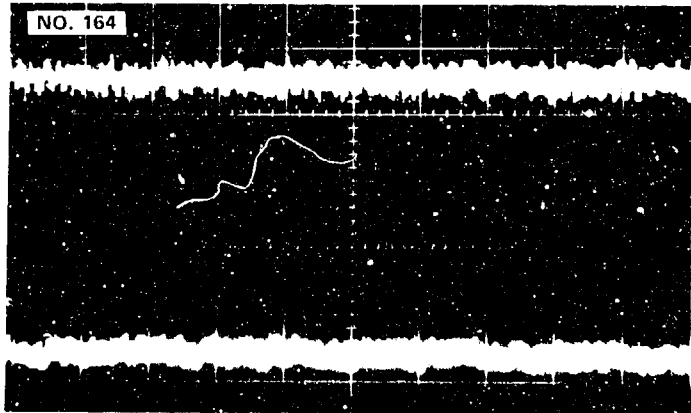
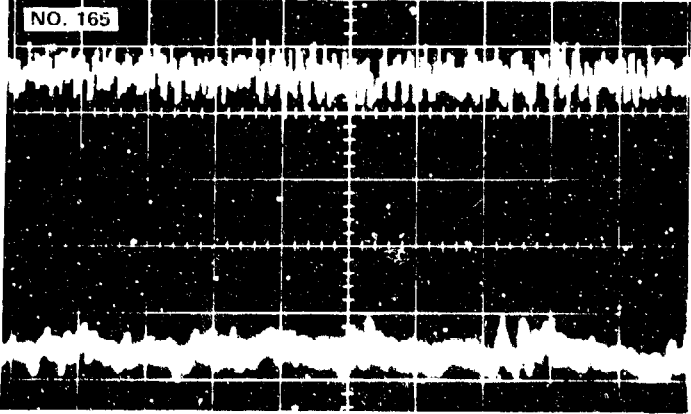
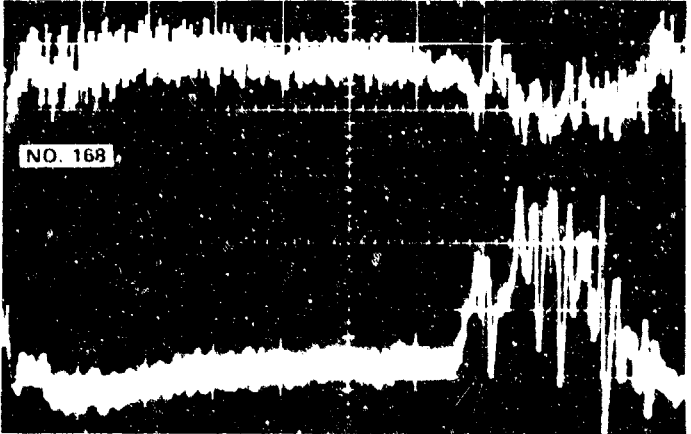
VERTICAL SENSITIVITY (mV/cm)	OSCILLOSCOPE DISPLAY FOR STATOR ROW 5 UNLOADED	MID-ANNULUS STAGGER ANGLE OF STATOR ROW 4 $\delta_{SM_4}$ (Degrees)
50		45.8
50		33.8
50		29.8

Figure 56 (Cont.) UNSTEADY PRESSURE RECORDS FROM VARIOUS ROTATING STALL SENSOR CONFIGURATIONS, INLET GUIDE VANE STAGGER ANGLE,  $\delta_{GV} = 24.5$  DEGREES

(e) SENSORS (8) AND (9), STATOR ROW 5 UNLOADED

RECORD  
UPPER  
LOWER

SENSOR LOCATION  
④ MID-ANNULUS 1/4 CHORD STATIC, STATOR ROW 5  
③ MID-ANNULUS 1/4 CHORD STATIC, STATOR ROW 4

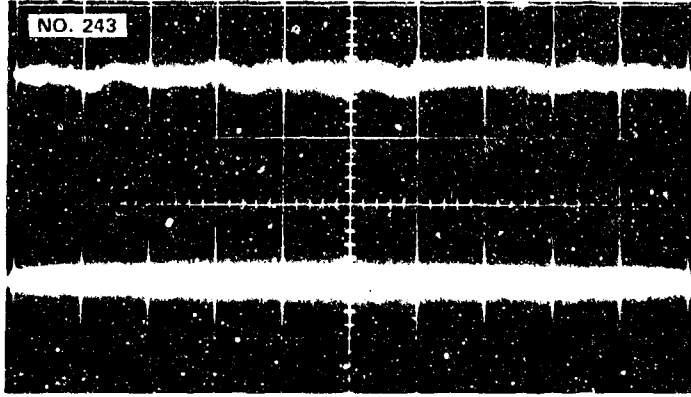
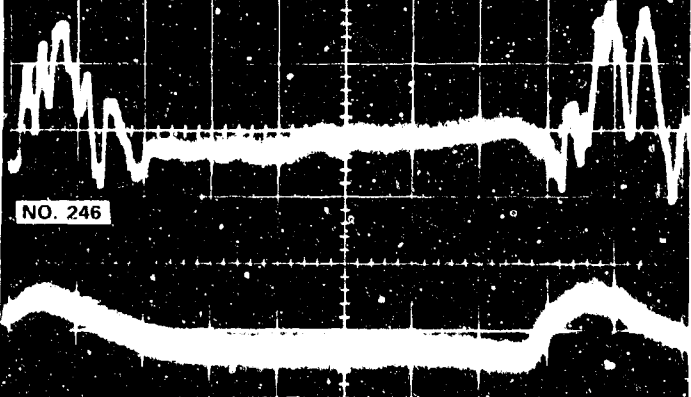
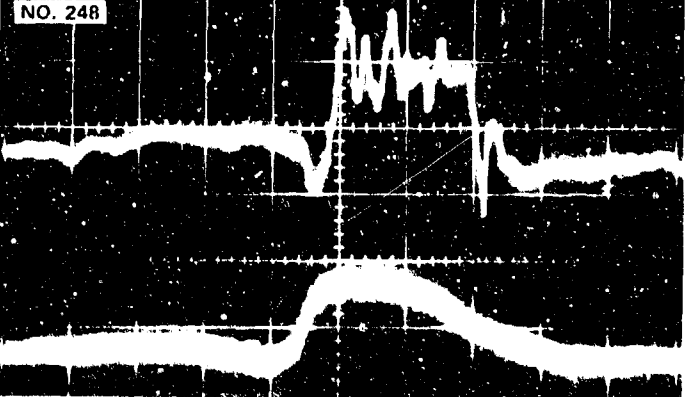
VERTICAL SENSITIVITY (mV/cm)	OSCILLOSCOPE DISPLAY FOR STATOR ROW 5 LOADED	MID-ANNULUS STAGGER ANGLE OF STATOR ROW 4 $\delta_{SM_4}$ (Degrees)
100		45.8
100		33.8
100		29.8

Figure 56 (Cont.) UNSTEADY PRESSURE RECORDS FROM VARIOUS ROTATING STALL SENSOR CONFIGURATIONS, INLET GUIDE VANE STAGGER ANGLE,  $\delta_{GV} = 24.5$  DEGREES

(f) SENSORS ④ AND ③, STATOR ROW 5 LOADED

**RECORD**

UPPER

LOWER

**SENSOR LOCATION**

② MID-ANNULUS TOTAL PRESSURE, STATOR ROW 5

⑥ OUTER WALL 1/4 CHORD STATIC, STATOR ROW 5

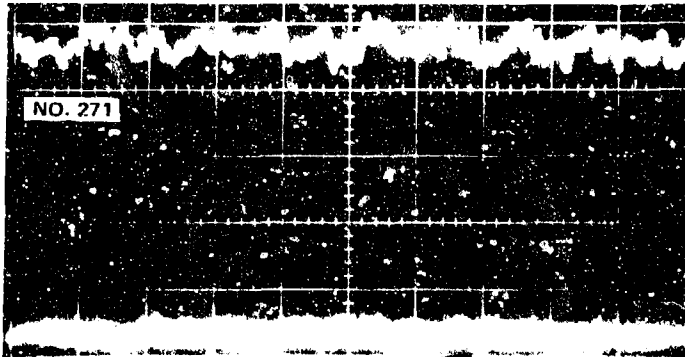
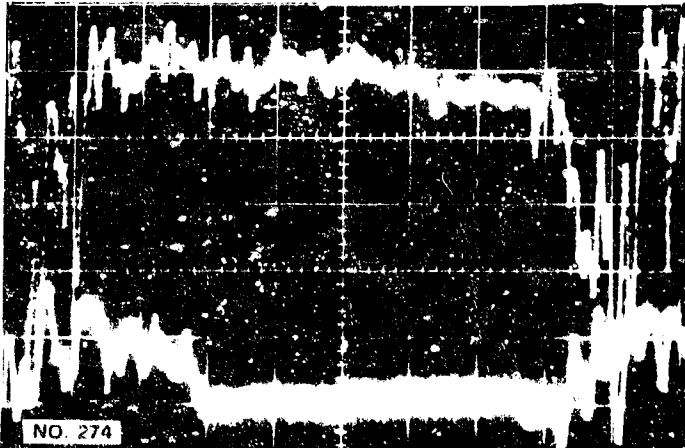
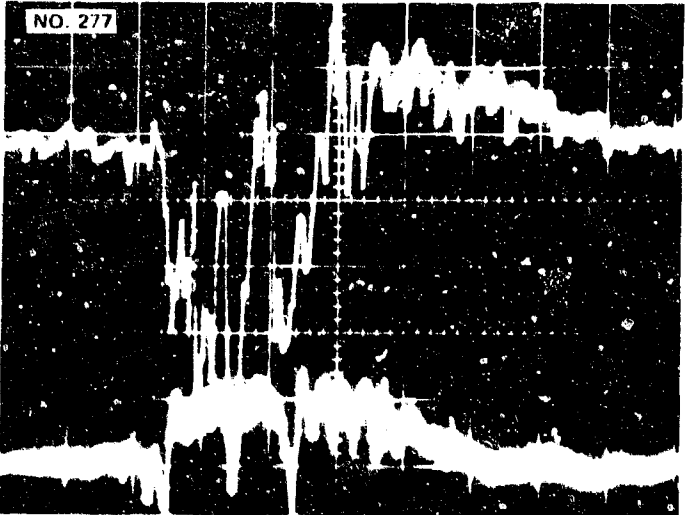
VERTICAL SENSITIVITY (mV/cm)	OSCILLOSCOPE DISPLAY FOR STATOR ROW 5 LOADED	MID-ANNULUS STAGGER ANGLE OF STATOR ROW 4 $\delta_{SM_4}$ (Degrees)
200		45.8
200		33.8
200		29.8

Figure 56 (Cont.) UNSTEADY PRESSURE RECORDS FROM VARIOUS ROTATING STALL SENSOR CONFIGURATIONS, INLET GUIDE VANE STAGGER ANGLE,  $\delta_{GV} = 24.5$  DEGREES

(g) SENSORS ② AND ⑥, STATOR ROW 5 LOADED

RECORD  
UPPER  
LOWER

SENSOR LOCATION

- ⑦ ROTOR-OUTER WALL  
③ MID-ANNULUS 1/2 CHORD STATIC, STATOR ROW 4

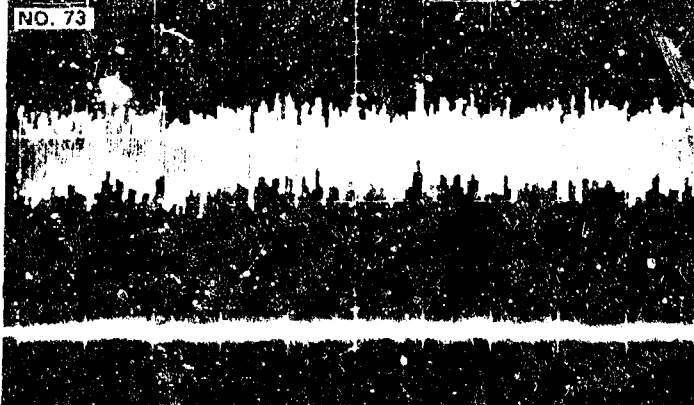
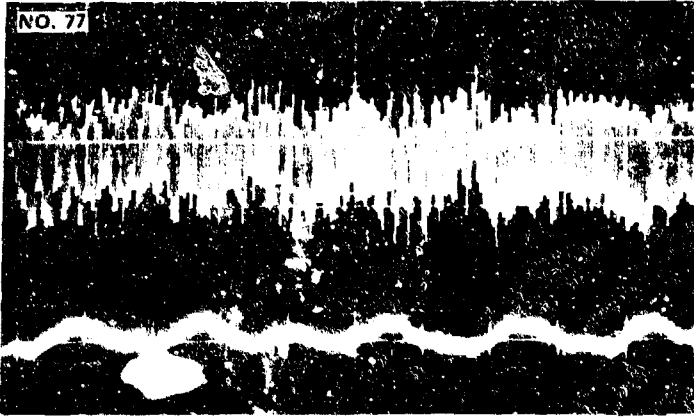
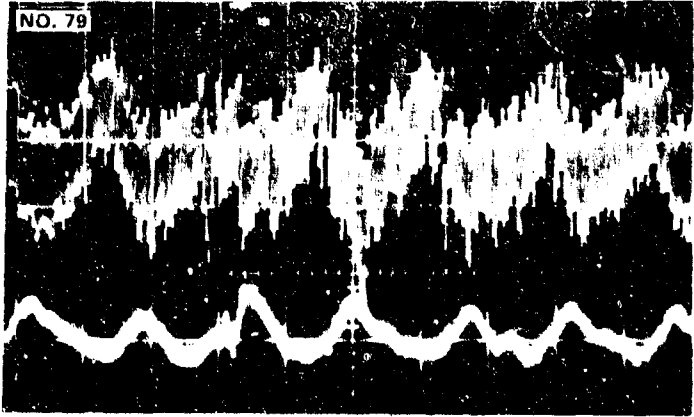
VERTICAL SENSITIVITY (mV/cm)	OSCILLOSCOPE DISPLAY FOR STATOR ROW 5 UNLOADED	MID-ANNULUS STAGGER ANGLE OF STATOR ROW 4 $\delta_{SM_4}$ (Degrees)
50		45.8
50		33.8
50		29.8

Figure 57 UNSTEADY PRESSURE RECORDS FROM VARIOUS ROTATING STALL SENSOR CONFIGURATIONS, INLET GUIDE VANE STAGGER ANGLE,  $\delta_{GV} = 40.5$  DEGREES

(a) SENSORS ⑦ AND ③, STATOR ROW 5 UNLOADED

RECORD

UPPER

LOWER

SENSOR LOCATION

① MID-ANNULUS TOTAL PRESSURE, STATOR ROW 4

⑤ OUTER-WALL ¼ CHORD STATIC, STATOR ROW 4

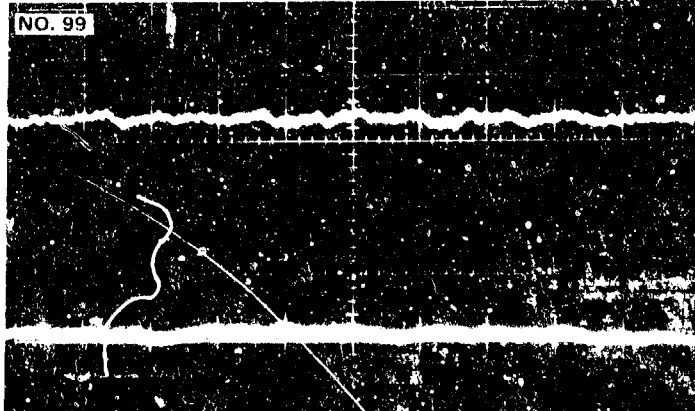
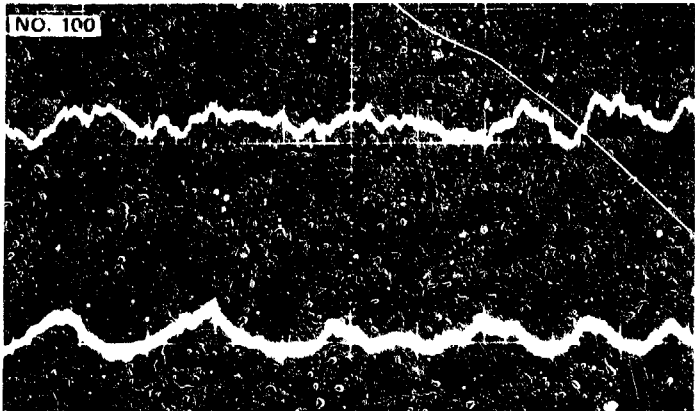
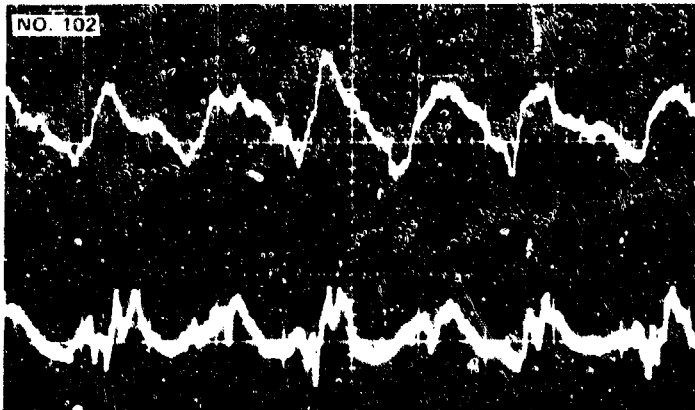
VERTICAL SENSITIVITY (mV/cm)	OSCILLOSCOPE DISPLAY FOR STATOR ROW 5 UNLOADED	MID-ANNULUS STAGGER ANGLE OF STATOR ROW 4 $\delta_{SM_4}$ (Degrees)
50		45.8
50		33.8
50		29.8

Figure 57 (Cont.) UNSTEADY PRESSURE RECORDS FROM VARIOUS ROTATING STALL SENSOR CONFIGURATIONS, INLET GUIDE VANE STAGGER ANGLE,  $\delta_{GV} = 40.5$  DEGREES

(b) SENSORS ① AND ⑤, STATOR ROW 5 UNLOADED



**RECORD**

UPPER

LOWER

**SENSOR LOCATION**

② MID-ANNULUS TOTAL PRESSURE, STATOR ROW 5

⑥ OUTER WALL ¼ CHORD STATIC, STATOR ROW 5

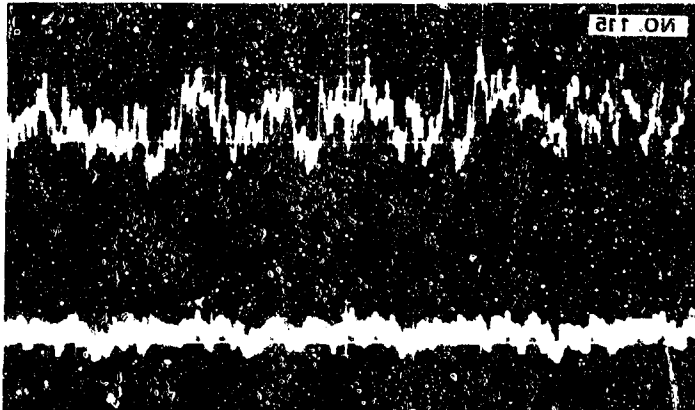
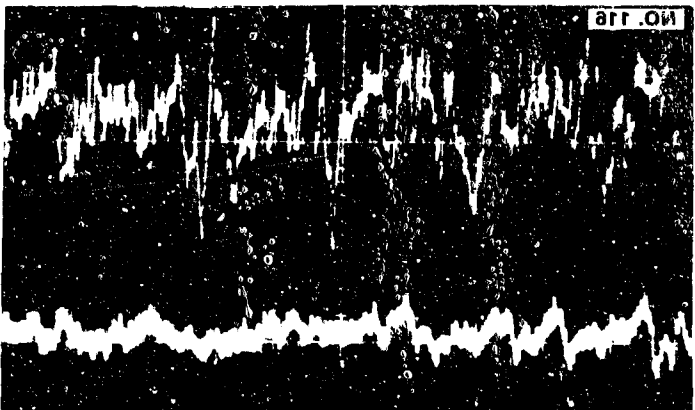
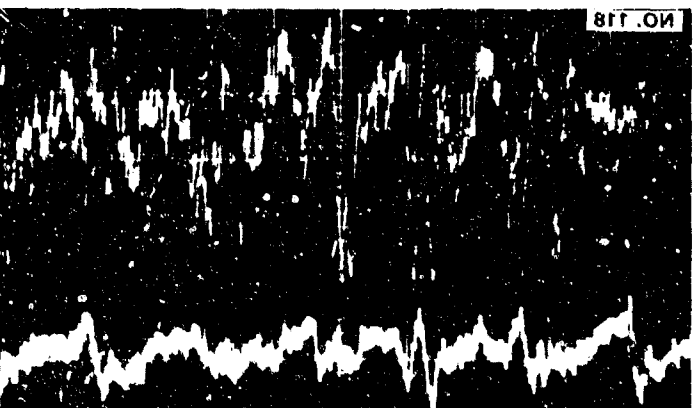
VERTICAL SENSITIVITY (mV/cm)	OSCILLOSCOPE DISPLAY FOR STATOR ROW 5 UNLOADED	MID-ANNULUS STAGGER ANGLE OF STATOR ROW 1 $\delta_{SM_4}$ (Degrees)
50		45.8
50		33.8
50		29.8

Figure 57 (Cont.) UNSTEADY PRESSURE RECORDS FROM VARIOUS ROTATING STALL SENSOR CONFIGURATIONS, INLET GUIDE VANE STAGGER ANGLE,  $\delta_{GV} = 40.5$  DEGREES

(c) SENSORS ② AND ⑥, STATOR ROW 5 UNLOADED

RECORD      SENSOR LOCATION  
 UPPER      ⑦ ROTOR-OUTER WALL  
 LOWER      ④ MID-ANNULUS 1/2 CHORD STATIC, STATOR ROW 5

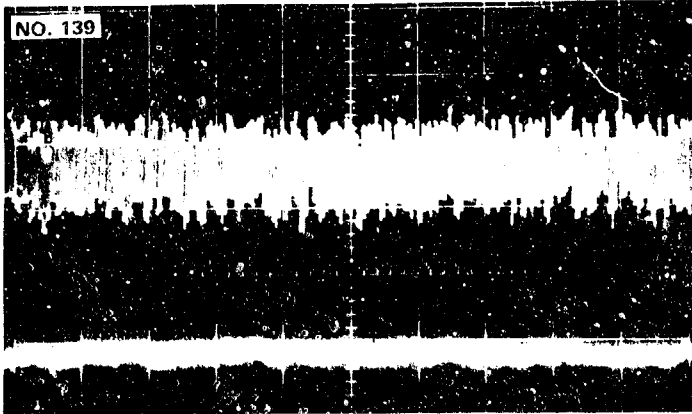
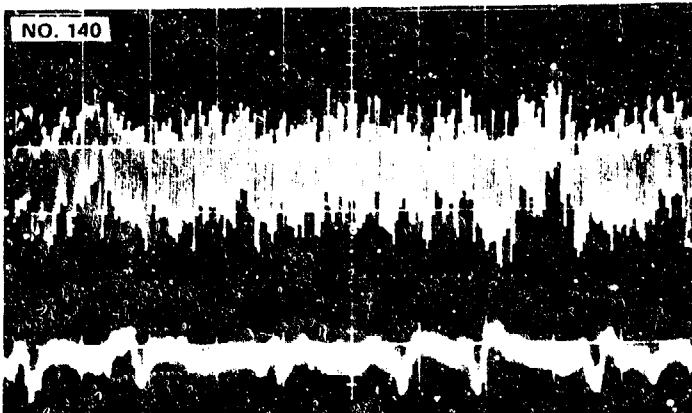
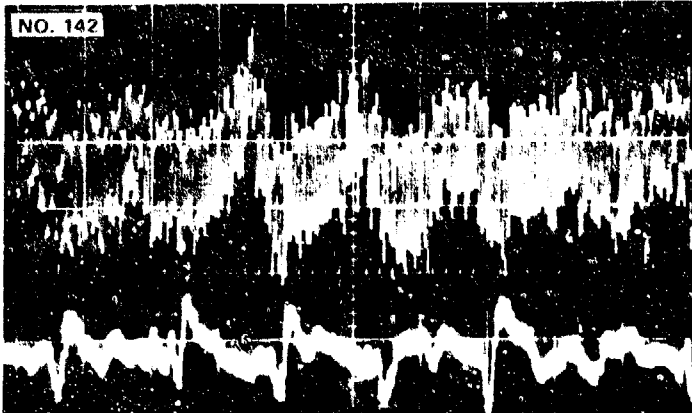
VERTICAL SENSITIVITY (mV/cm)	OSCILLOSCOPE DISPLAY FOR STATOR ROW 5 UNLOADED	MID-ANNULUS STAGGER ANGLE OF STATOR ROW 4 $\delta_{SM_4}$ (Degrees)
50		45.8
50		33.8
50		29.8

Figure 57 (Cont.) UNSTEADY PRESSURE RECORDS FROM VARIOUS ROTATING STALL SENSOR CONFIGURATIONS, INLET GUIDE VANE STAGGER ANGLE,  $\delta_{GV} = 40.5$  DEGREES

(d) SENSORS ⑦ AND ④, STATOR ROW 5 UNLOADED

RECORD  
UPPER  
LOWER

SENSOR LOCATION

- ⑧ OUTER WALL STATIC BETWEEN BLADES OF STATOR ROW 4  
⑨ OUTER WALL STATIC DOWNSTREAM OF STATOR ROW 5

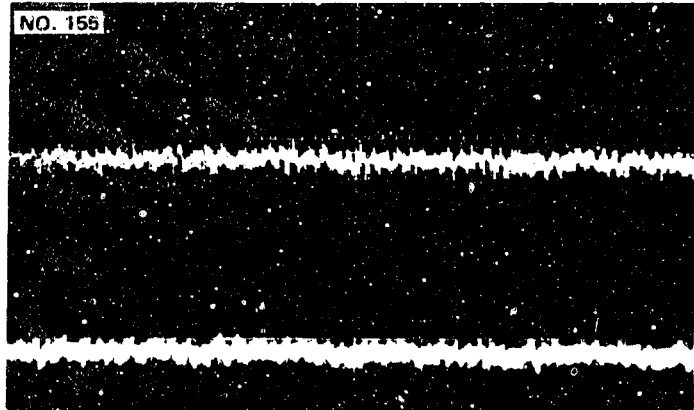
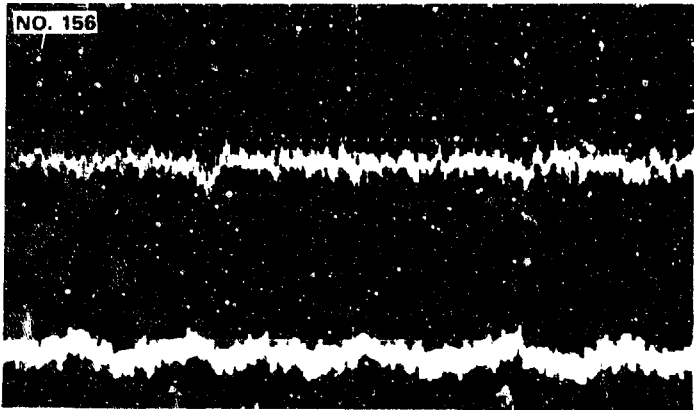
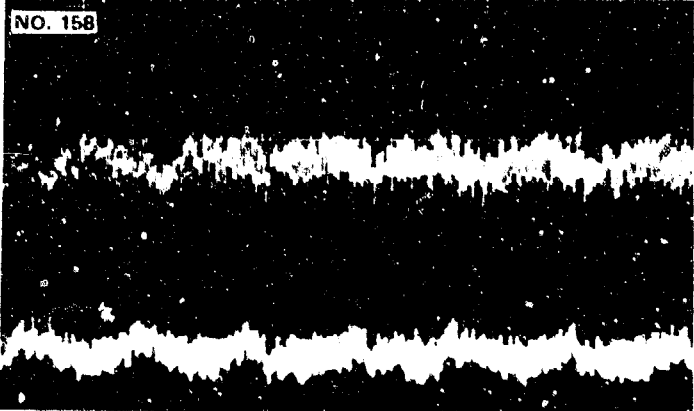
VERTICAL SENSITIVITY (mV/cm)	OSCILLOSCOPE DISPLAY FOR STATOR ROW 5 UNLOADED	MID-ANNULUS STAGGER ANGLE OF STATOR ROW 4 $\delta_{SM_4}$ (Degrees)
50		45.8
50		33.8
50		29.8

Figure 57 (Cont.) UNSTEADY PRESSURE RECORDS FROM VARIOUS ROTATING STALL SENSOR CONFIGURATIONS, INLET GUIDE VANE STAGGER ANGLE,  $\delta_{GV} = 40.5$  DEGREES

(e) SENSORS ⑧ AND ⑨, STATOR ROW 5 UNLOADED

RECORD      SENSOR LOCATION  
 UPPER      ④ MID-ANNULUS ¼ CHORD STATIC, STATOR ROW 5  
 LOWER      ③ MID-ANNULUS ¼ CHORD STATIC, STATOR ROW 4

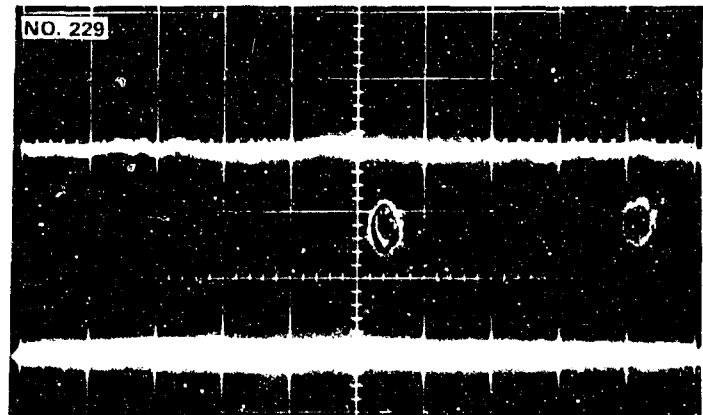
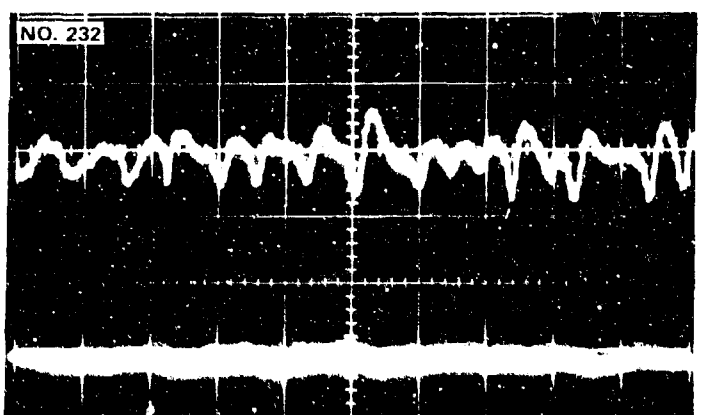
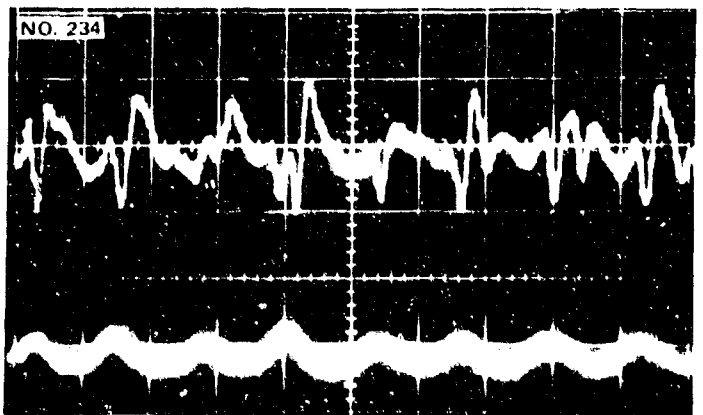
VERTICAL SENSITIVITY (mV/cm)	OSCILLOSCOPE DISPLAY FOR STATOR ROW 5 LOADED	MID-ANNULUS STAGGER ANGLE OF STATOR ROW 4 $\delta_{SM_4}$ (Degrees)
100		45.8
100		33.8
100		29.8

Figure 57 (Cont.) UNSTEADY PRESSURE RECORDS FROM VARIOUS ROTATING STALL SENSOR CONFIGURATIONS, INLET GUIDE VANE STAGGER ANGLE,  $\delta_{GV} = 40.5$  DEGREES

(f) SENSORS ④ AND ③, STATOR ROW 5 LOADED

RECORD  
UPPER  
LOWER

SENSOR LOCATION  
② MID-ANNULUS TOTAL PRESSURE, STATOR ROW 5  
⑥ OUTER WALL ¼ CHORD STATIC, STATOR ROW 5

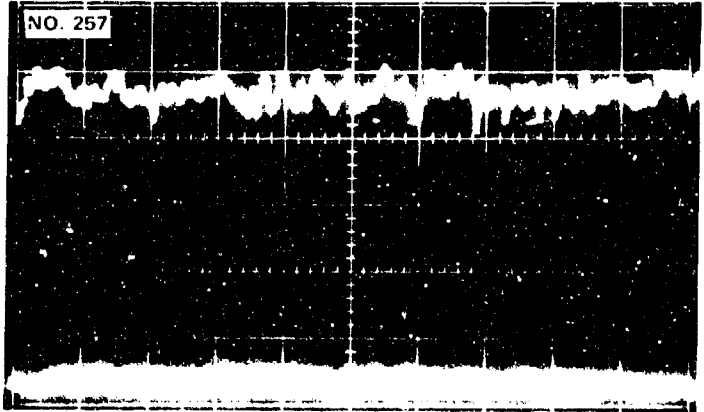
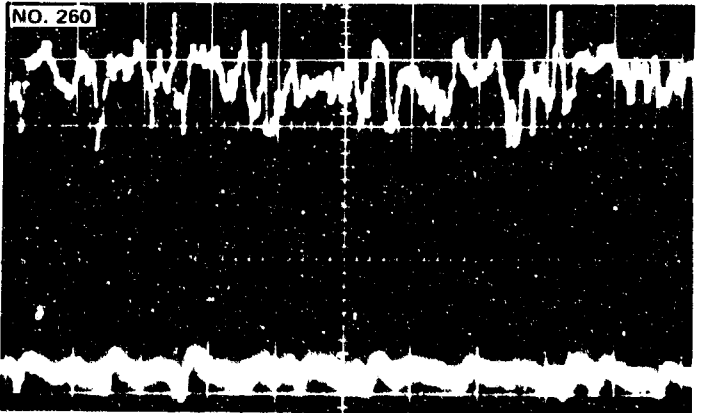
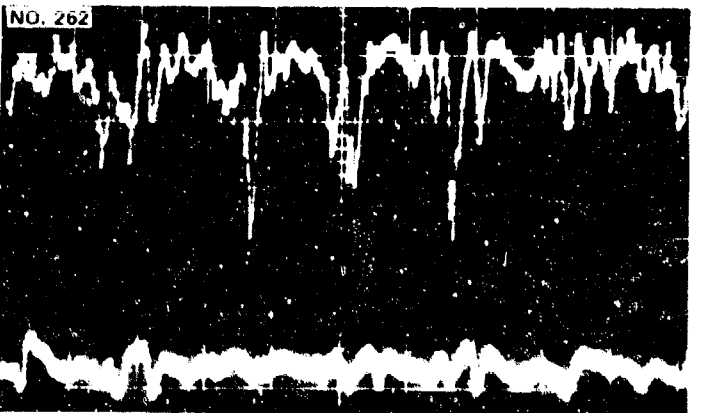
VERTICAL SENSITIVITY (mV/cm)	OSCILLOSCOPE DISPLAY FOR STATOR ROW 5 LOADED	MID-ANNULUS STAGGER ANGLE OF STATOR ROW 4 $\delta_{SM_4}$ (Degrees)
200		45.8
200		33.8
200		29.1

Figure 57 (Cont.) UNSTEADY PRESSURE RECORDS FROM VARIOUS ROTATING STALL SENSOR CONFIGURATIONS, INLET GUIDE VANE STAGGER ANGLE,  $\delta_{GV} = 40.5$  DEGREES

(g) SENSORS ② AND ⑥, STATOR ROW 5 LOADED

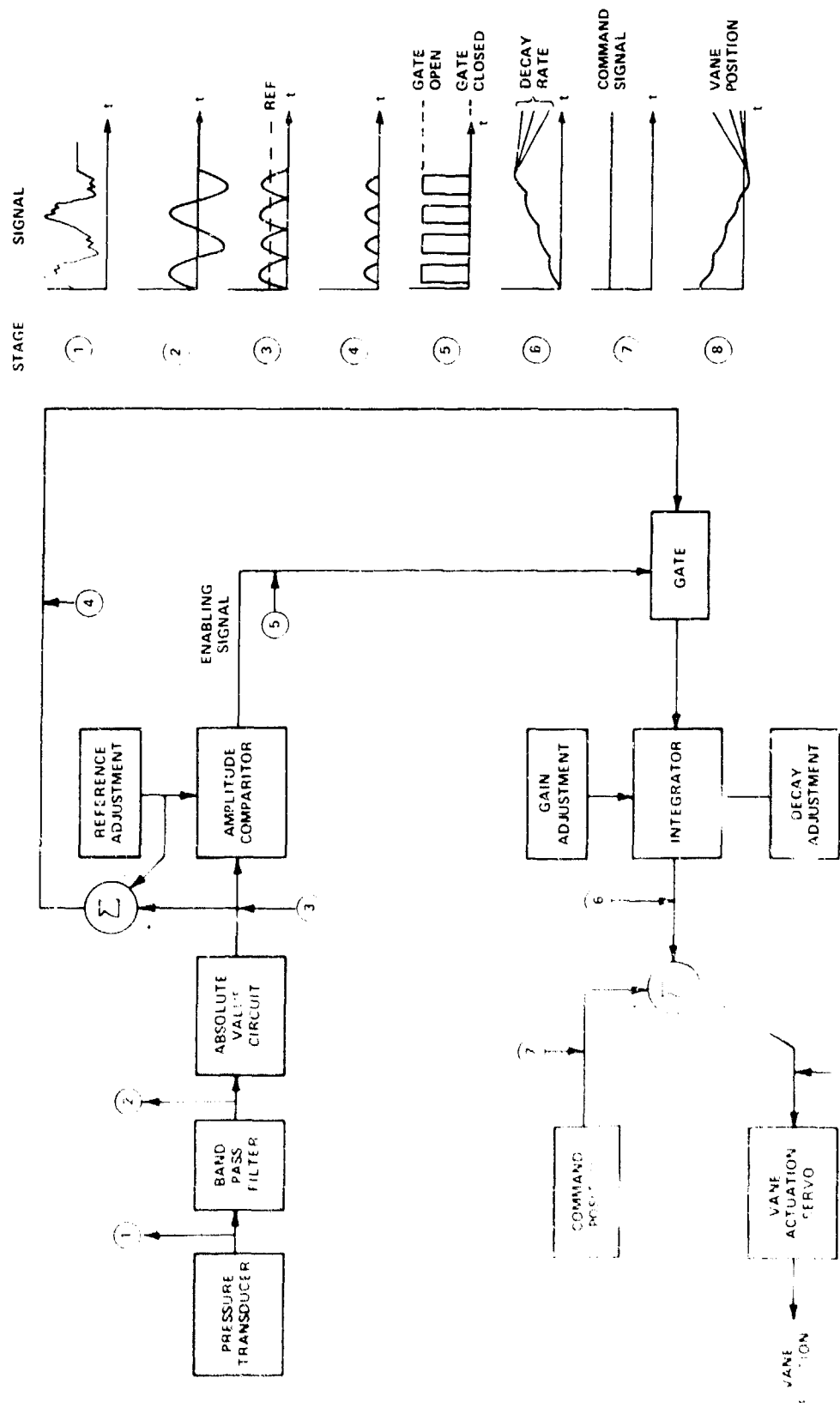


Figure 58 SIGNAL PROCESSING SUBSYSTEM

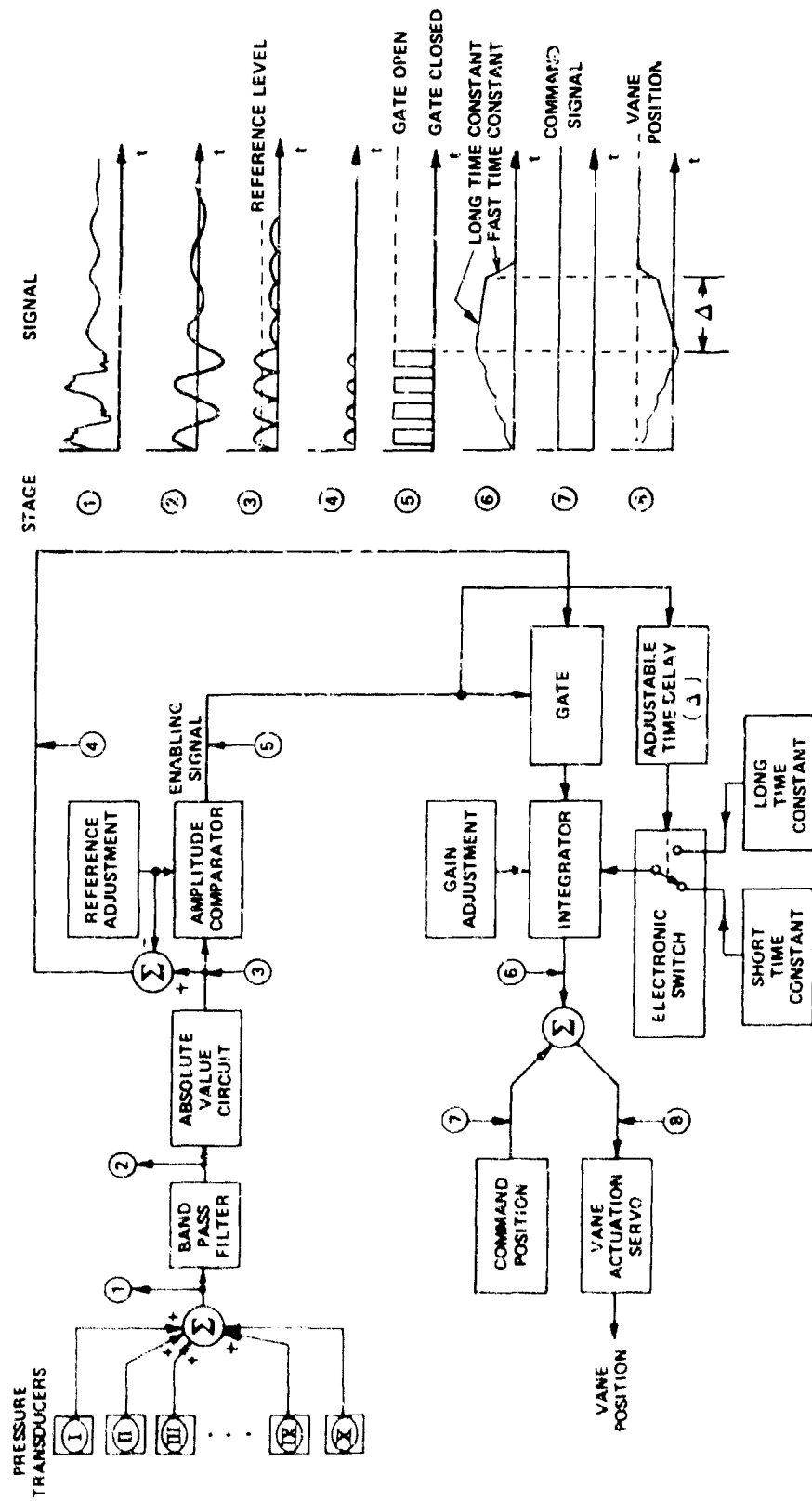


Figure 59 SYSTEM SIGNAL PROCESSING WITH TWO TIME CONSTANTS

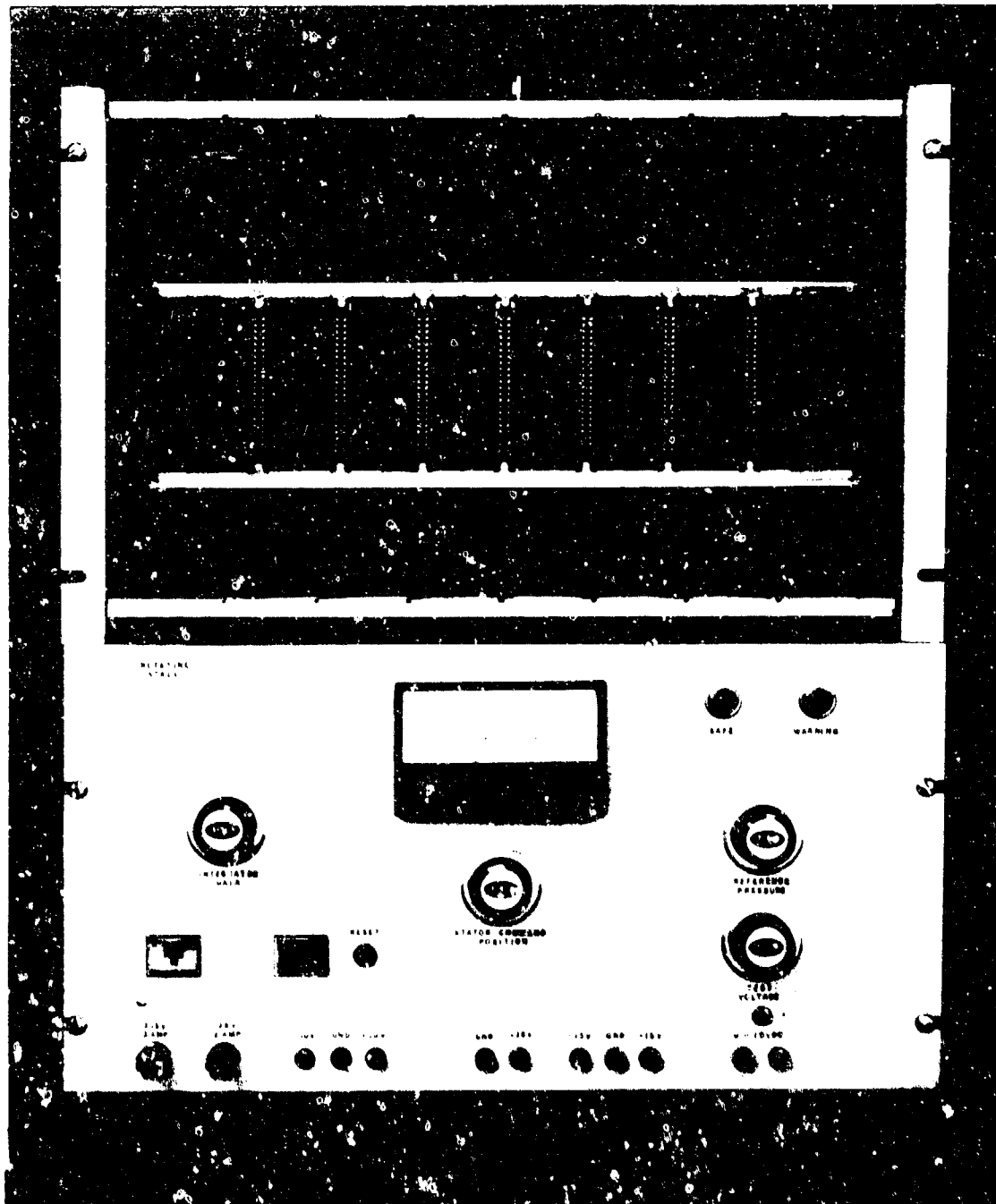


Figure 60 ELECTRONICS CONTROL PANEL FOR PROTOTYPE ROTATING STALL CONTROL SYSTEM



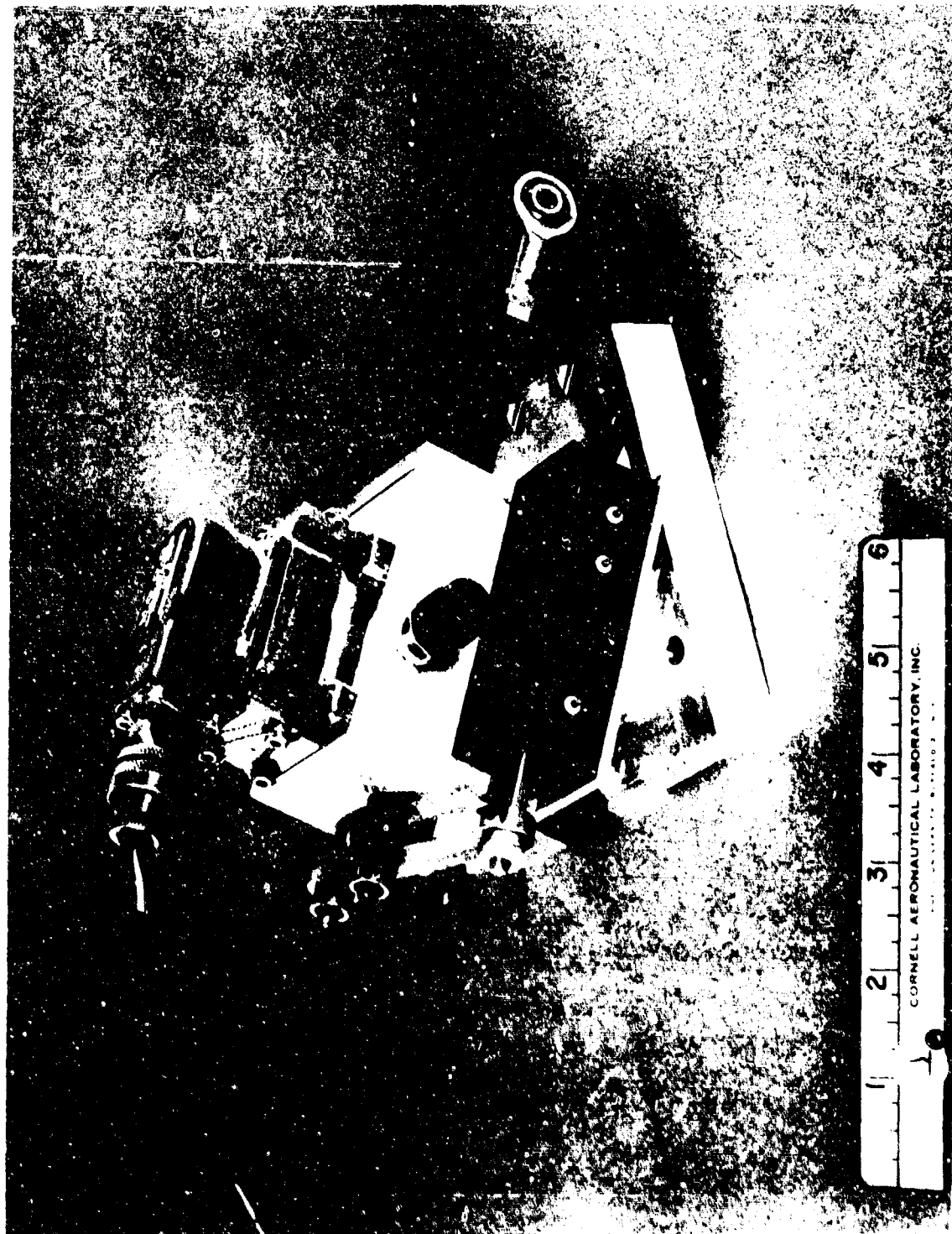


Figure 61 ACTUATOR VALVE AND FEEDBACK POTENTIOMETER ASSEMBLY

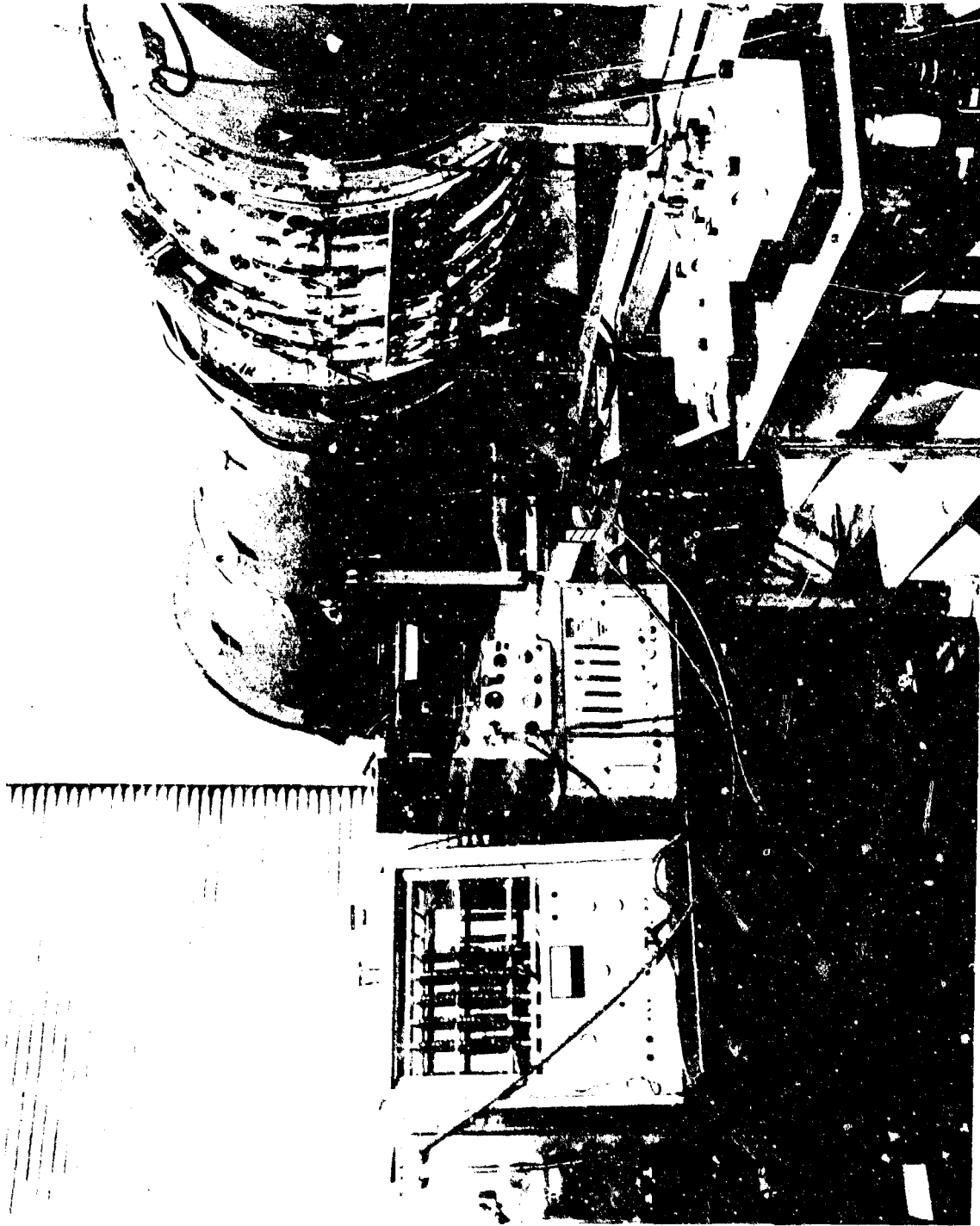


Figure 62 INSTALLATION OF ROTATING STALL CONTROL SYSTEM ON ROTATING ANNULAR CASCADE

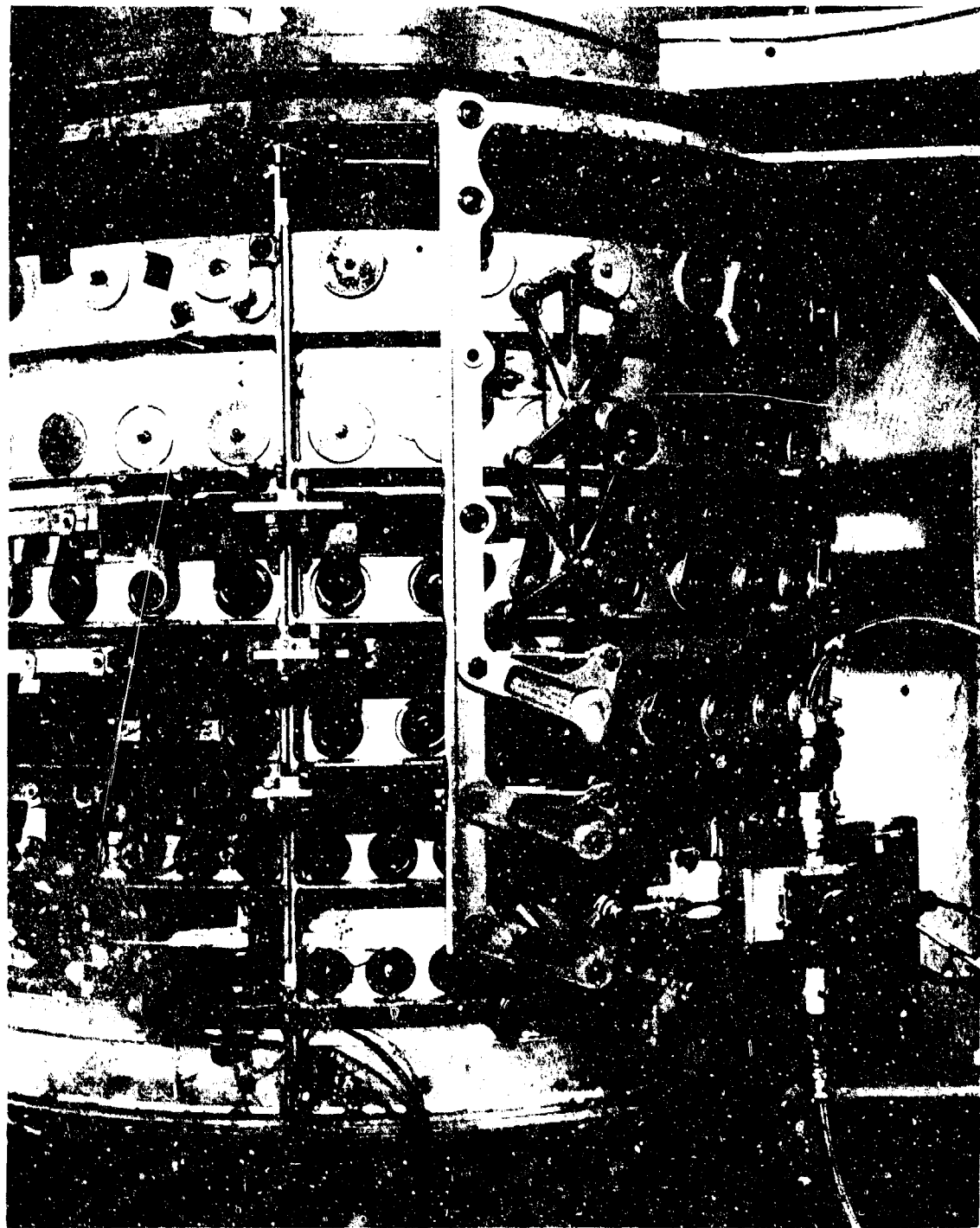


Figure 63 INSTALLATION OF ELECTRO-HYDRAULIC ACTUATOR ON ROTATING ANNULAR CASCADE

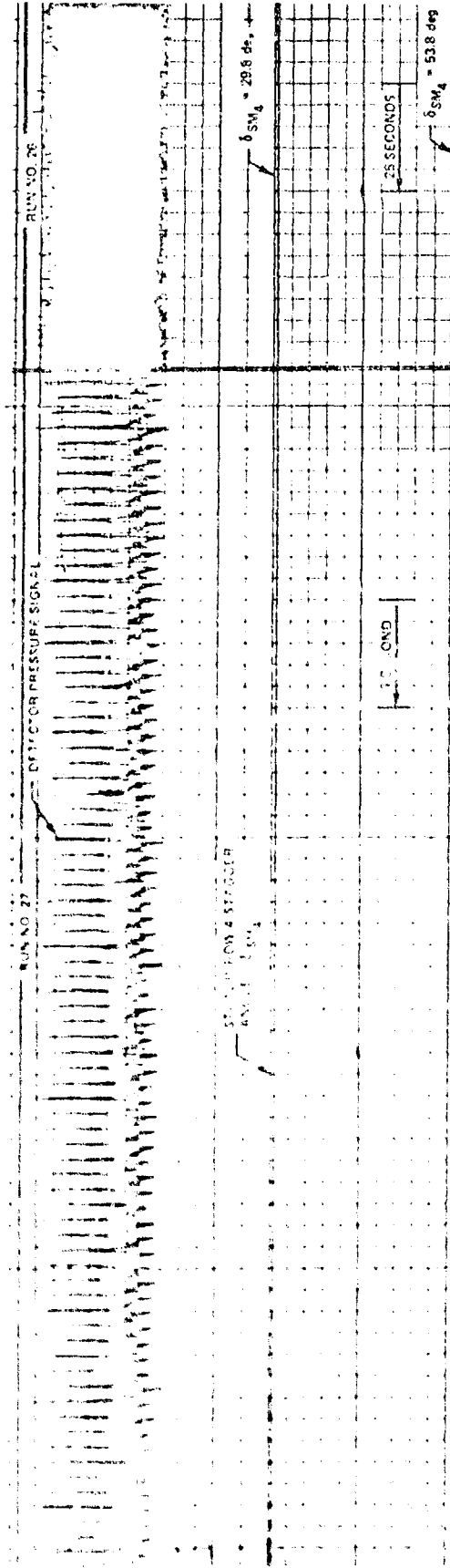


FIGURE 54 EFFECT OF DETECTOR REFERENCE LEVEL AND INTEGRATOR GAIN ON PERFORMANCE OF ROTATING STALL CONTROL. ANNULAR CASCADE CONFIGURATION. STATOR ROW 5 UNLOADED. GUIDE VANE STAGGER ANGLE,  $\delta_{GV} = 32.5 \text{ deg}$ . DETECTOR 5 CANAL. SUM OF (SENSOR 5) (OUTER WALL 1) CHORD STATIC, STATOR ROW 4); + 0.23 (SENSOR 7) (ROTOR OUTER WALL))

(\*) DETECTOR REFERENCE LEVEL = 1000

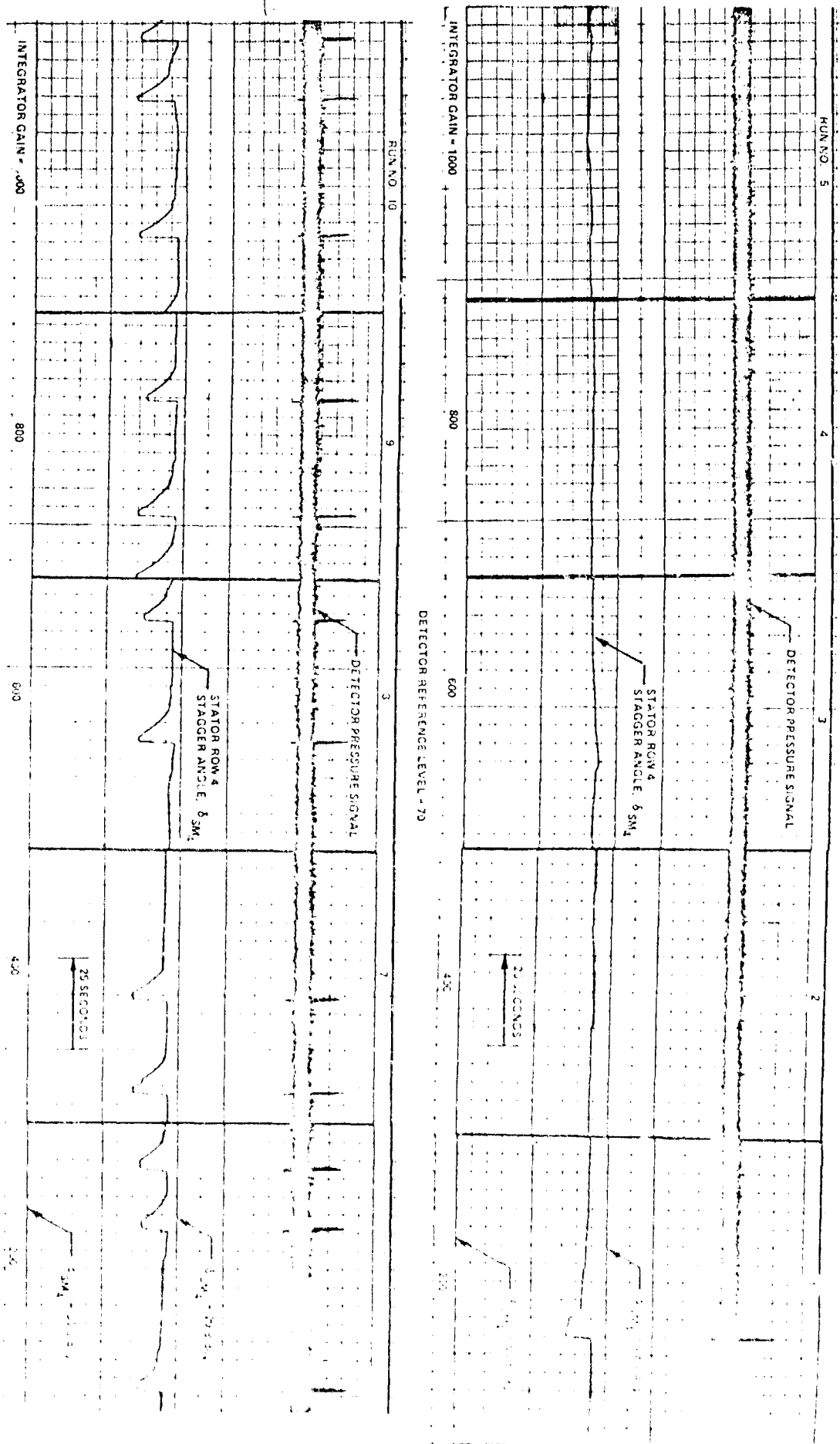


Figure 64 (Cont.) EFFECT OF DETECTOR REFERENCE LEVEL AND INTEGRATOR GAIN ON PERFORMANCE OF ROTATING STALL CONTROL  
 ANNULAR CASCADE CONFIGURATION: STATOR ROW 5 UNLOADED, CURVE VANE STAGGER ANGLE, 6.5° GV = 32.5°  
 DETECTOR SIGNAL: SUM OF SENSOR (5) (OUTER WALL 1/2 CHORD STATIC, STATOR ROW 4), (6) (OUTER WALL 1/2 CHORD STATIC, STATOR ROW 4), (7) (ROTOR OUTER WALL)  
 (a) DETECTOR REFERENCE LEVEL = 70 AND 80

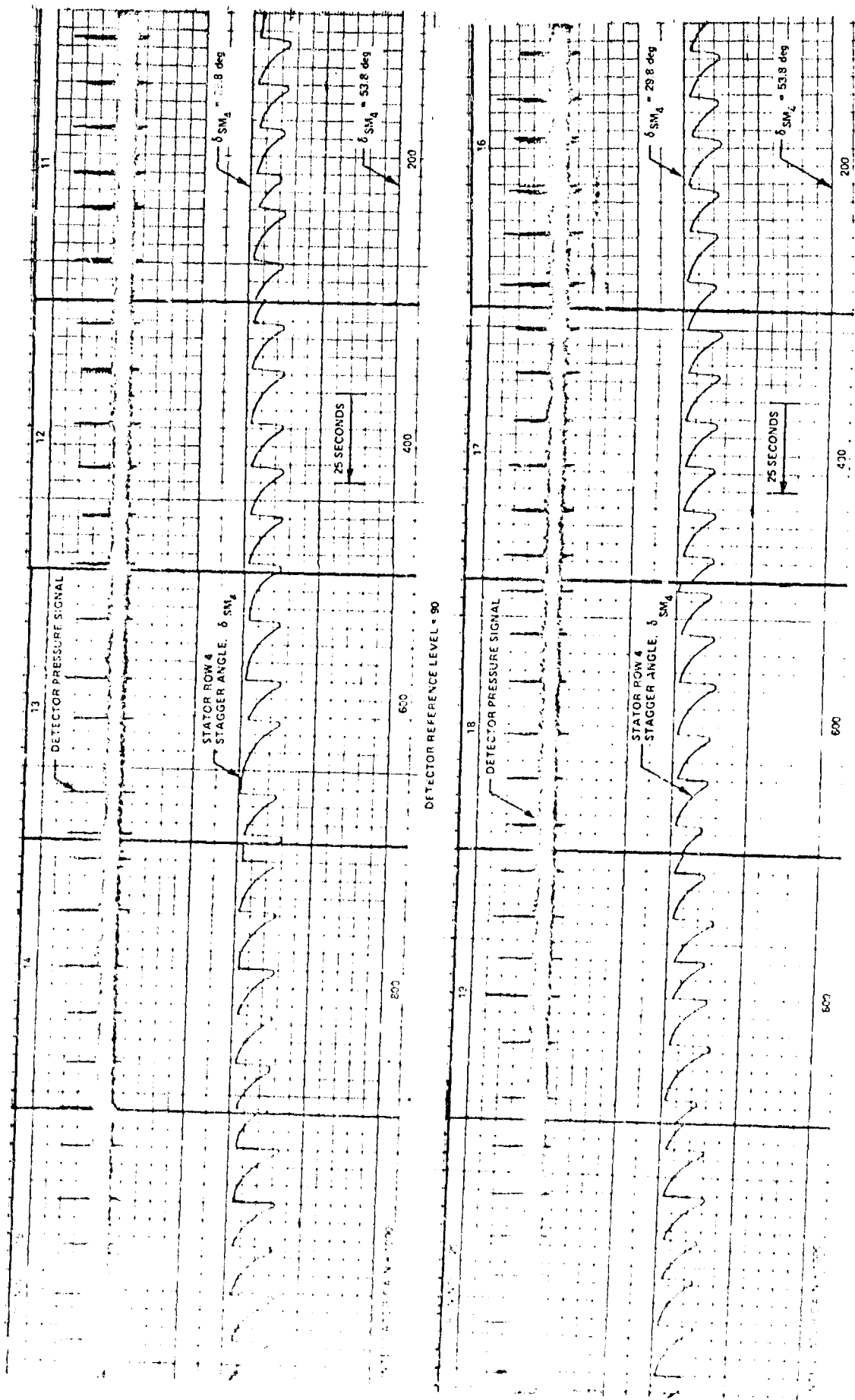


Figure 64 (Cont.) EFFECT OF DETECTOR REFERENCE LEVEL AND INTEGRATOR GAIN ON PERFORMANCE OF ROTATING STALL CONTROL.  
 ANGULAR CASCADE CONFIGURATION, STATOR ROW 5 UNLOADED, GUIDE VANE STAGGER ANGLE,  $\delta$  GV = 32.5 deg  
 DETECTOR SIGNAL SUM OF SENSOR 5 (OUTER WALL 1-4 CHORD STATIC, STATOR ROW 4) + 0.23 [SENSOR 7 (ROTOR OUTER WALL)]  
 (c) DETECTOR REFERENCE LEVEL = 90 AND 100

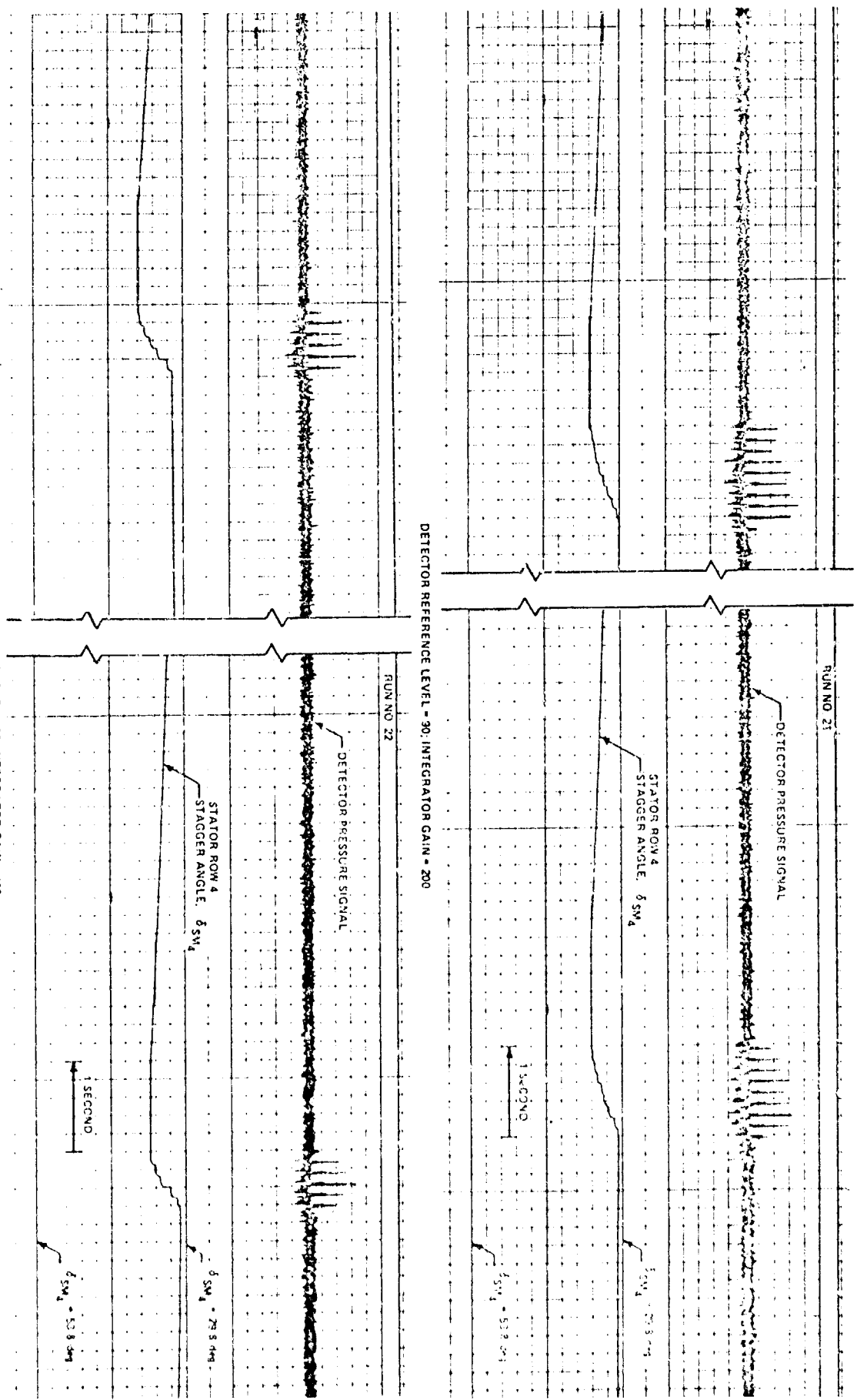


Figure 65 EFFECT OF INTEGRATOR GAIN ON PERFORMANCE OF ROTATING STALL CONTROL.  
 ANNULAR CASCADE CONFIGURATION: STATOR ROWS UNLOADED, GUIDE VANES STAGGER ANGLE,  $\delta$  GV = 32.5 deg  
 DETECTOR SIGNAL: SUM OF [SENSOR 5] OUTER WALL 14 CHORD STATIC STATOR ROW 4; + 0.23 [SENSOR 7] [ROTOR OUTER WALL];  
 (a) INTEGRATOR GAIN = 200 AND 400

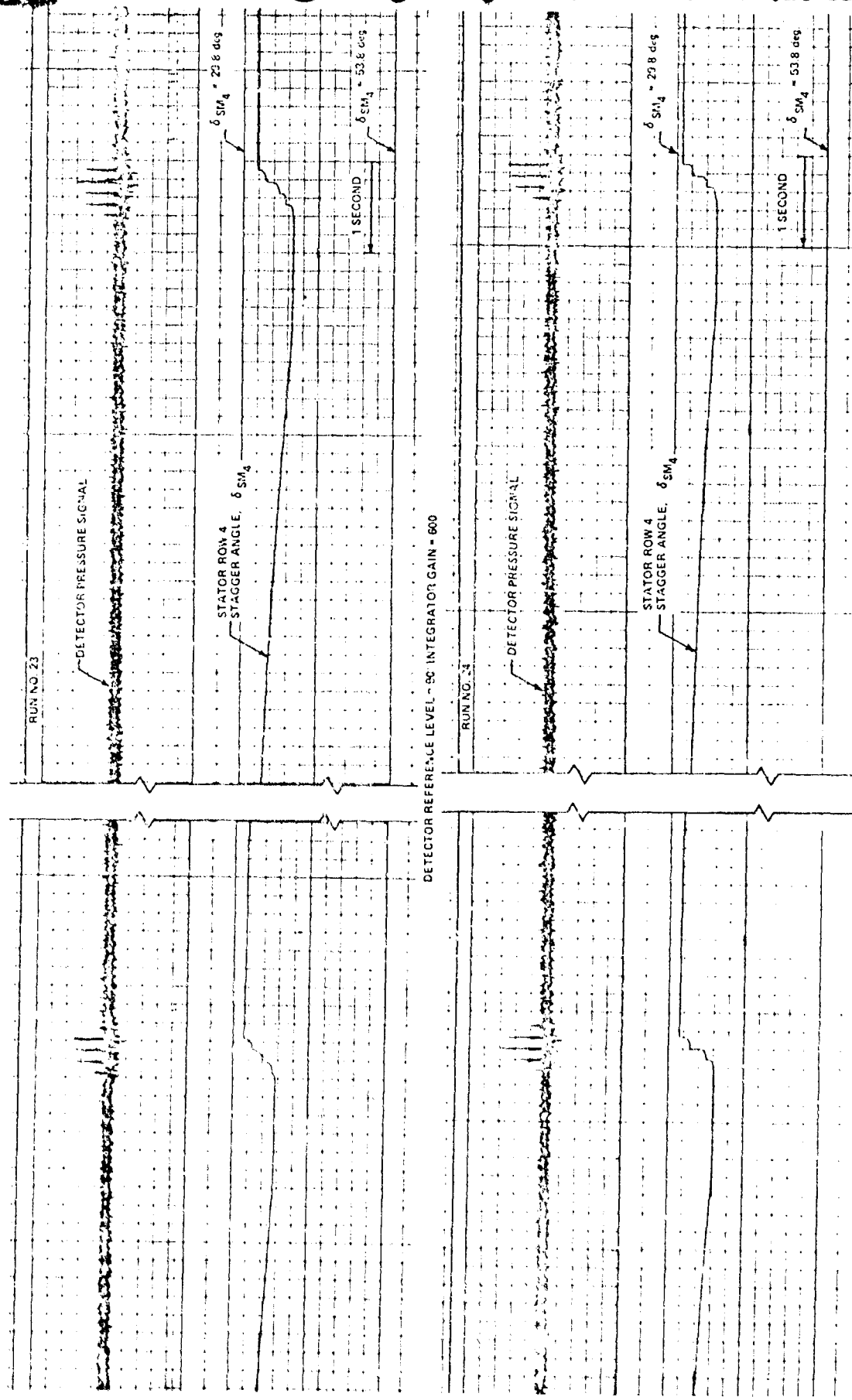


Figure 65 (Cont.) EFFECT OF INTEGRATOR GAIN ON PERFORMANCE OF ROTATING STALL CONTROL.  
 ANNULAR CASCADE CONFIGURATION: STATOR ROW 5 UNLOADED, GUIDE VANE STAGGER ANGLE,  $\delta_{GV} = 32.5 \text{ deg}$   
 DETECTOR SIGNAL: SUM OF [SENSOR ⑤ (OUTER WALL 1/4 CHORD STATIC, STATOR ROW 4)] + 0.23 [SENSOR ⑦ (INLET OUTER WALL)]  
 (b) INTEGRATOR GAIN = 600 AND 800



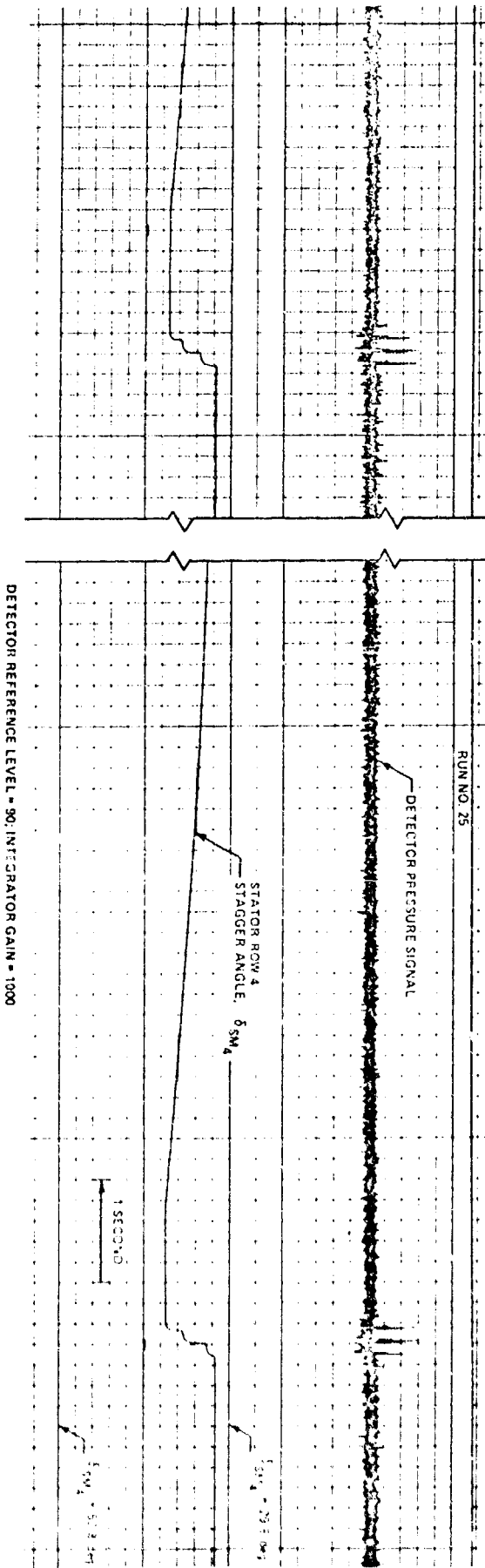


Figure 65 (Cont.) EFFECT OF INTEGRATOR GAIN ON PERFORMANCE OF ROTATING STALL CONTROL.  
 ANNULAR CASCADE CONFIGURATION: STATOR ROW 5 UNLOADED, GUIDE VANE STAGGER ANGLE,  $\delta_{GV} = 32.5 \text{ deg}$   
 DETECTOR SIGNAL, SUM OF ISENSOR (5) OUTER WALL 1/4 CHORD STATIC, STATOR ROW 4; + 0.23 ISENSOR (7) (ROTOR OUTER WALL);  
 (a) INTEGRATOR GAIN = 1000

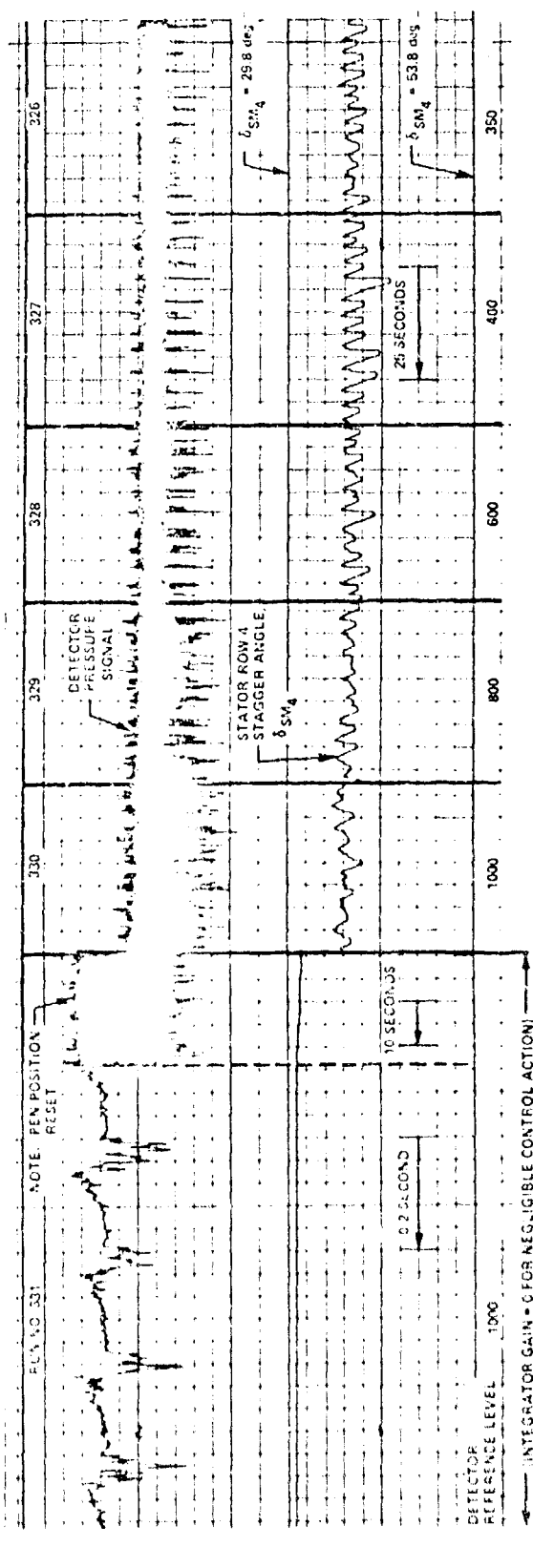
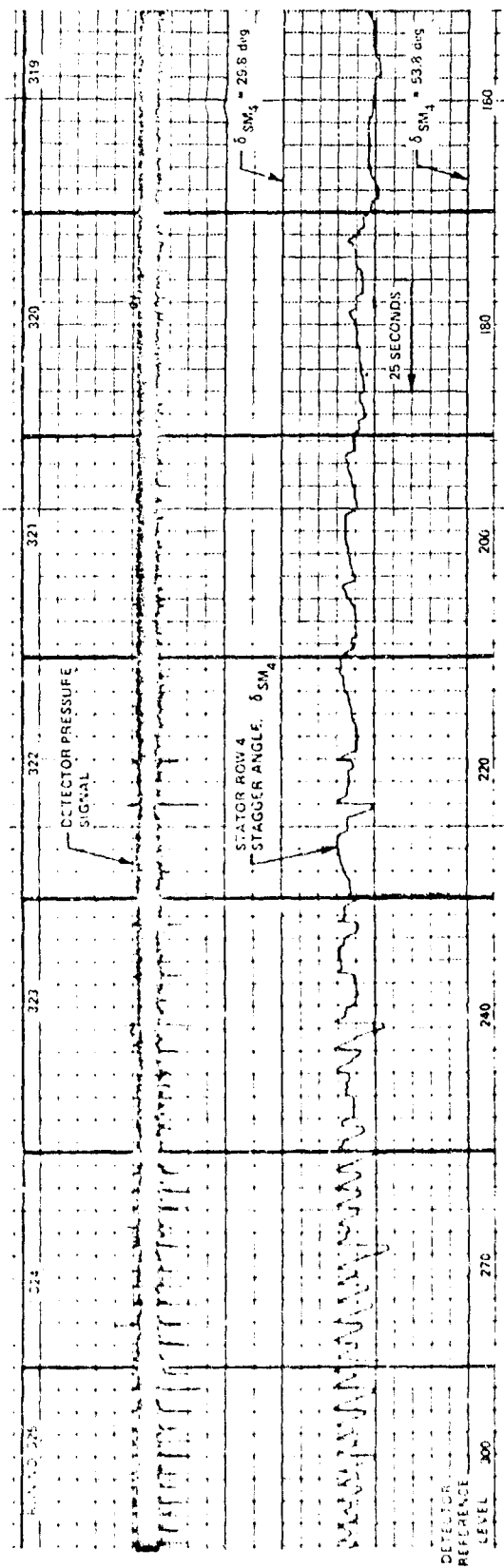


Figure 66 PERFORMANCE OF ROTATING STALL CONTROL AT VARIOUS DETECTOR REFERENCE LEVELS WITH INTEGRATOR GAIN = 800.

DETECTOR SIGNAL SENSOR (2), MID-ANNULUS TOTAL PRESSURE STATOR ROW 5

(A) ANNULAR CASCADE CONFIGURATION; STATOR ROW 5 LOADED; GUIDE VANE STAGGER ANGLE,  $\delta GV = 24.5 \text{ deg}$

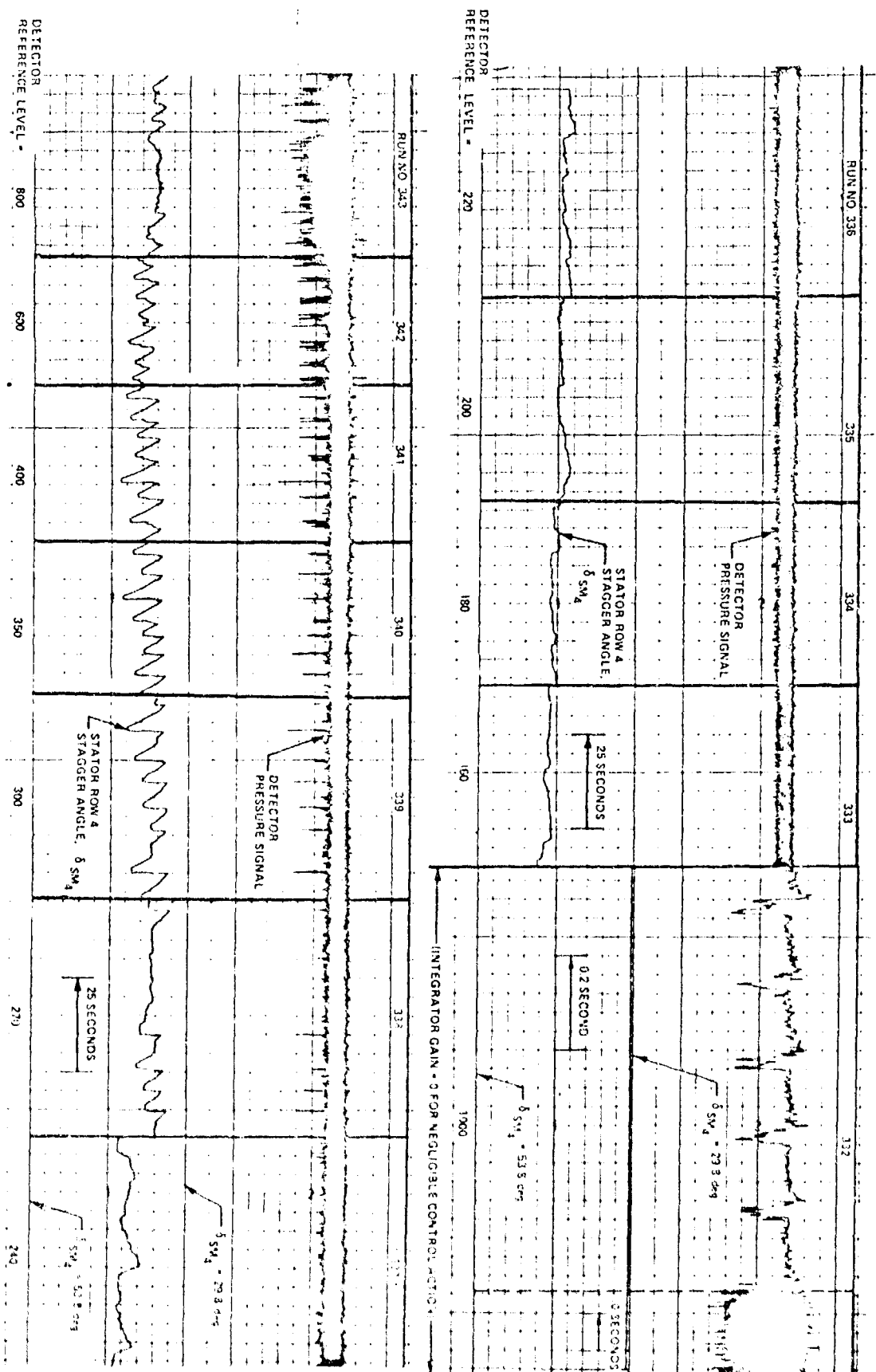


Figure 66 (Cont.) PERFORMANCE OF ROTATING STALL CONTROL AT VARIOUS DETECTOR REFERENCE LEVELS WITH INTEGRATOR GAIN = 800  
 DETECTOR SIGNAL: SENSOR ② MID ANNULUS TOTAL PRESSURE STATOR ROW 5  
 (b) ANNULAR CASCADE CONFIGURATION: STATOR ROW 5 LOADED, GUIDE VANE STAGGER ANGLE: 5.0° = 37.5 deg



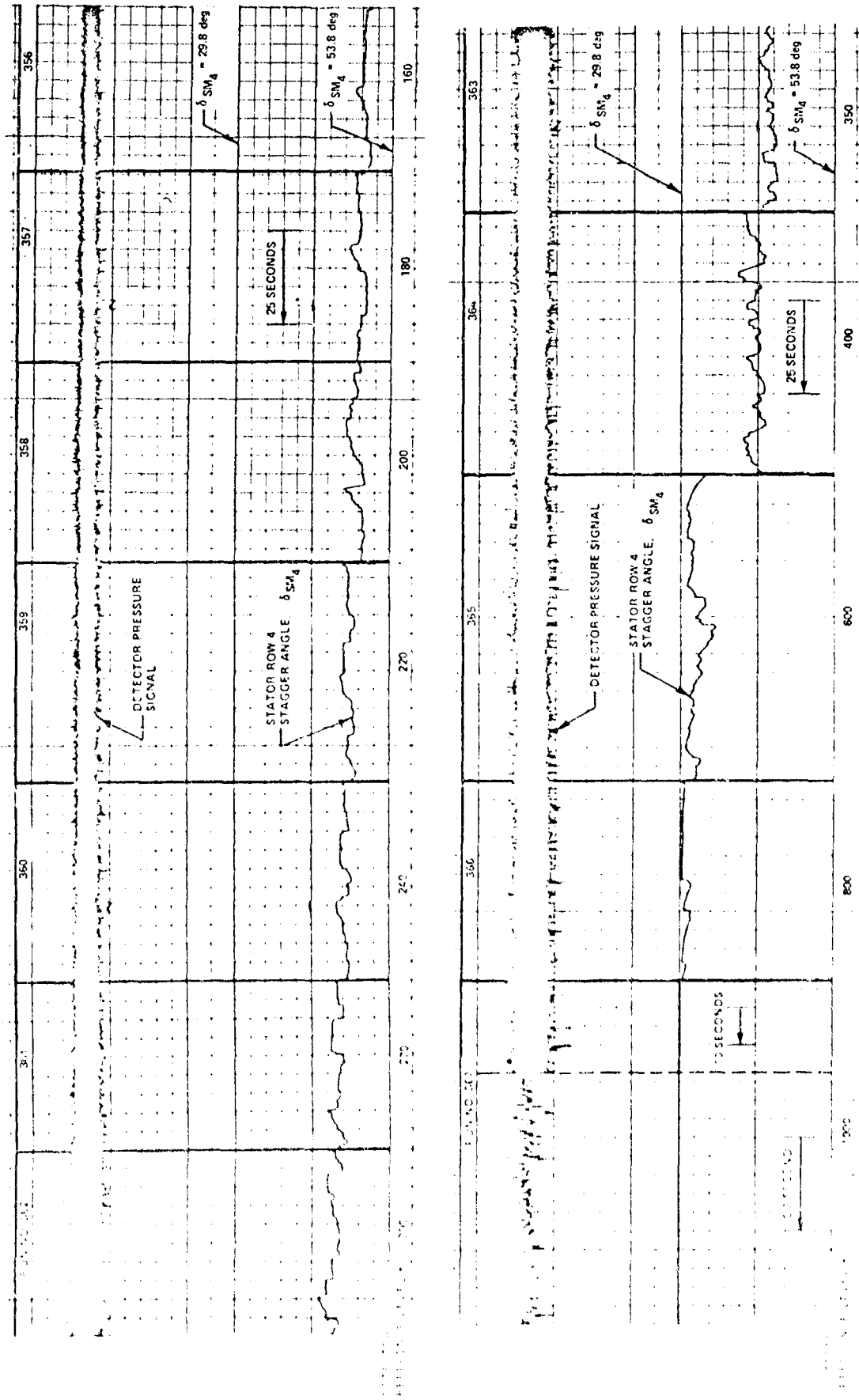


FIGURE 65. COMPARISON OF ROTATING STALL CONTROL AT VARIOUS DETECTOR REFERENCE LEVELS WITH INTEGRATOR GAIN = 800.  
 DETECTOR SIGNAL SENSOR 3 V/D ANALOG TOTAL PRESSURE STATOR ROW 5  
 4-ANNULAR CASCADE CONFIGURATION STATOR ROW 5 LOADED, GUIDE VANE STAGGER ANGLE,  $\delta_{GV} = 48.5 \text{ deg}$

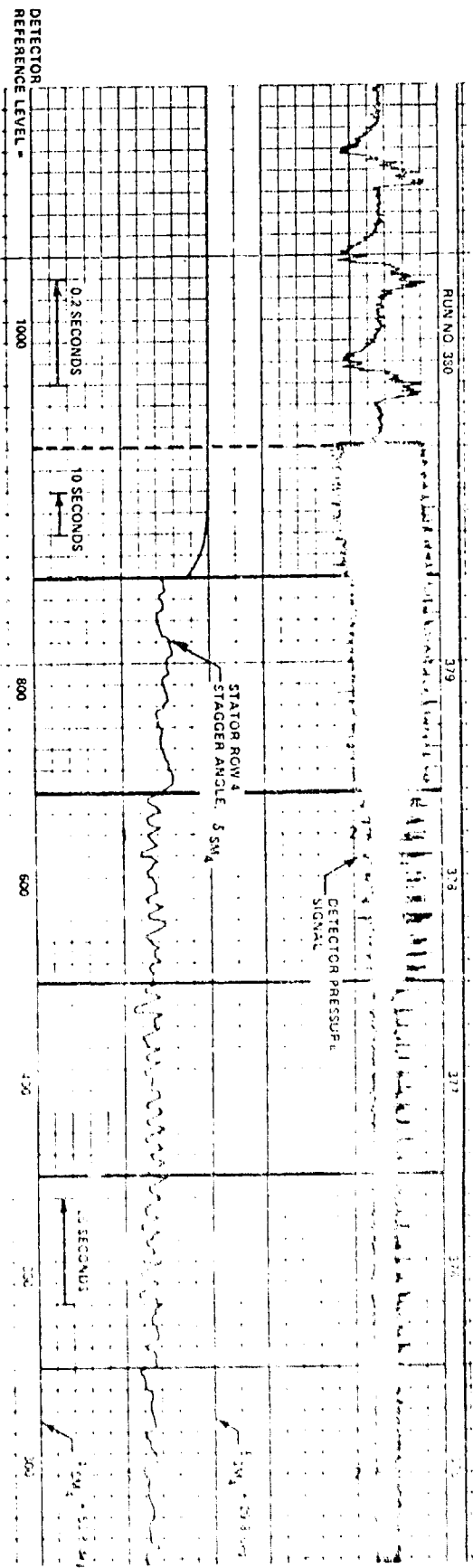
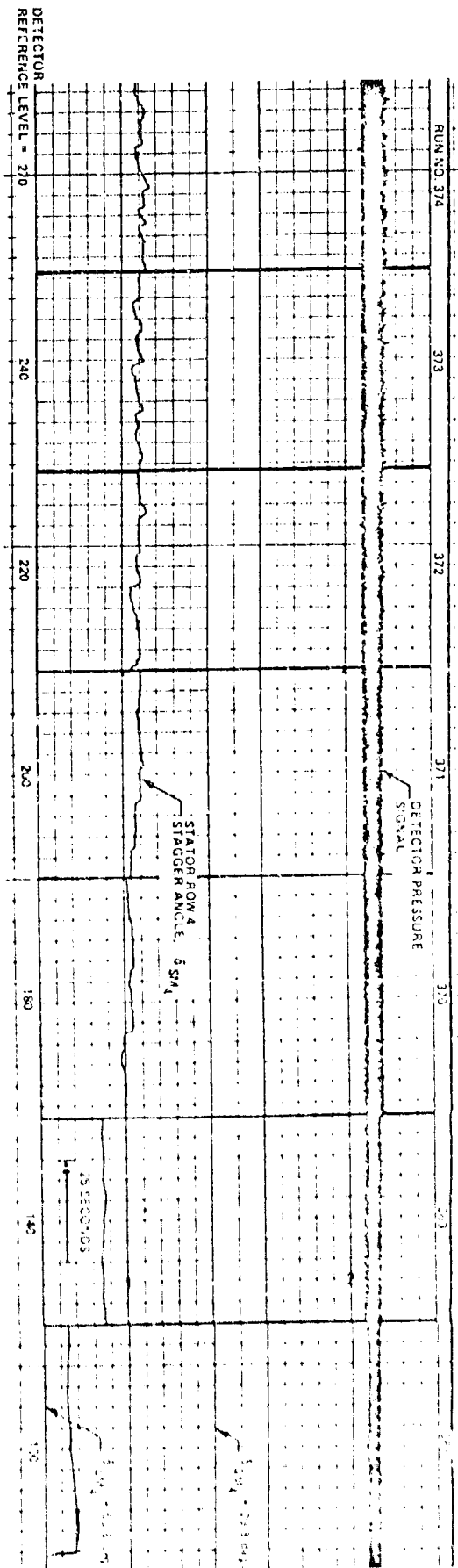


Figure 67 PERFORMANCE OF ROTATING STALL CONTROL AT VARIOUS DETECTOR REFERENCE LEVELS  
 WITH INTEGRATOR GAIN = 800.  
 DETECTOR SIGNAL: SENSOR (7), ROTOR OUTER WALL  
 ANNULAR CASCADE CONFIGURATION: STATOR ROW 5 LOADED, GUIDE VANE STAGGER ANGLE 5.0, 24.5 DEG



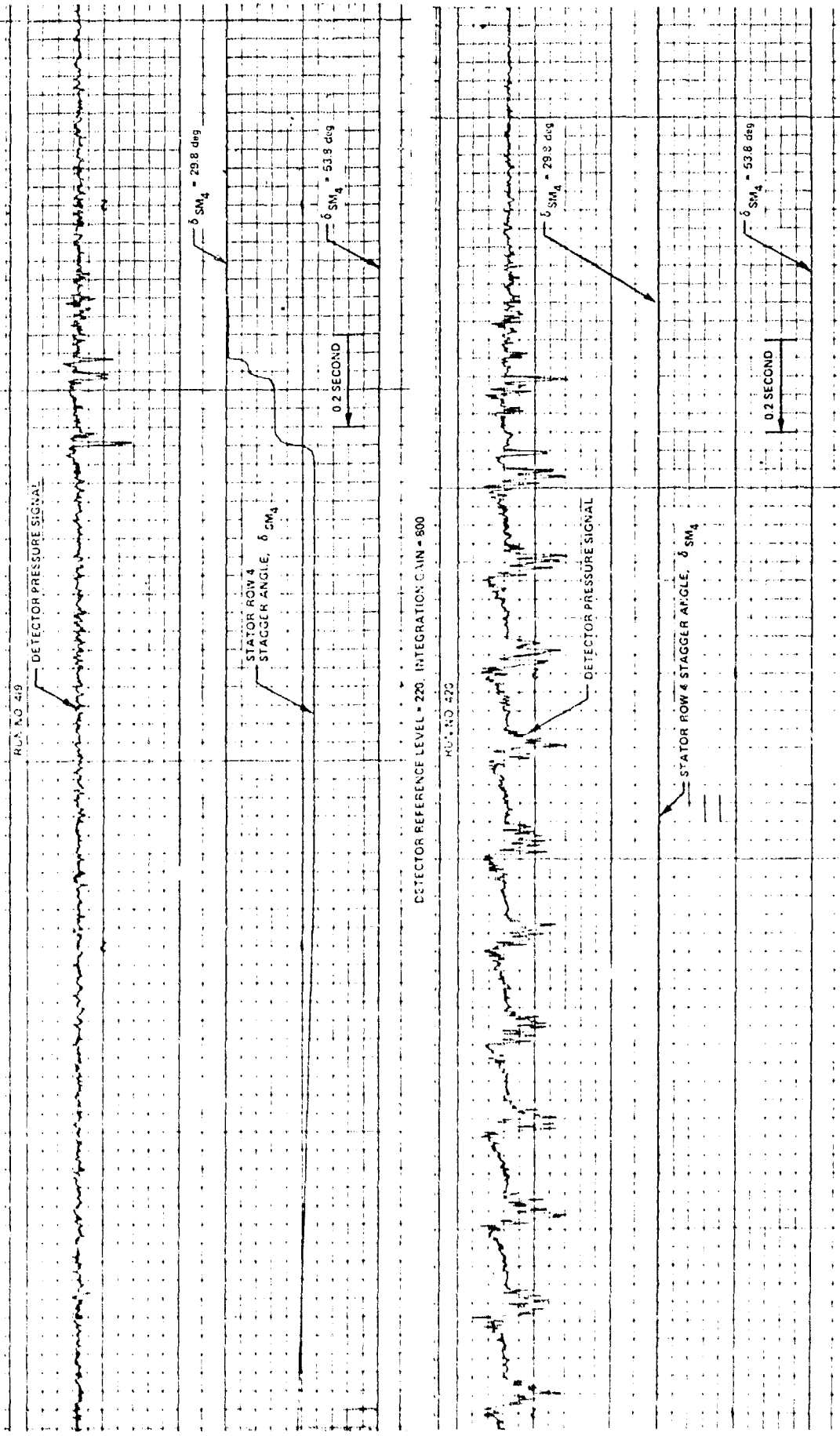


Figure 69 PERFORMANCE OF ROTATING STALL CONTROL DURING ROTOR ACCELERATION FROM 1000 rpm (NORMALLY UNSTALLED) TO 1250 rpm (NORMALLY STALLED).  
 ANNULAR CASCADE CONFIGURATION: STATOR ROW 5 LOADED, GUIDE VANE STAGGER ANGLE  $\delta G_V = 24.5 \text{ deg}$   
 (N) DETECTOR SIGNAL: SENSOR ②, MID-ANNULUS TOTAL PRESSURE, STATOR ROW 5

DETECTOR REFERENCE LEVEL = 1000  
 INTEGRATION GAIN = 3

NO CONTROL ACTION



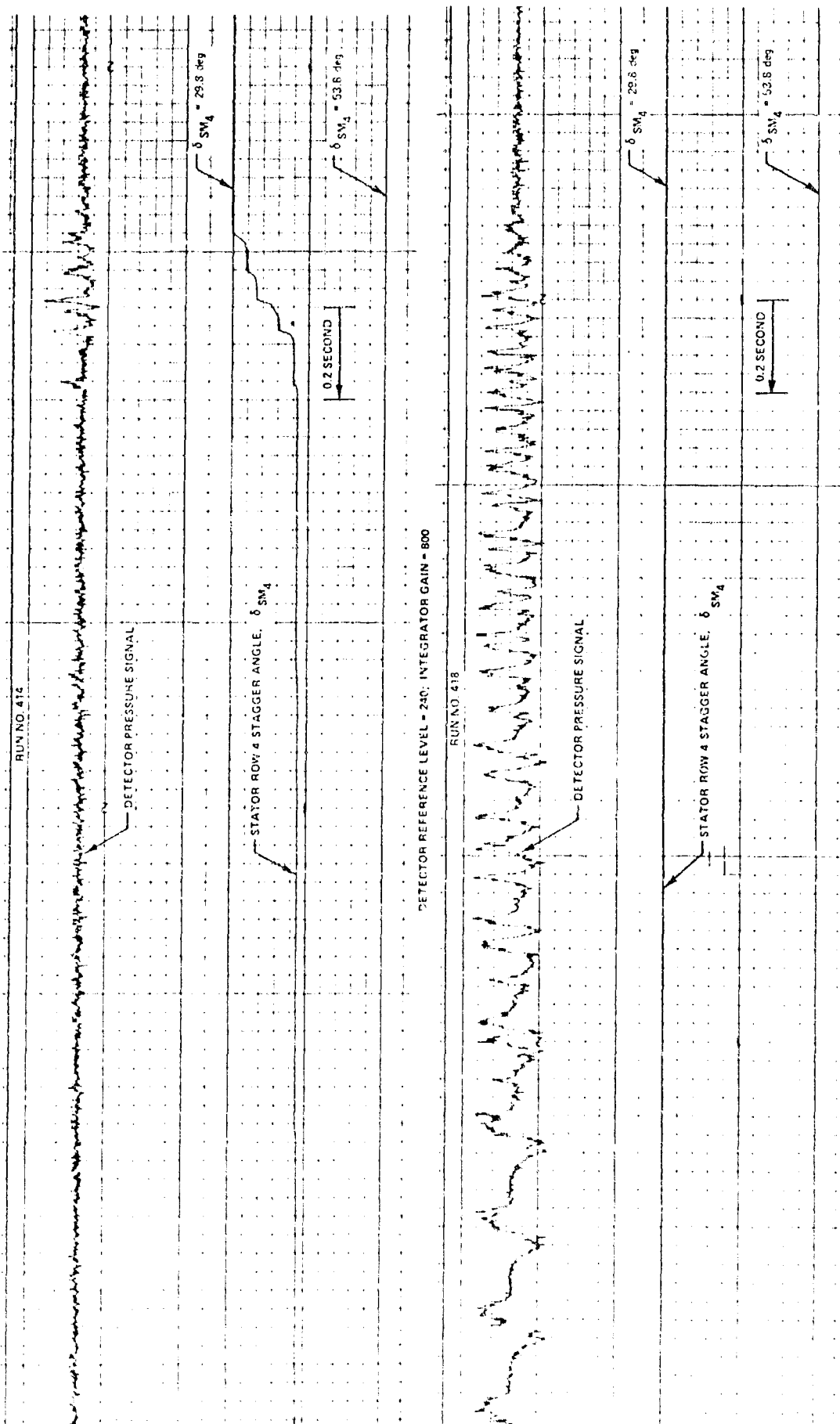
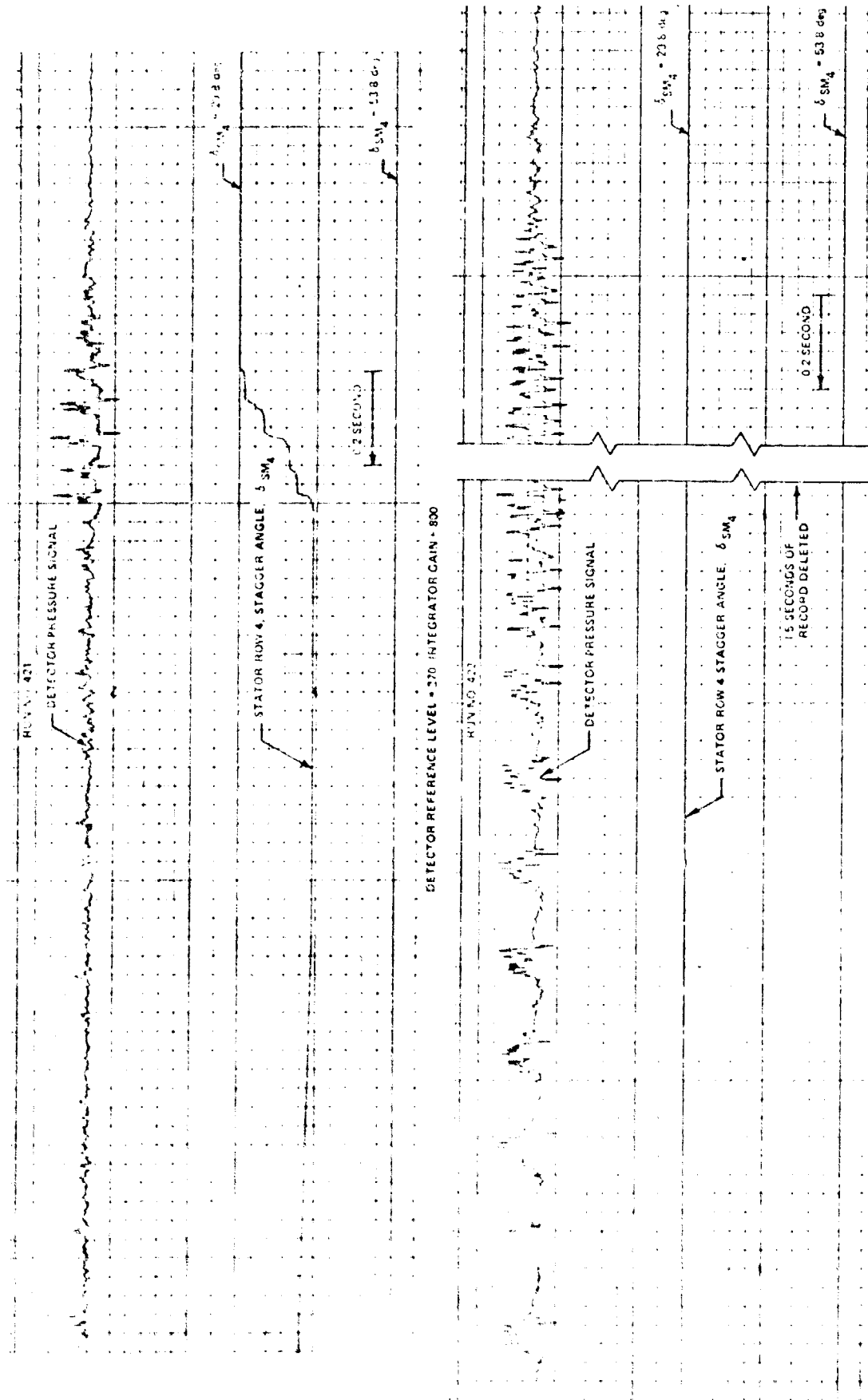


Figure C9 (cont.) PERFORMANCE OF ROTATING STALL CONTROL DURING ROTOR ACCELERATION FROM 1000 rpm (NORMALLY UNSTALLS) TO 1250 rpm (NORMALLY STALLED).  
 ANNULAR CASCADE CONFIGURATION: STATOR ROW 5 LOADED, GUIDE VANE STAGGER ANGLE  $\delta_{GV} = 24.5$   
 (S) DETECTOR SIGNAL; SENSOR (2) ROTOR OUTER WALL



DETECTOR REFERENCE LEVEL = 1000 ; INTEGRATOR GAIN = 0 ; NO CONTROL ACTION  
 PERFORMANCE OF ROTATING STALL CONTROL DURING ROTOR ACCELERATION FROM 1000 rpm  
 (NORMALLY INSTALLED) TO 1250 rpm (NORMALLY STALLED).

ANNUAL CASCADE CONFIGURATION. STATOR ROW 5 LOADED, GUIDE VANE STAGGER ANGLE  $\delta_{GV} = 24.5 \text{ deg}$   
 (1) DETECTOR SIGNAL - SENSOR (6) - OUTER WALL 1/2 CHORD STATIC, STATOR ROW 5

Preceding page blank

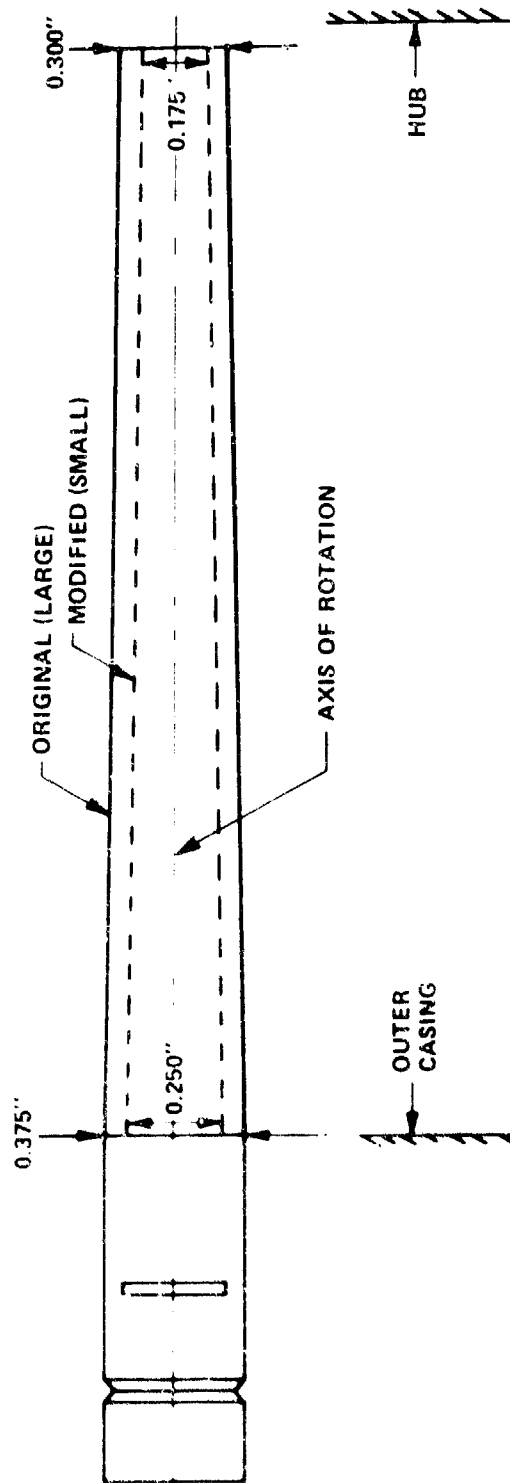


Figure 70 SKETCH OF DISTURBANCE GENERATORS USED IN EXPERIMENTAL DAMPING INVESTIGATION

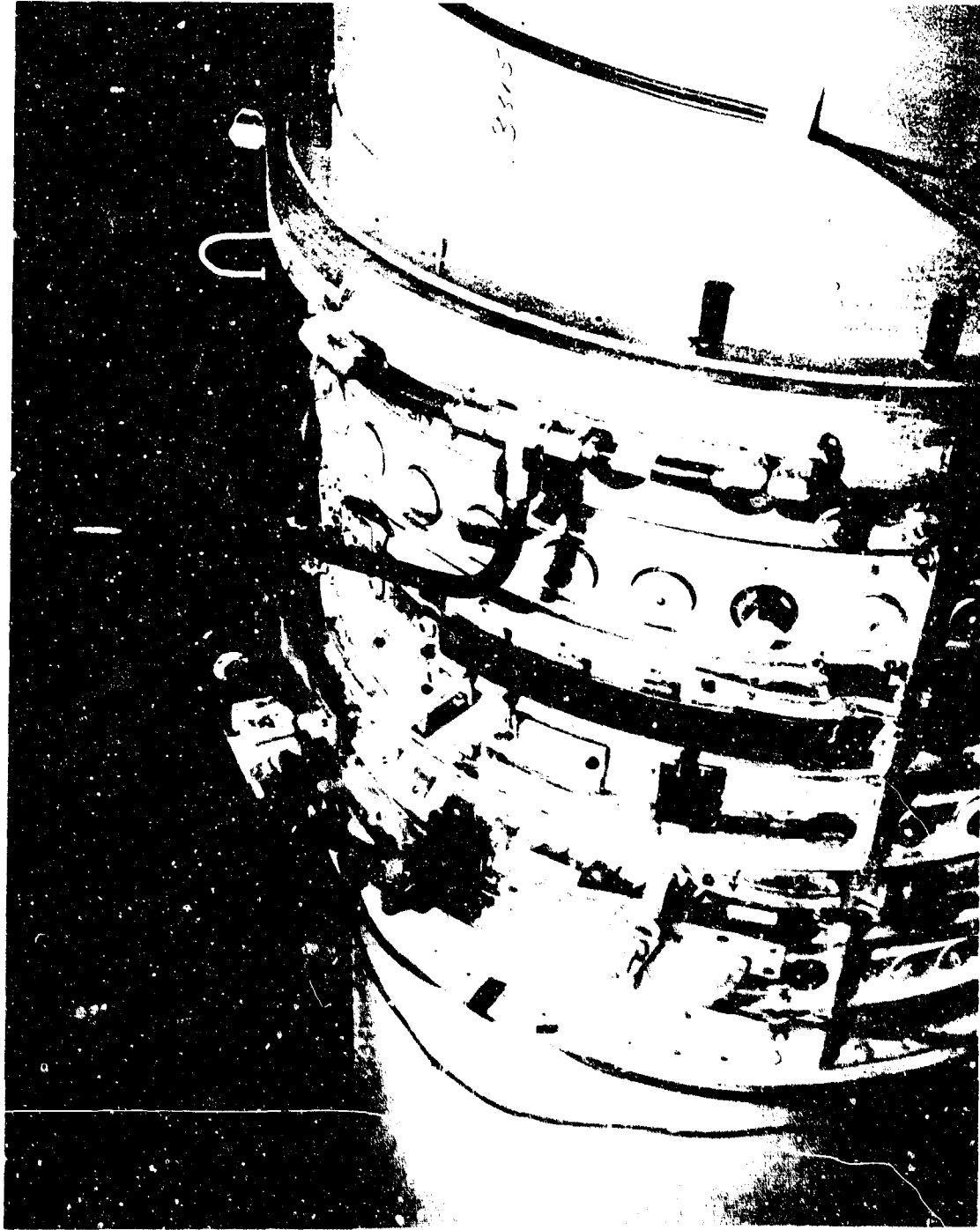


Figure 71 DISTURBANCE GENERATOR DRIVE MOUNTED ON ANNULAR CASCADE

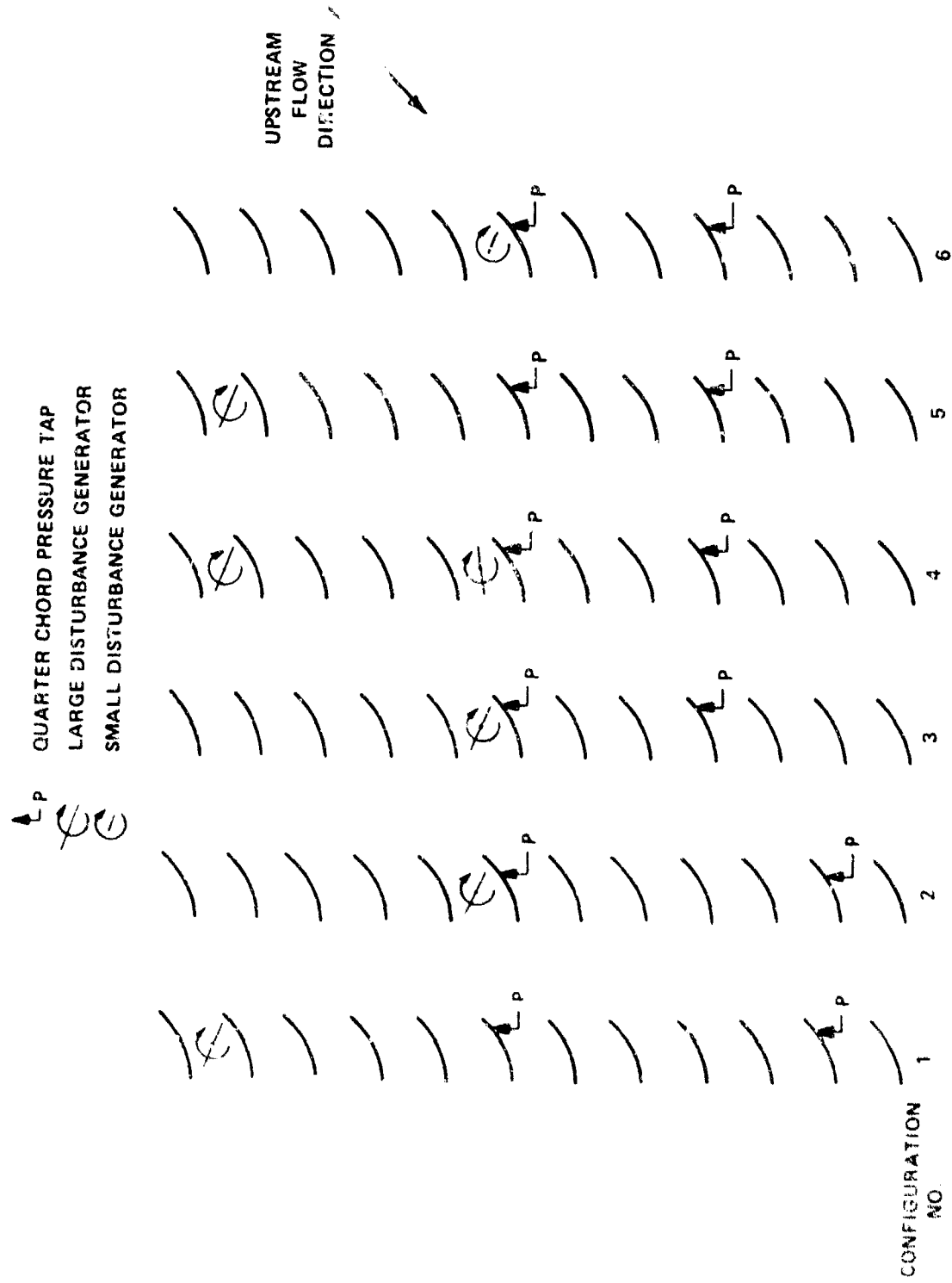


Figure 72 SCHEMATICS OF RELATIONSHIP BETWEEN DISTURBANCE GENERATORS AND QUARTER-CHORD  
 STATIC PRESSURE TAPS USED IN EXPERIMENTAL DAMPING INVESTIGATION



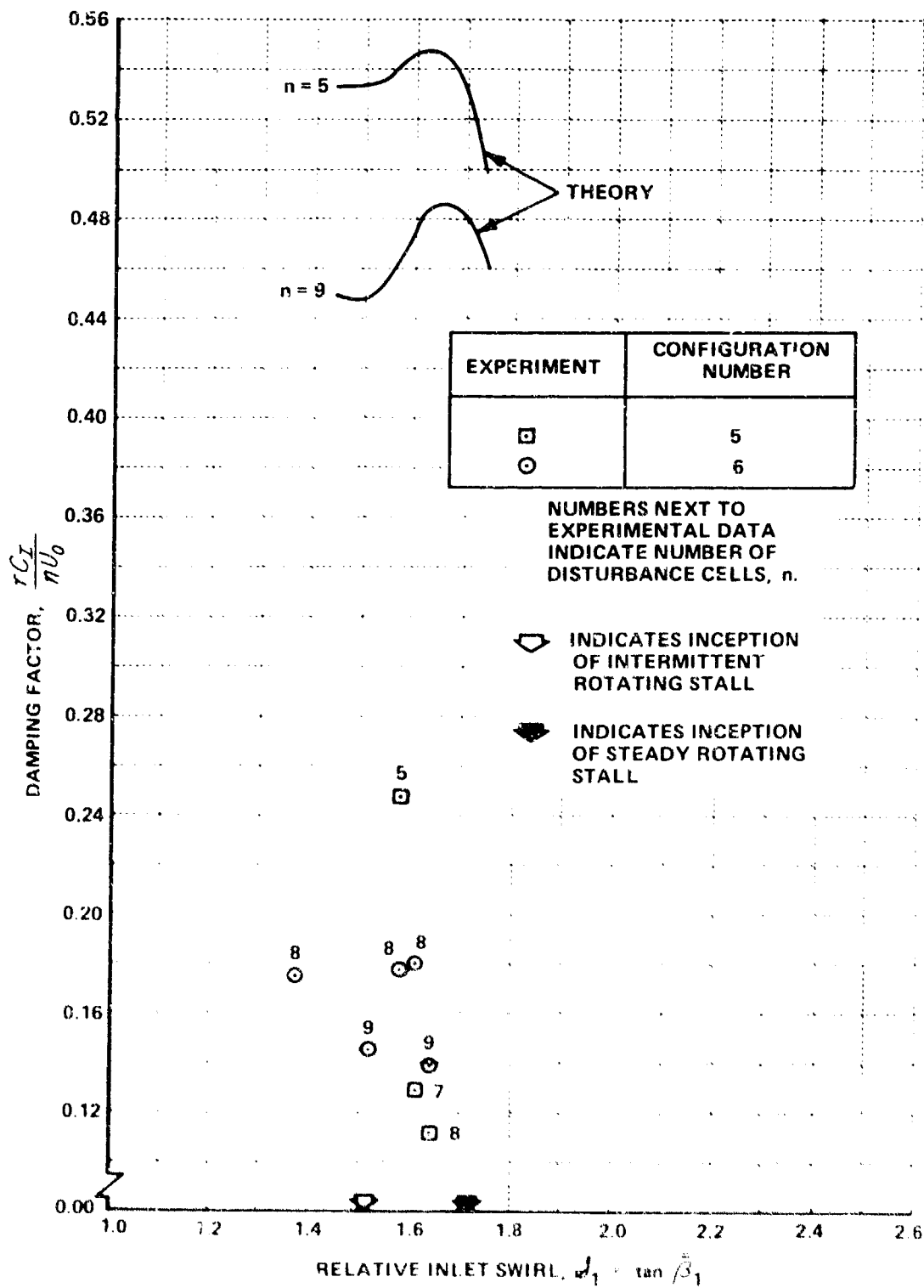


Figure 73 (Cont.) DAMPING MEASUREMENTS ON STATOR SET NO. 1  
 (b) STATOR STAGGER ANGLE,  $\delta_{SM} = 37.2$  DEG

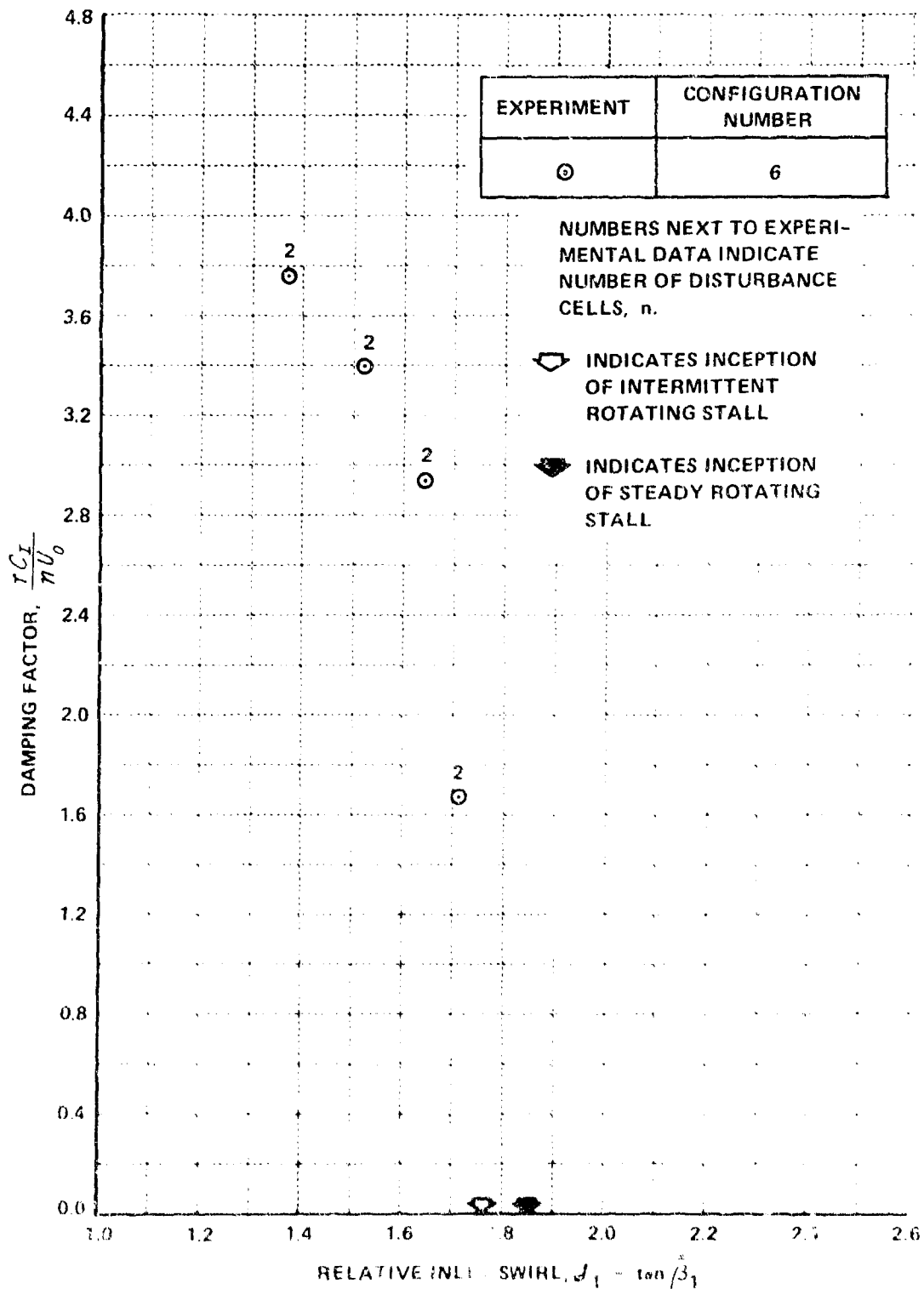


Figure 73 (Cont.) DAMPING MEASUREMENTS ON STATOR SET NO. 1  
 (c) STATOR STAGGER ANGLE,  $\delta_{SM} = 47.2$  DEG



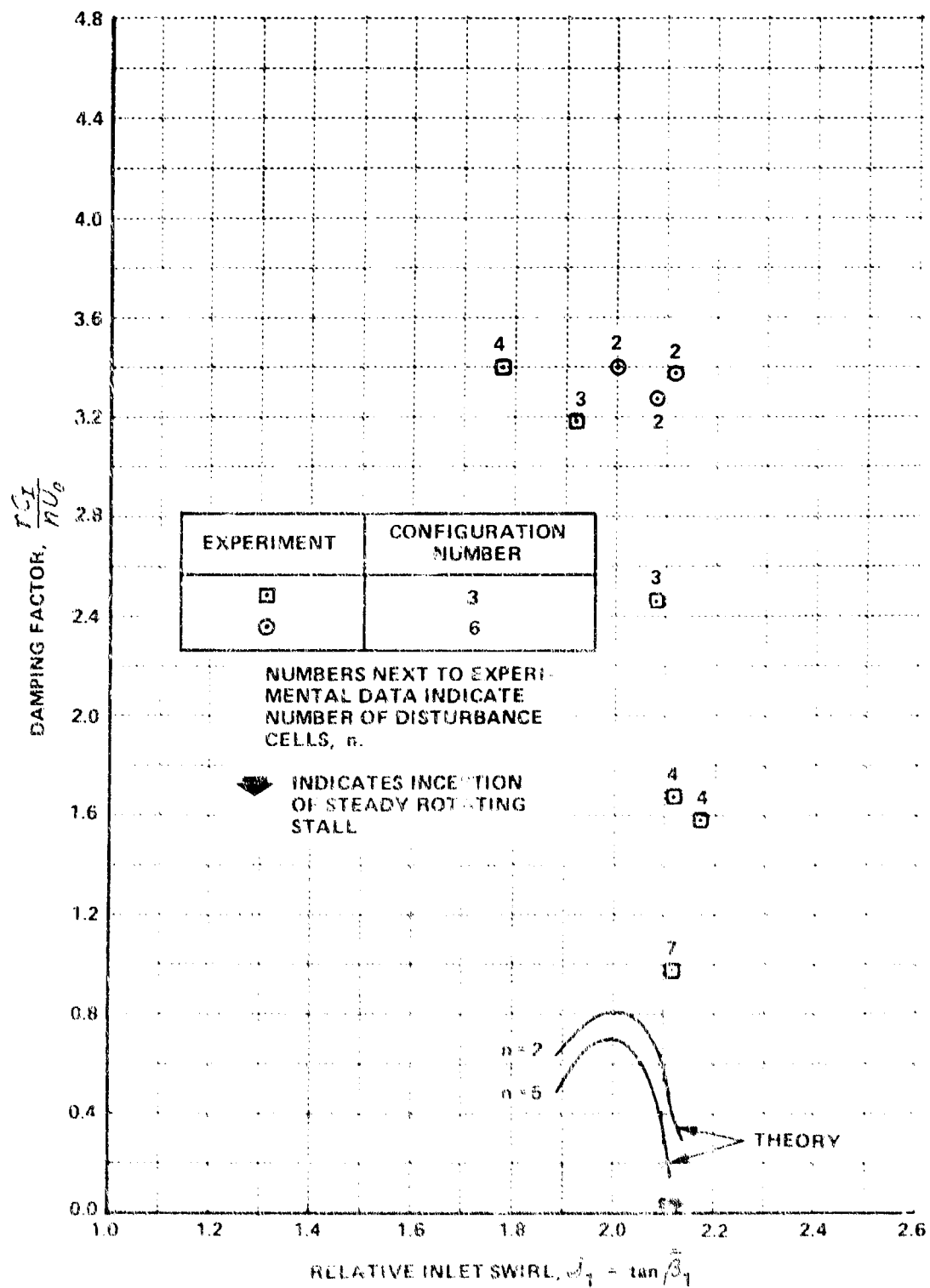


Figure 73 (Cont.) DAMPING MEASUREMENTS ON STATOR SET NO. 1

(d) STATOR STAGGER ANGLE,  $\delta_{SM} = 57.2$  DEG

## REFERENCES

1. Ludwig, G. R., Nenni, J. P. and Rice, R. S., Jr. An Investigation of Rotating Stall Phenomena in Turbine Engine Compressors AFAPL-TR-70-26, May 1970.
2. Duravant, J. C., Cascade Investigation of a Related Series of Six-Percent Thick Guide-Vane Profiles and Design Charts, NACA TN 3959, May 1957.
3. Kriebel, A. R., Seidel, B. S., and Schwind, R. G., Stall Propagation in a Cascade of Airfoils, NASA TR-61, 1960.
4. Sears, W. R. "Rotating Stall in Axial Compressors" Zeitschrift für angewandte Mathematik und Physik, Vol. 6, 1955, pg. 429.
5. Marble, F. E. "Propagation of Stall in a Compressor Blade Row" Journal of the Aeronautical Sciences, Vol. 24, No. 11, November 1957.
6. Stenning, A. H., Kriebel, A. R., Montgomery, S. R., Stall Propagation in Axial-Flow Compressor NACA TN 3580, June 1956.
7. Emmons, H. W., Kronauer, R. E., Rockett, J. A., "A Survey of Stall Propagation -- Experiment and Theory", Transactions of the American Society of Mechanical Engineers, Journal of Basic Engineering, Series D, Vol. 8, September 1959.
8. Falk, T. J. "Rotating Stall in Single Stage Axial Flow Compressors" Cornell University, AFOSR TN 56-512 (AD 110327) September 1956.
9. Leone, M. J., A Study of Existing Information on Rotating Stall With New Observations Concerning Changes in Stall-Cell Size and Number, Rensselaer Polytechnic Inst., TR A. E. 6810 September 1968.
10. Takata, H. and Nagano, S. "Nonlinear Analysis of Rotating Stall" American Society of Mechanical Engineering Transaction Series A Journal of Engineering for Power, Vol. 94, No. 4, pg. 279, October 1972.  
  
See also same title, Institute of Space and Aeronautical Science, University of Tokyo, Report No. 449 (1970) April 1970.
11. Brady, W. G. and Ludwig, G. R., Basic Studies of Rotating Stall and an Investigation of Flow-Instability Sensing Devices, Part I - Basic Studies of Rotating-Stall Flow Mechanisms, AFAPL TR-69-115, Part I, DDC No. AD-625783, October 1969.

REFERENCES (Cont'd)

12. Martin, A. W., Propulsion System Flow Stability Program (Dynamic) Phase I Final Technical Report, Part I. Summary, AFAPL-TR-68-142, Part I. December 1968.
13. Schubaur, G. B. and Skramstad, H. K. "Laminar Boundary Layer Oscillation and Stability of Laminar Flow" NACA Report 909, 1948.
14. Hildebrand, F. B., "Introduction to Numerical Analysis" McGraw-Hill Book Co. Inc., 1956, pg. 447.